An Investigation of the Structural and Electronic Properties of Covalently Bonded Molecular Networks on Metal Surfaces Formed Through Debromination Reactions

A thesis for the degree of

PHILOSOPHIAE DOCTOR

Catherine Doyle B.Sc.

School of Physical Sciences

Dublin City University

Research Supervisor

Dr. Tony Cafolla

External Examiner: Dr. Aidan Quinn

Internal Examiner: Prof. Greg Hughes

July 2013

Declaration

I hereby certify that this material, which I now submit for assessment on the programme of study leading to the award of Doctor of Philosophy is entirely my own work, that I have exercised reasonable care to ensure that the work is original, and does not to the best of my knowledge breach any law of copyright, and has not been taken from the work of others save and to the extent that such work has been cited and acknowledged within the text of my work.

Signed: _____

ID No.: _____

Date: _____

Acknowledgements

Firstly I would like to thank Dr. Tony Cafolla, my Ph.D. supervisor, for being so generous with his time, so knowledgeable and so involved. Tony's enthusiasm for physics and for science fiction helped make the last few years, particularly time spent at beamlines, a lot of fun.

Thanks to all the members of the Surface and Interface Research Laboratory, especially everyone who has worked here in SG11 - Mr. Tom Carpy, Dr. John Cunniffe, Dr. John Beggan, Dr. Hooi Ling Lee, Dr. Sergey Krasnikov and Dr. Cedric Volcke.

My Ph.D. project benefited hugely from our collaborations with researchers from Trinity College Dublin. Thank you to Prof. Mathias Senge, Dr. Natalia Sergeeva and the other members of the SFI Tetrapyrrole Laboratory for synthesising the molecules used in this work, to Dr. Cormac McGuinness and Ms. Anna Lawless for performing DFT calculations, and to Prof. Iggy McGovern, Dr. Nina Berner, Mr. Zhiming Wang and Dr. Olaf Lübben for being such good company on beamtimes.

I would like to acknowledge the help and assistance of the staff at the two synchrotron radiation facilities where I carried out experiments, especially Dr. Alexei Preobrajenski and Dr. Nikolay Vinogradov at MAX-lab, Lund University, Sweden, and Dr. Zheshen Li at ISA, Aarhus University, Denmark.

I gratefully acknowledge the Irish Research Council for Science, Engineering and Technology (IRCSET) for funding this project.

Thank you to everyone who made the nine years I've spent in DCU so enjoyable - our undergrad class, postgraduate students past and present, and the faculty and staff in the School of Physical Sciences.

Thank you to Mick Moriarty, my physics teacher in Dominican College, Griffith Avenue, for setting me on the road to studying physics at university.

Finally, sincere thanks to my parents, Marie and Seán, and my sister, Louise, who have been so supportive, encouraging and understanding through all my many years as a student.

to my family

Publications

Formation of Extended Covalently Bonded Ni Porphyrin Networks on the Au(111) Surface
S.A. Krasnikov, **C.M. Doyle**, N.N. Sergeeva, A.B. Preobrajenski, N.A. Vinogradov, Y.N. Sergeeva, A.A. Zakharov, M.O. Senge, A.A. Cafolla, *Nano Research* 2011 **4** 376-384.

Evidence for the Formation of an Intermediate Complex in the Direct Metalation of tetra(4-bromophenyl)-porphyrin on the Cu(111) Surface
C.M. Doyle, S.A. Krasnikov, N.N. Sergeeva, A.B. Preobrajenski, N.A. Vinogradov, Y.N. Sergeeva, M.O. Senge, A.A. Cafolla, *Chemical Communications* 2011 **47** 12134-12136

Ni-Cu Ion Exchange Observed for Ni(II) Metalated Porphyrins on Cu(111)
C.M. Doyle, J.P. Cunniffe, S.A. Krasnikov, A.B. Preobrajenski, Z. Li, N.N. Sergeeva, M.O. Senge, A.A. Cafolla, in preparation

Conference Contributions

Oral Presentations

The Formation of Covalently Bonded Porphyrin Networks on Metal Surfaces
ECOSS-26, Parma, Italy, 1st September 2009.

The Formation of Covalently Bonded Porphyrin Networks on Metal Surfaces
National Centre for Sensor Research (NCSR) 10th Anniversary Symposium, Dublin City University, 22nd October 2009.

The Formation of Covalently Bonded Porphyrin Networks on Metal Surfaces
NASM3, Manchester, England, 13th April 2010.

Comparison of Covalent Nano-Structure Formation on Metal Surfaces for Two, Three and Fourfold Symmetrical Brominated Molecules
ECOSS-29, Edinburgh, Scotland, 7th September 2012.

Conference Contributions

Poster Presentations

Preliminary Study of Tetrabromophenyl Porphyrin Molecules on Metal Surfaces using STM and Synchrotron Radiation
BOC Gases Postgraduate Poster Competition, School of Physical Sciences, Dublin City University, 20th February 2009. Second prize.

The Formation of Covalently Bonded Porphyrin Networks on Metal Surfaces
NASM3, Manchester, England, 13th April 2010. Winner, Applied Physics and Technology Division Best Student Poster Prize 2010.

The Formation of Covalently Bonded Nano-Networks on Metal Surfaces
ECOSS-27, Groningen, The Netherlands, 30th August 2010.

Porphyrin Networks on Cu(111) and Au(111) Surfaces
ISSC-18, Warwick, England, 4th April 2011.

Observation of an Intermediate State in the Metalation of H_2 5,10,15,20 tetra(4-bromophenyl)porphyrin by Cu(111) Surface Atoms
ECOSS-28, Wroclaw, Poland, 29th August 2011.

Observation of an Intermediate State in the Metalation of H_2 5,10,15,20 tetra(4-bromophenyl)porphyrin by Cu(111) Surface Atoms
BOC Gases Postgraduate Poster Competition, School of Physical Sciences, Dublin City University, 13th April 2012. First prize.

An Investigation of the Structural and Electronic Properties of Covalently Bonded Molecular Networks on Metal Surfaces Formed Through Debromination Reactions

by

Catherine Doyle

Abstract

This thesis discusses the deposition, self-assembly, network formation, and molecule-substrate interaction of brominated molecules with four-, three- and two-fold symmetry on the Au(111), Au(110), Ag(111) and Cu(111) metal surfaces. Characterisation was carried out using scanning tunneling microscopy (STM), x-ray photoelectron spectroscopy (XPS), low energy electron diffraction (LEED), and synchrotron radiation based photoelectron spectroscopy (PES) and x-ray absorption spectroscopy (XAS).

Covalently bonded nano-networks were formed via radical addition following thermal debromination of the molecules. Networks on the order of $10\,000\,\mathrm{nm}^2$ were observed on Au(111), and exhibited thermal stability up to 500 °C. Network formation was inhibited on Cu(111) by the significant molecule-substrate interaction, leading to mass transport of Cu atoms and the formation of Cu adatom islands on annealing at 350 °C and higher.

The Ag and Cu surfaces were sufficiently reactive to catalytically cleave the C-Br bond on deposition, leading to the formation of metal-coordinated protopolymer networks. These structures were converted to covalently bonded networks after subsequent thermal annealing.

The first reported *in situ* metalation of a free base porphyrin molecule using substrate atoms was carried out for 5,10,15,20-tetrakis(4-bromophenyl) porphyrin (H_2TBrPP) on Cu(111). This also constituted the first direct observation of the reaction intermediate state on a surface.

A Ni-Cu ion exchange was observed for Ni(II) 5,10,15,20-tetrakis(4-bromophenyl) porphyrin (NiTBrPP) and Ni(II) 5,15-dibromo-10,20-diphenyl porphyrin (NiDBrDPP) on Cu(111), whereby the Ni(II) ions in the porphyrin macrocycle exchanged with Cu atoms from the substrate, resulting in Cu-metalated porphyrins and metallic Ni atoms. The reaction enthalpy was the same for both NiDBrDPP/Cu(111) and NiTBrPP/Cu(111); however the entropy was greater for NiDBrDPP/Cu(111) than for NiTBrPP/Cu(111). This is attributed to the difference in symmetry of the molecules.

Contents

List of Figures

List of Tables

Chapter 1
Introduction and Motivation

Surface science is a broad field encompassing aspects of physics, chemistry and biology. It involves the formation, characterisation and manipulation of nano-scale structures on surfaces, in both ultra high vacuum and ambient conditions. The present work is concerned with the formation and characterisation of molecular architectures on metal surfaces in ultra high vacuum. The research undertaken constitutes an investigation of nano-networks formed *in situ* by the thermal dissociation of C-Br bonds and subsequent formation of covalently bonded structures. The effect of the symmetry of the initial molecular building blocks on the nano-networks is considered. In addition, some interesting and unexpected results involving molecule-substrate interactions are discussed.

This chapter introduces porphyrins, the organic molecules used in the present work. A brief overview of the literature pertaining to supramolecular structures and molecular frameworks is also presented, leading to the motivation for the present work. The chapter concludes with an outline of the thesis structure.

1.1 Porphyrins

Porphyrins are a family of organic molecules with a central pi-conjugated aromatic macrocycle consisting of four pyrrole rings ((C_4H_4NH) or (C_4H_4N)). Figure 1.1 shows a planar free base porphine, the most basic porphyrin molecule [1]. Two distinct nitrogen environments are indicated in the figure, iminic nitrogen which is bonded to two carbon atoms in the pyrrole ring, and pyrrolic nitrogen which is also bonded to hydrogen. The porphine macrocycle can be modified in various ways to form larger porphyrin molecules. A wide range of substituents including phenyl, thienyl, methyl, and octaethyl groups can be bonded to either the *meso* or *beta* positions on the macrocycle (Figure 1.1) [2–5]. Such modification of the porphine macrocycle often results in the larger porphyrin molecule exhibiting

non-planar distortions such as saddling or ruffling of the macrocycle, and axial rotation of the substituents [6–8].

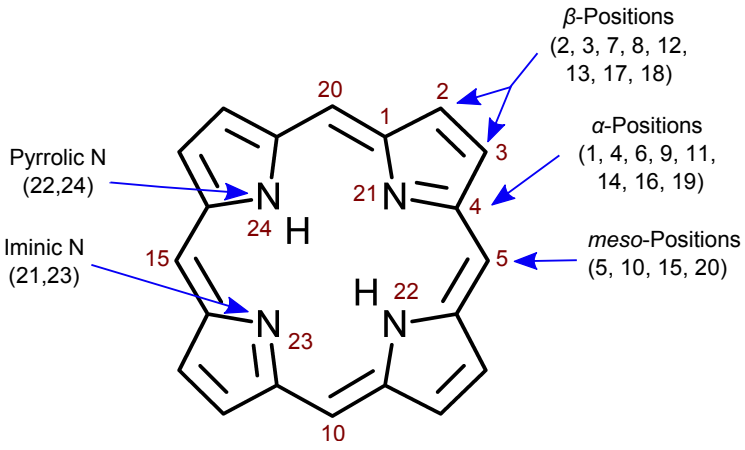

Figure 1.1: Structure of a porphine macrocycle, $C_{20}H_{14}N_4$. Hydrogens not shown explicitly, except for the hydrogens bonded to the pyrrolic nitrogen atoms.

Porphyrins are generally synthesised as free base molecules, using wet chemical techniques [2, 9]. It is also possible to modify the core of the macrocycle by incorporation of metal ions to form a metalated porphyrin. Porphyrins have been metalated with almost all of the transition elements and many other metals in the Periodic Table [10]. The choice of metal centre influences the electronic structure of the porphyrin, allowing the properties to be tailored to a particular application (Section 1.2). In 1960 Fleischer and Wang [11] proposed that the metalation proceeds via the formation of an intermediate state whereby the iminic nitrogen atoms bond to the metal ion, while the pyrrolic nitrogen atoms retain their hydrogen atoms, which then dissociate as H_2, leaving all four nitrogen atoms bonded to the metal ion [11–15]. Metalated porphyrins can also coordinate an axial ligand, for example Mn and Fe porphyrins are known to coordinate Cl atoms [16]. In blood, the haem group is an Fe-metalated porphyrin with the ability to coordinate O_2 as a ligand which, in turn, enables haemoglobin to transport oxygen around the human body [17, 18]. Similarly, the chlorophyll molecule has a Mg porphyrin as its functional unit [6, 19]. As such, porphyrin molecules are extremely significant in many biological systems.

In addition to the possibility of tuning the electronic and chemical structures of the porphyrin, the molecules are suitable for *in situ* deposition onto surfaces by means of thermal sublimation. As such, the adsorption of porphyins on surfaces has recently been the subject of extensive research [20–25].

1.2 Applications Involving Porphyrins

Porphyrins are involved in a wide and varied range of applications [26], some examples of which are discussed briefly here.

Porphyrins are utilised in several different methods of sensing. Arrays of porphyrins have been used as oxygen sensors, operating via phosphorescence quenching, whereby oxygen collides with a porphyrin and is excited into the singlet state, thereby quenching the phosphorescent signal of the porphyrins [27–30]. The quenching is reversible, so the porphyrin array can be reused. Platinum and palladium porphyrins have been found to exhibit good quenching efficiency [27–29]. Porphyrins have also been used to mimic the mammalian olfactory system [31]. This is achieved by exploiting the fact that many odiferous compounds can be coordinated by the metal ion in the porphyrin macrocycle. Rakow *et al.* have fabricated an array of metalloporphyrin dyes whereby a colour change denotes the presence of particular compounds bonded to the metal centres. The porphyrin array is sensitive to concentrations below 2 parts per million [31]. Cotton threads impregnated with Zn tetraphenyl porphyrin and Fe tetraphenyl porphyrin have recently been shown to be effective gas sensors [32].

The light-harvesting properties of porphyrins, as evidenced by their role in photosynthesis, are exploited to increase the efficiency of dye-sensitised solar cells (DSSC) [33–36]. Halogenated tetraphenyl porphyrin (TPP) molecules have been studied, with chlorine TPP substituted with twelve chlorine atoms found to be a more effective photosensitizer than either the fluorinated analogue or unsubstituted TPP [37]. In addition, solar cells using a zinc porphyrin dye have been shown to exceed 12 % efficiency [38].

Photodynamic therapy (PDT) is a cancer treatment which also makes use of the photosensitizing properties of porphyrins [9, 39]. The photosensitizers are absorbed by tumour cells, which are then irradiated with visible light. The excited porphyrins react with molecular oxygen to produce singlet oxygen, which is cytotoxic and leads to the death of the tumour cells. In some cases the vasculature is also damaged, starving the tumour of nutrients [40]. Cases of PDT stimulating an improved immune response have also been reported [41]. PDT

has many advantages over other cancer treatments, including being non-toxic and preferentially targeting tumour cells [41]. The accumulation of porphyrin photosensitizers in cancerous tissue is achieved by targeted delivery systems involving coupling the photosensitizer to a site-selective antibody [40].

The axial coordination of ligands by the metal centre of the porphyrin has applications in catalysis [42]. Speller *et al.* have reported an alkene to expoxide reaction catalysed by a Mn porphyrin at a liquid-solid interface [16]. The Mn porphyrins were deposited in an argon-saturated tetradecane solution onto a Au(111) surface, and reacted with molecular oxygen introduced to the system. Single oxygen atoms were coordinated by the Mn centres, with the atoms from each O_2 molecule distributed over two adjacent Mn porphyrins. An alkene was added to the surface of the liquid, and after diffusion to the liquid-solid interface an epoxidation reaction took place via the porphyrin-stabilised oxygen atoms [16].

Porphyrins also play an important role in molecular electronics [43]. Thanopoulos *et al.* have created a molecular junction using Au nanoparticles as electrodes and a free base porphine as a switch. The laser-induced switching behaviour derives from the two degenerate states arising from the distinct nitrogen chemical environments in the macrocycle (Figure 1.1) [44]. Porphyrins have also featured in other molecular electronic devices such as wires [45] and diodes [46].

1.3 Molecular Networks

The formation of molecular networks is one of the topics explored in this thesis. Such networks are a subject of intense research interest, as they open up numerous possibilities for nano-scale control and functionalisation on surfaces. One application of reproducible network formation is a 'bottom-up' alternative to the traditional 'top-down' lithographic approach of the semiconductor industry. Circumventing resolution problems which are a challenge faced by that industry, bottom-up fabrication would allow devices to be assembled on a molecule-by-molecule or atom-by-atom basis [47]. Other applications include molecular engineering, host-guest complexes, molecular sieves, and sensors [47–52]. The development of scanning tunneling microscopy (STM) as an analytical tool in the 1980s (Section 2.2) allows molecular networks to be imaged locally in real-space, which is an advantage in the characterisation of the nano-structures [53].

Several bonding strategies have been investigated for networks, and the nano-structures resulting from each are suited to different applications. For

creating nanoscale removable masks on surfaces in order to template the substrate for subsequent depositions, long range order is an important property of such networks, while thermal stability is less significant, and in some cases may even be undesirable. Suitable bonding strategies for network formation include hydrogen bonding and coordination by a metal atom [54].

Blunt *et al.* have formed an ordered array of hydrogen bonded tetracarboxylic acid molecules on graphite, which can be mapped onto a rhombus tiling [55], while Theobald *et al.* have reported a well-ordered hexagonal network based on hydrogen bonding between perylene tetra-carboxylic di-imide (PTCDI) and melamine on a Ag/Si(111) substrate, which has been used as a template for C_{60} fullerenes [56]. Well-ordered dicarboxylic acid networks stablilised by hydrogen bonding and van der Waals interactions have been observed on Au(111) [57], while a hydrogen bonded molecular network formed through a solution-based assembly of PTCDI and melamine on Au(111) has been used as a host structure for thiol molecules [58].

Many metal-organic coordinated networks (MOCN) have been reported in the literature, some of which are discussed in review articles by Stepanow [59] and Barth [60, 61]. Some notable examples include hexaphenyl molecules coordinated by Co atoms on Ag(111), producing a nano-network with long range order over an area of 240 000 nm^2 [62]. Similarly ordered networks have also been achieved on Ag(111) using triphenyl linkers coordinated by Co atoms [63]. Matena *et al.* have observed tetraazaperopyrene (TAPP) molecules forming a self-assembled hydrogen bonded structure on Cu(111), which is converted to a Cu-coordinated MOCN after annealing at 80 °C [64], while networks formed with carboxylate linker molecules coordinated by Fe atoms on Cu(100) have been used to host C_{60} fullerenes [65]. MOCNs on Au(111) featuring tripyridyl ligands coordinated with either Cu or Fe metal atoms have been shown to be thermally stable to 300 °C and 400 °C respectively [66].

The long range order achieved with hydrogen bonding and metal-organic coordination arises from the reversible nature of the bonds, so that most structural defects can correct themselves at the growth temperature, leading to 'self-healing' networks [53]. However, the reversible nature of the bonds can limit the thermal stability and strength of the networks [53]. For applications where robust networks which can withstand annealing at temperatures in excess of 400 °C are required, covalent bonding is a more appropriate bonding strategy. Once formed, the covalent bonds are thermally stable to at least 500 °C [67].

However, any structural defects which are present in the network cannot be corrected, a challenge known as the 'crystallization problem' [53]. Nevertheless, the benefits due to the stability of the networks have stimulated much research in this area [53, 68].

Extensive nano-networks have been achieved on Ag(111) by covalently bonding boronated molecules via a dehydration reaction [69–71]. A polyimide network has been observed on Au(111), formed by a condensation reaction between diamine and dianhydride molecules [72].

A popular method of forming covalently bonded networks is radical addition following carbon-halogen bond cleavage. This has been achieved for molecules functionalised with either iodine or bromine. The C-I and C-Br bond strengths are 2.81 eV and 3.46 eV respectively, as measured for C_6H_5I and C_6H_5Br [53, 73]. As the C-C bond strength is 4.8 eV [74], the halogen atom can be removed without dissociating the C-C bonds. Various methods of dissociating the carbon-halogen bond exist, including inducing bond cleavage with the STM tip [75], deposition on a catalytic substrate such as Cu [76], and thermal dissociation [2, 77].

Hla *et al.* demonstrated tip-induced dissociation of a halogenated phenyl molecule followed by radical addition in 2000 [75]. Iodobenzene, C_6H_5I, was dissociated to form a phenyl radical and iodine on Cu(111); two phenyl radicals were then moved to close proximity and covalently bonded to form biphenyl, which was then pulled along the surface by the tip to verify the covalent bond. Each step of the reaction was induced by the STM tip [75].

The on-surface analogue to the Ullmann reaction [78, 79], where the Cu substrate cleaves the carbon-halogen bond, has been used in the formation of nano-structures. Lipton-Duffin *et al.* have reported the catalytic cleaving of the C-I bonds in diiodobenzene, and the subsequent covalent bonding of the resultant radicals following annealing [76]. This surface-assisted bonding strategy has been used to fabricate hexagonal structures similar to graphene on Ag(111) from hexaiodo-substituted cyclohexa-m-phenylene molecular units [80].

Covalent bonding of triply iodinated monomers on Au(111) at room temperature has been reported, with further annealing leading to the growth of covalent networks [81, 82]. By comparison, covalent bonding of the brominated analogue, trisbromophenyl benzene (TBB), is only observed on Au(111) following annealing [77, 83], due to the difference in the C-I and C-Br bond strengths mentioned above [84]. TBB network formation on Cu(111) and Ag(110) has also been reported, where the surface-catalyzed C-Br bond cleavage at room

temperature results in an intermediate metal-coordinated network, which is then converted to a covalently bonded structure by annealing at 300 °C [85, 86]. Dibromo-bianthryl molecules have been polymerised into linear chains by thermal debromination and radical addition, and a subsequent thermal surface-assisted cyclodehydrogenation reaction results in the formation of graphene nano-ribbons on Au(111) [87].

All of the covalently bonded networks discussed thus far were formed on conducting substrates. Growth of nano-networks on an ultrathin insulating layer would decouple the networks from the substrate, an advantage in studying the electronic properties of the nano-structures [53]. Some progress has been made in this area; the formation of a covalently bonded Fe phthalocyanine network has been reported on monolayer islands of insulating NaCl on Ag(100) [71], while networks formed from a variety of halogenated benzoic acid monomers have been produced on calcite [88].

1.4 Covalently Bonded Porphyrin Networks

Given the numerous functionalisation possibilities of porphyrins (Section 1.2), and the nano-scale control offered by molecular network formation (Section 1.3), it is not surprising that the formation of covalently bonded porphyrin networks has been the subject of recent intensive investigations [2, 4, 89]. Raval *et al.* have reported network formation through the thermal linkage of tetra(mesityl)porphyrin molecules on Cu(110) [4]. The four methyl groups are deprotonated to form reactive CH_2 radicals, allowing the porphyrin units to bond covalently with each other [4].

An alternative bonding strategy, using the debromination reaction discussed above (Section 1.3), was demonstrated by Grill *et al.* in 2007. Brominated tetraphenyl porphyrin molecules were deposited on Au(111), and the bromine atoms were subsequently thermally dissociated [2]. The porphyrin radicals then diffused on the substrate and formed covalently bonded nano-structures. Network formation was also achieved by dissociating the bromine prior to deposition by sublimating the molecules at a higher temperature [2]. Singly and doubly brominated tetraphenyl porphyrin units were also studied, leading to the formation of bi-porphyrin molecules and linear chains respectively [2]. Grill *et al.* have also investigated network formation using a tetraphenyl porphyrin molecule substituted with two bromine and two iodine atoms in a linear *trans* arrangement [90]. The difference in the C-I and C-Br bond strengths allows for a stepwise

dissociation; the initial C-I bond cleavage results in the formation of linear chains, which can then be subsequently cross-linked following Br dissociation [90].

1.5 Thesis Outline

The work presented in this thesis focuses on brominated molecules adsorbed on surfaces and investigates covalent network formation and molecule-substrate interactions. The network formation is accomplished using the debromination and subsequent radical addition bonding strategy described by Grill *et al.* [2], a schematic of which is shown in Figure 1.2. The present work examines network formation using molecular units of four, three and two-fold symmetry on the Au(111), Au(110), Ag(111) and Cu(111) metal substrates.

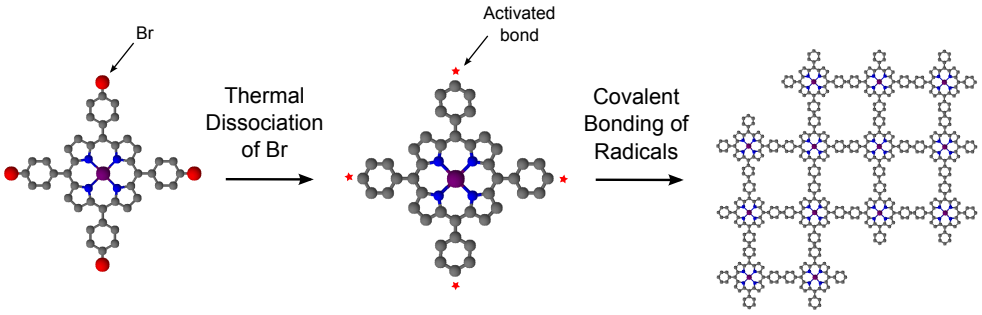

Figure 1.2: Bonding strategy for covalent network formation. Porphyrin molecules are thermally debrominated and diffuse on the surface to covalently bond at the former bromine sites, forming a nano-network. Based on [2].

The layout of the thesis is as follows: Chapter Two introduces the experimental techniques used in the present work: scanning tunneling microscopy, photoelectron spectroscopy, low energy electron diffraction, photoemission spectroscopy, and x-ray absorption spectroscopy. A brief introduction to density functional theory is also included. The relevant metal substrates and organic molecules employed in this work are also discussed.

The results for the four-fold tetrabromophenyl porphyrin (TBrPP) molecules on the Au(111), Ag(111) and Cu(111) substrates are presented and discussed in Chapter 3. Network formation is discussed, in addition to the *in situ* metalation of free base TBrPP.

Chapter 4 presents the results for the three-fold trisbromophenyl benzene (TBB) molecule on Au(111), Au(110), and Cu(111). Density Functional Theory

calculations performed by Dr. Cormac McGuinness and Ms. Anna Lawless from the School of Physical Sciences, Trinity College Dublin are also compared with photoemission and x-ray absorption spectroscopy data.

The results for the two-fold dibromo-diphenyl porphyrin (DBrDPP) molecule on the Au(111), Au(110), Ag(111) and Cu(111) substrates are presented in Chapter 5. The self-assembly of the molecules is considered, as well as the formation of metal-coordinated structures and covalently bonded nano-networks.

Chapter 6 presents spectroscopic evidence for a previously unreported Ni-Cu ion exchange for Ni(II)-metalated TBrPP and DBrDPP on the Cu(111) substrate. The enthalpy and entropy for each system is discussed.

Finally, Chapter 7 concludes the thesis with a summary of the results obtained and suggestions for some future experiments which would complement the present work.

1.6 Bibliography

[1] Chen, B.M.L. and Tulinsky, A., *Redetermination of the Structure of Porphine*, Journal of the American Chemical Society, **94** (1972) pp. 4144–4151.

[2] Grill, L., Dyer, M., Lafferentz, L., Persson, M., Peters, M., and Hecht, S., *Nano-architectures by covalent assembly of molecular building blocks*, Nature Nanotechnology, **2** (2007) pp. 687–691.

[3] Boyle, N.M., Rochford, J., and Pryce, M.T., *Thienyl-Appended porphyrins: Synthesis, photophysical and electrochemical properties, and their applications*, Coordination Chemistry Reviews, **254** (2010) pp. 77–102.

[4] In't Veld, M., Iavicoli, P., Haq, S., Amabilino, D.B., and Raval, R., *Unique intermolecular reaction of simple porphyrins at a metal surface gives covalent nanostructures*, Chemical Communications, 13 (2008) pp. 1536–1538.

[5] Bai, Y., Buchner, F., Kellner, I., Schmid, M., Vollnhals, F., Steinrueck, H.P., Marbach, H., and Gottfried, J.M., *Adsorption of cobalt (II) octaethylporphyrin and 2H-octaethylporphyrin on Ag(111): new insight into the surface coordinative bond*, New Journal of Physics, **11** (2009) pp. 125004–1–125004–15.

[6] Senge, M.O., *Exercises in molecular gymnastics - bending, stretching and twisting porphyrins*, Chemical Communications, 3 (2006) pp. 243–256.

[7] Medforth, C.J., Senge, M.O., Smith, K.M., Sparks, L.D., and Shelnutt, J.A., *Nonplanar Distortion Modes for Highly Substituted Porphyrins*, Journal of the American Chemical Society, **114** (1992) pp. 9859–9869.

[8] Vangberg, T. and Ghosh, A., *A first-principles quantum chemical analysis of the factors controlling ruffling deformations of porphyrins: Insights from the molecular structures and potential energy surfaces of silicon, phosphorus, germanium, and arsenic porphyrins and of a peroxidase compound I model*, Journal of the American Chemical Society, **121** (1999) pp. 12154–12160.

[9] Senge, M.O., Fazekas, M., Pintea, M., Zawadzka, M., and Blau, W.J., *5,15-A_2B_2- and 5,15-A_2BC-Type Porphyrins with Donor and Acceptor*

Groups for Use in Nonlinear Optics and Photodynamic Therapy, European Journal of Organic Chemistry, 29 (2011) pp. 5797–5816.

[10] Vaid, T.P., *A Porphyrin with a C = C Unit at Its Center*, Journal of the American Chemical Society, **133** (2011) pp. 15838–15841.

[11] Fleischer, E.B. and Wang, J.H., *The Detection of a Type of Reaction Intermediate in the Combination of Metal Ions with Porphyrins*, Journal of the American Chemical Society, **82** (1960) pp. 3498–3502.

[12] Inada, Y., Sugimoto, Y., Nakano, Y., Itoh, N., and Funahashi, S., *Formation and deprotonation kinetics of the sitting-atop complex of copper(II) ion with 5,10,15,20-tetraphenylporphyrin relevant to the porphyrin metalation mechanism. Structure of copper(II)-pyridine complexes in acetonitrile as determined by EXAFS spectroscopy*, Inorganic Chemistry, **37** (1998) pp. 5519–5526.

[13] Inamo, M., Kamiya, N., Inada, Y., Nomura, M., and Funahashi, S., *Structural characterization and formation kinetics of sitting-atop (SAT) complexes of some porphyrins with copper(II) ion in aqueous acetonitrile relevant to porphyrin metalation mechanism. Structures of aquacopper(II) and Cu(II)-SAT complexes as determined by XAFS spectroscopy*, Inorganic Chemistry, **40** (2001) pp. 5636–5644.

[14] Shubina, T.E., Marbach, H., Flechtner, K., Kretschmann, A., Jux, N., Buchner, F., Steinrueck, H.P., Clark, T., and Gottfried, J.M., *Principle and mechanism of direct porphyrin metalation: Joint experimental and theoretical investigation*, Journal of the American Chemical Society, **129** (2007) pp. 9476–9483.

[15] De Luca, G., Romeo, A., Scolaro, L.M., Ricciardi, G., and Rosa, A., *Sitting-Atop Metallo-Porphyrin Complexes: Experimental and Theoretical Investigations on Such Elusive Species*, Inorganic Chemistry, **48** (2009) pp. 8493–8507.

[16] Hulsken, B., van Hameren, R., Gerritsen, J.W., Khoury, T., Thordarson, P., Crossley, M.J., Rowan, A.E., Nolte, R.J.M., Elemans, J.A.A.W., and Speller, S., *Real-time single-molecule imaging of oxidation catalysis at a liquid-solid interface*, Nature Nanotechnology, **2** (2007) pp. 285–289.

[17] Hoard, J.L., *Stereochemistry of Hemes and Other Metalloporphyrins*, Science, **174** (1971) pp. 1295–1302.

[18] Castro, C.E., *Theory of Hemeprotein Reactivity*, Journal of Theoretical Biology, **33** (1971) pp. 475–490.

[19] Fleming, I., *Absolute Configuration and Structure of Chlorophyll*, Nature, **216** (1967) pp. 151–152.

[20] Otsuki, J., *STM Studies on Porphyrins*, Coordination Chemistry Reviews, **254** (2010) pp. 2311–2341.

[21] Elemans, J.A.A.W., van Hameren, R., Nolte, R.J.M., and Rowan, A.E., *Molecular materials by self-assembly of porphyrins, phthalocyanines, and perylenes*, Advanced Materials, **18** (2006) pp. 1251–1266.

[22] Klappenberger, F., Weber-Bargioni, A., Auwaerter, W., Marschall, M., Schiffrin, A., and Barth, J.V., *Temperature Dependence of Conformation, Chemical State, and Metal-Directed Assembly of Tetrapyridyl-porphyrin on Cu(111)*, Journal of Chemical Physics, **129** (2008) pp. 214702–1–214702–10.

[23] Xiao, J., Ditze, S., Chen, M., Buchner, F., Stark, M., Drost, M., Steinrueck, H.P., Gottfried, J.M., and Marbach, H., *Temperature-Dependent Chemical and Structural Transformations from 2H-tetraphenylporphyrin to Copper(II)-Tetraphenylporphyrin on Cu(111)*, Journal of Physical Chemistry C, **116** (2012) pp. 12275–12282.

[24] Buchner, F., Kellner, I., Hieringer, W., Goerling, A., Steinrueck, H.P., and Marbach, H., *Ordering aspects and intramolecular conformation of tetraphenylporphyrins on Ag(111)*, Physical Chemistry Chemical Physics, **12** (2010) pp. 13082–13090.

[25] Iancu, V., Deshpande, A., and Hla, S.W., *Manipulating Kondo temperature via single molecule switching*, Nano Letters, **6** (2006) pp. 820–823.

[26] Kadish, K.M., Smith, K.M., and Guilard, R. (Editors), The Porphyrin Handbook Volume 6 - Applications: Past, Present and Future, 1st ed., Academic Press, San Diego, 2000.

[27] Amao, Y., Asai, K., Miyashita, T., and Okura, I., *Novel optical oxygen sensing material: Platinum porphyrin-fluoropolymer film*, Polymers for Advanced Technologies, **11** (2000) pp. 705–709.

[28] Amao, Y. and Okura, I., *Optical oxygen sensor devices using metalloporphyrins*, Journal of Porphyrins and Phthalocyanines, **13** (2009) pp. 1111–1122.

[29] Mills, A., *Optical Oxygen Sensors*, Platinum Metals Review, **41** (1998) pp. 115–127.

[30] Douglas, P. and Eaton, K., *Response characteristics of thin film oxygen sensors, Pt and Pd octaethylporphyrins in polymer films*, Sensors and Actuators B - Chemical, **82** (2002) pp. 200–208.

[31] Rakow, N.A. and Suslick, K.S., *A colorimetric sensor array for odour visualization*, Nature, **406** (2000) pp. 710–713.

[32] Dini, F., Filippini, D., Paolesse, R., Lundstrom, I., and Natale, C.D., *Computer screen assisted digital photography*, Sensors and Actuators B - Chemical, **179** (2013) pp. 46–53.

[33] Ishida, M., Park, S.W., Hwang, D., Koo, Y.B., Sessler, J.L., Kim, D.Y., and Kim, D., *Donor-Substituted beta-Functionalized Porphyrin Dyes on Hierarchically Structured Mesoporous TiO_2 Spheres. Highly Efficient Dye-Sensitized Solar Cells*, Journal of Physical Chemistry C, **115** (2011) pp. 19343–19354.

[34] Griffith, M.J., James, M., Triani, G., Wagner, P., Wallace, G.G., and Officer, D.L., *Determining the Orientation and Molecular Packing of Organic Dyes on a TiO_2 Surface Using X-ray Reflectometry*, Langmuir, **27** (2011) pp. 12944–12950.

[35] Campbell, W.M., Burrell, A.K., Officer, D.L., and Jolley, K.W., *Porphyrins as Light Harvesters in the Dye-Sensitized TiO_2 Solar Cell*, Coordination Chemistry Reviews, **248** (2004) pp. 1363–1379.

[36] O'Regan, B. and Graetzel, M., *A Low-Cost, High-Efficiency Solar-Cell Based on Dye-Sensitized Colloidal TiO_2 Films*, Nature, **353** (1991) pp. 737–740.

[37] Wrobel, D., Siejak, A., and Siejak, P., *Photovoltaic and spectroscopic studies of selected halogenated porphyrins for their application in organic solar cells*, Solar Energy Materials and Solar Cells, **94** (2010) pp. 492–500.

[38] Yella, A., Lee, H.W., Tsao, H.N., Yi, C., Chandiran, A.K., Nazeeruddin, M.K., Diau, E.W.G., Yeh, C.Y., Zakeeruddin, S.M., and Graetzel, M., *Porphyrin-Sensitized Solar Cells with Cobalt (II/III)-Based Redox Electrolyte Exceed 12 Percent Efficiency*, Science, **334** (2011) pp. 629–634.

[39] Bonnett, R., *Photosensitizers of the Porphyrin and Phthalocyanine Series for Photodynamic Therapy*, Chemical Society Reviews, **24** (1995) pp. 19–33.

[40] Dolmans, D., Fukumura, D., and Jain, R.K., *Photodynamic therapy for cancer*, Nature Reviews Cancer, **3** (2003) pp. 380–387.

[41] Castano, A.P., Mroz, P., and Hamblin, M.R., *Photodynamic therapy and anti-tumour immunity*, Nature Reviews Cancer, **6** (2006) pp. 535–545.

[42] Meunier, B., *Metalloporphyrins as Versatile Catalysts for Oxidation Reactions and Oxidative DNA Cleavage*, Chemical Reviews, **92** (1992) pp. 1411–1456.

[43] Jurow, M., Schuckman, A.E., Batteas, J.D., and Drain, C.M., *Porphyrins as molecular electronic components of functional devices*, Coordination Chemistry Reviews, **254** (2010) pp. 2297–2310.

[44] Thanopulos, I., Paspalakis, E., and Yannopapas, V., *Optical Switching of Electric Charge Transfer Pathways in Porphyrin: A Light-Controlled Nanoscale Current Router*, Nanotechnology, **19** (2008) pp. 445202–1–445202–14.

[45] Tsuda, A. and Osuka, A., *Fully conjugated porphyrin tapes with electronic absorption bands that reach into infrared*, Science, **293** (2001) pp. 79–82.

[46] Koiry, S.P., Jha, P., Aswal, D.K., Nayak, S.K., Majumdar, C., Chattopadhyay, S., Gupta, S.K., and Yakhmi, J.V., *Diodes based on bilayers comprising of tetraphenyl porphyrin derivative and fullerene for hybrid nanoelectronics*, Chemical Physics Letters, **485** (2010) pp. 137–141.

[47] Bartels, L., *Tailoring molecular layers at metal surfaces*, Nature Chemistry, **2** (2010) pp. 87–95.

[48] Lafferentz, L., Ample, F., Yu, H., Hecht, S., Joachim, C., and Grill, L., *Conductance of a Single Conjugated Polymer as a Continuous Function of Its Length*, Science, **323** (2009) pp. 1193–1197.

[49] Bombis, C., Ample, F., Lafferentz, L., Yu, H., Hecht, S., Joachim, C., and Grill, L., *Single Molecular Wires Connecting Metallic and Insulating Surface Areas*, Angewandte Chemie International Edition, **48** (2009) pp. 9966–9970.

[50] Tashiro, K. and Aida, T., *Metalloporphyrin hosts for supramolecular chemistry of fullerenes*, Chemical Society Reviews, **36** (2007) pp. 189–197.

[51] Elemans, J.A.A.W., Lei, S., and De Feyter, S., *Molecular and Supramolecular Networks on Surfaces: From Two-Dimensional Crystal Engineering to Reactivity*, Angewandte Chemie International Edition, **48** (2009) pp. 7298–7332.

[52] Bonifazi, D., Mohnani, S., and Llanes-Pallas, A., *Supramolecular Chemistry at Interfaces: Molecular Recognition on Nanopatterned Porous Surfaces*, Chemistry - A European Journal, **15** (2009) pp. 7004–7025.

[53] Lackinger, M. and Heckl, W.M., *A STM perspective on covalent intermolecular coupling reactions on surfaces*, Journal of Physics D - Applied Physics, **44** (2011) pp. 464011–1–464011–14.

[54] Barth, J.V., *Molecular architectonic on metal surfaces*, Annual Review of Physical Chemistry, **58** (2007) pp. 375–407.

[55] Blunt, M.O., Russell, J.C., del Carmen Gimenez-Lopez, M., Garrahan, J.P., Lin, X., Schroeder, M., Champness, N.R., and Beton, P.H., *Random Tiling and Topological Defects in a Two-Dimensional Molecular Network*, Science, **322** (2008) pp. 1077–1081.

[56] Theobald, J.A., Oxtoby, N.S., Phillips, M.A., Champness, N.R., and Beton, P.H., *Controlling molecular deposition and layer structure with supramolecular surface assemblies*, Nature, **424** (2003) pp. 1029–1031.

[57] Xiao, W.D., Jiang, Y.H., Aiet-Mansour, K., Ruffieux, P., Gao, H.J., and Fasel, R., *Chiral Biphenyldicarboxylic Acid Networks Stabilized by Hydrogen Bonding*, Journal of Physical Chemistry C, **114** (2010) pp. 6646–6649.

[58] Madueno, R., Raisanen, M.T., Silien, C., and Buck, M., *Functionalizing hydrogen-bonded surface networks with self-assembled monolayers*, Nature, **454** (2008) pp. 618–621.

[59] Stepanow, S., Lin, N., and Barth, J.V., *Modular assembly of low-dimensional coordination architectures on metal surfaces*, Journal of Physics: Condensed Matter, **20** (2008) pp. 184002–1–184002–15.

[60] Barth, J.V., *Fresh perspectives for surface coordination chemistry*, Surface Science, **603** (2009) pp. 1533–1541.

[61] Lin, N., Stepanow, S., Ruben, M., and Barth, J.V., *Surface-Confined Supramolecular Coordination Chemistry*, Topics in Current Chemistry, **287** (2009) pp. 1–44.

[62] Kuehne, D., Klappenberger, F., Decker, R., Schlickum, U., Brune, H., Klyatskaya, S., Ruben, M., and Barth, J.V., *High-Quality 2D Metal-Organic Coordination Network Providing Giant Cavities within Mesoscale Domains*, Journal of the American Chemical Society, **131** (2009) pp. 3881–3883.

[63] Schlickum, U., Decker, R., Klappenberger, F., Zoppellaro, G., Klyatskaya, S., Ruben, M., Silanes, I., Arnau, A., Kern, K., Brune, H., and Barth, J.V., *Metal-organic honeycomb nanomeshes with tunable cavity size*, Nano Letters, **7** (2007) pp. 3813–3817.

[64] Matena, M., Stoehr, M., Riehm, T., Bjoerk, J., Martens, S., Dyer, M.S., Persson, M., Lobo-Checa, J., Mueller, K., Enache, M., Wadepohl, H., Zegenhagen, J., Jung, T.A., and Gade, L.H., *Aggregation and Contingent Metal/Surface Reactivity of 1,3,8,10-Tetraazaperopyrene (TAPP) on Cu(111)*, Chemistry - A European Journal, **16** (2010) pp. 2079–2091.

[65] Stepanow, S., Lingenfelder, M., Dmitriev, A., Spillmann, H., Delvigne, E., Lin, N., Deng, X.B., Cai, C.Z., Barth, J.V., and Kern, K., *Steering molecular organization and host-guest interactions using two-dimensional nanoporous coordination systems*, Nature Materials, **3** (2004) pp. 229–233.

[66] Shi, Z., Liu, J., Lin, T., Xia, F., Liu, P.N., and Lin, N., *Thermodynamics and Selectivity of Two-Dimensional Metallo-supramolecular Self-Assembly*

Resolved at Molecular Scale, Journal of the American Chemical Society, **133** (2011) pp. 6150–6153.

[67] Krasnikov, S.A., Doyle, C.M., Sergeeva, N.N., Preobrajenski, A.B., Vinogradov, N.A., Sergeeva, Y.N., Zakharov, A.A., Senge, M.O., and Cafolla, A.A., *Formation of extended covalently bonded Ni porphyrin networks on the Au(111) surface*, Nano Research, **4** (2011) pp. 376–384.

[68] Gourdon, A., *On-Surface Covalent Coupling in Ultrahigh Vacuum*, Angewandte Chemie International Edition, **47** (2008) pp. 6950–6953.

[69] Zwaneveld, N.A.A., Pawlak, R., Abel, M., Catalin, D., Gigmes, D., Bertin, D., and Porte, L., *Organized Formation of 2D Extended Covalent Organic Frameworks at Surfaces*, Journal of the American Chemical Society, **130** (2008) pp. 6678–6679.

[70] Coratger, R., Calmettes, B., Abel, M., and Porte, L., *STM observations of the first polymerization steps between hexahydroxy-tri-phenylene and benzene-di-boronic acid molecules*, Surface Science, **605** (2011) pp. 831–837.

[71] Abel, M., Clair, S., Ourdjini, O., Mossoyan, M., and Porte, L., *Single Layer of Polymeric Fe-Phthalocyanine: An Organometallic Sheet on Metal and Thin Insulating Film*, Journal of the American Chemical Society, **133** (2011) pp. 1203–1205.

[72] Treier, M., Richardson, N.V., and Fasel, R., *Fabrication of Surface-Supported Low-Dimensional Polyimide Networks*, Journal of the American Chemical Society, **130** (2008) pp. 14054–14055.

[73] McMillen, D.F. and Golden, D.M., *Hydrocarbon Bond-Dissociation Energies*, Annual Review of Physical Chemistry, **33** (1982) pp. 493–532.

[74] Szwarc, M., *Energy of the Central C-C Bond in Diphenyl*, Nature, **161** (1948) pp. 890–891.

[75] Hla, S.W., Bartels, L., Meyer, G., and Rieder, K.H., *Inducing all steps of a chemical reaction with the scanning tunneling microscope tip: Towards single molecule engineering*, Physical Review Letters, **85** (2000) pp. 2777–2780.

[76] Lipton-Duffin, J.A., Ivasenko, O., Perepichka, D.F., and Rosei, F., *Synthesis of Polyphenylene Molecular Wires by Surface-Confined Polymerization*, Small, **5** (2009) pp. 592–597.

[77] Blunt, M.O., Russell, J.C., Champness, N.R., and Beton, P.H., *Templating molecular adsorption using a covalent organic framework*, Chemical Communications, **46** (2010) pp. 7157–7159.

[78] Ullmann, F. and Bielecki, J., Berichte der Deutschen Chemischen Gesellschaft, **34** (1901) pp. 2174–2185.

[79] Hassan, J., Sevignon, M., Gozzi, C., Schulz, E., and Lemaire, M., *Aryl-aryl bond formation one century after the discovery of the Ullmann reaction*, Chemical Reviews, **102** (2002) pp. 1359–1469.

[80] Bieri, M., Treier, M., Cai, J., Ait-Mansour, K., Ruffieux, P., Groening, O., Groening, P., Kastler, M., Rieger, R., Feng, X., Muellen, K., and Fasel, R., *Porous graphenes: two-dimensional polymer synthesis with atomic precision*, Chemical Communications, 45 (2009) pp. 6919–6921.

[81] Schloegl, S., Heckl, W.M., and Lackinger, M., *On-surface radical addition of triply iodinated monomers on Au(111) - the influence of monomer size and thermal post-processing*, Surface Science, **606** (2012) pp. 999–1004.

[82] Eder, G., Smith, E.F., Cebula, I., Heckl, W.M., Beton, P.H., and Lackinger, M., *Solution Preparation of Two-Dimensional Covalently Linked Networks by Polymerization of 1,3,5-Tri(4-iodophenyl)benzene on Au(111)*, ACS Nano, **7** (2013) pp. 3014–3021.

[83] Russell, J.C., Blunt, M.O., Garfitt, J.M., Scurr, D.J., Alexander, M., Champness, N.R., and Beton, P.H., *Dimerization of Tri(4-bromophenyl)benzene by Aryl-Aryl Coupling from Solution on a Gold Surface*, Journal of the American Chemical Society, **133** (2011) pp. 4220–4223.

[84] Bjork, J., Hanke, F., and Stafstrom, S., *Mechanisms of Halogen-Based Covalent Self-Assembly on Metal Surfaces*, Journal of the American Chemical Society, **135** (2013) pp. 5768–5775.

[85] Gutzler, R., Walch, H., Eder, G., Kloft, S., Heckl, W.M., and Lackinger, M., *Surface mediated synthesis of 2D covalent organic frameworks: 1,3,5-tris(4-bromophenyl)benzene on graphite(001), Cu(111), and Ag(110)*, Chemical Communications, 29 (2009) pp. 4456–4458.

[86] Walch, H., Gutzler, R., Sirtl, T., Eder, G., and Lackinger, M., *Material- and Orientation-Dependent Reactivity for Heterogeneously Catalyzed Carbon-Bromine Bond Homolysis*, Journal of Physical Chemistry C, **114** (2010) pp. 12604–12609.

[87] Cai, J., Ruffieux, P., Jaafar, R., Bieri, M., Braun, T., Blankenburg, S., Muoth, M., Seitsonen, A.P., Saleh, M., Feng, X., Muellen, K., and Fasel, R., *Atomically precise bottom-up fabrication of graphene nanoribbons*, Nature, **466** (2010) pp. 470–473.

[88] Kittelmann, M., Rahe, P., Nimmrich, M., Hauke, C.M., Gourdon, A., and Kuehnle, A., *On-Surface Covalent Linking of Organic Building Blocks on a Bulk Insulator*, ACS Nano, **5** (2011) pp. 8420–8425.

[89] Mohnani, S. and Bonifazi, D., *Supramolecular architectures of porphyrins on surfaces: The structural evolution from 1D to 2D to 3D to devices*, Coordination Chemistry Reviews, **254** (2010) pp. 2342–2362.

[90] Lafferentz, L., Eberhardt, V., Dri, C., Africh, C., Comelli, G., Esch, F., Hecht, S., and Grill, L., *Controlling on-surface polymerization by hierarchical and substrate-directed growth*, Nature Chemistry, **4** (2012) pp. 215–220.

Chapter 2
Experimental Techniques and Methods

The results presented in this thesis were obtained under ultra-high vacuum conditions at pressures of 1×10^{-9} mbar and below. This chapter introduces the various experimental techniques used in the present work. The underlying theory is outlined, and the experimental apparatus is discussed. The single crystal metal surfaces and molecules deposited onto these substrates are also discussed.

2.1 Omicron Ultra High Vacuum System

A schematic of the vacuum system used in this work is shown in Figure 2.1 [1], with labelled photographs shown in Figure 2.2. The following discussion relates to Figure 2.1. The system consists of an analysis chamber (1); a preparation chamber (2); a scanning tunneling microscope chamber (STM) (3) and a fast entry load lock (FEL) (4). The preparation and analysis chambers have respective base pressures of $<1 \times 10^{-10}$ mbar and $<5 \times 10^{-11}$ mbar, maintained by an ion pump and titanium sublimation pumps (10) on each chamber. A turbo molecular pump (9) backed by a rotary pump is also attached, through a pneumatically operated gate valve, to the preparation chamber [2, 3]. These pumps are used during the initial pump down procedure and during Ar^+ ion sputtering of the metal substrates.

Gate valves (7) isolate the analysis chamber, preparation chamber, and fast entry load lock from each other. This allows a sample to be placed in the load lock and subsequently transferred into the preparation chamber using the magnetic transfer rod (13) without venting the system. The preparation chamber is equipped with an argon ion sputter gun, a manipulator with resistive heating capability, and three evaporators used for molecular deposition. The analysis chamber includes a manipulator with direct and resistive heating capability; a DAR 400 twin-anode x-ray source; an EA 125 energy analyser used for x-ray photoelectron spectroscopy (XPS), and an Omicron low energy electron

diffraction (LEED) system. A wobble stick is used to transfer samples between the manipulator and the STM. The Omicron VT STM chamber is attached to the analysis chamber.

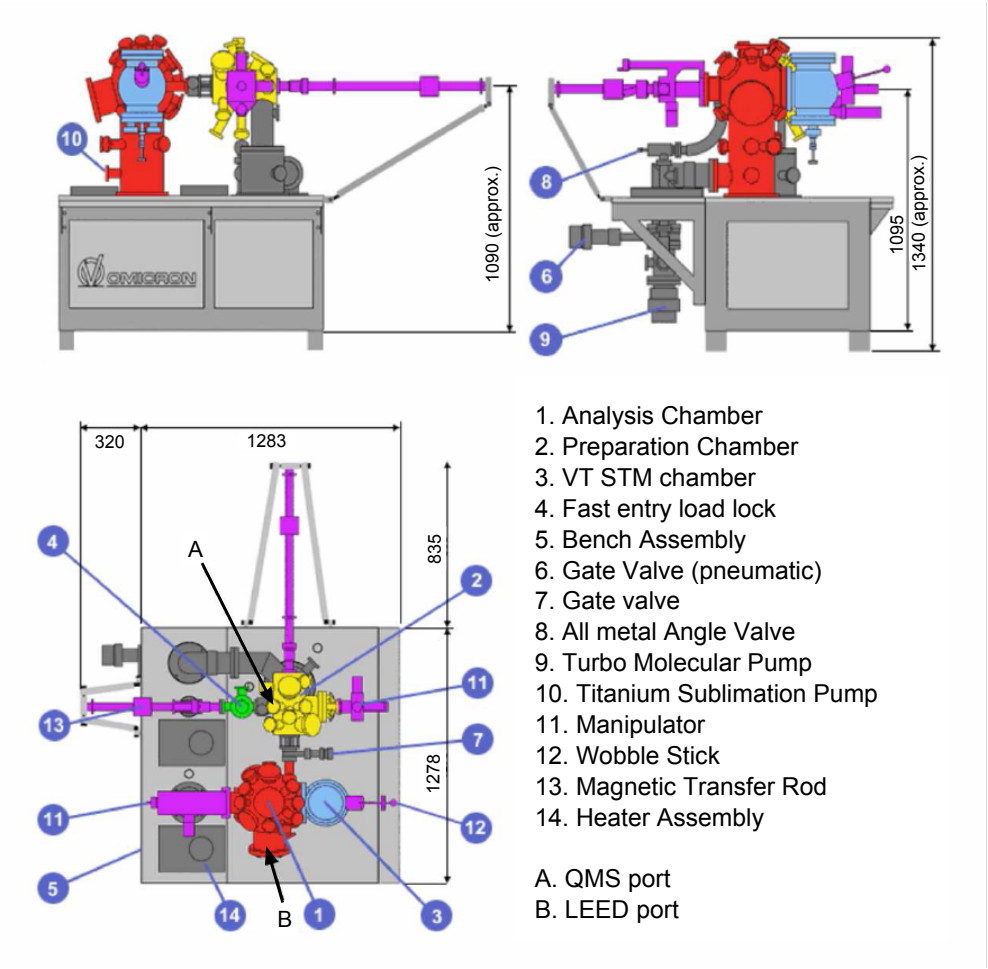

Figure 2.1: Schematic of Omicron UHV system, Surface Science Laboratory, School of Physical Sciences, Dublin City University. All dimensions in mm [1].

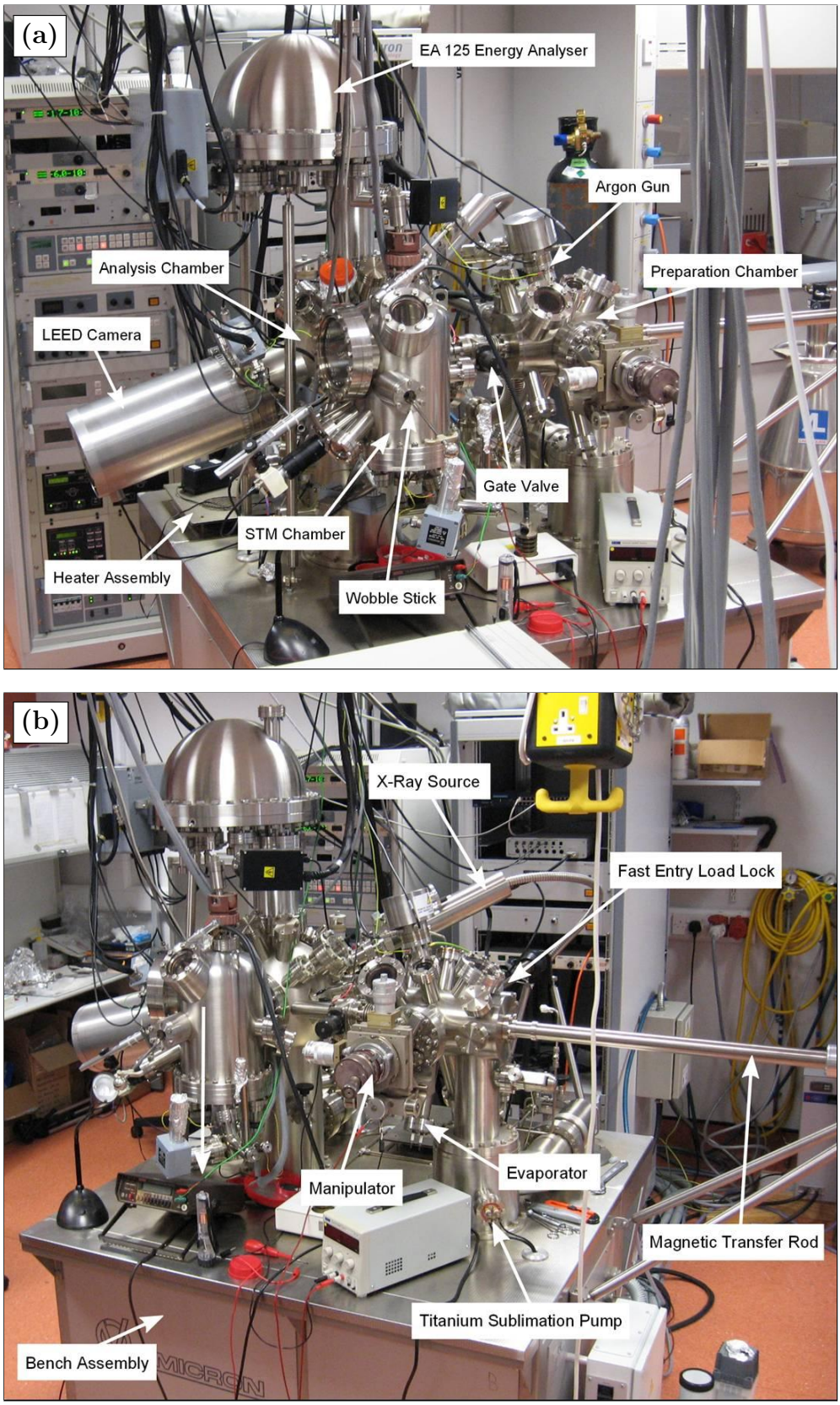

Figure 2.2: Omicron UHV system, Surface Science Laboratory, School of Physical Sciences, Dublin City University.

2.2 Scanning Tunneling Microscopy

2.2.1 Theory and Instrumentation

Scanning tunneling microscopy (STM) was developed at IBM Zurich in the early 1980s [4], and its scientific significance was recognised when Gerd Binnig and Heinrich Rohrer shared the Nobel Prize in Physics in 1986 for its invention. The basic principle of STM operation is simple. A metallic tip and a conducting sample are separated by a distance on the order of angstroms, across which quantum tunneling can occur. The STM provides direct, real-space information about local surface structure, including non-periodic structures, with resolution on the atomic scale [5, 6].

In a one-dimensional case, the Schrödinger equation is written as follows:

$$-\frac{\hbar^2}{2m}\frac{\mathrm{d}^2}{\mathrm{d}z^2}\,\psi(z) + U(z)\,\psi(z) = E\,\psi(z) \tag{2.1}$$

where $\psi(z)$ is the wavefunction of the electron, $U(z)$ is the potential experienced by the electron, E is the energy of the electron, and m is the electron mass [7]. In the classically allowed regions shown in Figure 2.3 where $E > U$, the Schrödinger equation has the solutions

$$\psi(z) = \psi(0)\,e^{\pm ikz} \tag{2.2}$$

where

$$k = \frac{\sqrt{2m(E-U)}}{\hbar} \tag{2.3}$$

representing a travelling wave [7]. In the classically forbidden region where $E < U$, the solutions are of the form

$$\psi(z) = \psi(0)\,e^{\pm\alpha z} \tag{2.4}$$

where

$$\alpha = \frac{\sqrt{2m(U-E)}}{\hbar} \tag{2.5}$$

and is known as the decay constant [7]. The solution in the $+z$ direction

$$\psi(z) = \psi(0)e^{-\alpha z} \tag{2.6}$$

describes the electron wavefunction decaying exponentially in the barrier region. If the barrier is sufficiently narrow, the wavefunction can penetrate through to

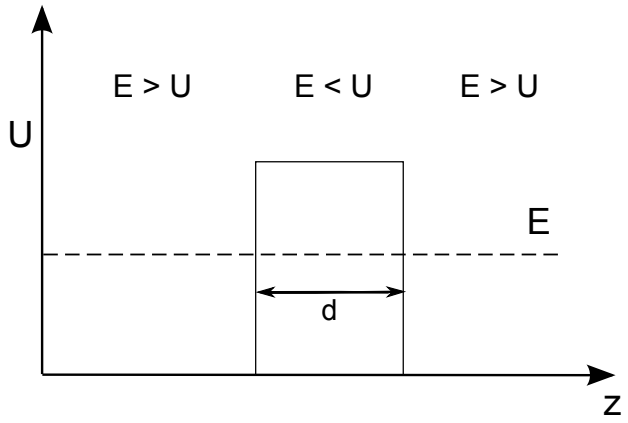

Figure 2.3: Simple 1D model of a barrier, showing classically allowed and forbidden regions.

the other side [7]. The probability density P of the wavefunction tunneling through the barrier is proportional to the square of the wavefunction (Equation 2.6), that is

$$P \propto | \psi(0) |^2 \, e^{-2\alpha z} \tag{2.7}$$

This simple model of quantum tunneling may be applied to STM, where a conducting sample and metallic tip are separated by a vacuum gap of width d. The tunnel current I depends exponentially on the tip-sample separation d [8], with

$$I \propto e^{-2\alpha d} \tag{2.8}$$

The tunnel current I typically increases by an order of magnitude for a 1 Å decrease in the tip-sample separation d [5, 8–10]. Conversely, for a current constant to within several percent, d varies on the order of 0.01 Å [9]. It is this extreme sensitivity of the tunnel current to the tip-sample separation that leads to the atomic resolution obtainable with STM [5].

The above synopsis describes the basic theory behind STM, but in reality the tunnel current includes a complicated convolution of the tip and sample electronic structures [9]. In order to simplify the tip-sample interaction, Tersoff and Hamann [6, 11] modelled the STM tip as a mathematical point source of current [8]. They derived an expression showing that in addition to an exponential dependence on

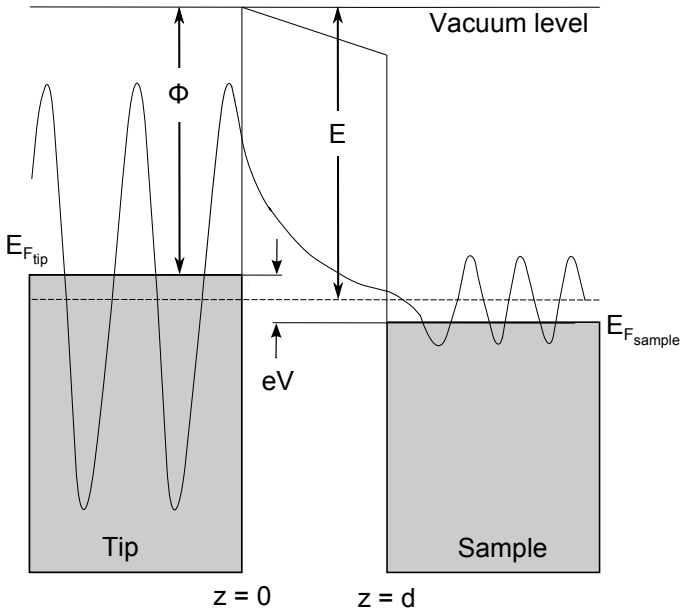

Figure 2.4: An electron wavefunction with energy E tunneling from the tip to the sample across a vacuum gap of width d. In the situation shown, the tip is negatively biased with respect to the sample by a voltage V.

tip-sample separation, the tunnel current I also depends on the local density of states of the surface, ρ, at the Fermi level E_F, measured at the tip position r_t [6, 8–11], i.e.

$$I \propto \rho(r_t, E_F) \tag{2.9}$$

Figure 2.4 shows an electron tunneling across a vacuum gap of width d from the tip to the sample. The work function ϕ is defined as the minimum energy required to excite an electron to the vacuum level. When the Fermi level, E_F, is referenced to the vacuum level then $E_F = -\phi$. In Figure 2.4, the work functions of the tip and sample are assumed to be equal. When both sample and tip are grounded, the Fermi levels $E_{F_{sample}}$ and $E_{F_{tip}}$ are aligned, and there is no net tunnel current [7]. If the tip is biased negatively with respect to the sample by a voltage V (Figure 2.4), $E_{F_{tip}}$ will move relative to $E_{F_{sample}}$ by eV. Electrons occupying energy levels between $E_{F_{tip}}$ and $E_{F_{tip}} - eV$ can then tunnel across the gap into the empty states of the sample between $E_{F_{sample}}$ and $E_{F_{sample}} + eV$. For the case where the tip is biased positively with respect to the sample by a voltage V, electrons occupying states between $E_{F_{sample}}$ and $E_{F_{sample}} - eV$ can tunnel across

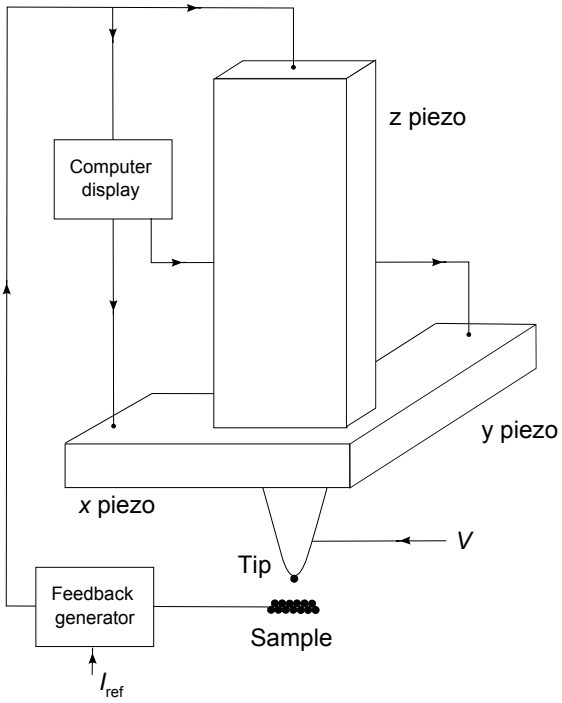

Figure 2.5: A schematic view of the STM, showing the feedback system used to control the tip-sample separation during operation.

to empty states in the tip between $E_{F_{tip}}$ and $E_{F_{tip}} + eV$. Hence the tunnel current is proportional to the applied voltage V. Depending on the applied bias, either filled or empty states of the sample may be probed by the tip.

A schematic diagram of a standard STM configuration is shown in Figure 2.5. Typical STM resolution is <10 Å parallel to the surface and 0.01 Å perpendicular to the surface plane [5, 9]. The tip is scanned over a given area of the surface using a piezo tube scanner [7, 12], which can be positioned with an accuracy of $<1 \times 10^{-4}$ Å [9]. In order to achieve atomic resolution, the tip-sample separation must be stable on the order of 0.1 pm [5]. Hence various methods are used to minimise disturbance from external vibration. One widespread method of vibration isolation is to suspend the sample holder assembly and piezo tube scanner from the STM chamber by metal springs, the vibrations of which are damped using a magnetic eddy-current damping system [5, 7]. If the STM chamber is part of a larger UHV system, environmental vibrations can be minimised by mounting the UHV system on a concrete block, a viscoelastic base, or pneumatic legs [5, 7]. In addition, the STM apparatus itself is designed to

maximise rigidity and minimise low frequency vibrational modes [5, 7].

The two principal modes of STM operation are constant current and constant height [9]. When operating in constant current mode, a feedback system is employed to adjust the tip-sample separation in order to maintain the current at the set value. Thus the motion of the tip perpendicular to the surface is a measure of the topography of the surface, or more precisely, the local density of states (LDOS). In constant height mode the tip-sample separation is kept constant while the tip is scanned over the surface, so that the tunnel current is a measure of the surface features.

2.2.2 Experimental Details and Data Analysis

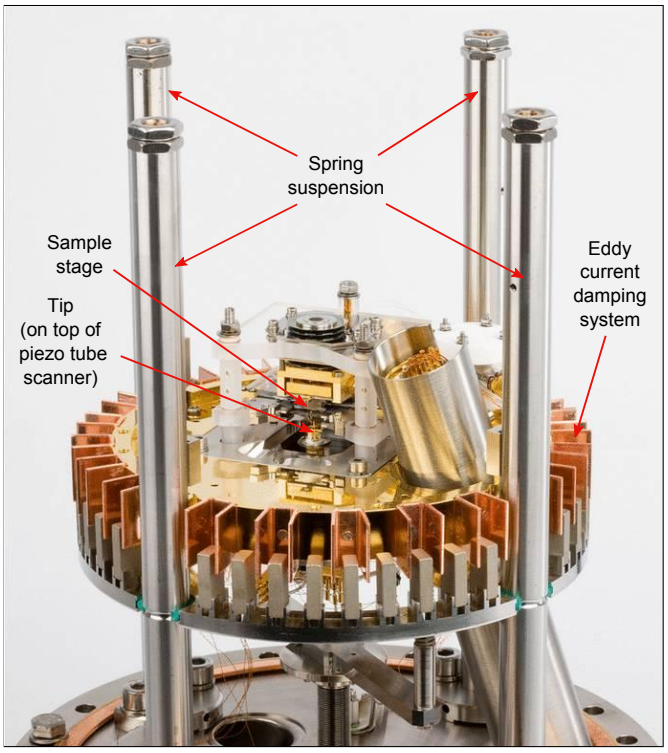

Figure 2.6: The Omicron VT STM, from [13].

The STM system used in the present work is an Omicron Variable Temperature STM (VT-STM) [13, 14]. The main components are labelled in Figure 2.6.

Many different methods of tip preparation exist, with some informative overviews available [7, 15]. The tips used in the present work were prepared via an electrochemical etching process, similar to that outlined in the literature [16–18],

using an Omicron Tip Etching Kit [19]. In a typical tip preparation procedure, a 7 mm length of 0.15 mm diameter tungsten wire was immersed in a 2.5 molar NaOH solution, so that 2 mm of the wire was below the meniscus. The tungsten wire was surrounded by a stainless steel loop that was negatively biased by 6 V with respect to the wire. The etching process proceeded via the electrochemical reactions discussed by Zhang *et al.* [16]. As the tip was preferentially etched at the meniscus of the NaOH solution [16], the immersed portion of the wire dropped off under its own weight after several minutes, creating a sharp tip on the remaining piece of tungsten wire. The tip was then rinsed several times in deionised water to remove any remaining NaOH, before being mounted in an Omicron tip holder and transferred into the vacuum system through the fast entry load lock. The tip was conditioned on a clean metal surface, by applying voltage pulses to the tip using the Nanostructuring feature in the Omicron SCALA PRO 5.0 for Windows software [13]. Further conditioning involved scanning the tip in a high electric field at high scan speeds, and in extreme cases, performing a controlled crash of the tip into a clean Au substrate in order to coat the tip in Au atoms [7].

STM images were recorded at room temperature, with the tip starting at the bottom left corner of the image. The fast axis is along the horizontal direction, with the slow axis along the vertical direction. No drift correction was applied, but analysis of time-lapsed images of a region of the surface indicates that the drift is less than $1 \times 10^{-2}\,\mathrm{nm\,s^{-1}}$. Images were recorded at scan frequencies of up to 10 Hz. The STM images presented in this thesis were analysed using the WSxM software package [20, 21]. A plane was subtracted from each image, and the images were then equalised to maximise contrast. Scalebars represent 20 % of the horizontal dimension of the image, and were added to the images using Inkscape [22]. Unless otherwise stated, all STM images have a square aspect ratio. The bias conditions are shown in the figure captions in the format (V_{bias},I_{tunnel}).

2.3 X-Ray Photoelectron Spectroscopy

2.3.1 Theory and Instrumentation

X-ray photoelectron spectroscopy (XPS) is a non-local qualitative surface science technique. The principle of XPS is illustrated in Figure 2.7. Based on Einstein's Photoelectric Law, the technique involves interrogating a sample with photons of known energy and analysing the kinetic energy of the ejected photoelectrons in order to calculate their binding energy. In its simplest form, the photoelectric

equation is stated as follows:

$$E_K = h\nu - E_b \tag{2.10}$$

where E_K is the kinetic energy of the ejected photoelectron, $h\nu$ is the energy of the incident photon, and E_b is the binding energy of the electron in the sample [9, 23]. However, Equation 2.10 does not account for the work function of the sample, ϕ_s, and hence a more correct statement of the photoelectric equation is

$$E_K = h\nu - E_b - \phi_s \tag{2.11}$$

Implicit in the above discussion is the assumption that no rearrangement of electrons in the sample takes place following the ejection of the photoelectron, and that the binding energy of the photoelectron is simply the difference between the (n-1)-electron final state and the n-electron initial state [23], i.e.

$$E_b = E_f(n-1) - E_i(n) \tag{2.12}$$

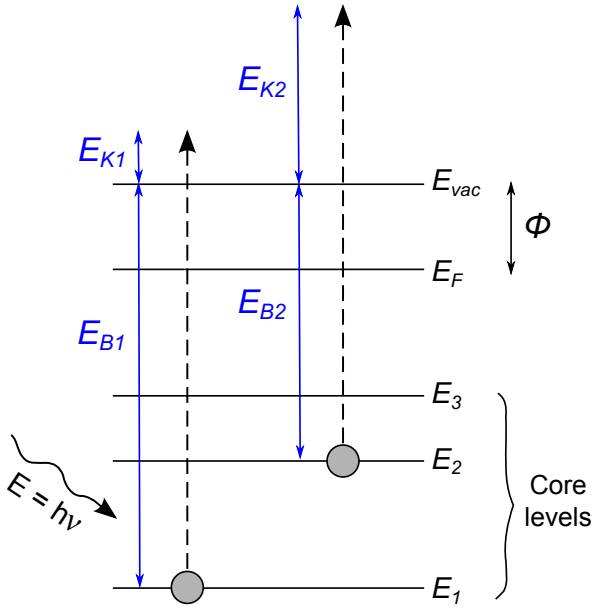

Figure 2.7: Principle of XPS. A photon with energy $h\nu$ excites bound electrons, which are ejected from the sample with kinetic energy, E_K, related to the core level binding energy, E_b.

A more accurate model of the photoemission process includes a rearrangement of the electrons in the sample due to the creation of the core hole, however the more simple one-electron model will suffice for the data analysis undertaken in this thesis.

The kinetic energy of the photoelectrons is analysed by an electron energy analyser, discussed in more detail below. If the sample and the analyser share a common ground, Equation 2.11 must be modified to indicate that the relevant work function is that of the spectrometer rather than the sample (see Figure 2.8), with

$$E_K = h\nu - E_b - \phi_{sp} \tag{2.13}$$

where ϕ_{sp} is the work function of the spectrometer. Therefore, for a known $h\nu$ and ϕ_{sp} and a measured E_K, the binding energy E_b of the photoelectron can be calculated. As every element has a characteristic set of core level binding energies, XPS can be used to determine the composition of a sample [23, 24]. XPS can detect changes in binding energy of an electron due to the chemical environment, making it a useful tool for investigating the chemical state and bonding configuration of a sample [9].

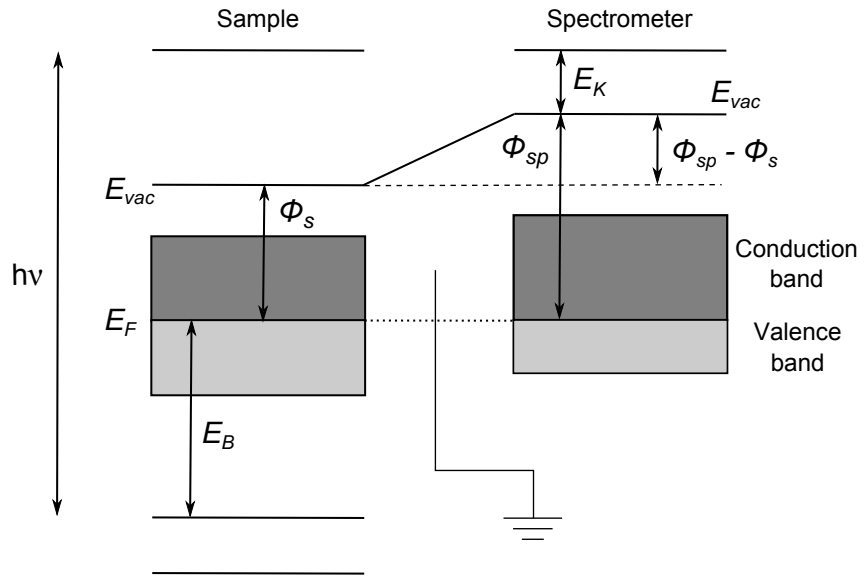

Figure 2.8: Energy level diagram for a sample and analyser with a common ground. It is the work function of the spectrometer, ϕ_{sp}, which must be taken into account, rather than the work function of the sample, ϕ_s.

The elastically scattered photoelectrons contribute to a peak in the measured XPS spectrum at a well-defined kinetic energy E_K, however some photoelectrons undergo inelastic scattering and other energy-loss interactions before emerging from the sample, and contribute to a continuum background at lower kinetic energy [9, 23, 24]. Energy-loss events include coupling to bulk or surface plasmons, resulting in discrete 'plasmon peaks' in the XPS spectra, as well as interactions with other bound electrons in the sample. The exiting photoelectron can excite another electron into a higher energy bound state or into a continuum state above the vacuum level; in this case discrete shake-up peaks and broader shake-off features are also observed in the inelastic background [9].

For core levels with orbital angular momentum $l > 0$, i.e. p, d and f orbitals, the spin of the electron can couple with the orbital angular momentum, resulting in the formation of two spin-orbit split states with $j = l \pm s$ [23]. Each state has degeneracy $2j+1$, and the ratio of the degeneracies gives the relative intensities of the corresponding peaks in the XPS data [23]. For example, a d orbital will split into $d_{3/2}$ and $d_{5/2}$ components, with an intensity ratio of $2:3$. It is possible to resolve spin-orbit split doublets with XPS, given a sufficient spin-orbit splitting and analyser resolution.

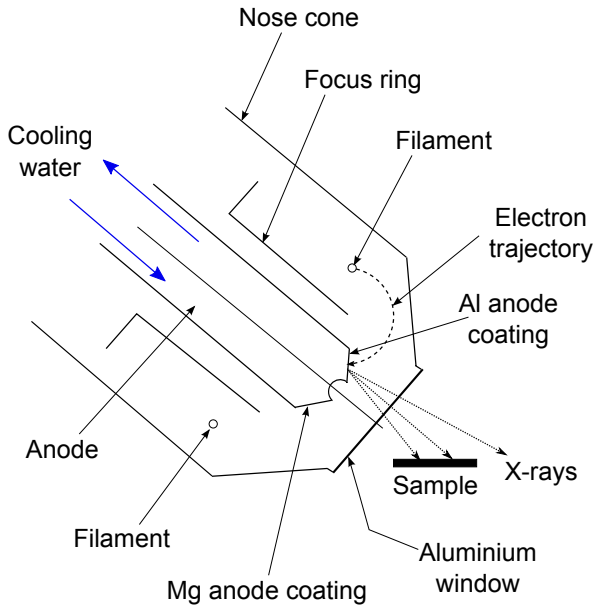

Figure 2.9: Schematic of a Mg/Al twin anode x-ray source.

A Mg/Al twin anode is the most commonly used x-ray source for laboratory-based XPS studies (Figure 2.9). Electrons are emitted from a filament via thermionic emission and are then accelerated to the anode by an applied potential of approximately 15 kV. The electrons impinge on the anode material and excite bound electrons to higher energy levels. The core hole is then filled by an electron with the resultant emission of an x-ray photon or an Auger electron. Mg and Al are chosen for anode materials as the characteristic x-ray emission spectrum for each element is dominated by a single emission line, associated with the $2p_{1/2} \rightarrow 1s$ and $2p_{3/2} \rightarrow 1s$ transitions, and labelled $K_{\alpha 1,2}$ [9]. The energy of the main Mg x-ray emission line is 1253.6 eV, while the main Al line is at 1486.7 eV [9].

The electron energy analyser may be modelled as a band pass filter for electrons with kinetic energy E_P, the pass energy of the analyser [25]. Upon reaching the analyser, the photoelectrons are accelerated or retarded so that their kinetic energy equals E_P. The electrons then travel through the analyser to the detector, where they are counted [23]. By scanning the initial retarding voltage over the kinetic energy range under investigation, a spectrum is accumulated.

One of most widely used electron energy analyser designs is the Concentric Hemispherical Analyser (CHA) (Figure 2.10) [9]. The analyser consists of two concentric hemispheres of radius R_1 and R_2, with the entrance and exit slits centred on $R_0 = (R_1 + R_2)/2$ [23, 25]. A potential V is applied to the hemispheres such that the outer is negatively biased and the inner positively biased with respect to V_0, the potential at R_0. An electron travelling along a spherical path of radius R_0 has kinetic energy E_P, and will successfully travel around the analyser without colliding with either hemisphere [23, 25]. V_0 and E_P are related by [25]

$$e\,V_0 = E_P\,(\frac{R_2}{R_1} - \frac{R_1}{R_2}) \tag{2.14}$$

while the resolution, ΔE, of the analyser is given by

$$\Delta E = E_P\,(\frac{d}{2\,R_0} + \alpha^2) \tag{2.15}$$

where d is the slit width and α is the half angle (in radians) of the photoelectrons entering the analyser (Figure 2.10) [25]. It can be seen from Equation 2.15 that if the pass energy is kept constant throughout an XPS experiment, the resolution of the analyser will also remain constant [23]. Typically electrons with an energy

within 10 % of the pass energy will travel through the analyser and be counted [23]. Hence increasing E_P will result in an increased count rate and an improved signal to noise ratio; however it can be seen from Equation 2.15 that for maximum resolution, E_P should be as low as possible. Hence, a balance must be found between resolution and count rate.

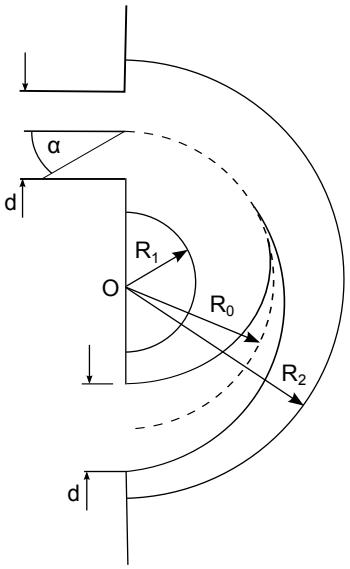

Figure 2.10: Schematic of a concentric hemispherical analyser (CHA). Electrons travelling in a spherical path of radius R_0 will reach the exit slit of the analyser and be counted.

2.3.2 Experimental Details and Data Analysis

An Omicron DAR 400 Mg/Al twin anode X-ray source was used in the present work. A concentric hemispherical Omicron EA 125 Energy Analyser equipped with a linear array of five channeltron detectors, each with an amplification of 10^7 to 10^8 was used [25]. The operation of the x-ray source was controlled using the Omicron 554-S X-ray Source Control Package software [26], while the spectra were acquired using the Omicron EIS/EIS Sphera software [27].

The spectra were analysed using Microcal Origin [28]. Backgrounds were subtracted from the data; in some cases linear or polynomial backgrounds were sufficient, while in other cases a Shirley background was subtracted [29]. The spectra were also normalised to the number of scans.

The profile of the photoemission peaks can be modelled as a convolution of

two different line-shapes; a Lorentzian line-shape resulting from the finite lifetime of the core hole, and a Gaussian line-shape due to thermal and instrumental broadening. A Voigt line-shape is a convolution of a Gaussian and a Lorentzian,

$$V(E,\sigma,\gamma) = \int_{-\infty}^{\infty} G(E',\sigma)L(E-E',\gamma)dE' \tag{2.16}$$

where the Gaussian component G at energy E and of linewidth $2\sigma\ln(2)$ is defined as

$$G(E;\sigma) = \frac{e^{-E/2\sigma^2}}{2\pi\sigma} \tag{2.17}$$

and the Lorentzian component L at energy E and of linewidth 2γ is defined as

$$L(E;\gamma) = \frac{\gamma}{\pi(E^2+\gamma^2)} \tag{2.18}$$

The peaks were fitted with either Gaussian or Voigt line-shapes as appropriate, using the Aanalyzer [30] and Fityk [31] curve-fitting software.

An approximate calibration of the molecular coverage was obtained by using XPS spectra in conjunction with STM. Defining a monolayer as one complete molecular layer on the substrate with no growth of additional layers, a monolayer coverage was determined from the measured ratio of the C 1s peak and an appropriate substrate peak (e.g. Au 4d, Ag 3d or Cu 2p core levels). Hence the coverage of subsequent molecular depositions could be evaluated, with an accuracy of $\pm 10\,\%$.

2.4 Low Energy Electron Diffraction

2.4.1 Theory and Instrumentation

First discovered by Davisson and Germer in 1927 and later developed by Farnsworth and co-workers as an analytical surface science tool in the 1960s [32], low energy electron diffraction (LEED) is a reciprocal space technique suitable for investigating periodic surface structures. An electron beam is incident on a sample; if the sample has a periodicity comparable to the de Broglie wavelength of the incident electrons, diffraction will occur. The resulting diffraction pattern contains information about the periodicity of the sample.

Any vector in a crystal lattice can be defined by

$$\vec{V} = m_1\vec{a} + m_2\vec{b} + m_3\vec{c} \tag{2.19}$$

where m_1, m_2 and m_3 are integers, $\vec{a}$, $\vec{b}$ and $\vec{c}$ are the primitive basis vectors for that lattice, and $\vec{a} \cdot (\vec{b} \times \vec{c})$ is the volume of the unit cell, the smallest repeatable unit of the crystal structure [9, 33, 34]. Similarly, any vector in the reciprocal lattice can be defined by

$$\vec{g_{hkl}} = h\vec{a}^* + k\vec{b}^* + l\vec{c}^* \tag{2.20}$$

where h, k and l are integers known as the Miller indices which can be used to define any plane in the crystal [33], and the primitive basis vectors $\vec{a}^*$, $\vec{b}^*$ and $\vec{c}^*$ are defined as [9]

$$\vec{a}^* = 2\pi \frac{\vec{b} \times \vec{c}}{\vec{a} \cdot (\vec{b} \times \vec{c})},\ \vec{b}^* = 2\pi \frac{\vec{c} \times \vec{a}}{\vec{a} \cdot (\vec{b} \times \vec{c})},\ \vec{c}^* = 2\pi \frac{\vec{a} \times \vec{b}}{\vec{a} \cdot (\vec{b} \times \vec{c})} \tag{2.21}$$

For an electron diffraction experiment, the wave-vector is a measure of the momentum of both the incident and diffracted beams, with the incident beam having a wave-vector of $\vec{k_0}$, while the diffracted beam has a wave-vector of $\vec{k_1}$ [33]. Momentum must be conserved for elastic scattering, that is there can be a change in the direction of the diffracted beam, but not a change in the magnitude of the momentum, i.e.

$$| \vec{k_0} | = | \vec{k_1} | \tag{2.22}$$

This condition for diffraction can be represented in reciprocal space using the Ewald sphere construction (Figure 2.11(a)) [9, 33]. Diffraction only occurs when this sphere intersects with a reciprocal lattice point [33]. The conservation of momentum gives the condition that

$$\vec{k_1} - \vec{k_0} = \vec{g}_{hkl} \tag{2.23}$$

It can be seen from Figure 2.11(a) that

$$\sin\theta = \frac{| \vec{g}_{hkl} | /2}{| \vec{k_0} |} \tag{2.24}$$

Using

$$| \vec{g}_{hkl} | = (h^2 + k^2 + l^2)^{1/2}\, 2\pi/a \tag{2.25}$$

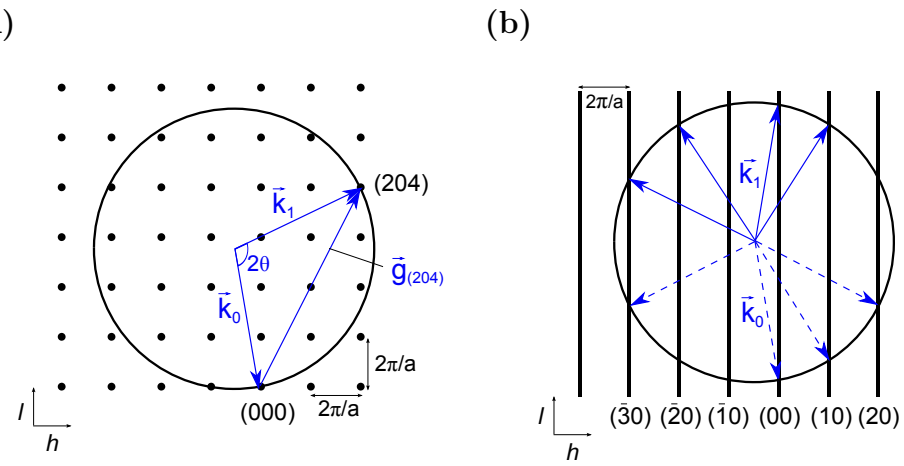

Figure 2.11: Ewald sphere in reciprocal space, for (a) three dimensions and (b) two dimensions. Diffraction occurs when the Ewald sphere intersects the reciprocal lattice points or rods. The solid vectors in (b) represent back-scattered electrons, while the dashed lines are forward-scattered electrons.

it can be shown [33] that Equation 2.24 is equivalent to

$$n\lambda = 2a \sin\theta \tag{2.26}$$

the well-known Bragg condition for diffraction [9, 33].

For diffraction at the surface, as is the case for LEED, a two-dimensional analysis is appropriate. The real space separation between planes perpendicular to the surface normal is now infinite, which corresponds to zero separation in reciprocal space. Hence the reciprocal lattice is now represented as infinite reciprocal lattice rods (Figure 2.11(b)). Diffraction will occur at every point where the Ewald sphere intersects one of the reciprocal lattice rods [9, 33]. As $E \propto \vec{k}^2$ for a free electron, increasing the kinetic energy of the incident electrons will increase the radius of the corresponding Ewald sphere, leading to a larger number of diffraction spots.

Adsorbed layers which exhibit periodicity can also be studied using LEED. The lattice vectors of the overlayer may be some integer multiple of the substrate basis vectors, meaning that the overlayer is commensurate with the substrate. If this is not the case, the overlayer is said to be incommensurate with the substrate. Any overlayer structure can be defined relative to the substrate lattice using Wood's notation, where the overlayer lattice vectors $\vec{a}_{over}$ and $\vec{b}_{over}$ are related to

the substrate lattice vectors $\vec{a}_{sub}$ and $\vec{b}_{sub}$ by

$$\begin{pmatrix} \vec{a}_{over} \\ \vec{b}_{over} \end{pmatrix} = \begin{pmatrix} W_{11} & W_{12} \\ W_{21} & W_{22} \end{pmatrix} \begin{pmatrix} \vec{a}_{sub} \\ \vec{b}_{sub} \end{pmatrix} \tag{2.27}$$

Figure 2.12 shows a typical LEED set-up. Electrons are produced via thermionic emission in the electron gun, which is normal to the sample. The electrons are then accelerated towards the sample, with a variable kinetic energy. Both elastically and inelastically scattered electrons are produced; a system of grids is designed to discriminate between them. An adjustable negative voltage is applied to grids G_2 and G_3 in order to stop the inelastically scattered electrons reaching the screen and contributing to a diffuse background signal [33]. In this rear view set-up, only back-scattered electrons will be detected. The fluorescent screen (S in Figure 2.12) is at a high positive potential of approximately 5 kV; the elastically scattered electrons are accelerated to the screen where they excite fluorescence in a pattern corresponding to the diffraction spots. The diffraction pattern is imaged with a camera located behind the electron gun.

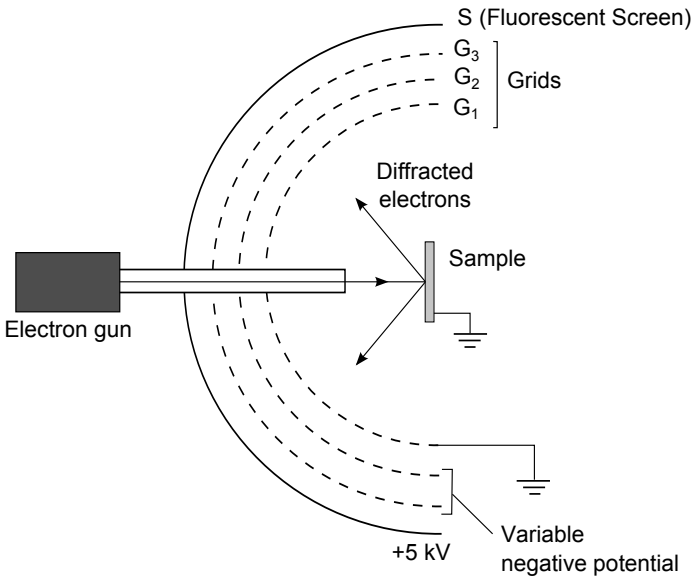

Figure 2.12: Schematic of a LEED experimental set-up.

2.4.2 Experimental Details and Data Analysis

A rear view Omicron Spectaleed system was used in the present work. The electron gun is equipped with a lanthanum-hexaboride (LaB_6) filament, which displays good emission characteristics at low power inputs, and yields a higher emission current than the conventional thoriated tungsten filaments [35].

The LEED images presented in this thesis have been inverted in order to increase the contrast of the diffraction spots. This was accomplished using the GIMP image processing software [36]. Simulated LEED patterns have been generated using the LEEDpat software [37]. The program takes the basis vectors of a periodic structure as an input, and calculates the LEED pattern. It is also possible with this software to simulate a LEED pattern for an overlayer, defined relative to the substrate using Wood's notation.

For the molecular overlayer structures studied in this work, the substrate and overlayer diffraction patterns cannot be imaged simultaneously due to the relative sizes of the reciprocal lattice vectors. However the overlayer lattice parameter can be calibrated relative to the substrate lattice vector using the following analysis [38, 39]. A series of LEED images of the substrate diffraction pattern are recorded at different electron energies, and an arbitrary distance in the LEED pattern, such as the distance between two diagonal spots, is plotted as a function of the inverse of the square root of the kinetic energies. A similar graph is constructed for the overlayer diffraction pattern. The following relationship then holds between the substrate and overlayer lattice constants and the beam energies [38],

$$\frac{a_{overlayer}}{a_{substrate}} = \frac{\sqrt{E_{substrate}}}{\sqrt{E_{overlayer}}} \tag{2.28}$$

Thus if the lattice parameter of the substrate is known then the overlayer lattice constant, $a_{overlayer}$, can be calculated.

2.5 Synchrotron Radiation

First noticed in the 1940s as an energy loss phenomenon in electron storage rings [40, 41], synchrotron radiation has developed into a valuable tool in many disciplines, including surface science and nanotechnology. Synchrotron radiation is the electromagnetic radiation emitted over a broad wavelength range by charged particles following a curved trajectory at relativistic speeds [41]. In a synchrotron radiation facility, electrons are steered around a storage ring by magnets, emitting radiation as they are accelerated. As measured in the laboratory frame of reference, the radiation undergoes a relativistic Doppler shift and is emitted in a narrow cone with a divergence of $1/\gamma$, where

$$\gamma = \frac{1}{\sqrt{1 - \frac{v^2}{c^2}}} \tag{2.29}$$

v is the velocity of the electrons, and c is the speed of light in vacuum [40, 41]. This highly directional radiation travels down a beamline, where a monochromator is used to select desired wavelengths. In addition, the radiation has a high degree of linear polarisation in the plane of the storage ring, and the brilliance is far superior to more conventional x-ray sources [41, 42].

Figure 2.13 shows a schematic of a typical synchrotron facility. The electrons are accelerated to relativistic velocities in a booster ring, before injection into a storage ring, which consists of straight sections joined by bending magnets. Synchrotron radiation is emitted as the electrons accelerate around the ring, and is directed down beamlines to experimental stations where particular wavelengths may be selected by a monochromator. The earliest synchrotron radiation facilities exclusively used bending magnets to produce the radiation. More recent facilities have incorporated insertion devices such as undulators and wigglers, so-called as they are 'inserted' into the straight sections of the storage ring [43].

The synchrotron radiation experiments in the present work were carried out at two beamlines: the D1011 beamline at the MAX-II storage ring in MAX-lab, Lund University, Sweden (Figure 2.14(a)), and the SX-700 beamline at the ASTRID storage ring in the Institute for Storage Ring Facilities (ISA), Aarhus University, Denmark (Figure 2.14(b)). Both beamlines use bending magnets to produce the synchrotron radiation. The experimental station of each beamline features a preparation chamber equipped with a LEED system and a sputter

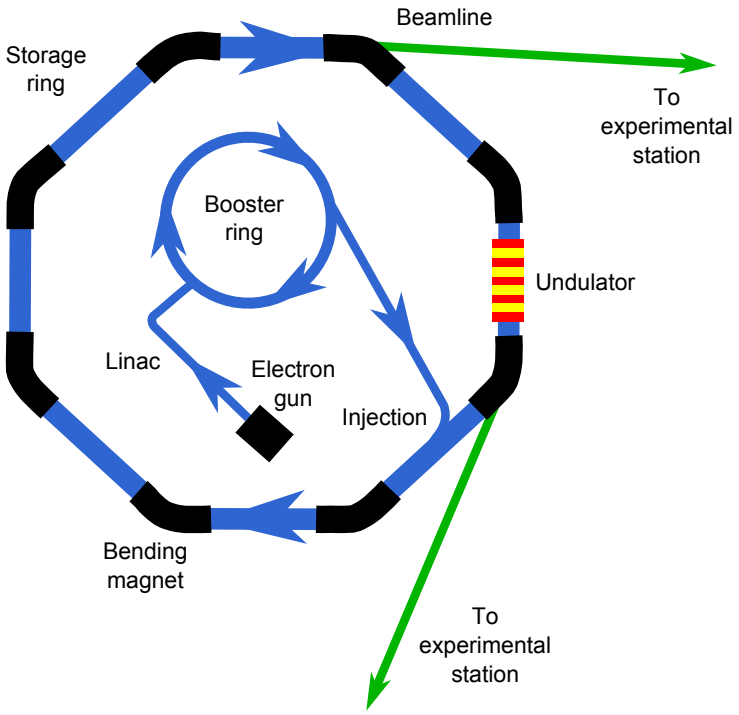

Figure 2.13: Schematic of a synchrotron radiation facility.

gun, as well as several ports for molecular deposition by thermal evaporation, and an analysis chamber equipped with a concentric hemispherical electron energy analyser. In addition, the analysis chamber at the D1011 beamline has a microchannel plate (MCP) detector for electron yield measurements [44].

The D1011 beamline has a photon energy range of 40 eV–1500 eV, an energy resolution E/dE of 1.5×10^3–1.3×10^4, and a photon flux at the sample of 10^{10}–10^{11} photons/sec/100 mA [44]. The SX-700 beamline has a photon energy range of 6 eV–700 eV, a resolving power of 200–2500, and a photon flux at the sample of 10^{10} photons/sec/100 mA [45].

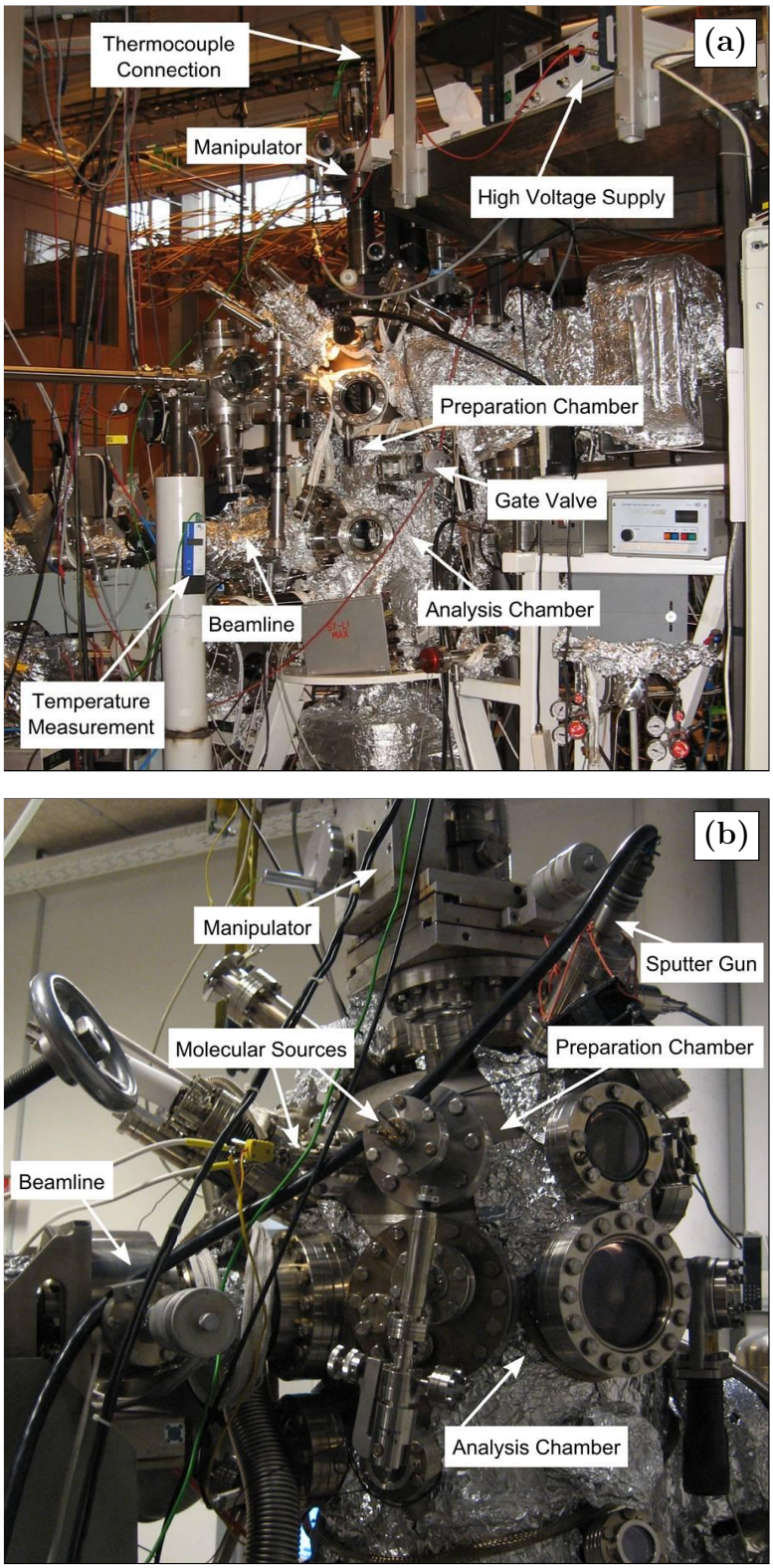

Figure 2.14: Experimental stations at synchrotron radiation facilities. (a) D1011 beamline, MAX-lab, Lund University, Sweden, (b) SX-700 beamline, ISA, Aarhus University, Denmark.

2.6 Photoemission Spectroscopy

Photoemission spectroscopy (PES) is the same physical process as XPS (Section 2.3), but the two techniques have been separated in this chapter to highlight the different considerations associated with using synchrotron radiation as the photon source as opposed to either a Mg or an Al x-ray anode source.

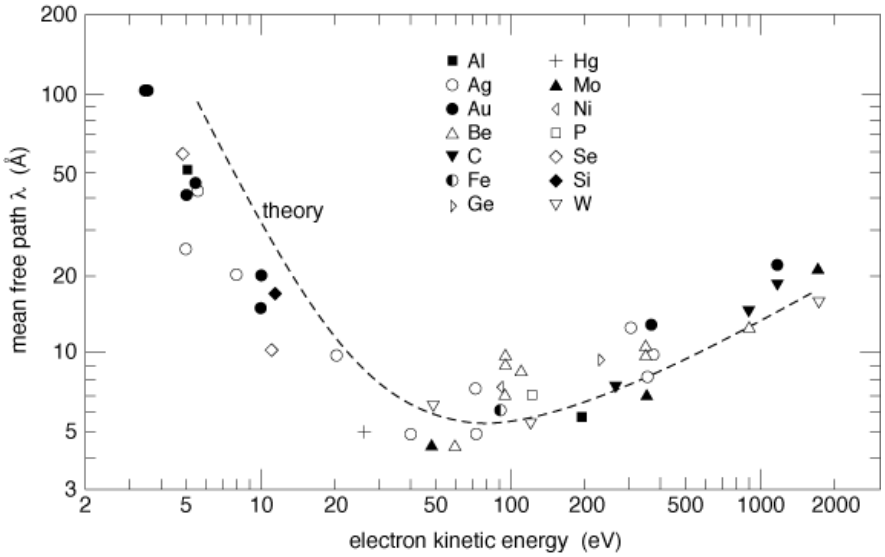

Figure 2.15: Universal curve of the energy-dependent inelastic mean free path of electrons [46].

The photoionisation cross-section of an energy level is a measure of the probability of a photoelectron being ejected from that energy level. Cross-sections as a function of photon energy are tabulated and plotted for each element [47]. As discussed in Section 2.5, photons of the appropriate wavelength may be selected from the broadband synchrotron radiation at an experimental beamline. This allows specific energy levels to be targeted according to their wavelength-dependent cross-section. In addition, prudent choice of the photon energy can result in enhanced surface sensitivity. The universal curve for the inelastic mean free path (IMFP) (Figure 2.15) indicates electrons with kinetic energies of approximately 100 eV have an IMFP of approximately 5 Å [9, 48, 49]. As roughly 95 % of detected electrons originate within a distance of three times the IMFP of the surface [23], if the photon energy is chosen to be approximately 100 eV greater than the binding energy of the targeted energy level, the resulting spectrum will be surface sensitive to a depth of approximately 15 Å.

The photoemission spectra were background-subtracted and curve-fitted as

discussed earlier (Subsection 2.3.2). In addition, the spectra were normalised to the beam current. Where possible, the binding energy was referenced to the Fermi level. Where the Fermi level could not be measured, e.g. after multi-layer depositions, the binding energy was aligned to that of a Fermi-corrected scan of the same photoemission peak.

2.7 X-Ray Absorption Spectroscopy

2.7.1 Theory and Instrumentation

X-ray absorption spectroscopy (XAS) is a synchrotron-radiation based surface science technique which probes the unoccupied energy levels of a sample [42]. XAS can be sub-divided into different techniques depending on which region of the absorption spectrum is analysed [33]. As the analysis presented in this thesis focuses on the near-edge region of the absorption spectrum, Near Edge X-ray Absorption Fine Structure (NEXAFS) is the relevant technique discussed here. However, the shorter terminology XAS will be used for convenience.

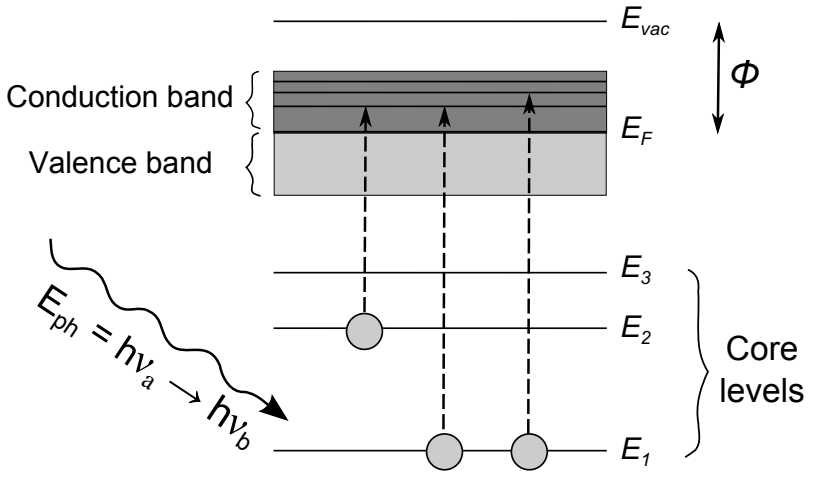

Figure 2.16: Principle of x-ray absorption spectroscopy.

The principle of XAS is illustrated in Figure 2.16. The sample is interrogated with monochromatic x-rays which are scanned over the energy range of interest [42]. When the photon energy matches the difference between two energy levels, absorption occurs resulting in the excitation of a bound electron. A typical XA spectrum consists of sharp peaks and broader features superimposed on a

background that can be modelled by a step function. The sharp peaks are due to core level excitations into discrete unoccupied energy levels below the vacuum level, while the broader features are due to excitations into the continuum states above the vacuum level. The step-wise background is due to the increase in the absorption processes that occurs as the photon energy exceeds the ionisation potential of each successive energy level, with the onset of each step known as an absorption edge [33, 50]. For transitions from the 1s energy level (i.e. the K-shell of the atom), there is a single absorption edge, known as the K-edge. The absorption peaks are labelled π^* or σ^* depending on the symmetry of the unoccupied energy level [42].

The core hole resulting from the absorption process is subsequently filled, with the corresponding emission of either a fluorescent photon or an Auger electron, hence the fluorescence and Auger emission signals are a measure of the absorption [42]. While in principle it is possible to measure the absorption directly, in practice it is usually measured indirectly using these secondary processes. The Auger electron signal is the more commonly used measurement, as the cross-section for Auger emission is much higher than that for fluorescence emission for elements with low atomic number [48]. In addition, electron detection offers increased surface sensitivity relative to fluorescence detection, as electrons from deep in the sample are unlikely to have sufficient energy to overcome the work function due to energy loss through inelastic scattering [42]. Hence absorption measured by electron detection has an information depth of approximately 5 nm [42]. The surface sensitivity is further increased by the use of a retarding voltage to discriminate against lower kinetic energy electrons before they reach the detector, a method known as Partial Electron Yield (PEY) [42]. Microchannel plates or channeltrons are commonly used detectors for electron yield measurement [42].

As mentioned in Section 2.5, synchrotron radiation exhibits a high degree of linear polarisation in the plane of the storage ring. This enables orientation information to be extracted from XA spectra measured at different angles of incidence for adsorbed molecular layers. Chemical bonds and the corresponding molecular orbitals are highly directional, and the probability of a transition into an unfilled state depends on the relative orientation of the electric field vector to the molecule [42]. In general, σ^* and π^* orbitals are oriented parallel and perpendicular to the bond direction [42]. For a planar π-conjugated molecule such as benzene, the σ^* orbitals lie in the molecular plane, while the π^* orbitals

are normal to the plane of the molecule (Figure 2.17) [51, 52]. Hence if the XA spectrum is recorded at two different angles of incidence such that the electric field vector moves through an angle close to 90° with respect to the plane of the molecule, the intensity of peaks relating to π^* and σ^* transitions will show an opposite angular dependence. Assuming the planar π-conjugated molecule is parallel to the substrate, features assigned to π^* transitions will have a maximum intensity for a grazing incident angle, i.e. when the electric field vector of the incident radiation has a large component normal to the surface. Conversely, features assigned to transitions to σ^* states will have an intensity maximum at normal incidence, i.e. when the electric field vector is parallel to the surface. It is possible to extract quantitative information about the molecular orientation using a method developed by Stöhr and Outka [50, 52], which is discussed in more detail below.

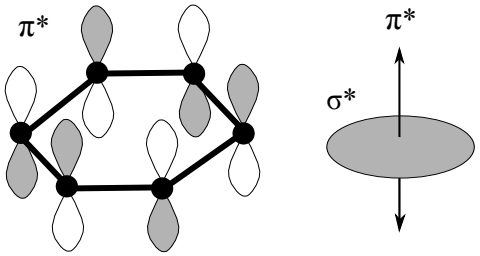

Figure 2.17: Orientation of π^* and σ^* molecular orbitals for benzene.

2.7.2 Experimental Details and Data Analysis

C and N K-edge and Ni L-edge absorption spectra were recorded at the D1011 beamline, using a microchannel plate detector in PEY mode. The XA spectra were divided by reference spectra measured from the clean crystal samples. These reference spectra account for any carbon, nitrogen or nickel contamination present in the system which could influence the shape of the absorption spectra. For the XA spectra presented in Chapter 4, a calibration of the monochromator energy was carried out in the C K-edge region. Substrate photoemission peaks were measured in first and second order at a range of photon energies in the C K-edge region, allowing the absolute photon energy to be calculated. This photon energy was plotted against the nominal monochromator energy, giving a slope and intercept which was then applied as a correction to the nominal photon

energies. The calibration was verified by comparing the reference spectrum with literature, for the decrease in intensity at 284.7 eV due to carbon absorption on the mirrors in the beamline [53].

Molecular orientation information was extracted from XA spectra recorded at grazing and normal incidence, using the 'building block' analysis of Stöhr and Outka [50, 52], whereby molecules are modelled as being built from simple units such as diatomic molecules and aromatic rings. Figure 2.18 shows the geometry of the incident x-rays and a molecular orbital on the surface for both a vector orbital (Figure 2.18(a)) and a planar orbital (Figure 2.18(b)) as described by Stöhr and Outka. The propagation vector of the incident x-rays makes an angle θ with the x-axis of the sample, while the vectors $\vec{O}$ and $\vec{N}$ are oriented at angles of α and γ with respect to the surface normal in the case of vector and planar molecular orbitals respectively.

In the case of a sample with threefold or higher symmetry, the resonance intensities associated with the parallel and perpendicular components of the electric field of the synchrotron radiation, $I^{\parallel}$ and $I^{\perp}$, are given by the following equations [52]: for a vector orbital (Figure 2.18(a)),

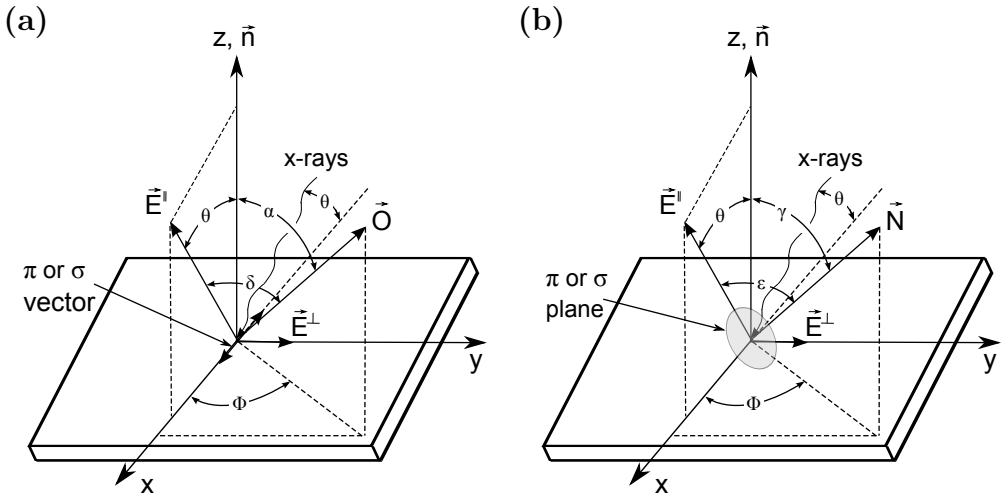

Figure 2.18: Orientation of molecular orbitals with respect to electric field of synchrotron radiation incident on the sample, for both a vector orbital (a) and a planar orbital (b). Based on Figures 4 and 5 in [52].

$$I_v^{\parallel} = \frac{A}{3}[1 + \frac{1}{2}(3\cos^2\theta - 1)\,(3\cos^2\alpha - 1)] \tag{2.30a}$$

$$I_v^{\perp} = \frac{1}{2}\,A\sin^2\alpha \tag{2.30b}$$

where A is a constant, while for a planar orbital (Figure 2.18(b)),

$$I_p^{\parallel} = \frac{2B}{3}[(1 - \frac{1}{4}\,(3\cos^2\theta - 1)\,(3\cos^2\gamma - 1)] \tag{2.31a}$$

$$I_p^{\perp} = \frac{B}{2}\,(1 + \cos^2\gamma) \tag{2.31b}$$

where B is a constant. For a given polarization P the total resonance intensity I for either a vector or a planar molecular orbital is given by

$$I = C[P\,I^{\parallel} + (1 - P)\,I^{\perp}] \tag{2.32}$$

where C is a constant [52].

Equations 2.30, 2.31 and 2.32 can be used to calculate the total resonance intensity I at grazing (θ=20°) and normal (θ=90°) incidence. Figure 2.19 shows $I(20)/I(90)$ and $I(90)/I(20)$ plotted as a function of orbital polar angle α for the vector orbital case (Figure 2.19(a)) and polar angle γ for the planar orbital case (Figure 2.19(b)) for a polarization value of 0.85. For samples measured at grazing and normal incidence, the ratio of the peak intensities can be used in conjunction with the plots shown in Figure 2.19 to estimate the angle of $\vec{O}$ or $\vec{N}$ with respect to the surface. If the orientation of the orbital with respect to the molecule is known, the molecular orientation with respect to the surface can then be determined.

It should be noted that the intensity ratios of the peaks, and hence the estimated angles between the molecules and the surface plane, are sensitive to the background subtraction, normalisation and fitting of the XAS data. In addition, the plots shown in Figure 2.19 depend on the polarization factor P, chosen as 0.85 here [52]; however the value of P will vary for different synchrotron beamlines. Also, the building block model neglects conjugation and delocalisation of the electrons [52].

A step function was subtracted from the XA spectra to account for the background, and the absorption lines were fitted with appropriate line-shapes,

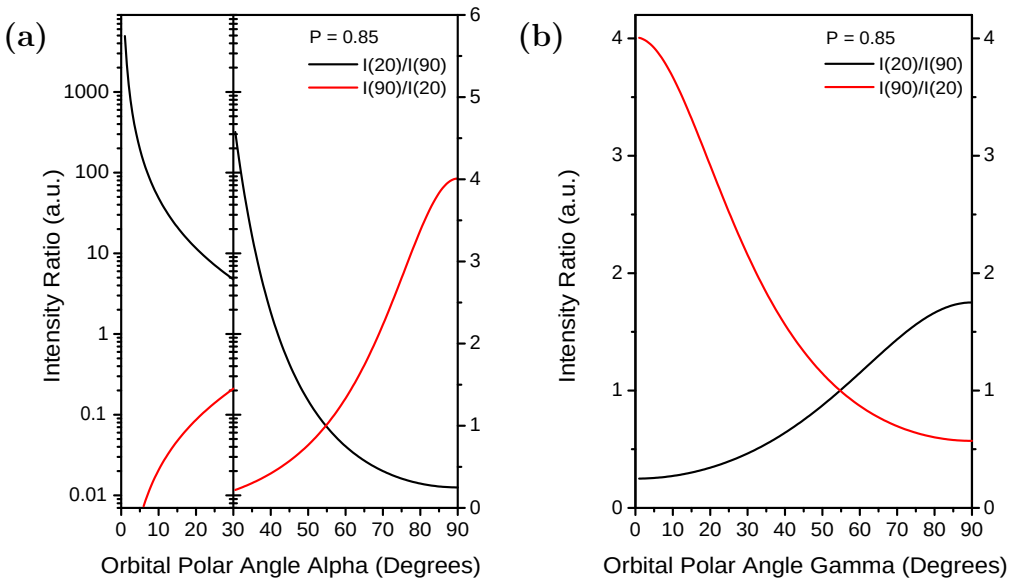

Figure 2.19: Ratio of total resonance intensity I at grazing incidence and normal incidence as a function of orbital polar angle for vector molecular orbitals (a) and planar molecular orbitals (b). Intensity scale in (a) plotted partly on a logarithmic and partly on a linear scale for clarity [52].

using the Fityk analysis software [31]. The graphs in Figure 2.19 for $\theta = 20°$ and $\theta = 90°$ were then used to find the polar tilt angle of each molecular orbital.

The angle dependent XA spectra presented in this thesis have been normalised to the maximum intensity in each spectrum.

2.8 Materials

2.8.1 Metal Surfaces

The metal substrates used in the present work, Au(111), Au(110), Ag(111) and Cu(111), were all single crystals purchased from Surface Preparation Laboratory in the Netherlands [54]. The crystals were cut with an orientation accuracy of $< 0.5°$.

Au(111), Ag(111) and Cu(111) Surfaces

Au, Ag and Cu are all face-centered cubic (fcc) crystals. The closest separation between atoms in the (111) plane is $a/\sqrt{2}$, where a is the lattice parameter. For

a simple cubic lattice the interplane separation d is given by $a/\sqrt{h^2+k^2+l^2}$, therefore the interplane separation for (111) planes is $a/\sqrt{3}$. Figure 2.20 shows a fcc crystal with the (111) plane highlighted. The relevant lattice parameters, in-plane atomic separation, and interplane spacing are given in Table 2.1.

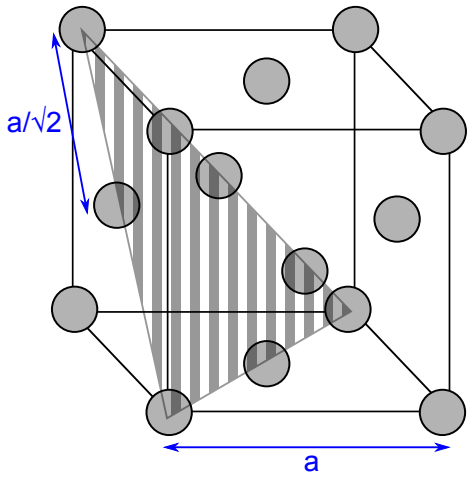

Figure 2.20: (111) plane of a face-centred cubic crystal, a is the lattice parameter.

Table 2.1: Lattice parameters, in-plane atomic separation, and interplane spacing for Au(111), Ag(111) and Cu(111).

Element	Lattice parameter a [b] (Å)	In-plane atomic separation $a/\sqrt{2}$ (Å)	Interplane separation $a/\sqrt{3}$ (Å)
Au	4.08	2.88	2.36
Ag	4.09	2.89	2.36
Cu	3.61	2.55	2.08

b = [34]

The clean Ag(111) and Cu(111) surfaces have a 1×1 reconstruction, while the clean Au(111) surface has a $22 \times \sqrt{3}$ reconstruction, known as the 'herringbone' reconstruction. First observed by van Hove *et al.* [55], this reconstruction is due to transitions between fcc and hexagonal close-packed (hcp) regions which result

in the zig-zag pattern observed in STM images [56]. Figure 2.21 shows atomically resolved STM images for the Ag(111), Cu(111) and Au(111) surfaces, along with a larger scale image of the Au(111) surface where the $22 \times \sqrt{3}$ reconstruction is visible.

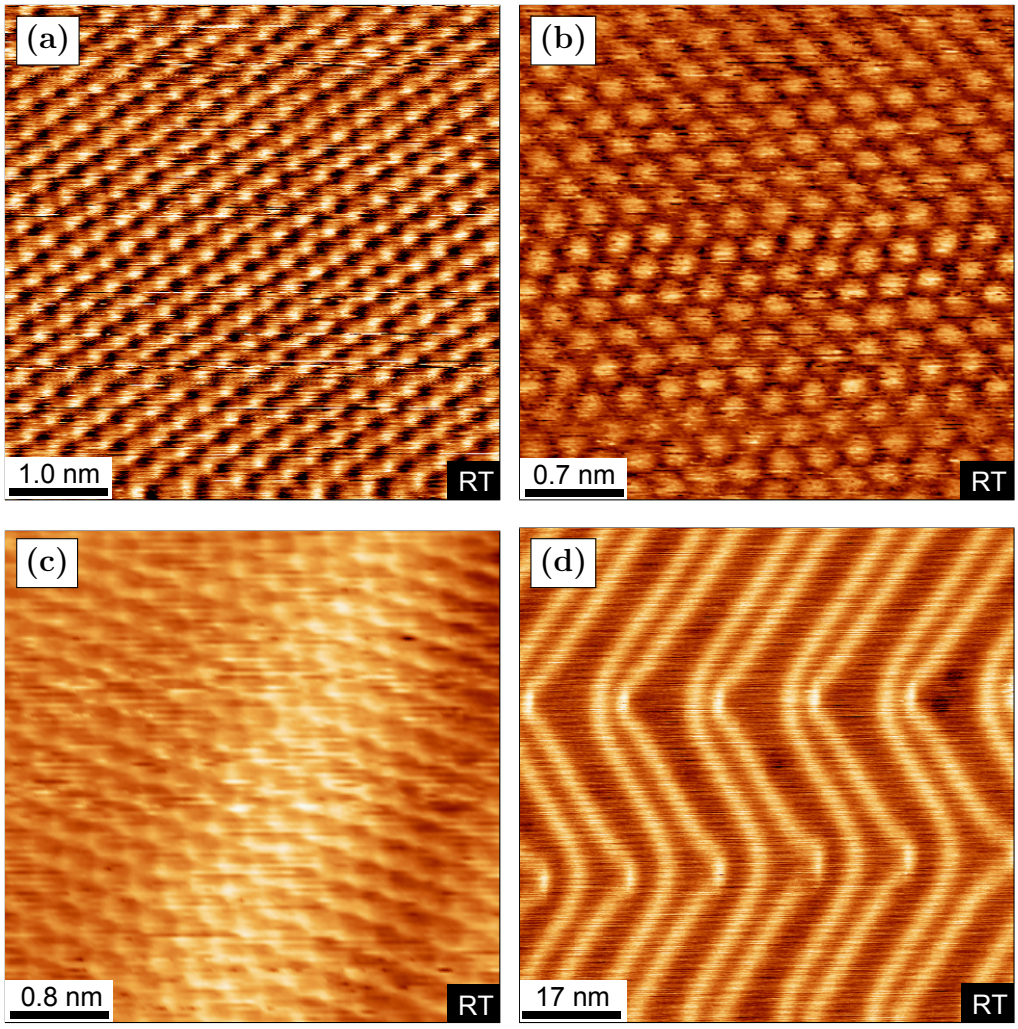

Figure 2.21: STM for atomically clean (111) surfaces. (a) Ag(111), (+0.04 V,1.00 nA), (b) Cu(111), (−0.03 V,2.50 nA), (c) Au(111), (+1.12 V,0.47 nA), (d) Au(111), (+1.01 V,0.03 nA).

Au(110) Surface

The Au(110) surface exhibits two different 'missing row' reconstructions, having 2×1 [57–59] and 3×1 periodicities [60, 61]. Figure 2.22 shows a schematic of the two missing row reconstructions, and Figure 2.23 shows STM and LEED images demonstrating the different periodicities of the 2×1 and 3×1 reconstructions.

The periodicities of the Au rows in the STM images were calculated using WSxM [20, 21] by summing the horizontal lines in an image, dividing by the total number of horizontal lines, and analysing the periodicity of the resulting line profile (Y-average tool, WSxM).

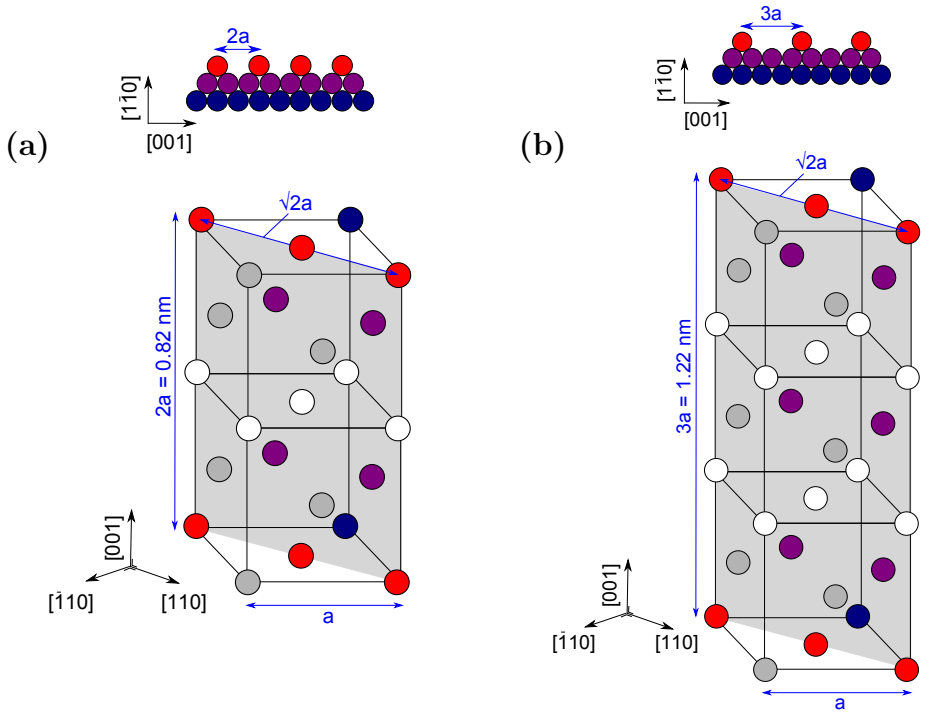

Figure 2.22: Schematic of the (a) 2×1 and (b) 3×1 reconstructions of Au(110).

Surface Preparation

The samples were mounted on tantalum spades and held in place by lengths of tantalum wire 0.15 mm in diameter spot-welded to the spade. Cycles of argon bombarding and annealing were used for *in situ* cleaning of the sample, consisting of a 20 minute bombard followed by a 10 minute anneal at 450 °C. The cleanliness of the sample was verified using XPS, LEED and STM.

2.8.2 Organic Molecules

The molecules used in the present work were deposited on the surface by thermal evaporation, using a Knudsen cell consisting of a molybdenum crucible in a tungsten wire basket (Figure 2.24). The crucible was resistively heated by

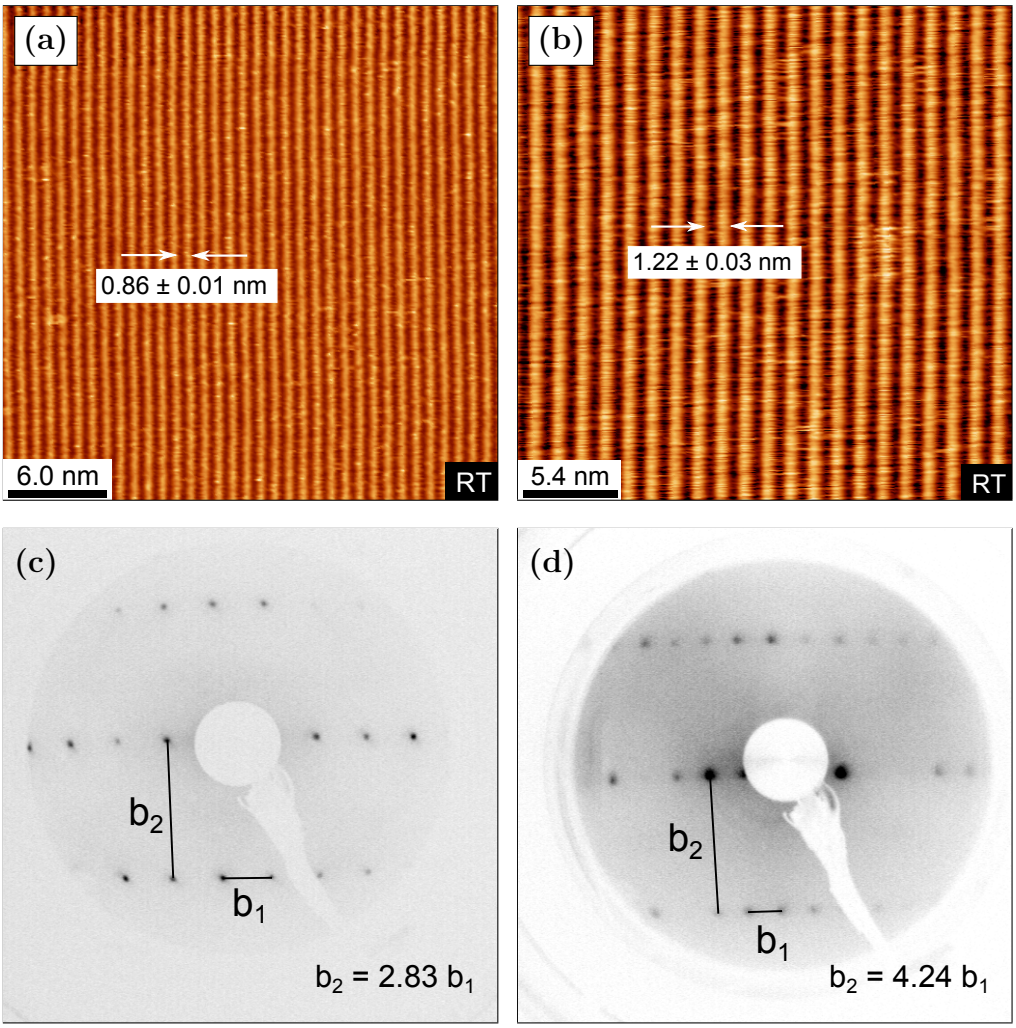

Figure 2.23: STM and LEED for the 2×1 (left) and 3×1 (right) Au(110) reconstructions. (a) (+0.16 V,1.58 nA), (b) (−1.12 V,0.15 nA), (c) recorded at 80.5 eV, (d) recorded at 75.8 eV.

passing current through the tungsten wire. The temperature of the cell was monitored by a thermocouple connection on the base of the crucible. Before deposition the molecules were thoroughly degassed at temperatures slightly above those used for evaporation. Approximate deposition temperatures for the tetrabromophenyl porphyrin, dibromo-diphenyl porphyrin, and trisbromophenyl benzene molecules were 300 °C, 250 °C and 200 °C respectively, while the C_{60} molecules were evaporated at 400 °C.

Drawings of the organic molecules are shown in Figure 2.25, along with nominal dimensions determined from ChemSketch [62]. The four-fold

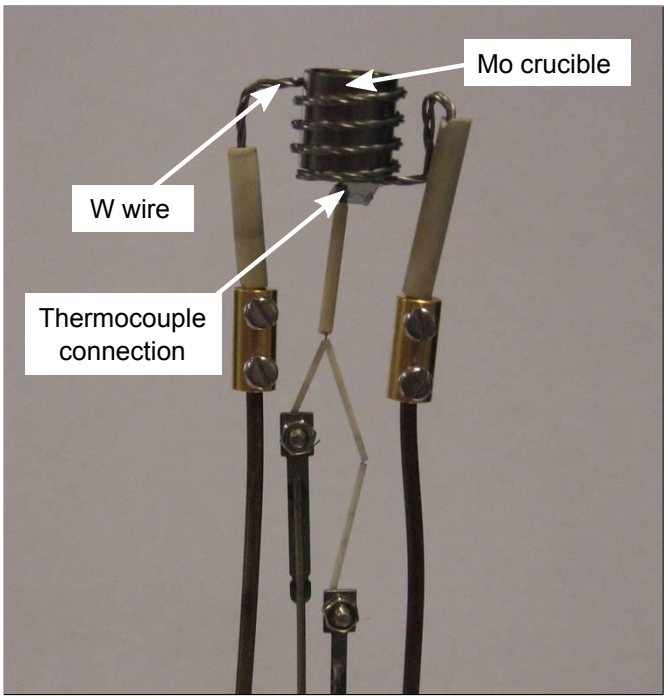

Figure 2.24: A Knudsen cell used for molecular evaporations.

porphyrins, Ni(II) 5,10,15,20-tetrakis(4-bromophenyl) porphyrin (NiTBrPP), and 5,10,15,20-tetrakis(4-bromophenyl) porphyrin (H_2TBrPP), were synthesised, purified and characterised in the SFI Tetrapyrrole Laboratory, School of Chemistry, Trinity College Dublin (TCD), following published procedures [63]. The three-fold 1,3,5-tris(4-bromophenyl) benzene (TBB) was purchased from TCI Europe N.V. [64]. The two-fold Ni(II) 5,15-dibromo-10,20-diphenyl porphyrin (NiDBrDPP) was also synthesised in the SFI Tetrapyrrole Laboratory, TCD. The C_{60} fullerenes were purchased from Sigma-Aldrich [65].

2.9 Density Functional Theory

Density Functional Theory (DFT) is a widely-used quantum computational technique, employed to calculate electronic properties of materials. DFT is concerned with the electron density, which always depends on three spatial coordinates, regardless of the complexity of the system [66, 67]. Hohenberg and Kohn [68] proved that for a molecular system with a non-degenerate ground state, the energy of that ground state is completely determined by the electron density $\rho(\vec{r})$. The aim of DFT is to minimise the energy functional $E[\rho(\vec{r})]$, in order to find the lowest energy configuration.

Chapter 4 includes the results of DFT calculations carried out for the TBB molecule by Dr. Cormac McGuinness and Ms. Anna Lawless in the School of Physics, TCD, using the Stockholm-Berlin (StoBe) implementation of the deMon package [69].

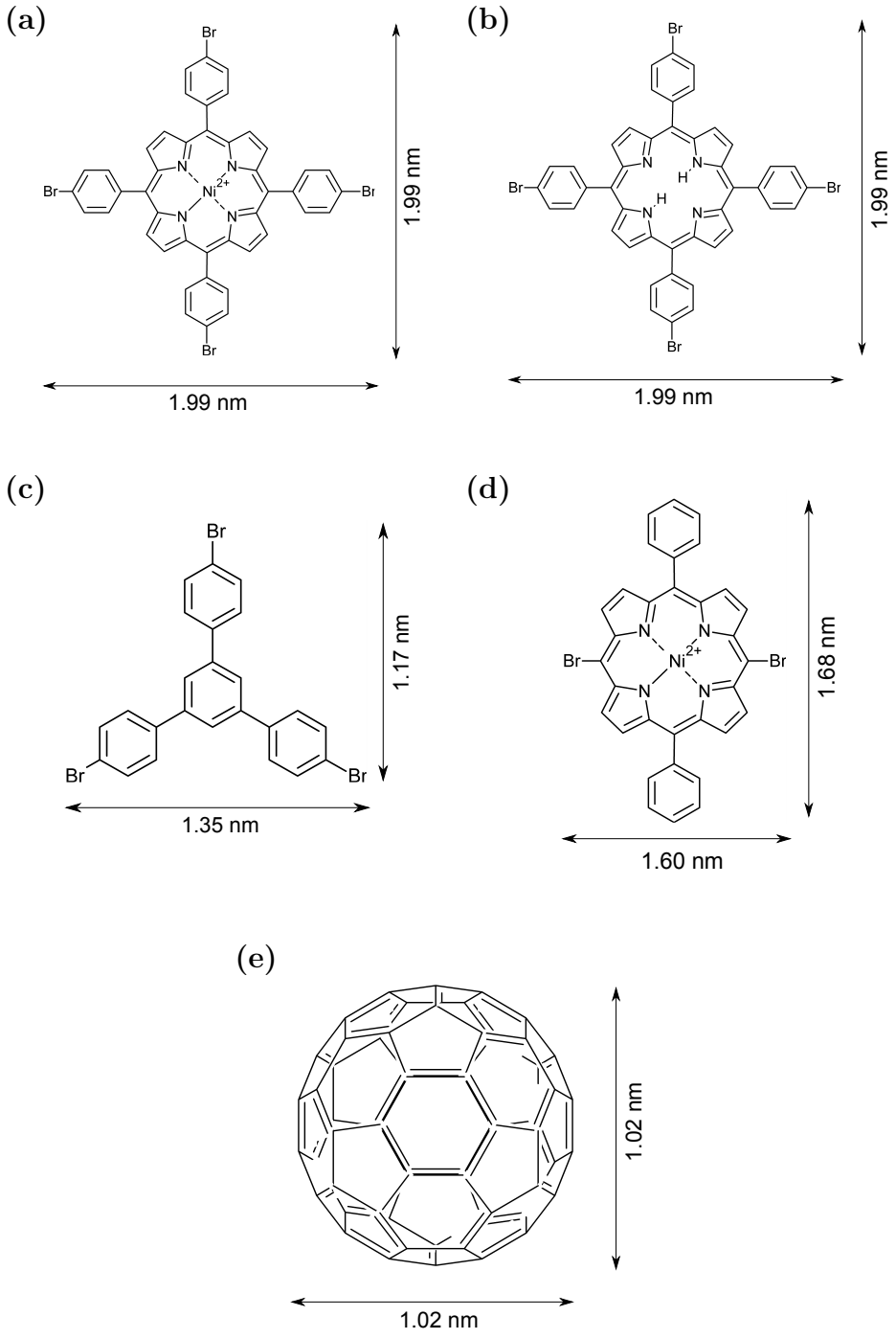

Figure 2.25: Organic molecules used in the present work. (a) NiTBrPP ($C_{44}H_{24}N_4NiBr_4$), (b) H_2TBrPP ($C_{44}H_{26}N_4Br_4$), (c) TBB ($C_{24}H_{15}Br_3$), (d) NiDBrDPP ($C_{32}H_{18}N_4NiBr_2$), (e) fullerene (C_{60}). Hydrogen atoms not explicitly shown, except for those bonded to the pyrrolic nitrogen atoms in H_2TBrPP.

2.10 Bibliography

[1] Sheerin, G., Ordering of Organic Molecules on Templated Surfaces, Ph.D. thesis, Dublin City University, Dublin, 2006.

[2] Wilson, R., *Vacuum Technology for Applied Surface Science*, in Surface Analysis - The Principal Techniques, edited by J.C. Vickerman, 1st ed., pp. 9–42, John Wiley & Sons, Chichester, 1997.

[3] Tompkins, H.G., Vacuum Technology: A Beginning, 1st ed., AVS, New York, 2002.

[4] Binnig, G., Rohrer, H., Gerber, C., and Weibel, E., *Surface Studies by Scanning Tunneling Microscopy*, Physical Review Letters, **49** (1982) pp. 57–61.

[5] Wiesendanger, R., Scanning Probe Microscopy and Spectroscopy: Methods and Applications, 1st ed., Cambridge University Press, Cambridge, 1998.

[6] Tersoff, J. and Hamann, D.R., *Theory of the Scanning Tunneling Microscope*, Physical Review B, **31** (1985) pp. 805–813.

[7] Chen, C.J., Introduction to Scanning Tunneling Microscopy, 2nd ed., Oxford Science Publications, New York, 2008.

[8] Tersoff, J. and Lang, N.D., *Theory of Scanning Tunneling Microscopy*, in Scanning Tunneling Microscopy, edited by J.A. Stroscio and W.J. Kaiser, 1st ed., pp. 1–29, Academic Press, Inc., San Diego, 1993.

[9] Woodruff, D.P. and Delchar, T.A., Modern Techniques of Surface Science, 2nd ed., Cambridge University Press, Cambridge, 1994.

[10] Leggett, G.J., *Scanning Tunnelling Microscopy and Atomic Force Microscopy*, in Surface Analysis - The Principal Techniques, edited by J.C. Vickerman, 1st ed., pp. 393–449, John Wiley & Sons, Chichester, 1997.

[11] Tersoff, J. and Hamann, D.R., *Theory and Application for the Scanning Tunneling Microscope*, Physical Review Letters, **50** (1983) pp. 1998–2001.

[12] Binnig, G. and Smith, D.P.E., *Single-Tube 3-Dimensional Scanner for Scanning Tunneling Microscopy*, Review of Scientific Instruments, **57** (1986) pp. 1688–1689.

[13] Omicron NanoTechnology GmbH, URL `http://www.omicron.de/en/products/variable-temperature-spm/instrument-concept`, accessed July 2013.

[14] The VT SPM User's Guide, 1st ed., Omicron Nanotechnology, Taunusstein, Germany, 2000.

[15] Melmed, A.J., *The Art and Science and Other Aspects of Making Sharp Tips*, Journal of Vacuum Science & Technology B, **9** (1991) pp. 601–608.

[16] Zhang, R. and Ivey, D.G., *Preparation of sharp polycrystalline tungsten tips for scanning tunneling microscopy imaging*, Journal of Vacuum Science & Technology B, **14** (1996) pp. 1–10.

[17] Ekvall, I., Wahlstrom, E., Claesson, D., Olin, H., and Olsson, E., *Preparation and characterization of electrochemically etched W tips for STM*, Measurement Science & Technology, **10** (1999) pp. 11–18.

[18] Yu, Z.Q., Wang, C.M., Du, Y., Thevuthasan, S., and Lyubinetsky, I., *Reproducible tip fabrication and cleaning for UHVSTM*, Ultramicroscopy, **108** (2008) pp. 873–877.

[19] Tip Etching Kit User Manual, 1st ed., Omicron Nanotechnology, Taunusstein, Germany, 1998.

[20] Horcas, I., Fernandez, R., Gomez-Rodriguez, J.M., Colchero, J., Gomez-Herrero, J., and Baro, A.M., *WSxM: A Software for Scanning Probe Microscopy and a Tool for Nanotechnology*, Review of Scientific Instruments, **78** (2007) pp. 013705–1–013705–8.

[21] Nanotec Electronica S.L., *WSxM*, URL `www.nanotec.es`, accessed July 2013.

[22] *Inkscape*, URL `www.inkscape.org`, accessed July 2013.

[23] Ratner, B.D. and Castner, D.G., *Electron Spectroscopy for Chemical Analysis*, in Surface Analysis - The Principal Techniques, edited by J.C. Vickerman, 1st ed., pp. 43–98, John Wiley & Sons, Chicester, 1997.

[24] Moulder, J.F., Stickle, W.F., Sobol, P.E., and Bomben, K.D., Handbook of X-ray Photoelectron Spectroscopy, 1st ed., Perkin-Elmer Corporation, Minnesota, 1992.

[25] EA 125 Energy Analyser User Guide, 2nd ed., Omicron Nanotechnology, Taunusstein, Germany, 2006.

[26] 554-S X-ray Source Control Package User Guide, 1st ed., Omicron Nanotechnology, Taunusstein, Germany, 2008.

[27] EIS/EIS Sphera Software User Guide, 2nd ed., Omicron Nanotechnology, Taunusstein, Germany, 2008.

[28] *Microcal Origin*, URL `www.originlab.com`, accessed July 2013.

[29] Shirley, D.A., *High-Resolution X-Ray Photoemission Spectrum of Valence Bands of Gold*, Physical Review B, **5** (1972) pp. 4709–4714.

[30] Herrera-Gomez, A., *Aanalyzer*, URL `http://qro.cinvestav.mx/~aanalyzer/`, accessed July 2013.

[31] Wojdyr, M., *Fityk*, URL `http://fityk.nieto.pl/`, accessed July 2013.

[32] Farnsworth, H.E., *Preparation, Structural Characterization, and Properties of Atomically Clean Surfaces*, Journal of Vacuum Science & Technology, **20** (1982) pp. 271–280.

[33] Flavell, W.R., *Surface Structure Determination by Interference Techniques*, in Surface Analysis - The Principal Techniques, edited by J.C. Vickerman, 1st ed., pp. 313–397, John Wiley & Sons, Chichester, 1997.

[34] Kittel, C., Introduction to Solid State Physics, 8th ed., John Wiley & Sons, New Jersey, 2005.

[35] SPECTALEED Optics and Electron Gun User's Guide, 4th ed., Omicron Nanotechnology, Taunusstein, Germany, 1999.

[36] *GIMP, the GNU Image Manipulation Program*, URL `www.gimp.org`, accessed July 2013.

[37] Hermann, K. and Van Hove, M.A., *LEEDpat*, URL `http://www.fhi-berlin.mpg.de/KHsoftware/LEEDpat/`, accessed July 2013.

[38] Lackinger, M., Griessl, S., Heckl, W.M., and Hietschold, M., *Coronene on Ag(111) investigated by LEED and STM in UHV*, Journal of Physical Chemistry B, **106** (2002) pp. 4482–4485.

[39] Lee, H.L., Strategies for the Formation of Covalently Bonded Nano-Networks on Metal Surfaces through Amine Reactions, Ph.D. thesis, Dublin City University, Dublin, 2012.

[40] Attwood, D., Soft X-Rays and Extreme Ultraviolet Radiation, 1st ed., Cambridge University Press, Cambridge, 2000.

[41] Margaritondo, G., Introduction to Synchrotron Radiation, 1st ed., Oxford University Press, New York, 1988.

[42] Hahner, G., *Near edge X-ray absorption fine structure spectroscopy as a tool to probe electronic and structural properties of thin organic films and liquids*, Chemical Society Reviews, **35** (2006) pp. 1244–1255.

[43] Kunz, C., *Synchrotron radiation: third generation sources*, Journal of Physics: Condensed Matter, **13** (2001) pp. 7499–7510.

[44] MAX-lab, *Beamline D1011, MAX-lab*, URL `https://www.maxlab.lu.se/node/38`, accessed July 2013.

[45] ISA, *The SX700 beamline at ASTRID*, URL `http://www.isa.au.dk/facilities/astrid/beamlines/sx700/sx700.asp`, accessed July 2013.

[46] Zangwill, A., Physics at Surfaces, 1st ed., Cambridge University Press, Cambridge, 1988.

[47] Yeh, J.J. and Lindau, I., Atomic Subshell Photoionization Cross Sections and Asymmetry Parameters, 1st ed., Academic Press, Inc., Stanford, 1985.

[48] Mathieu, H.J., *Auger Electron Spectroscopy*, in Surface Analysis - The Principal Techniques, edited by J.C. Vickerman, 1st ed., pp. 99–133, John Wiley & Sons, Chichester, 1997.

[49] Seah, M.P., *Quantification of AES and XPS*, in Practical Surface Analysis, Volume 1: Auger and X-ray Photoelectron Spectroscopy, edited by D. Briggs and M.P. Seah, 2nd ed., pp. 201–255, John Wiley & Sons, Chichester, 1990.

[50] Stohr, J., NEXAFS Spectroscopy, 2nd ed., Springer-Verlag, Heidelberg, 1996.

[51] Narioka, S., Ishii, H., Ouchi, Y., Yokoyama, T., Ohta, T., and Seki, K., *XANES Spectroscopic Studies of Evaporated Porphyrin Films - Molecular-Orientation and Electronic-Structure*, Journal of Physical Chemistry, **99** (1995) pp. 1332–1337.

[52] Stohr, J. and Outka, D.A., *Determination of Molecular Orientations on Surfaces from the Angular-Dependence of Near-Edge X-Ray-Absorption Fine-Structure Spectra*, Physical Review B, **36** (1987) pp. 7891–7905.

[53] Lopez, S., Dunlop, H.M., Benmalek, M., Tourillon, G., Wong, M.S., and Sproul, W.D., *XPS, XANES and ToF-SIMS characterization of reactively magnetron-sputtered carbon nitride films*, Surface and Interface Analysis, **25** (1997) pp. 827–835.

[54] Surface Preparation Laboratory, URL `www.spl.eu`, accessed July 2013.

[55] Van Hove, M.A., Koestner, R.J., Stair, P.C., Biberian, J.P., Kesmodel, L.L., Bartos, I., and Somorjai, G.A., *The Surface Reconstructions of the (100) Crystal Faces of Iridium, Platinum and Gold: 1. Experimental-Observations and Possible Structural Models*, Surface Science, **103** (1981) pp. 189–217.

[56] Kilian, L., Umbach, E., and Sokolowski, M., *A refined structural analysis of the PTCDA monolayer on the reconstructed Au(111) surface - "Rigid or distorted carpet?"*, Surface Science, **600** (2006) pp. 2633–2643.

[57] Doyen, G., Drakova, D., Barth, J.V., Schuster, R., Gritsch, T., Behm, R.J., and Ertl, G., *Scanning-Tunneling-Microscope Imaging of Clean and Alkali-Metal-Covered Cu(110) and Au(110) Surfaces*, Physical Review B, **48** (1993) pp. 1738–1749.

[58] Kuehnle, A., Linderoth, T.R., Hammer, B., and Besenbacher, F., *Chiral recognition in dimerization of adsorbed cysteine observed by scanning tunnelling microscopy*, Nature, **415** (2002) pp. 891–893.

[59] dos Reis, D.D., Negreiros, F.R., de Carvalho, V.E., and Soares, E.A., *Geometry of the Au(110)-(1 x 2) missing-row clean surface: A New LEED and DFT study*, Surface Science, **604** (2010) pp. 568–573.

[60] Moritz, W. and Wolf, D., *Structure Determination of the Reconstructed Au(110) Surface*, Surface Science, **88** (1979) pp. L29–L34.

[61] Binnig, G., Rohrer, H., Gerber, C., and Weibel, E., *(111) Facets as the Origin of Reconstructed Au(110) Surfaces*, Surface Science, **131** (1983) pp. L379–L384.

[62] *ACD/ChemSketch*, URL `www.acdlabs.com/resources/freeware/chemsketch/`, accessed July 2013.

[63] Grill, L., Dyer, M., Lafferentz, L., Persson, M., Peters, M., and Hecht, S., *Nano-architectures by covalent assembly of molecular building blocks*, Nature Nanotechnology, **2** (2007) pp. 687–691.

[64] TCI Europe N.V., URL `www.tcichemicals.com/en/eu`, accessed July 2013.

[65] Sigma-Aldrich, URL `www.sigmaaldrich.com/ireland.html`, accessed July 2013.

[66] Hehre, W.J., A Guide to Molecular Mechanics and Quantum Chemical Calculations, 1st ed., Wavefunction, Inc., California, 2003.

[67] Levine, I.N., Quantum Chemistry, 5th ed., Prentice-Hall, Inc., New Jersey, 2000.

[68] Hohenberg, P. and Kohn, W., *Inhomogeneous Electron Gas*, Physical Review B, **136** (1964) pp. B864–B871.

[69] Hermann, K., et al., StoBe-deMon version 3.0. 2008.

Chapter 3
Structural and Electronic Properties of Brominated Four-fold Symmetrical Porphyrin Molecules on Metal Surfaces

3.1 Introduction

In situ carbon-halogen bond scission has been shown to be an effective method of forming covalently bonded structures on surfaces [1–3]. Grill *et al.* used this method to form porphyrin nano-networks on Au(111) from brominated tetraphenyl porphyrin molecules (Figure 1.2) [4]. There have been many further studies in this area, as previously discussed (Section 1.4) [5–8].

Porphyrins are conventionally synthesised and metalated in solution [4]. In 1960, Fleischer *et al.* [9] proposed that the metalation occurs via the formation of an intermediate state, where the iminic nitrogen atoms of the porphyrin macrocycle bond to the metal ion in solution while the pyrrolic nitrogen atoms retain their hydrogen atoms. The metalation then proceeds with the subsequent loss of the hydrogen, resulting in the metal ion bonding to the four nitrogen atoms of the macrocycle [9].

In recent years, the *in situ* metalation of porphyrins on metal surfaces has been studied extensively. Free base porphyrin molecules have been metalated on surfaces using deposited atoms including zinc [10–12], nickel [13], cobalt [10, 13], iron [14–17], and cerium [18]. Porphyrin molecules have also been successfully metalated *in situ* using substrate atoms [19–25].

This chapter investigates the self-assembly and formation of molecular networks of free base 5,10,15,20 tetrakis(4-bromophenyl) porphyrin (H_2TBrPP) (Figure 3.1(a)) and Ni(II) 5,10,15,20 tetrakis(4-bromophenyl) porphyrin (NiTBrPP) (Figure 3.1(b)) on the Au(111), Ag(111) and Cu(111) metal surfaces. The *in situ* metalation of H_2TBrPP on the Au(111) surface with deposited

Ni atoms is demonstrated. The first reported *in situ* metalation of free base porphryin molecules using surface atoms is described, for the self-metalation of H_2TBrPP on Cu(111). This also constitutes the first direct observation of the intermediate state [9] on a surface [19].

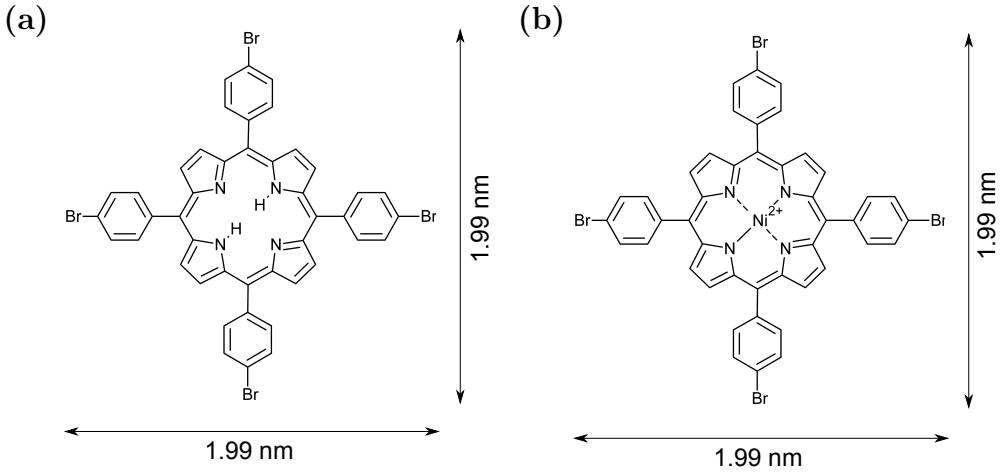

Figure 3.1: Structure of (a) H_2TBrPP ($C_{44}H_{26}N_4Br_4$), (b) NiTBrPP ($C_{44}H_{24}N_4NiBr_4$), with nominal dimensions determined from ChemSketch [26]. Hydrogen atoms not explicitly shown, except for the hydrogen atoms bonded to the pyrrolic nitrogen atoms in H_2TBrPP.

3.2 STM and Photoemission Study of NiTBrPP and H_2TBrPP on the Au(111) Surface

3.2.1 Analysis for Deposition at Room Temperature

Figure 3.2 shows STM images for a monolayer of NiTBrPP deposited on the Au(111) $22 \times \sqrt{3}$ surface at room temperature (3.2(a) and 3.2(b)), and subsequently annealed at 100 °C (3.2(c) and 3.2(d)) and 120 °C (3.2(e) and 3.2(f)). The molecules self-assemble at these temperatures; no covalent bonding occurs. At a monolayer coverage the NiTBrPP molecules pack together in four different configurations. The unit cells for these configurations are shown in Figure 3.2, and the parameters are given in Table 3.1. The dimensions of each unit cell were determined by analysing approximately one hundred unit cells in the STM images. The insets in Figure 3.2(a) and Figure 3.2(b) show the molecular packing

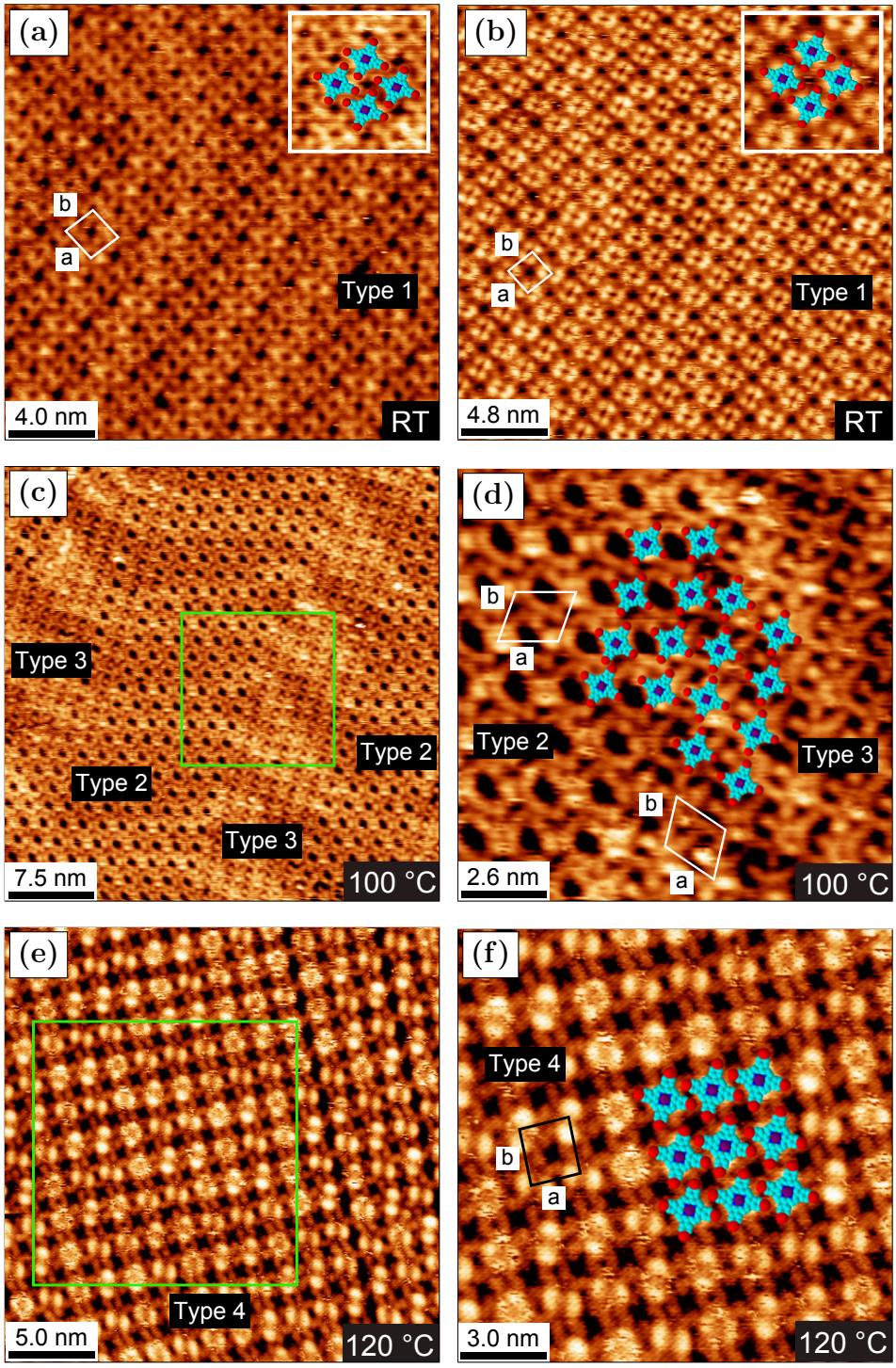

Figure 3.2: STM for 1 ML of NiTBrPP deposited on room temperature Au(111) and subsequently annealed at 100 °C and 120 °C. (a) (+1.24 V,0.23 nA), inset (+1.07 V,0.23 nA), 5.0 nm × 5.0 nm, (b) (+1.58 V,0.18 nA), inset (+1.58 V,0.18 nA), 5.0 nm × 5.0 nm, (c) and (d) (−1.45 V,0.19 nA), (e) and (f) (−2.00 V,0.50 nA). Enlarged views of the highlighted areas in (c) and (e) are shown in (d) and (f) respectively. (e) and (f) shows a differently prepared surface to (a) - (d).

in greater detail. Figure 3.2(d) and 3.2(f) show enlarged views of the highlighted areas in Figure 3.2(c) and 3.2(e) respectively. For Type 1, Type 2 and Type 4 packing, the phenyl rings of adjacent molecules are parallel to each other, resulting in one pore per every four NiTBrPP molecules. This configuration is known as $\pi - \pi$ stacking [27]. In contrast, the phenyl rings of adjacent molecules in domains exhibiting Type 3 packing are oriented perpendicular to each other, a configuration known as T-stacking [27]. The porphyrin macrocycle is imaged with both four-fold (Figure 3.2(a) - 3.2(d)) and two-fold symmetry (Figure 3.2(e) and 3.2(f)). The two-fold symmetry is due to a saddling distortion of the macrocycle, where two pyrrole rings bend towards the surface, and two pyrrole rings bend away from the surface [23, 27].

Table 3.1: Length of unit cell vectors and angle between vectors for different molecular packing configurations of NiTBrPP on Au(111) shown in Figure 3.2.

Packing	a (nm)	b (nm)	θ (°)
Type 1	1.55 ± 0.02	1.58 ± 0.02	85.5 ± 1.7
Type 2	1.72 ± 0.03	1.50 ± 0.01	74.9 ± 1.2
Type 3	1.64 ± 0.10	1.50 ± 0.01	89.0 ± 1.9
Type 4	1.70 ± 0.01	2.00 ± 0.01	90.5 ± 1.5

Figure 3.3 shows NiTBrPP nano-networks on Au(111) formed after annealing the molecular layers at the temperatures shown [5]. Debromination has occurred, and the porphyrin radicals have covalently bonded to form nano-networks, according to the bonding scheme shown in Figure 1.2 [4]. The nano-networks do not exhibit any long-range order, but do include small areas of ordered four-fold nano-mesh. Statistical analysis of ten STM images featuring a total of 500 pores reveals that approximately 25 % of the pores are square. Figure 3.3(f) shows a network that has been annealed at 400 °C. The network remains intact on the surface, with the same degree of order as seen after annealing at lower temperatures. This demonstrates the thermal stability of the nano-networks, and is a feature of the irreversible nature of covalent bonds [5]. Following network formation, the porphyrins appear four-fold symmetrical in the STM images (Figure 3.3), with no molecules imaging as two-fold symmetrical, indicating that the macrocycles are no longer distorted.

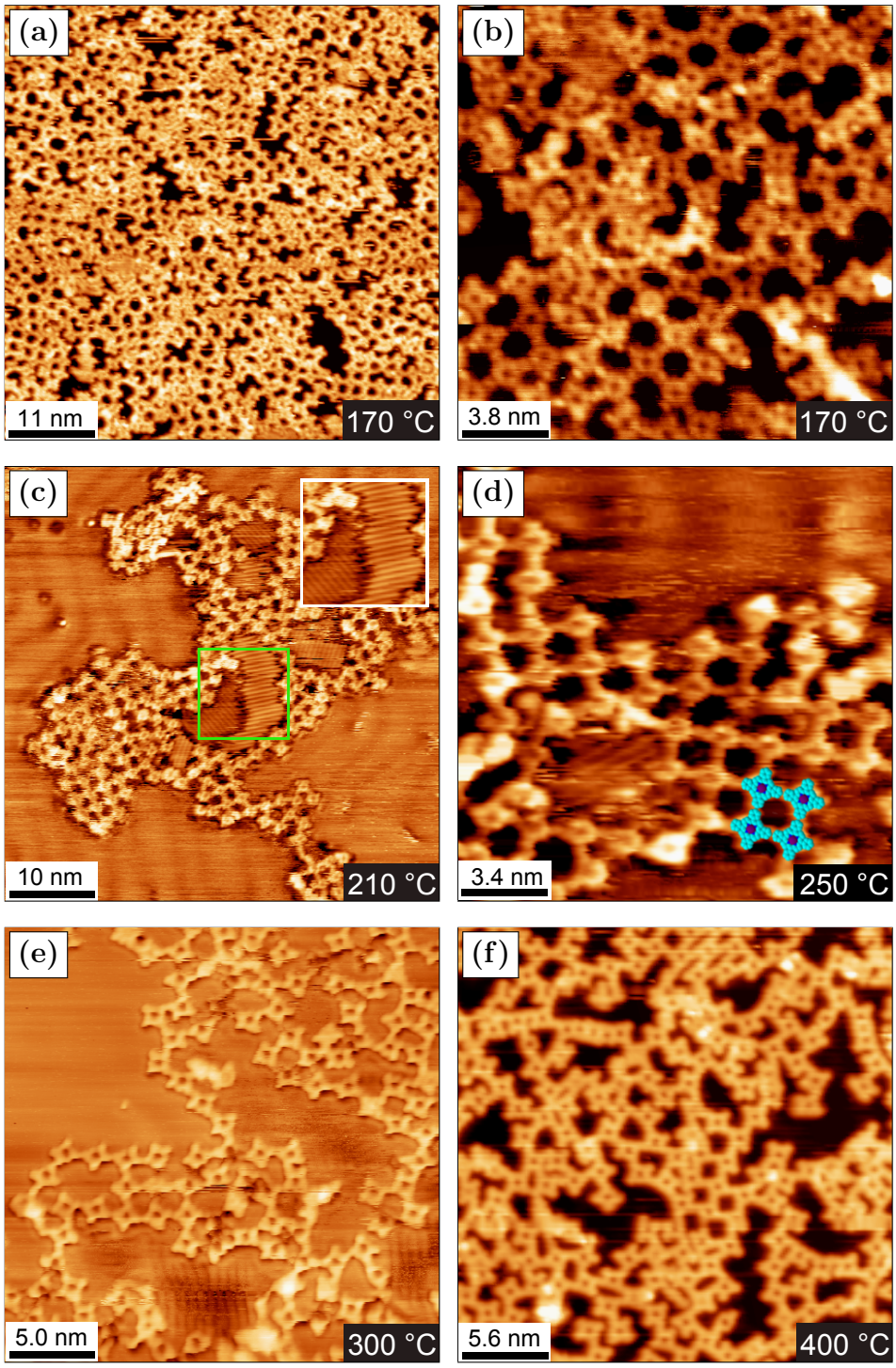

Figure 3.3: STM for NiTBrPP on Au(111), network formation after annealing molecules deposited at room temperature. (a) (+1.00 V,1.00 nA), (b) (+0.79 V,0.50 nA), (c) (−0.70 V,0.88 nA), (d) (+1.26 V,0.15 nA), (e) (−0.77 V,2.70 nA), (f) (−0.90 V,0.80 nA). An enlarged view of the highlighted area in (c) is shown in the inset. (a), (b) and (f) show a surface with 0.9 ML coverage, (c) - (e) show a differently prepared surface with 0.4 ML coverage.

The inset in Figure 3.3(c) shows an enlarged view of the highlighted area in the main figure. Two domains of 2×1 reconstruction are visible, with a periodicity of 0.51 ± 0.02 nm in the 2× direction. The 2×1 domains are oriented at 120° to each other. To our knowledge, no similar structures have been reported in the literature. However, this 2×1 structure has been observed for NiTBrPP deposited on Ag(111) (Subsection 3.3.1), NiDBrDPP deposited on Au(111) (Section 5.2) and Cu(111) (Section 5.5), and previously, for deposition of the three-fold molecule 1,3,5-tris(4-aminophenyl) benzene on the Au(111) surface [28]. Therefore the reconstruction is independent of the substrate, the molecular symmetry, the presence of bromine, and the STM bias conditions. The reconstruction has only been observed for areas of the surface enclosed by molecular structures, either islands of self-assembled molecules, protopolymer structures or covalently bonded networks. One possible explanation is that the reconstruction is a charge density wave; however, this is unlikely as the periodicity in the 2× direction is independent of the tunnel bias. An alternative explanation is that the 2×1 reconstruction is a local change in the electronic structure of the surface, caused by electronic charge transfer from the substrate. Another possibility is that the reconstruction is the relaxation of surface atoms in order to relieve strain induced by the proximity of the molecules. At present, the cause of the 2×1 reconstruction remains an open question, which requires further theoretical investigation.

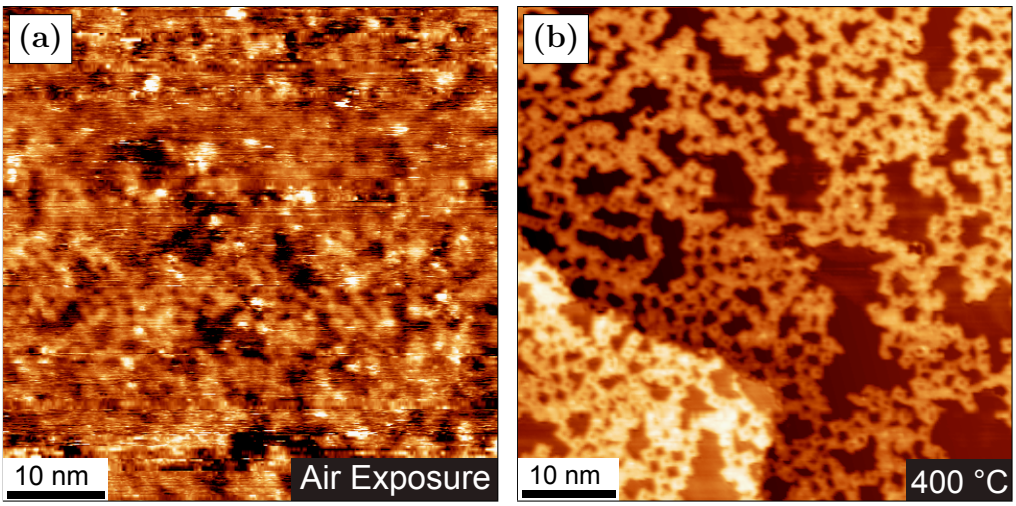

Figure 3.4: STM for NiTBrPP nano-network, (a) following exposure to ambient and (b) recovered by thermal annealing. (a) (+1.54 V,1.45 nA), (b) (+1.00 V,1.00 nA).

In order to further investigate the stability of the nano-networks, a NiTBrPP network was exposed to ambient conditions for 60 hours. Figure 3.4(a) shows an STM image recorded after the sample was reintroduced to UHV conditions. As expected, a layer of adsorbed material from the air is present on the sample, although there is some evidence for the network underneath this layer. Figure 3.4(b) shows an STM image recorded after annealing the sample at 400 °C. The adsorbed material has been removed, and the network has been recovered intact. The sample was further annealed at 500 °C, with no observed disruption to the network [5]. Hence, the covalently bonded networks exhibit significant thermal stability and can be recovered after exposure to ambient. This is an important finding for applications, such as sensor development using porphyrin networks.

Figure 3.5 shows Br 3d PES and Br 3p XPS data for NiTBrPP deposited on Au(111) at room temperature and annealed at the temperatures shown. The Br 3d core level spectra shown in Figure 3.5(a) have been fitted with two Voigt doublets with $3d_{5/2}$ binding energies of 70.3 eV and 70.2 eV respectively and a spin-orbit splitting of 1.0 eV. A reasonable fit for the spectrum recorded after room temperature deposition could not be obtained for a single component with a branching ratio of 0.66, therefore an additional component was used to fit the spectrum, despite the energy separation of the components being less than the resolution of the system. The component at 70.2 eV is assigned to bromine in the initial monolayer, while the component at 70.3 eV is assigned to bromine in the second and subsequent monolayers. The bromine in the first layer has shifted to a lower binding energy relative to the bromine in subsequent layers due to a weak interaction of the porphyrin molecule with the Au surface. After annealing at 150 °C, an additional doublet with a $3d_{5/2}$ binding energy of 67.9 eV is present, and is assigned to bromine which has dissociated from the NiTBrPP molecule and is on the Au(111) surface. The intensity of the component at 70.3 eV has decreased by approximately 90 %, due to the desorption of bromine from the surface during the anneal. C 1s photoemission spectra were not recorded for this experiment; however C 1s spectra for similar debromination experiments involving NiTBrPP show no decrease in the C 1s signal, indicating that Br is dissociating from the porphyrin molecules. After annealing at 200 °C there is no longer a component at 70.3 eV, as Br in the second and subsequent monolayers has desorbed from the Au surface. There is still bromine bonded to the NiTBrPP molecules, with a very small amount of dissociated bromine on the surface.

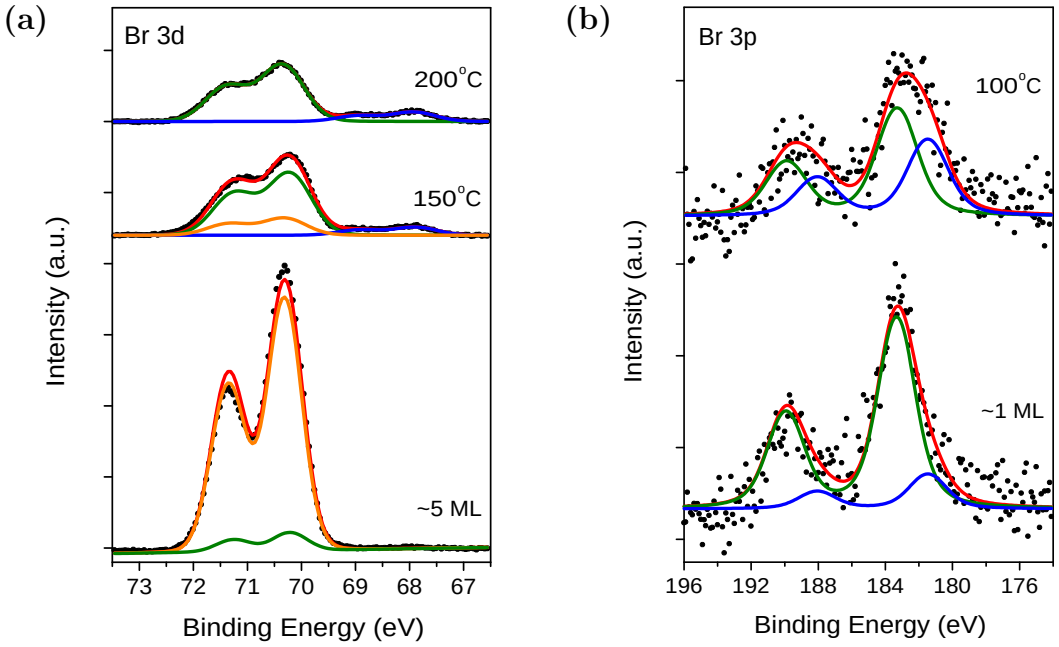

Figure 3.5: PES and XPS for NiTBrPP deposited on room temperature Au(111) and annealed at the temperatures shown. (a) PES for Br 3d region, hν = 170.0 eV, (b) XPS for Br 3p region, hν = 1486.7 eV. (a) corresponds to a surface with 5 ML coverage, (b) corresponds to a differently prepared surface with 1 ML coverage (Figure 3.2(a) - (d)).

Further evidence for the dissociation of the Br on annealing is shown in Figure 3.5(b), which shows XPS data recorded after the deposition of 1 ML of NiTBrPP at room temperature and subsequent annealing at 100 °C. The Br 3p core levels have been fitted with two Voigt doublets, with $3p_{3/2}$ binding energies of 183.4 eV and 181.5 eV respectively, and a spin-orbit splitting of 6.6 eV. The higher binding energy component at 183.4 eV is assigned to bromine atoms bonded to the NiTBrPP molecules, while the lower binding energy component is assigned to bromine on the surface. After annealing at 100 °C, approximately 40 % of the bromine bonded to the porphyrin has desorbed from the surface. The spectrum recorded after annealing at 100 °C suggests that partial debromination has occurred in the monolayer NiTBrPP coverage annealed at 120 eV (Figure 3.2(e) and 3.2(f)). However, as the molecules are too tightly packed at that coverage to diffuse on the surface, no network formation is observed.

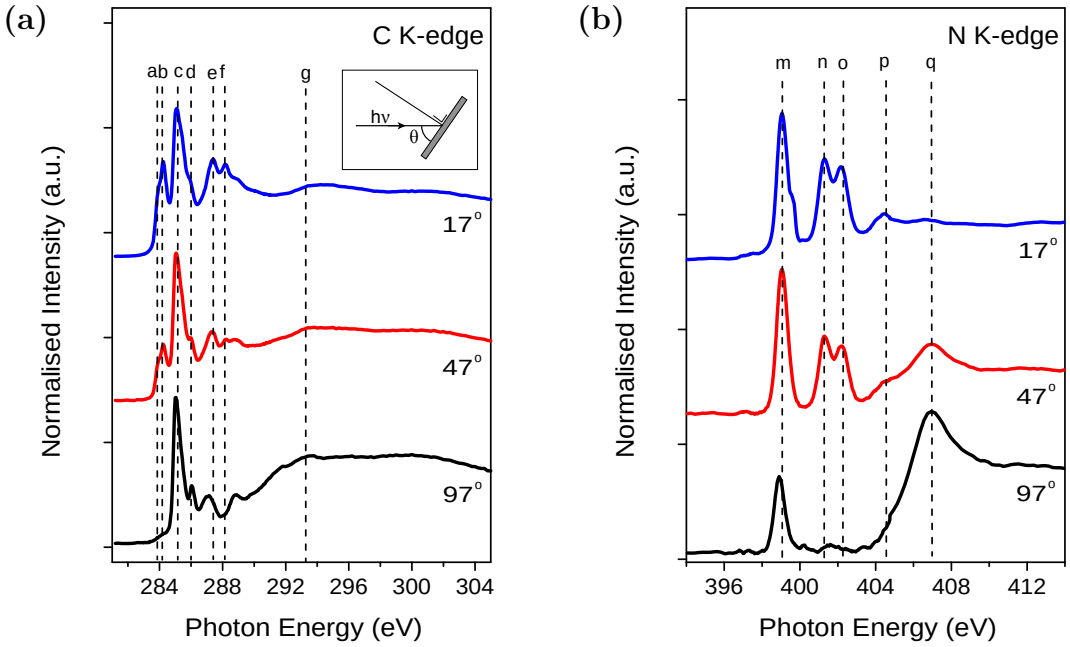

Figure 3.6: (a) C K-edge and (b) N K-edge XAS for 5 ML of NiTBrPP deposited on room temperature Au(111). Inset in (a) shows angle θ between incoming x-ray photon and sample plane. Spectra were recorded at three different angles of incidence, and correspond to the 5 ML spectrum shown in Figure 3.5(a).

Figure 3.6(a) shows C K-edge x-ray absorption spectra recorded at room temperature for three different angles of incidence for 5 ML of NiTBrPP on Au(111). The energies of the absorption lines and assignments are given in Table 3.2. Peaks *a* and *b* are assigned to transitions from the C 1s orbital to the lowest unoccupied molecular orbital (LUMO) centred on the π-conjugated porphyrin macrocycle [29, 30, 33]. Goldoni *et al.* [33] have shown that these two absorption lines arise from the inequivalent carbon sites in the macrocycle, with peaks *a* and *b* assigned to transitions into the LUMO from C 1s orbitals localised on the *meso* and *beta* carbon atoms respectively (Figure 1.1). Schmidt *et al.* [29] have observed an absorption line at 285.35 eV which they assign to transitions to π^* molecular orbitals on the phenyl rings; however this absorption line is not resolved in the present work.

The spectral features assigned to transitions to molecular orbitals localised

Table 3.2: Absorption line energies and assignments for C K-edge XA spectra for 5 ML of NiTBrPP deposited on Au(111) at room temperature shown in Figure 3.6(a). Also included is a comparison with the features observed in the C K-edge XA spectra of ZnTPP [29] and H_2TPP [30].

Absorption Line	NiTBrPP (Fig. 3.6(a)) (eV)	ZnTPP [a] (eV)	H_2TPP [b] (eV)	Assignment
a	283.9	283.95	283.8	$\pi^*_{\text{macrocycle}}$ [a,b]
b	284.2	284.30	—	$\pi^*_{\text{macrocycle}}$ [a]
c	285.1	285.05	284.9	$\pi^*_{\text{phenyl rings}}$ [a,b]
c_2	—	285.35	—	$\pi^*_{\text{phenyl rings}}$ [a]
d	286.0	285.90	—	$\pi^*_{\text{macrocycle}}$ [a]
e	287.4	287.70	287.6	$\pi^*_{\text{macrocycle}}$ [a,b]
f	288.2	288.80	288.6	$\sigma^*_{\text{phenyl rings}}$; $\pi^*_{\text{macrocycle}}$ [a]
g	293.3	—	293	σ^* [b]

a = [29], b = [30]

on the porphyrin macrocycle, labelled *a* and *b* in Figure 3.6(a), show an angular dependence, with the intensity decreasing as θ goes from grazing to normal incidence. The spectrum recorded at 97° shows almost zero intensity in the absorption lines labelled *a* and *b* when the electric field vector of the incoming x-rays is parallel to the surface. As these absorption lines are assigned to transitions to π^* molecular orbitals localised on the porphyrin macrocycle, this indicates that the macrocycle lies parallel to the surface, with a very small tilt angle. The absorption lines labelled *c* and *d*, related to transitions to π^* molecular orbitals on the phenyl rings, have similar intensities at all three angles of incidence, suggesting that the phenyl rings are oriented at a range of different angles with respect to the surface. The spectral features corresponding to the phenyl rings and the macrocycle are separated in the absorption spectrum, hence the NiTBrPP XA spectrum can be considered a superposition of the absorption spectra of the phenyl rings and the porphyrin macrocycle [33]. The application of

Table 3.3: Absorption line energies and assignments for N K-edge XA spectra for 5 ML of NiTBrPP deposited on Au(111) at room temperature shown in Figure 3.6(b). Also included is a comparison with the features observed in the N K-edge XA spectra of NiP [31], NiTPP [31] and NiOEP [32].

Absorption Line	NiTBrPP (Fig. 3.6(b)) (eV)	NiP [a] (eV)	NiTPP [a] (eV)	NiOEP [b] (eV)	Assignment
m	399.0	399.0	399.0	399.0	$\pi^*_{\text{N-Ni}}$ [a,b]
n	401.3	401.4	401.4	401.3	$\pi^*_{\text{N-C}}$ [a,b]
o	402.2	402.0	402.0	402.1	$\pi^*_{\text{N-C}}$ [a]
p	404.5	404.2	404.4	404.0	$\pi^*_{\text{N-Ni}}$ [b]
q	407.0	406.8	407.0	407.1	$\sigma^*_{\text{N-C}}$ [c]

a = [31], b = [32], c = [30]

the so-called 'building block principle' for the extraction of molecular orientation information from the spectra is thus justified [33, 34]. Using the method outlined in Section 2.7, together with Equations 2.30, 2.31 and 2.32 [34, 35], an angle for the orientation of the macrocycle with respect to the electric field vector of the incident photons can be extracted from the intensity ratios of the absorption lines measured at grazing and normal incidence. An angle of $27.8 \pm 6.5^\circ$ is calculated using this analysis. This may be interpreted to indicate that the macrocyle is tilted at this angle with respect to the surface, however this is unlikely. A more reasonable interpretation is that this angle is a measure of the distortion of the macrocycle on the surface, indicating that the macrocycle has adopted a non-planar geometry such as a saddle distortion [23, 27]. A more detailed analysis is required to calculate the exact orientation of the pyrrole rings with respect to the surface; such an analysis is not carried out in this thesis. Similarly, an angle of $65.2 \pm 5.1^\circ$ is calculated, relating to the orientation of the phenyl rings with respect to the electric field vector. This angle confirms that the phenyl rings are tilted with respect to the macrocycle, but is not the exact angle of rotation of the phenyl rings with respect to the surface. The calculated angle relating to the orientation of the macrocycle is in agreement with the angles of $\pm 20^\circ$ and $\pm 25^\circ$ calculated for CoTPP on Cu(111) [36], and CuTPP on Cu(111) [20] respectively.

The calculated angle relating to the phenyl ring orientation is in agreement with the angle of 60° reported for CuTPP on Cu(111) [20].

Figure 3.6(b) shows the corresponding N K-edge XA spectra for NiTBrPP on Au(111), recorded at the same three angles of incidence. The assignments of the absorption lines are given in Table 3.3, together with literature values for the absorption lines observed for NiP [31], NiTPP [31], and NiOEP [32]. The initial peak, labelled *m* in Figure 3.6(b), is related to transitions from the N 1s orbital to a hybridised Ni 3d π^*-N 2p π^* orbital, and is a single peak due to the equivalence of the four nitrogen atoms in the metalated macrocycle [31]. Absorption lines *n* and *o* are assigned to transitions into N-C π^* orbitals on the pyrrole rings [31], and decrease in intensity as the angle of incidence increases, while peak *q* is assigned to transitions into N-C σ^* orbitals on the pyrrole rings [30, 37–39], and increases in intensity as the angle of incidence increases. These results imply that the plane of the nitrogen atoms in the macrocycle is mostly parallel to the Au surface.

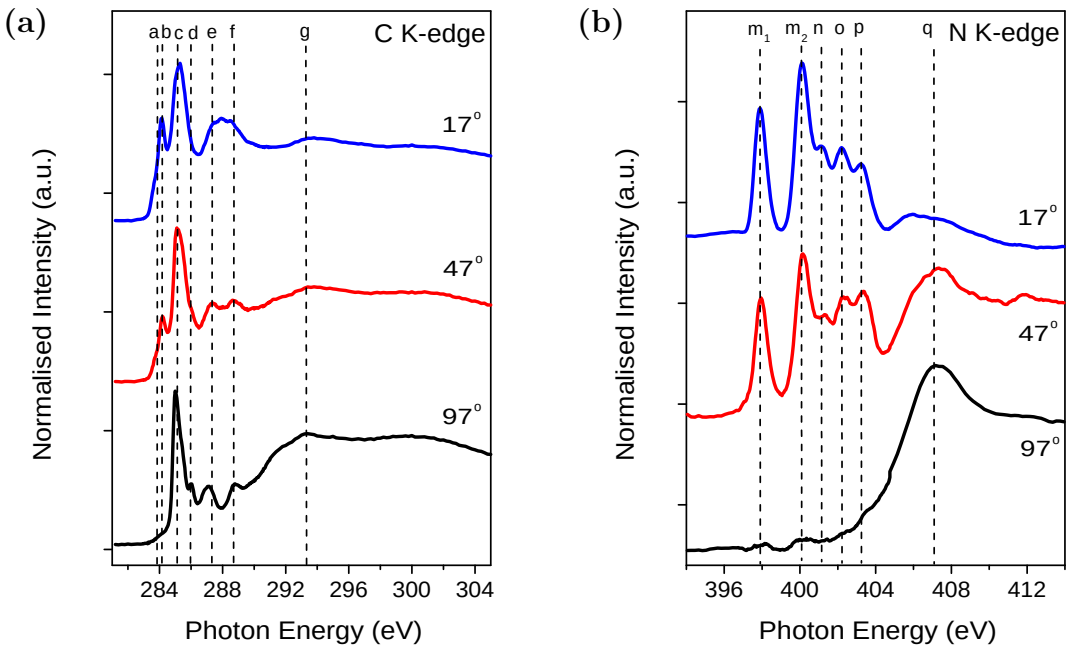

Figure 3.7: (a) C K-edge and (b) N K-edge XAS for 1.5 ML of H_2TBrPP deposited on room temperature Au(111). Spectra recorded at three different angles of incidence.

Table 3.4: Absorption line energies and assignments for C K-edge XA spectra for 1.5 ML of H_2TBrPP deposited on Au(111) at room temperature shown in Figure 3.7(a). Also included is a comparison with the features observed in the C K-edge XA spectra of H_2TPP [29, 30].

Absorption Line	H_2TBrPP (Fig. 3.7(a)) (eV)	H_2TPP [a] (eV)	H_2TPP [b] (eV)	Assignment
a	283.9	283.85	283.8	$\pi^*_{\text{macrocycle}}$ [a,b]
b	284.2	284.25	—	$\pi^*_{\text{macrocycle}}$ [a]
c	285.2	285.00	284.9	$\pi^*_{\text{phenyl rings}}$ [a,b]
c_2	—	285.30	—	$\pi^*_{\text{phenyl rings}}$ [a]
d	286.0	286.45	—	$\pi^*_{\text{macrocycle}}$ [a]
e	287.3	287.45	287.6	$\pi^*_{\text{macrocycle}}$ [a,b]
f	288.8	288.40	288.6	$\sigma^*_{\text{phenyl rings}}$; $\pi^*_{\text{macrocycle}}$ [a]
g	293.3	—	293	σ^* [b]

a = [29], b = [30]

Figure 3.7(a) shows C K-edge absorption spectra for 1.5 ML of H_2TBrPP deposited on Au(111) at room temperature. The absorption line energies and assignments are given in Table 3.4, together with absorption line energies for H_2TPP [29, 30]. The peak positions and assignments are similar to those for NiTBrPP (Table 3.2), with the same variation in the intensity of the features assigned to transitions to π^* molecular orbitals localised on the porphyrin macrocycle (peaks labelled *a* and *b*) as the angle of incidence increases. Using the angle-dependent intensity ratios, angles of $26.9 \pm 0.2°$ and $63.0 \pm 4.7°$ are calculated for the macrocycle and phenyl rings respectively, indicating a similar degree of distortion as observed for the NiTBrPP molecules.

The corresponding N K-edge XA spectra are shown in Figure 3.7(b), with the absorption lines and their assignment listed in Table 3.5. The main difference between the N K-edge spectra for H_2TBrPP (Figure 3.7(b)) and NiTBrPP (Figure 3.6(b)) is the presence of the two absorption lines labelled m_1 and m_2

Table 3.5: Absorption line energies and assignments for N K-edge XA spectra for 1.5 ML of H_2TBrPP deposited on Au(111) at room temperature shown in Figure 3.7(b). Also included is a comparison with features observed in the N K-edge XA spectra of H_2TPP [29] and H_2P [31, 40].

Peak	H_2TBrPP (Fig. 3.7(b)) (eV)	H_2TPP [a] (eV)	H_2P [b] (eV)	H_2P [c] (eV)	Assignment
m_1	397.9	397.55	398.2	397.9	=N- $\rightarrow \pi^*_{\text{macrocycle}}$ [a,b]
m_2	400.1	399.8	400.3	400.0	NH $\rightarrow \pi^*_{\text{macrocycle}}$ [a,b]
n	401.1	400.8	—	401.3	N $\rightarrow \pi^*_{\text{macrocycle}}$ [a]
o	402.2	401.85	402.3	402.5	=N- $\rightarrow \pi^*_{\text{macrocycle}}$ [b]
p	403.2	402.60 - 405.70	403.9	403.3	NH $\rightarrow \pi^*_{\text{macrocycle}}$ [b]
q	407.1	—	406.8	407.2	$\sigma^*_{\text{N-C}}$ [b]

a = [29], b = [40], c = [31]

in the H_2TBrPP spectra, related to the chemically different environments of the iminic (=N-) and pyrrolic (NH) nitrogen atoms [29, 31, 40]. The features m_1, m_2, n, o and p in Figure 3.7(b), all assigned to transitions to π^* states on the macrocycle, show a strong angular dependence as before, with the intensity of these absorption lines decreasing as θ goes from grazing to normal incidence, while the intensitiy of peak q, assigned to transitions to σ^* states, increases in intensity.

Figure 3.8 shows C K-edge XA spectra measured after the 1.5 ML coverage of H_2TBrPP, shown in Figure 3.7, was annealed at 250 °C. STM, PES and XPS data show that nano-networks will have formed at this temperature (Figure 3.3 and Figure 3.5). These spectra all show absorption lines at energies of 284.2 eV, 285.2 °C, 287.3 eV and 292.7 eV respectively. The first three absorption lines are at the same energies as the corresponding lines for the unannealed H_2TBrPP (Table 3.4), while the broad feature at 292.7 eV is at a similar energy to peak g. The absorption lines related to transitions to π^* states localised on the porphyrin macrocycle (peaks a and b in Figure 3.7(a)) are no longer clearly resolved in Figure 3.8. This is to be expected, as nano-network formation

results in a delocalisation of electrons over the π-conjugated structure, leading to broader features in the absorption spectra. Similarly, the absorption line at 285.2 eV, assigned to transitions to π^* states on the phenyl rings, is no longer as well-resolved as for the deposited 1.5 ML coverage (Figure 3.7(a)), also as a consequence of the electron delocalisation. The angles relating to the orientations of the macrocycle and phenyl rings are calculated as $24.5 \pm 2.0°$ and $36.5 \pm 2.9°$ respectively, implying that the macrocycle has a similar geometry following network formation, while the phenyl ring orientation has changed. This is to be expected, as the porphyrin molecules bond covalently at the phenyl rings.

In conclusion, the porphyrin macrocycle adopts a distorted geometry on the surface, with the phenyl rings rotated at some angle with respect to the macrocycle. The absorption lines observed in the N K-edge spectra may be used to distinguish between free base and metalated porphyrins, as the iminic and pyrrolic environments in H_2TBrPP give rise to two separate absorption lines.

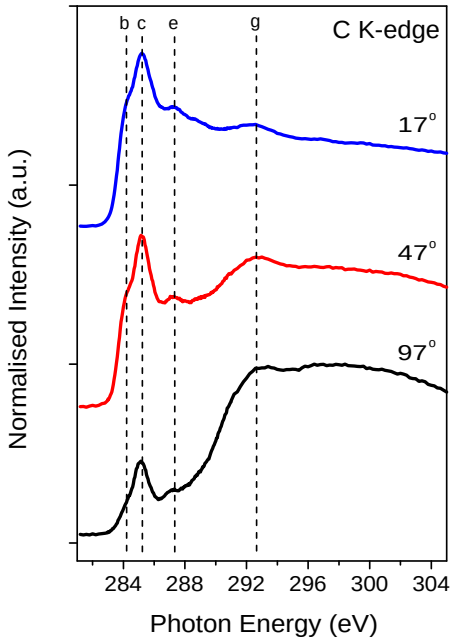

Figure 3.8: C K-edge XAS for 1.5 ML of H_2TBrPP on Au(111) after annealing at 250 °C following deposition at room temperature (Figure 3.7). Spectra were recorded at three different angles of incidence.

Metalation of H_2TBrPP on Au(111) with Deposited Ni atoms

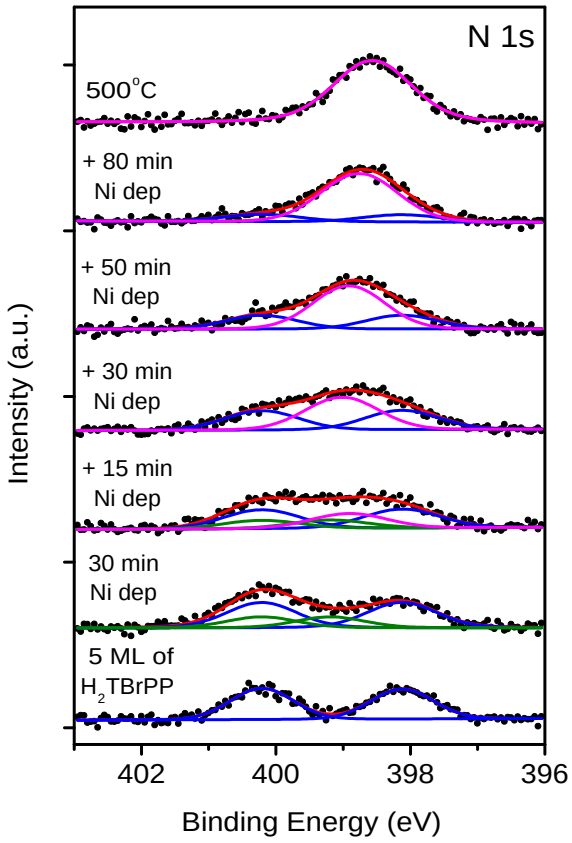

Figure 3.9: PES for 5 ML of H_2TBrPP deposited on room temperature Au(111), followed by deposition of Ni atoms and subsequent annealing at 500 °C. N 1s region, hν = 490 eV.

Figure 3.9 shows a sequence of N 1s PES spectra recorded after the deposition of 5 ML of H_2TBrPP on Au(111) at room temperature, and the subsequent deposition of Ni atoms. The 5 ML spectrum was fitted with two Voigt peaks with binding energies of 398.1 eV and 400.2 eV, assigned to nitrogen atoms in the iminic and pyrrolic chemical environments respectively [11, 30]. As expected for H_2TBrPP, the iminic and pyrrolic components are equal in intensity for the as-deposited porphyrin. The spectrum recorded after the initial 30 minute deposition of Ni shows a decrease in the intensity of the iminic component at 398.1 eV, while the intensity of the pyrrolic component at 400.2 eV remains

unchanged. Furthermore, an additional component is observed at a binding energy of 399.1 eV. This new feature is assigned to iminic nitrogen atoms in the porphyrin macrocycle interacting with the Ni atoms [11, 30]. The component at 400.1 eV has not decreased in intensity, indicating that the pyrrolic nitrogen atoms retain their hydrogen bonds. Hence the intermediate state proposed by Fleischer and Wang [9] is present on the surface, together with H_2TBrPP molecules which are not interacting with the deposited Ni atoms.

As the Ni coverage is increased, the intensities of the iminic and pyrrolic components decrease, while a new peak at 398.9 eV binding energy grows in intensity. This peak is attributed to nitrogen atoms in fully-metalated NiTBrPP [30], and accounts for approximately 65 % of the total nitrogen signal after 205 minutes of Ni deposition. There is a shift in the binding energy of the peak to 398.8 eV, in agreement with the value reported by Gottfried *et al.* for Ni metalation of H_2TPP on Au(111) [30]. Finally, the sample was annealed at 500 °C to fully metalate the H_2TBrPP molecules, resulting in a single peak at 398.6 eV [17]. The presence of this single peak in the N 1s spectrum signifies the full metalation of the porphyrin layer.

3.2.2 STM and Photoemission Study of NiTBrPP/Au(111) Deposited at Elevated Temperatures

NiTBrPP was deposited onto Au(111) while the substrate was held at elevated temperatures, in order to investigate whether debromination occurring on deposition has an effect on network formation. Figure 3.10 shows STM images recorded after sub-monolayer deposition of NiTBrPP onto the Au(111) $22 \times \sqrt{3}$ surface held at 80 °C (Figure 3.10(a)) and 100 °C (Figure 3.10(b)), and subsequently annealed at the temperatures shown (Figure 3.10(c) - (f)). For a 0.5 ML coverage deposited on Au(111) at 80 °C (Figure 3.10(a)), areas of self-assembled NiTBrPP are observed which exhibit a molecular packing, labelled as Type 5, that was not observed for deposition at room temperature. The unit cell vectors for this packing configuration are 1.72 ± 0.01 nm and 1.61 ± 0.01 nm respectively, with an angle of $108.2 \pm 1.7°$. For a molecular coverage of 0.6 ML deposited on the substrate at 100 °C, both self-assembly and covalent networking are observed coexisting in the same molecular domain (Figure 3.10(b)). Annealing at higher temperatures results in covalent network formation, with nano-networks

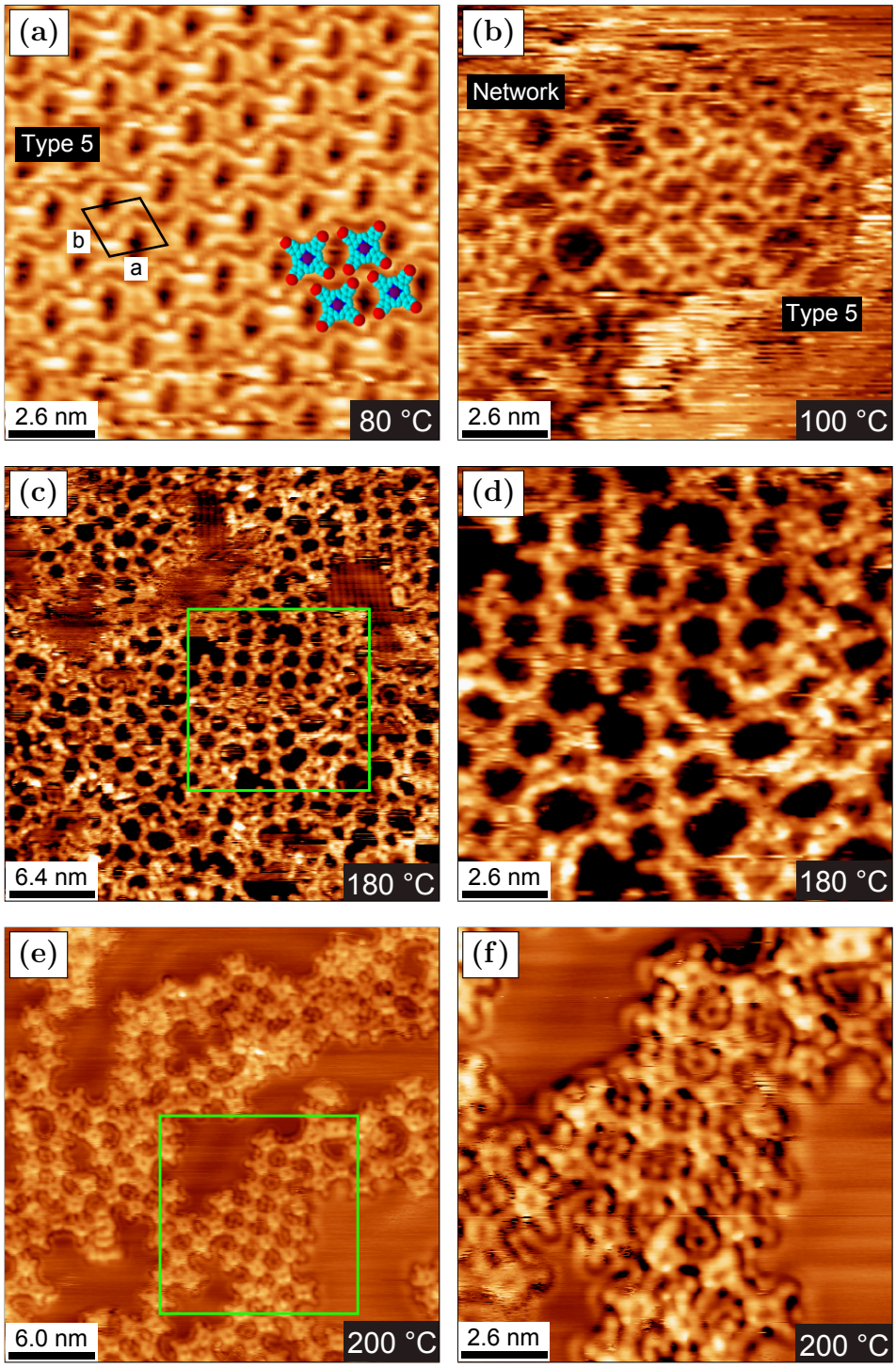

Figure 3.10: STM for NiTBrPP deposited on Au(111) held at elevated temperature. (a) (+1.48 V,0.28 nA), (b) (+0.86 V,0.21 nA), (c) and (d) (+1.24 V,0.28 nA), (e) (+1.20 V,0.34 nA), (f) (+0.82 V,0.34 nA). (d) and (f) show enlarged views of the highlighted areas in (c) and (e). (a), (e) and (f) show a surface with 0.5 ML coverage, (b) - (d) show a differently prepared surface with 0.6 ML coverage.

featuring regions of ordered four-fold nano-mesh as seen previously (Figure 3.3) [5]. Enlarged views of the highlighted areas in Figure 3.10(c) and (e) are shown in Figure 3.10(d) and (f). There is a perturbation in the local charge density of the surface in the pores around the periphery of the nano-network shown in Figure 3.10(e) and (f). Rojas *et al.* have observed a similar phenomenon for H_2TPP adsorbed on Cu(111), and have attributed it to the molecules drawing charge from the substrate and forming a surface dipole [41]. An alternative explanation for the structure within the network pores is the presence of dissociated Br atoms, as proposed by Gutzler *et al.* for a similar structure observed in the pores of a hexagonal TBB nano-network on Ag(110) [3].

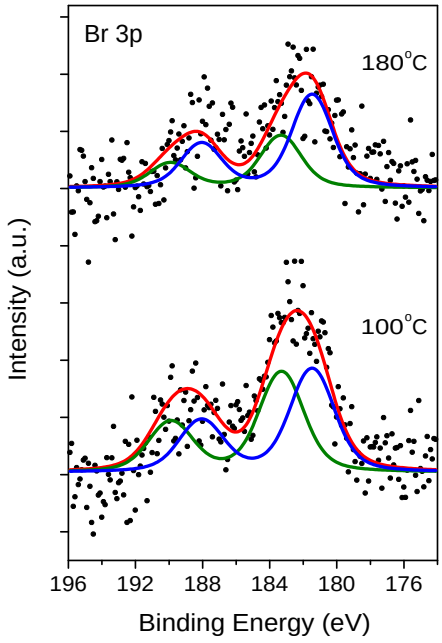

Figure 3.11: XPS for 0.6 ML of NiTBrPP deposited on Au(111) held at 100 °C, and subsequently annealed at 180 °C. Br 3p region, hν = 1486.7 eV. Spectra recorded from the surface shown in Figure 3.10(b) - (d).

Figure 3.11 shows Br 3p XPS data recorded after deposition of NiTBrPP onto the Au(111) substrate held at 100 °C. The surface was subsequently annealed at 180 °C. Both spectra were fitted with two Voigt doublets with $3p_{3/2}$ binding energies of 181.5 eV and 183.3 eV respectively, and a spin-orbit splitting of 6.6 eV. As above (Figure 3.5(b)), the doublets at 181.5 eV and 183.3 eV are assigned

to dissociated bromine on the surface and bromine bonded to the NiTBrPP phenyl rings respectively. The intensities of the doublets are approximately equal for deposition onto the hot Au(111), in comparison to the spectra recorded after a NiTBrPP layer deposited at room temperature was annealed at 100 °C (Figure 3.5(b)), where dissociated bromine accounts for approximately 40 % of the total Br signal. The bromine bonded to the NiTBrPP desorbs preferentially after annealing at 180 °C (Figure 3.11), in agreement with the STM data showing network formation at that temperature (Figure 3.10).

In summary, five different molecular packing configurations have been observed for NiTBrPP on Au(111), at both room temperature and 80 °C. Annealing at temperatures of 170 °C or higher results in the formation of covalently bonded networks. The nano-networks do not exhibit long range order, but small groups of ten to twenty molecules form ordered four-fold nano-mesh. Analysis of the angular dependence of the x-ray absorption lines shows that the porphyrin macrocycles adopt a distorted geoometry on the surface, and that the phenyl rings are rotated with respect to the macrocycle. The absorption lines in the C K-edge XA spectra are no longer well-resolved after network formation, due to the delocalisation of electronic charge over the π-conjugated network.

3.3 STM and Photoemission Study of NiTBrPP on the Ag(111) Surface

3.3.1 Analysis for Deposition at Room Temperature

Figure 3.12 shows the Br 3p XPS data measured after deposition of 0.8 ML of NiTBrPP on the Ag(111) 1×1 surface held at room temperature, and subsequently annealed at 100 °C and 200 °C. The spectra were fitted with two Voigt doublets, with binding energies of 181.8 eV and 184.1 eV respectively, and a spin-orbit splitting of 6.4 eV. As above, the lower binding energy doublet is assigned to dissociated bromine, and the higher assigned to bromine bonded to the NiTBrPP molecule. In contrast to NiTBrPP deposited on Au(111) at room temperature (Figure 3.5(b)), the doublet assigned to dissociated bromine is now the largest component, accounting for 70 % of the total Br signal. As such, network formation on room temperature Ag(111) is expected to occur more readily than on room temperature Au(111). After annealing the molecular layer at 100 °C and 200 °C (Figure 3.12), only a small fraction of the bromine remains

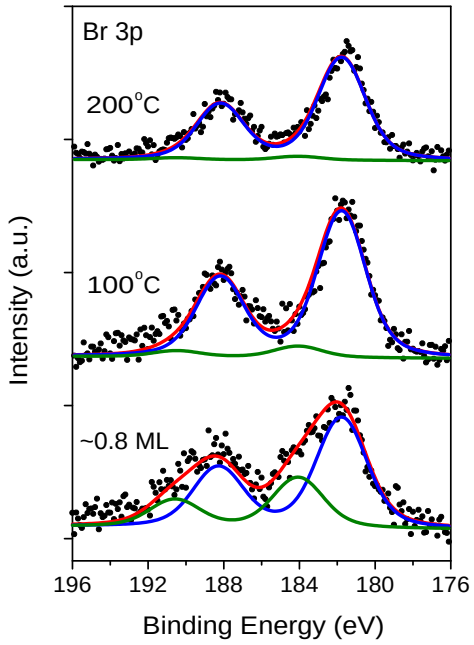

Figure 3.12: XPS for 0.8 ML of NiTBrPP deposited on room temperature Ag(111) and subsequently annealed at 100 °C and 200 °C. Br 3p region, hν = 1486.7 eV.

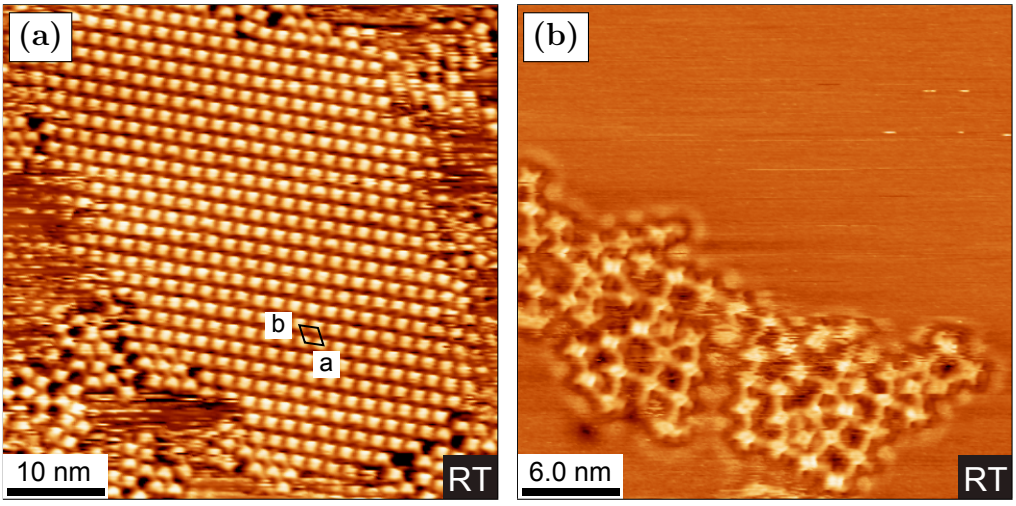

Figure 3.13: STM for NiTBrPP deposited on room temperature Ag(111). (a) (+1.26 V,0.28 nA), (b) (−1.71 V,0.26 nA). (a) shows a surface with 0.8 ML coverage corresponding to the room temperature spectrum shown in Figure 3.12, (b) shows a differently prepared surface with 0.6 ML coverage.

bonded to the porphyrin molecules, with dissociated bromine accounting for almost all of the Br signal.

Figure 3.13 shows STM images recorded after deposition of 0.8 ML (Figure 3.13(a)) and 0.6 ML (Figure 3.13(b)) of NiTBrPP on Ag(111) 1×1 held at room temperature. An island of self-assembled porphyrin molecules is observed in Figure 3.13(a), with unit cell parameters $a = 1.80 \pm 0.01$ nm, $b = 1.81 \pm 0.01$ nm and $\theta = 111.8 \pm 0.6°$ determined as above. Figure 3.13(b) shows an example of nano-network formation at room temperature, with an average centre-to-centre distance between adjacent porphyrin molecules of 1.96 ± 0.13 nm (see Table 3.6). The NiTBrPP molecules appear as four-fold symmetrical on the Ag(111) surface, in contrast to the Au(111) surface (Figure 3.2(e) and 3.2(f)), indicating that no saddle distortion is present for the macrocycle on Ag(111).

Figure 3.14 shows STM images recorded after annealing at the temperatures shown. Similar to the networks formed on Au(111) (Figure 3.3), the nano-networks on Ag(111) cover regions of approximately 5000 nm^2 in area, but do not display long range order. Areas of local order where groups of up to twenty molecules form a four-fold nano-mesh are present within the networks. Figure 3.14(c) is a zoomed image of the highlighted region in 3.14(b), showing some of these locally ordered groups of molecules. The networks are thermally stable up to at least 400 °C, as seen in Figure 3.14(f).

An uncovered area of the Ag surface shows a 2×1 reconstruction with a periodicity of 0.44 ± 0.01 nm in the $2\times$ direction, (Figure 3.14(e)), similar to that discussed previously for NiTBrPP on Au(111) (Figure 3.3(c)). Hence the reconstruction is not exclusive to the gold surface.

The centre-to-centre distances for the networks annealed at different temperatures are shown in Table 3.6. Networks formed at room temperature and 100 °C exhibit a larger centre-to-centre distance than networks annealed at 200 °C and higher, suggesting that the networks formed at room temperature and 100 °C are not covalently bonded; instead, it is proposed that they are coordinated with silver atoms from the substrate in a so-called 'protopolymer' structure. Such protopolymers have been reported previously as a precursor to the covalent bonding of various phenyl radicals on Ag(110) [3] and Cu(111) [2, 3, 8, 42, 43]. Protopolymer networks are distinguished from covalently bonded networks by the increased centre-to-centre distance between adjacent molecules [3, 8].

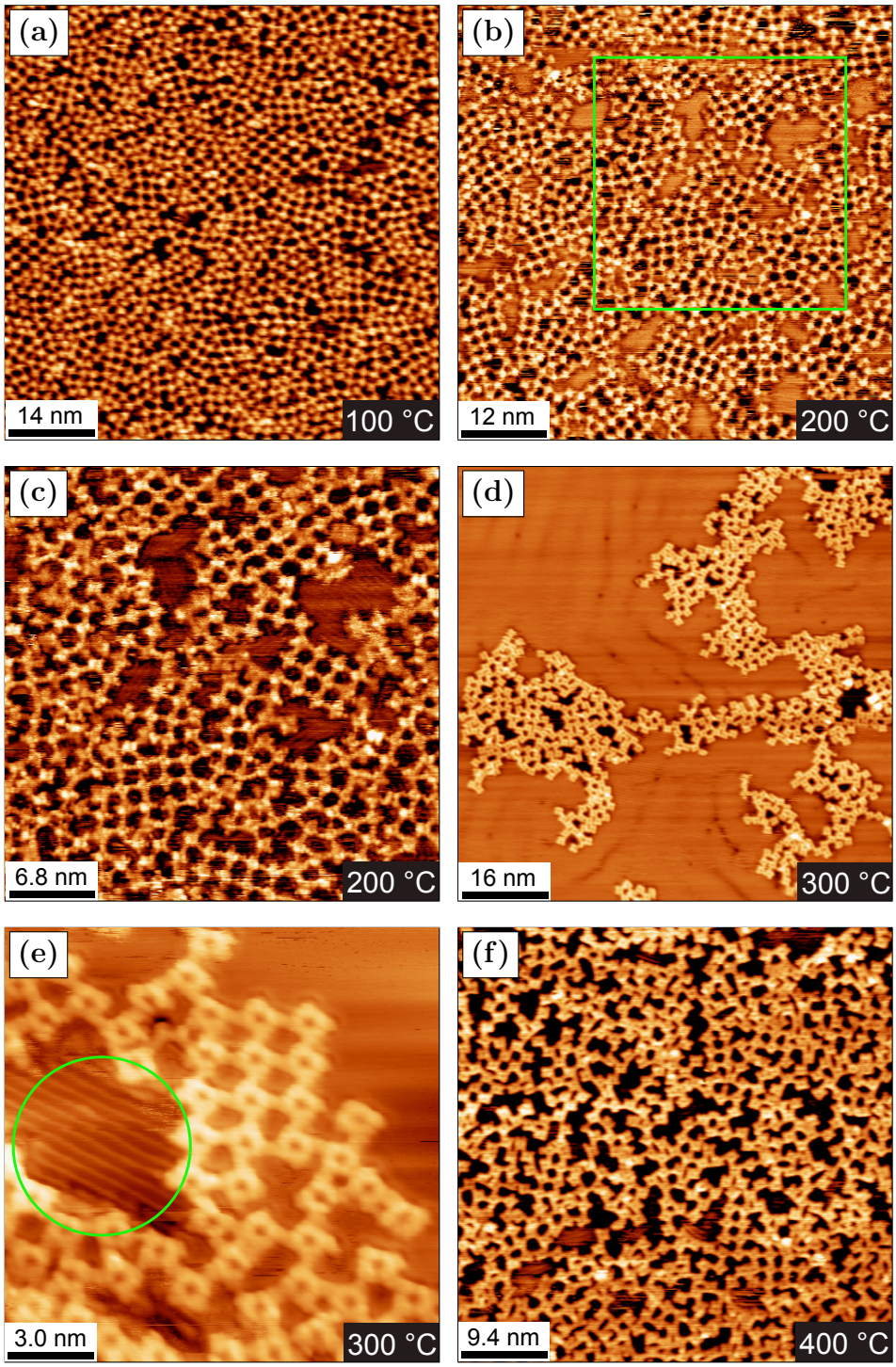

Figure 3.14: STM for NiTBrPP on Ag(111), network formation after annealing molecular layers deposited at room temperature. (a) (+1.07 V,0.23 nA), (b) and (c) (−1.93 V,0.28 nA), (d) (+1.29 V,0.25 nA), (e) (−0.39 V,0.55 nA), (f) (+0.84 V,0.20 nA). Enlarged view of the highlighted area in (b) is shown in (c). (a) shows the surface with 0.8 ML coverage (Figure 3.13(a)) annealed at 100 °C and corresponds to the 100 °C spectrum in Figure 3.12, (b) - (f) show the surface with 0.6 ML coverage (Figure 3.13(b)) annealed at the temperatures shown.

Table 3.6: Centre-to-centre distances for adjacent porphyrins for NiTBrPP nano-networks on Ag(111), shown in Figure 3.13, Figure 3.14 and Figure 3.15. Centre-to-centre distance analysed using nearest neighbour distances for Figure 3.13(b) and Figure 3.14(a), and mean value across several cells for Figure 3.14(c), (e) and (f) and Figure 3.15(a) and (b).

Figure	Temperature (°C)	Average Centre-to-centre Distance (nm)
3.13(b)	20	1.96 ± 0.13
3.14(a)	100	1.88 ± 0.14
3.15(a)	100	2.02 ± 0.04
3.14(c)	200	1.72 ± 0.08
3.14(e)	300	1.60 ± 0.16
3.14(f)	400	1.68 ± 0.09
3.15(b)	400	1.67 ± 0.06

3.3.2 STM and Photoemission Study of NiTBrPP/Ag(111) Deposited at Elevated Temperatures

Figure 3.15(a) shows an STM image recorded after deposition of 0.6 ML of NiTBrPP onto a hot Ag(111) surface held at 100 °C and subsequently annealed at 400 °C (Figure 3.15(b)). The molecules form a nano-network at 100 °C (Figure 3.15(a)). The network shown in the bottom right of Figure 3.15(a) covers 500 nm^2 and includes approximately 100 NiTBrPP molecules bonded in a regular, ordered configuration; the network in the top left of the image covers 330 nm^2 and features approximately 50 molecules. These networks are the largest ordered structures observed in the present work. The centre-to-centre distance measured for these networks is 2.02 ± 0.04 nm, suggesting that they are protopolymers coordinated by Ag atoms (Table 3.6). A further 0.2 ML was deposited onto this surface and the network was subsequently annealed at 400 °C (Figure 3.15(b)), resulting in a centre-to-centre distance of 1.67 ± 0.06 nm, in good agreement with the distances previously measured for covalently bonded networks (Table 3.6). After annealing at 400 °C, the network exhibits a similar degree of order to that

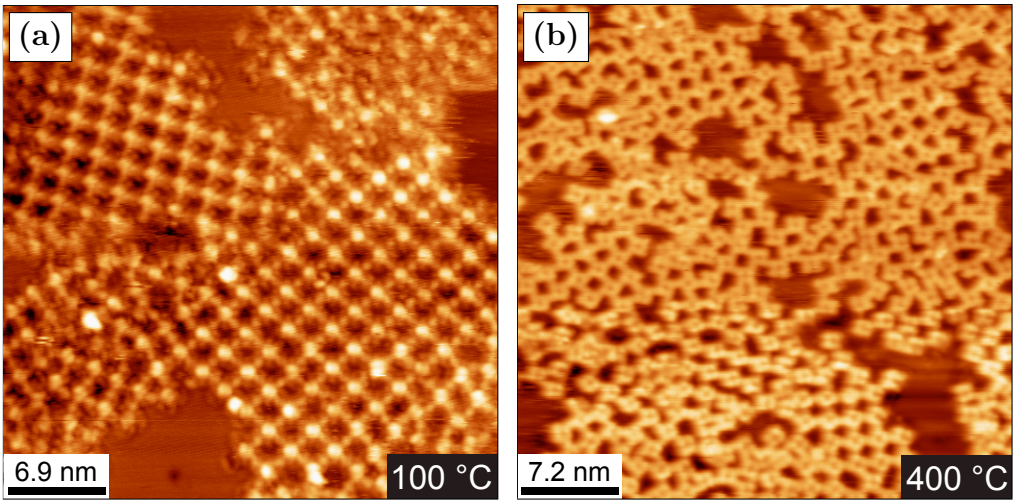

Figure 3.15: STM for NiTBrPP deposited on Ag(111) held at 100 °C, and subsequently annealed at 400 °C. (a) (−1.67 V,0.30 nA), (b) (−0.58 V,0.10 nA). (a) shows a surface with a 0.6 ML coverage, (b) shows the surface following the deposition of an additional 0.2 ML and annealing at 400 °C.

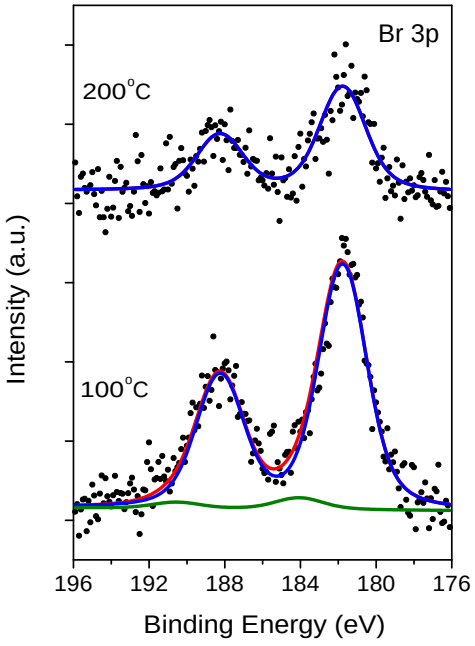

Figure 3.16: XPS for NiTBrPP deposited on Ag(111) held at 100 °C and 200 °C. Br 3p region, hν = 1486.7 eV. 100 °C spectrum corresponds to a coverage of 0.8 ML, 200 °C spectrum corresponds to a 1 ML coverage.

seen in Figure 3.14, as well as the same thermal stability.

Figure 3.16 shows Br 3p XPS data for 0.8 ML of NiTBrPP deposited on Ag(111) held at 100 °C, and a 1 ML coverage deposited on the substrate held at 200 °C. The 100 °C spectrum was fitted with two Voigt doublets at $3p_{3/2}$ binding energies of 181.8 eV and 184.1 eV respectively, and a spin-orbit splitting of 6.5 eV. The components are assigned to dissociated Br and bromine bonded to the NiTBrPP molecules respectively. Very little bromine remains bonded to the porphyrin molecules, with the lower binding energy component accounting for 96 % of the total bromine signal. For deposition onto the Ag(111) substrate at 200 °C, only the doublet at 181.8 eV is present, indicating that all Br has dissociated from the NiTBrPP molecules.

In summary, protopolymer networks are observed for NiTBrPP on Ag(111) at room temperature and 100 °C. These networks exhibit a greater degree of order than covalently bonded networks seen previously on Au(111) (Section 3.2), and include areas of four-fold nano-mesh composed of approximately one hundred porphyrin molecules. Covalently bonded networks, distinguishable by their shorter centre-to-centre distance for adjacent molecules, are formed after annealing the surface at 200 °C.

3.4 STM and Photoemission Study of H_2TBrPP and NiTBrPP on the Cu(111) Surface

3.4.1 Analysis for Deposition at Room Temperature

Figure 3.17 shows N 1s photoemission spectra for H_2TBrPP deposited on the Cu(111) 1×1 surface held at room temperature [19]. The spectrum recorded after deposition of a 5 ML coverage was fitted with two Gaussian peaks with respective binding energies of 398.2 eV (A_1) and 400.2 eV (A_2). As before (Figure 3.9), these peaks are assigned to nitrogen atoms in the iminic (=N-) and pyrrolic (NH) chemical environments of the porphyrin macrocycle [11, 19, 30]. After deposition of a 1.5 ML coverage, the peak at 398.2 eV is broader, while the width of the component at 400.2 eV remains unchanged. The 1.5 ML spectrum was fitted with four Gaussian line-shapes, at binding energies of 398.2 eV, 398.7 eV, and 400.2 eV. Two of the peaks at 398.2 eV and 400.2 eV binding energy have equal intensity, while a second peak at 400.2 eV binding energy has the same intensity as the peak at 398.7 eV. The peak at 398.7 eV is assigned to iminic

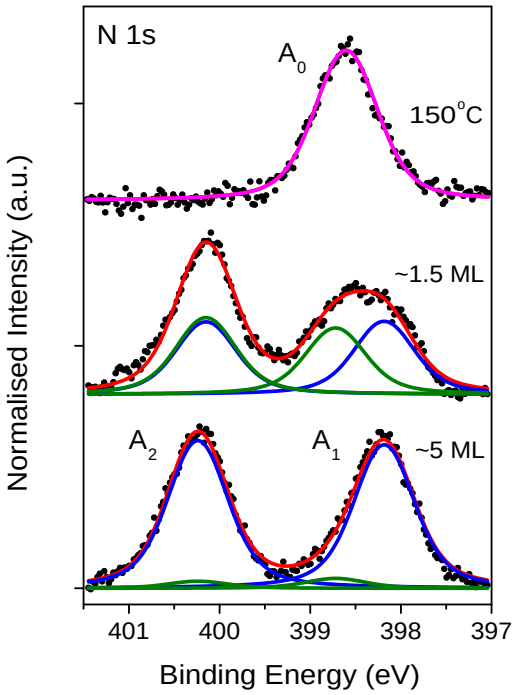

Figure 3.17: PES for H_2TBrPP on room temperature Cu(111). Deposition of 5 ML and 1.5 ML coverages, subsequent annealing at 150 °C. N 1s region, hν = 470 eV. 5 ML coverage corresponds to one surface, 1.5 ML coverage corresponds to a second surface.

N atoms which are interacting with Cu atoms from the substrate, similar to the iminic N atoms interacting with the metallic Ni on the Au(111) surface as discussed above and shown in Figure 3.9. As the relative intensity and width of the peak at 400.2 eV has not changed, this indicates that the pyrrolic N atoms have retained their hydrogen atoms, and that the H_2TBrPP molecules have not been fully metalated. As such, the Gaussian line-shapes of equal intensity at 398.7 eV and 400.2 eV are again attributed to the formation of an intermediate state as described by Fleischer and Wang [9] (Figure 3.9). After annealing the 1.5 ML surface at 150 °C, a single peak is observed in the N 1s core level spectrum, at 398.6 eV binding energy (A_0). Hence, the H_2TBrPP molecules have been fully metalated by Cu atoms from the substrate, and the molecular layer present on the surface consists of CuTBrPP [19]. These results constitute the first reported *in situ* metalation of a free base porphyrin molecule on a surface using substrate

atoms, and the first direct observation of this intermediate state on a surface [19]. In previous studies of *in situ* porphyrin metalation using deposited metal atoms, the presence of the intermediate state had either been inferred from core level PES [10, 11], or had not been detected [12–14]. Several studies of *in situ* self-metalation of free base porphyrin molecules using surface atoms have been subsequently published [20–25].

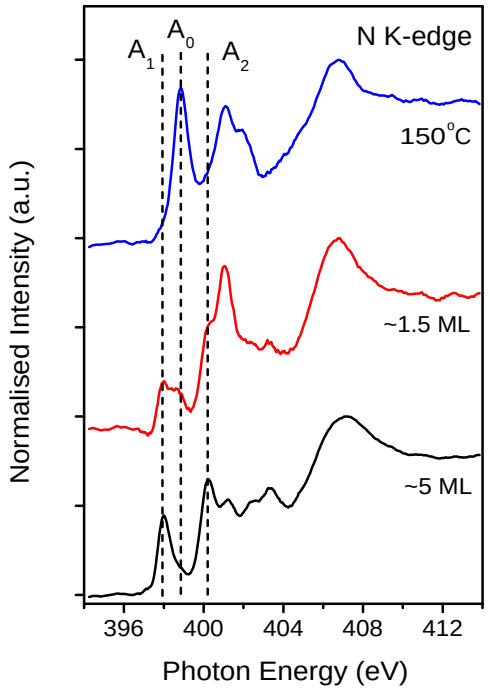

Figure 3.18: N K-edge XAS for H_2TBrPP on room temperature Cu(111). Deposition of 5 ML and 1.5 ML coverages, subsequent annealing at 150 °C. Spectra measured at $\theta = 47°$. Spectra measured from the same surfaces as data shown in Figure 3.17.

Figure 3.18 shows the N K-edge XA spectra recorded from the same surfaces as the photoemission spectra shown in Figure 3.17. The absorption lines at 398.0 eV (A_1) and 400.2 eV (A_2) for the 5 ML coverage are assigned to transitions to empty molecular orbitals of π^* character localised on the porphyrin macrocycle from electrons in the N 1s core level for iminic and pyrrolic nitrogen atoms respectively [19, 25, 29]. The intensity of these absorption lines decreases for the 1.5 ML coverage, corresponding to the formation of the intermediate state. The XA

spectrum measured after annealing the molecular layer at 150 °C is characteristic of a metalated porphyrin [31, 32], with a single absorption line present at 398.8 eV (A_0), assigned to a transition from the N 1s core level of the four equivalent nitrogen atoms in CuTBrPP (see Table 3.11) [19, 25].

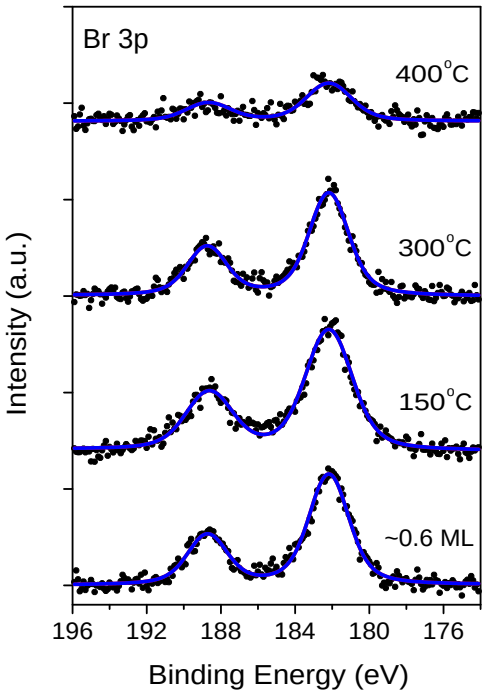

Figure 3.19: XPS for 0.6 ML of NiTBrPP deposited on room temperature Cu(111) and subsequently annealed. Br 3p region, hν = 1486.7 eV.

Table 3.7: Binding energy of dissociated bromine on Au(111), Ag(111) and Cu(111) substrates.

Substrate	Br $3p_{3/2}$ Binding Energy (eV)	Figure
Au(111)	181.5	3.5(b)
Ag(111)	181.8	3.12
Cu(111)	182.2	3.19

Figure 3.19 shows the Br 3p XPS spectra for a 0.6 ML coverage of NiTBrPP on room temperature Cu(111), annealed at 150 °C, 300 °C and 400 °C. The Br 3p spectra were each fitted with a single Voigt doublet at a $3p_{3/2}$ binding energy of 182.2 eV, with a spin-orbit splitting of 6.5 eV; this component is assigned to dissociated bromine on the surface. No other components are present in the spectrum, indicating that Cu(111) is sufficiently reactive to catalyse C-Br bond scission at room temperature, as reported previously [2, 3].

The binding energy of the dissociated bromine on Au(111), Ag(111) and Cu(111) are shown in Table 3.7. A clear trend is observed, with the Br $3p_{3/2}$ binding energy increasing with the reactivity of the substrate (Au(111) < Ag(111) < Cu(111)) [44].

Figure 3.20(a) - 3.20(d) shows 0.2 ML of H_2TBrPP on room temperature Cu(111), while Figure 3.20(e) and 3.20(f) show 0.3 ML and 0.6 ML coverages respectively. The H_2TBrPP molecules are immobilised on the surface and can be imaged at submonolayer coverages, in contrast to Au(111) where sub-monolayer coverages of TBrPP molecules could not be imaged due to the mobility of the porphyrins at room temperature, thus indicating an interaction between the H_2TBrPP and the Cu(111) surface. Immobilisation of H_2TPP on Cu(111) has been reported at room temperature [41]; in addition, XPS data show that the bromine has completely dissociated from the porphyrin molecule at room temperature (Figure 3.19). Therefore a Br-Cu interaction can be excluded as the cause of the immobilisation. The photoemission (Figure 3.17) and x-ray absorption spectra (Figure 3.18) show the formation of the intermediate complex at room temperature, whereby the iminic nitrogen atoms bond to Cu atoms from the substrate [19]. This interaction is the most probable cause of the immobilisation of the H_2TBrPP on the Cu(111) substrate. The formation of the intermediate state also explains the macrocycle imaging as two bright lobes. As the intermediate state involves the iminic nitrogen atoms bonding to a Cu atom, while the pyrrolic nitrogen atoms remain bonded to hydrogen [9], a saddle conformation is likely. A similar appearance was observed for CoTPP and CuTPP on Cu(111) at 30 K, with the imaging of the macrocycle as two lobes attributed to a bending of two of the pyrrole rings in a saddle conformation [45, 46]. The H_2TBrPP molecule exhibits a rectangular profile in Figure 3.20, rather than the expected square profile. Brede *et al.* also observed this rectangular profile, and attributed it to the tilt of the phenyl rings with respect to the macrocycle [46]. Further evidence for the molecule-substrate interaction is provided by the

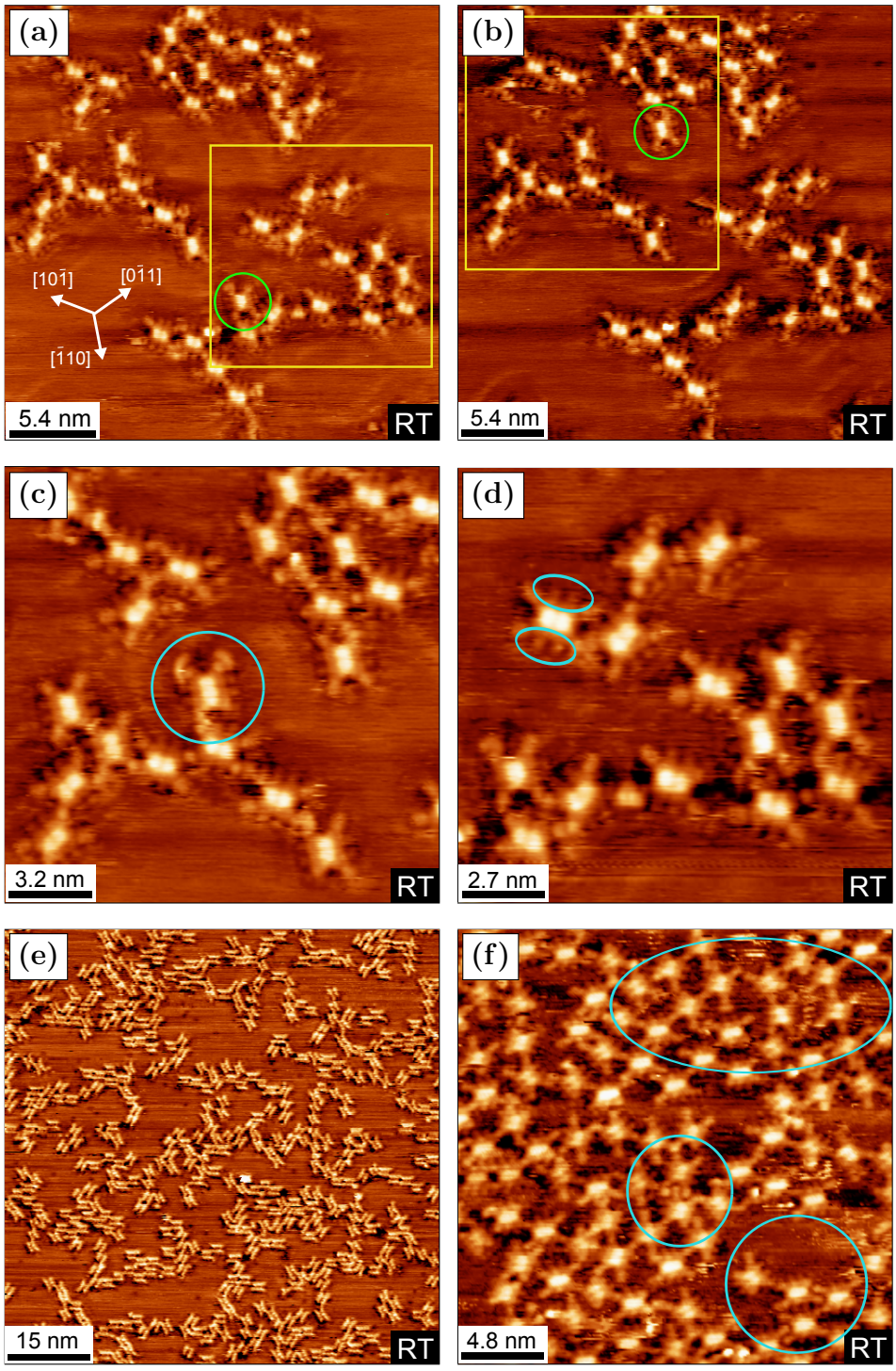

Figure 3.20: STM for H_2TBrPP deposited on room temperature Cu(111). (a) - (d) (−1.51 V,0.18 nA), (e) (−1.03 V,0.17 nA), (f) (−0.62 V,2.53 nA). (a) - (d) show a surface with 0.2 ML coverage, (e) shows a differently prepared surface with 0.3 ML coverage, and (f) shows another differently prepared surface with 0.6 ML coverage. (c) shows the area highlighted in (b), (d) shows a magnified view of the highlighted area in (a).

orientation of the H_2TBrPP on the Cu(111) surface, with all porphyrins aligned along one of three directions, at 120° to each other (Figure 3.20(a)). This suggests that the molecules are aligned along the three principal crystallographic directions in the Cu(111) surface [41, 46], indicating that the adsorption geometry is strongly influenced by the substrate.

A single mobile molecule is observed in the region of the surface shown in Figure 3.20(a) and 3.20(b), and is highlighted with a green circle. These two images show the same region of the surface, measured over a period of five minutes. The highlighted porphyrin moves from one group of molecules to the other as the area is scanned by the STM tip. In addition, the phenyl rings on some of the H_2TBrPP molecules are free to oscillate, as shown by the highlighted porphyrin in Figure 3.20(c).

Two pairs of raised protrusions appear on opposite sides of each H_2TBrPP molecule, highlighted in Figure 3.20(d). The protrusions are spaced 0.52 ± 0.05 nm apart [19], which corresponds to twice the atomic spacing along the principal crystallographic directions of the Cu(111) surface. It is proposed that these protrusions are copper atoms which have been raised out of the surface plane due to a local distortion caused by the molecular adsorption and the formation of the intermediate state [19]. An alternative explanation for the protrusions is that they are Cu adatoms which are attracted to, or immobilised by, the H_2TBrPP molecules [47]. Such Cu adatom capture was observed for H_2P on the Cu(110) surface by Dyer *et al.* [47]. However, the number and location of captured adatoms differed for each porphyrin molecule [47], in contrast to Figure 3.20(d), where the arrangement of protrusions is identical for each H_2TBrPP molecule. In addition, Dyer *et al.* quote a residing time for the captured adatoms on the order of 'a few minutes' [47], whereas no change was observed in the arrangement of the protrusions relative to the porphyrin molecules over a period of ten minutes (Figure 3.20(a) - 3.20(d)). Hence the protrusions are assigned to Cu atoms raised out of the surface plane, rather than captured Br or Cu adatoms [19]. Such a distortion suggests a model for the self-metalation whereby the Cu atom which metalates the porphyrin is extracted from the surface plane underneath the macrocycle, as opposed to an adatom diffusing along the surface underneath the adsorbed porphyrins.

Some examples of local bonding of H_2TBrPP molecules, and of the interlocking of phenyl rings of adjacent porphyrin molecules, are highlighted in Figure 3.20(f). The literature suggests that the porphyrin molecules have formed

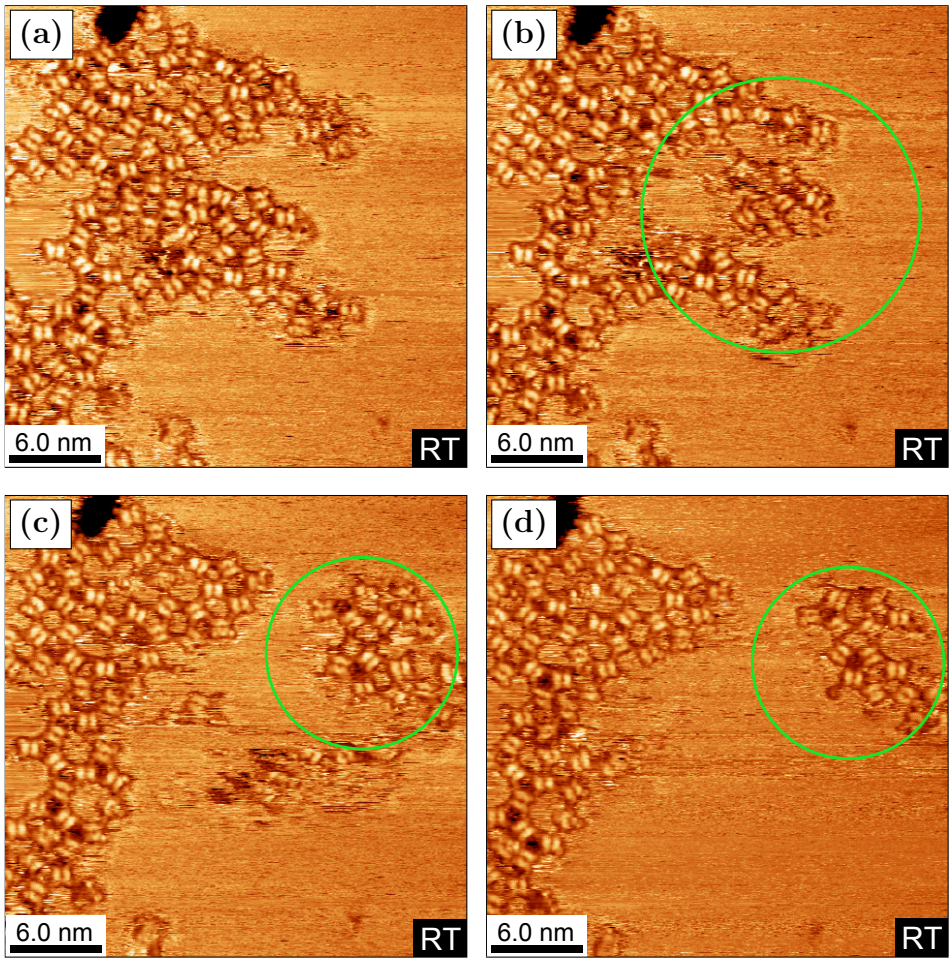

Figure 3.21: STM for 0.3 ML of NiTBrPP deposited on room temperature Cu(111). (−0.16 V,1.90 nA). (a) - (d) show the same region of the surface, imaged over a period of ten minutes.

protopolymer networks coordinated by Cu atoms at room temperature, rather than covalently bonded structures [2, 3, 8, 42, 43].

NiTBrPP was deposited on the Cu(111) surface at room temperature. STM images recorded after deposition of a 0.3 ML coverage are shown in Figure 3.21(a) - 3.21(d), for the same region of the surface imaged over a period of ten minutes. The bromine has dissociated from the porphyrin molecules on deposition (Figure 3.19), leading to the formation of protopolymer networks as discussed above. Some NiTBrPP are mobile on the surface, as evidenced by the highlighted areas in Figure 3.21(b) - 3.21(d), where small groups of molecules detach from the main structure to form a separate smaller structure. The mobility of the NiTBrPP molecules is further evidence that the observed structures are protopolymers, as

such mobility is not expected for covalently bonded networks [48].

NiTBrPP molecules show significantly greater mobility on the Cu(111) substrate at room temperature than H_2TBrPP (Figure 3.20), where only one mobile molecule is observed over the same period of time. The increased mobility of metalated porphyrins on Cu(111) compared to free base porphyrins has been noted previously [23, 49], where it was attributed to the absence of a N-Cu interaction for metalated porphyrins. Chapter 6 discusses a Ni-Cu ion exchange for Ni-metalated porphyrins on Cu(111), however there is no evidence for an intermediate state in this process, as the N 1s photoemission spectra indicate that the porphyrins remain fully metalated throughout the exchange.

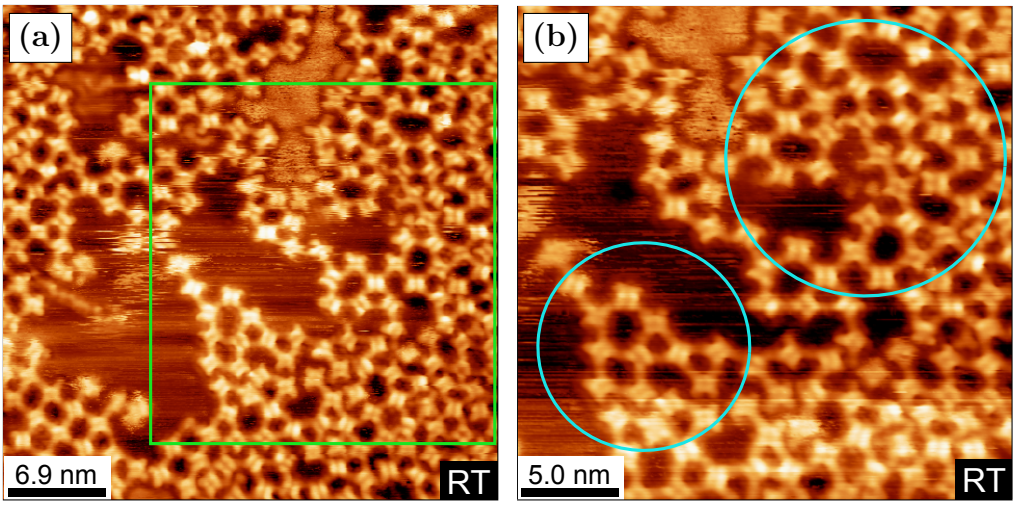

Figure 3.22: STM for 0.7 ML of NiTBrPP deposited on room temperature Cu(111). (a) and (b) (−0.76 V,0.37 nA). (b) shows the highlighted area in (a).

Figure 3.22 shows STM data measured after deposition of 0.7 ML of NiTBrPP on room temperature Cu(111), with Figure 3.22(b) showing the highlighted area in Figure 3.22(a). Examples of protopolymer network which include square pores are indicated with circles in Figure 3.22(b). The degree of order within the networks is comparable to that observed for NiTBrPP deposited on room temperature Ag(111) (Figure 3.13(b)).

Figure 3.23(a) shows C K-edge absorption spectra recorded after deposition of 5 ML of H_2TBrPP on Cu(111) at room temperature, measured at three different angles of incidence. The energies and assignments for the absorption lines are listed in Table 3.8, along with literature values for H_2TPP [20, 29, 30]. The energies of the absorption lines are in good agreement with those measured for

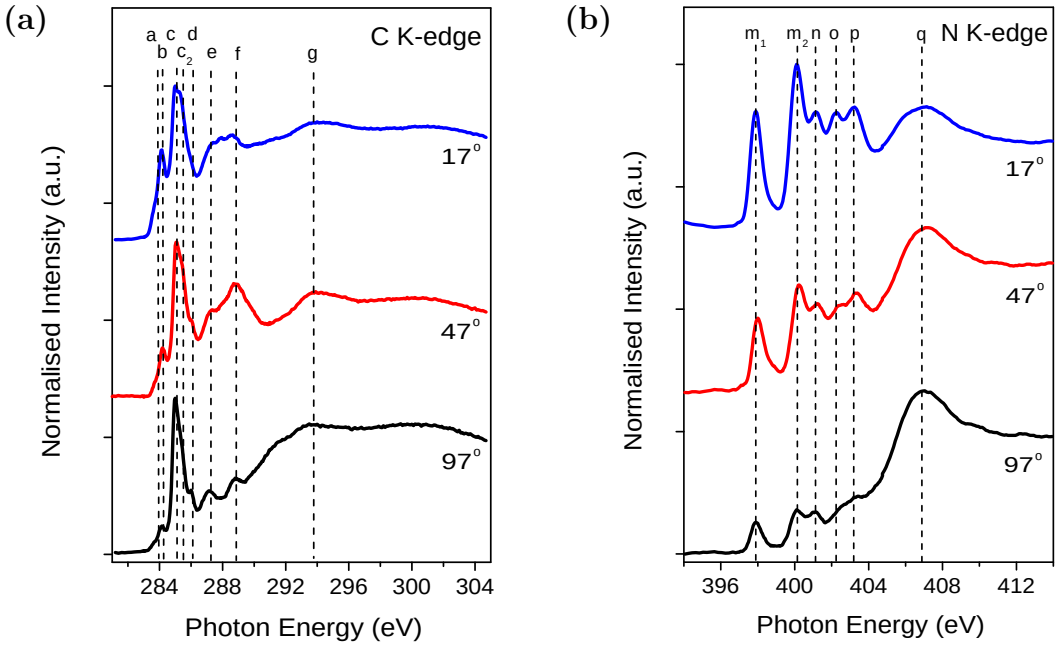

Figure 3.23: (a) C K-edge and (b) N K-edge XAS for 5 ML of H_2TBrPP deposited on room temperature Cu(111). Spectra recorded at three different angles of incidence.

H_2TBrPP on Au(111) (Table 3.4). There is now evidence for line c_2 at 285.4 eV. Peaks a and b, assigned to transitions to π^* states localised on the porphyrin macrocycle, are still most intense at grazing incidence, but are now also resolved at normal incidence (Figure 3.23(a)), in contrast to the C K-edge XA spectra measured on Au(111) (Figure 3.7(a)), indicating a different adsorption geometry for the macrocycle on the Cu(111) surface. An angle of $36.2 \pm 1.8°$ relating to the orientation of the macrocycle is calculated from the analysis of the angular dependence of the intensities of the absorption lines [34, 35]. Compared to the angle of $27.8 \pm 6.5°$ calculated for 5 ML of NiTBrPP on Au(111), this indicates that the macrocycle exhibits a greater degree of distortion on Cu(111) than on Au(111). An angle of $56.5 \pm 4.5°$ is calculated for the orientation of the phenyl rings, implying a similar geometry on Cu(111) as for Au(111).

Figure 3.23(b) shows the corresponding N K-edge XA spectra for 5 ML of H_2TBrPP on Cu(111), with the absorption line energies and assignments given in

Table 3.8: Absorption line energies and assignments for C K-edge XA spectra for 5 ML of H_2TBrPP deposited on Cu(111) at room temperature shown in Figure 3.23(a). Also included is a comparison with the features observed in the C K-edge XA spectra of H_2TPP [29, 30].

Absorption Line	H_2TBrPP (Fig. 3.23(a)) (eV)	H_2TPP [a] (eV)	H_2TPP [b] (eV)	Assignment
a	283.8	283.85	283.8	$\pi^*_{\text{macrocycle}}$ [a,b]
b	284.2	284.25	—	$\pi^*_{\text{macrocycle}}$ [a]
c	285.1	285.00	284.9	$\pi^*_{\text{phenyl rings}}$ [a,b]
c_2	285.4	285.30	—	$\pi^*_{\text{phenyl rings}}$ [a]
d	286.1	286.45	—	$\pi^*_{\text{macrocycle}}$ [a]
e	287.2	287.45	287.6	$\pi^*_{\text{macrocycle}}$ [a,b]
f	288.9	288.40	288.6	$\sigma^*_{\text{phenyl rings}}$; $\pi^*_{\text{macrocycle}}$ [a]
g	293.7	—	293	σ^* [b]

a = [29], b = [30]

Table 3.9, together with literature values for H_2TPP [20, 29] and H_2P [40]. Similar to the C K-edge spectra, there is good agreement between the absorption lines for H_2TBrPP on Cu(111) (Table 3.9) and Au(111) (Table 3.5). The absorption lines at 397.9 eV and 400.2 eV, labelled m_1 and m_2 respectively, decrease in intensity as the angle of incidence moves from grazing to normal incidence, but exhibit non-zero intensity at normal incidence. This is in contrast to the behaviour observed on Au(111) (Figure 3.7(b)), implying a change in the orientation of the N atoms with respect to the Cu substrate.

Figure 3.24(a) shows C K-edge XA spectra for 1.5 ML of H_2TBrPP deposited on Cu(111) at room temperature and then annealed at 150 °C. Photoemission (Figure 3.17) and x-ray absorption (Figure 3.18) spectroscopy indicate that the H_2TBrPP molecules are metalated by Cu atoms from the surface, therefore the XA spectra shown in Figure 3.24(a) correspond to networked CuTBrPP. The absorption line energies and assignments are given in Table 3.10, along with

Table 3.9: Absorption line energies and assignments for N K-edge XA spectra for 5 ML H_2TBrPP deposited on Cu(111) at room temperature shown in Figure 3.23(b). Also included is a comparison with the features observed in the N 1s XA spectra of H_2TPP [20, 29] and H_2P [40].

Peak	H_2TBrPP (Fig. 3.23(b)) (eV)	H_2TPP [a] (eV)	H_2TPP [b] (eV)	H_2P [c] (eV)	Assignment
m_1	397.9	397.6	397.55	398.2	=N- $\rightarrow \pi^*_{\text{macrocycle}}$ [a,b,c]
m_2	400.2	399.8	399.8	400.3	NH $\rightarrow \pi^*_{\text{macrocycle}}$ [a,b,c]
n	401.1	400.7	400.8	—	N $\rightarrow \pi^*_{\text{macrocycle}}$ [b]
o	402.3	401.6 - 402.3	401.85	402.3	=N- $\rightarrow \pi^*_{\text{macrocycle}}$ [c]
p	403.2	402.6 - 403.6	402.60 - 405.70	403.9	NH $\rightarrow \pi^*_{\text{macrocycle}}$ [a,c]
q	406.9	405 - 415	—	406.8	$\sigma^*_{\text{N-C}}$ [a,c]

a = [20], b = [29], c = [40]

literature values for H_2TPP metalated by surface Cu atoms on Cu(111) [20], and ZnTPP [29]. The absorption lines present in the metalated XA spectra are in good agreement with the lines observed in the spectra for 5 ML NiTBrPP deposited on Au(111) (Table 3.2), although several lines measured for 5 ML NiTBrPP are not present in the 1.5 ML CuTPP spectra (Figure 3.24(a)). Absorption lines were also absent from XA spectra measured after annealing of H_2TBrPP on Au(111) (Figure 3.8); this is attributed to the delocalisation of electrons throughout the covalently bonded network.

Figure 3.24(b) shows the corresponding N K-edge spectra for 1.5 ML of self-metalated H_2TBrPP. The absorption lines and assignments are listed in Table 3.11, along with literature values for H_2TPP metalated with Cu surface atoms on Cu(111) [20], and NiTPP [31]. There is good agreement with the absorption lines measured for 5 ML of NiTBrPP on the Au(111) substrate (Table 3.3), although there are some differences in the relative intensities of the absorption lines. In particular, peak *m* at 398.9 eV shows a greater angular dependence for the CuTBrPP on Cu(111) (Figure 3.24(b)) than for NiTBrPP

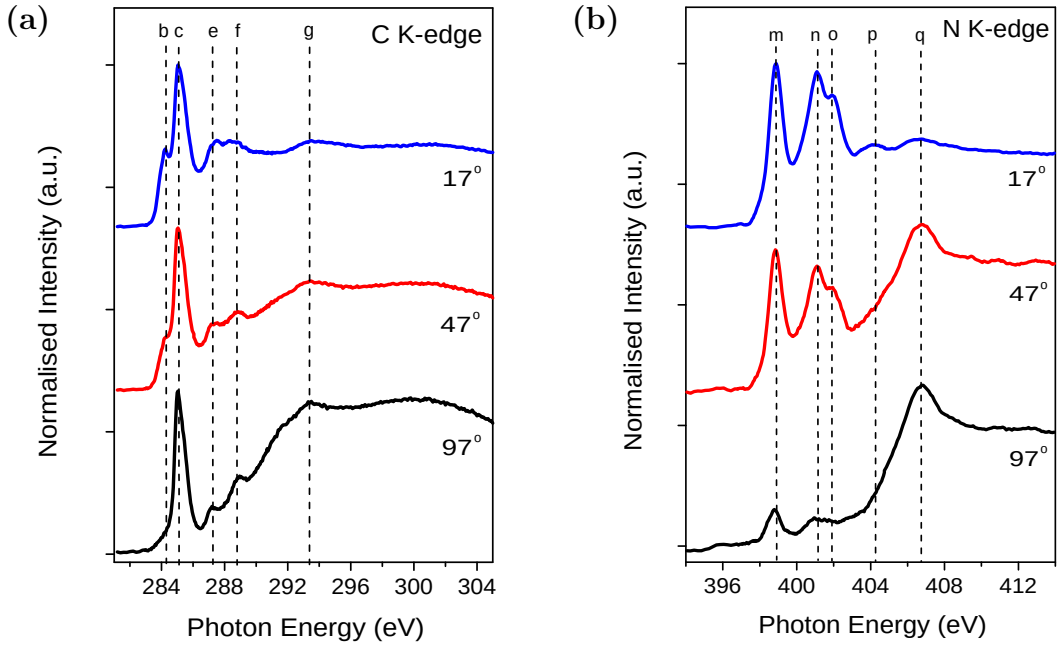

Figure 3.24: (a) C K-edge and (b) N K-edge XAS for 1.5 ML of networked and self-metalated H_2TBrPP on Cu(111), deposited at room temperature and annealed at 150 °C. Spectra recorded at three different angles of incidence.

on Au(111) (Figure 3.6(b)), indicating a greater degree of distortion for the CuTBrPP on Cu(111). The relative intensities for CuTBrPP (Figure 3.24(b)) are in good agreement with those reported by Diller *et al.* [20].

Figure 3.25 shows STM images recorded from H_2TBrPP deposited on Cu(111) at room temperature and subsequently annealed at 150 °C and 200 °C, resulting in the formation of CuTBrPP by *in situ* metalation [19]. The porphyrin molecules have networked locally in short covalently bonded chains. No extensive networks are observed, as the formation of the intermediate state on deposition (Figure 3.17) limits the mobility of the deposited H_2TBrPP as discussed previously, thus preventing the molecular diffusion necessary to form large-scale nano-networks.

Figure 3.26 shows the C 1s XPS spectra for 0.6 ML of NiTBrPP deposited on room temperature Cu(111) and annealed at 150 °C, 300 °C and 400 °C, as the protopolymer networks form and are then converted to covalently bonded

Table 3.10: Absorption line energies and assignments for C K-edge XA spectra for 1.5 ML of CuTBrPP on Cu(111) shown in Figure 3.24(a). Also included is a comparison with the features observed in the C K-edge XA spectra of CuTPP [20] and ZnTPP [29].

Absorption Line	CuTBrPP (Fig. 3.24(a)) (eV)	CuTPP [a] (eV)	ZnTPP [b] (eV)	Assignment
a	—	—	283.95	$\pi^*_{\text{macrocycle}}$ [b]
b	284.3	284.2	284.30	$\pi^*_{\text{macrocycle}}$ [a,b]
c	285.1	285.0	285.05	$\pi^*_{\text{phenyl rings}}$ [a,b]
c_2	—	285.4	285.35	$\pi^*_{\text{phenyl rings}}$ [a,b]
d	—	—	285.90	$\pi^*_{\text{macrocycle}}$ [b]
e	287.2	—	287.70	$\pi^*_{\text{macrocycle}}$ [b]
f	288.3	—	288.80	$\sigma^*_{\text{phenyl rings}}$; $\pi^*_{\text{macrocycle}}$ [b]
g	293.4	—	—	σ^* [a]

a = [20], b = [29]

structures by annealing. The C 1s spectrum measured after deposition of 0.6 ML of NiTBrPP was fitted with a Voigt line-shape at a binding energy of 284.4 eV. The area under the C 1s core level line-shape does not change as the sample is annealed, further confirming the thermal stability of the nano-networks.

Figure 3.27 shows a Cu 3p and Br 3d photoemission spectrum for 1 ML of H_2TBrPP deposited on room temperature Cu(111). A second deposition increased the coverage to 1.5 ML, which was subsequently annealed at the temperatures shown, up to 650 °C. The Br 3d core levels for 1 ML and 1.5 ML were fitted with two Voigt doublets with $3d_{5/2}$ binding energies of 68.6 eV and 70.5 eV respectively, and a spin-orbit splitting of 1.0 eV. The doublet at 68.6 eV binding energy is assigned to dissociated Br on the Cu(111) surface, while the doublet at 70.5 eV is assigned to bromine in the second molecular layer. The

Table 3.11: Absorption line energies and assignments for N K-edge XA spectra for 1.5 ML CuTBrPP on Cu(111) shown in Figure 3.24(b). Also included is a comparison with the features observed in the N K-edge XA spectra of CuTPP [20] and NiTPP [31].

Absorption Line	CuTBrPP (Fig. 3.24(b)) (eV)	CuTPP [a] (eV)	NiTPP [b] (eV)	Assignment
m	398.9	399.1	399	$\pi^*_{\text{N-metal}}$ [b]
n	401.1	401.4	401.4	$\pi^*_{\text{N-C}}$ [b]
o	401.9	402.3	402.3	$\pi^*_{\text{N-C}}$ [b]
p	404.2	—	404.4	$\pi^*_{\text{N-metal}}$ [b]
q	406.7	—	407	$\sigma^*_{\text{N-C}}$ [c]

a = [20], b = [31], c = [30]

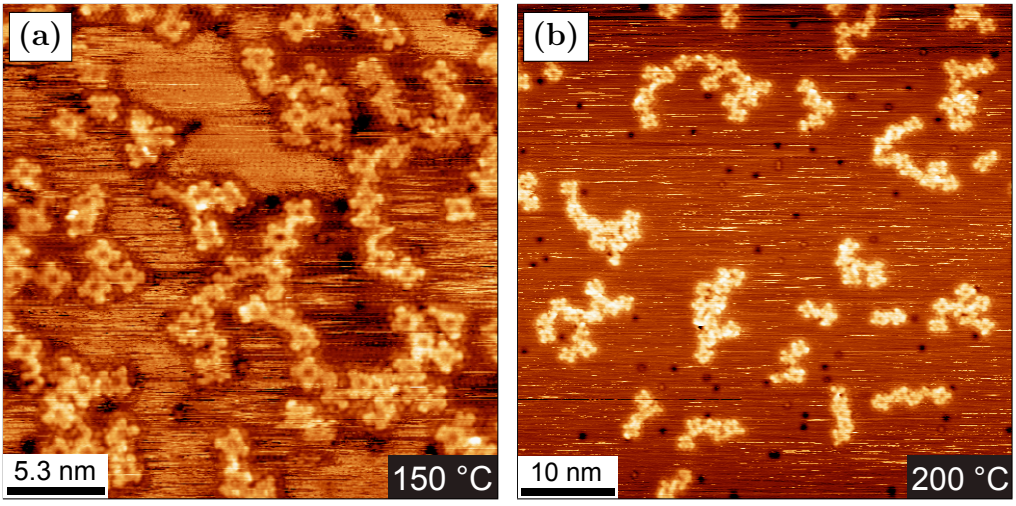

Figure 3.25: STM for H_2TBrPP deposited on room temperature Cu(111) and subsequently annealed at 150 °C and 200 °C. (a) (−0.48 V,2.06 nA), (b) (−0.02 V,0.10 nA). (a) shows the surface with 0.6 ML coverage (Figure 3.20(f)) annealed at 150 °C, (b) shows the surface with 0.2 ML coverage (Figure 3.20(a) - (d)) annealed at 200 °C.

latter is preferentially desorbed at 150 °C, while a small component at 68.6 eV remains on the surface up to 450 °C. No bromine is present on the sample after annealing at 650 °C, and the spectrum contains only the doublet at 74.8 eV assigned to the Cu 3p core levels.

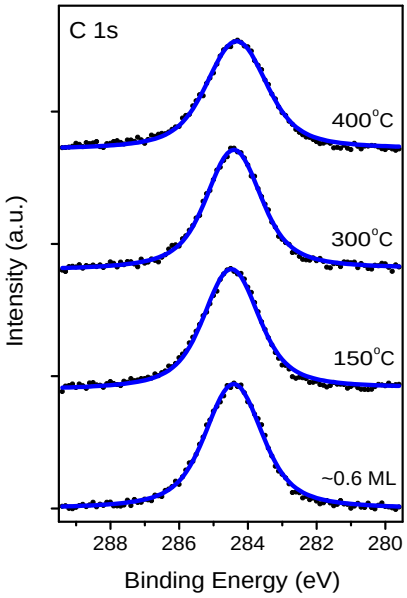

Figure 3.26: XPS for 0.6 ML of NiTBrPP deposited on room temperature Cu(111) and subsequently annealed up to 400 °C. C 1s region, hν = 1486.7 eV. Spectra correspond to Figure 3.19.

Figure 3.28 shows STM images of submonolayer coverages of H_2TBrPP on Cu(111) annealed at 300 °C, 450 °C and 520 °C. Large islands of agglomerated material are visible, with trenches and pits etched into the surface on terraces and at step edges. Some trenches are terminated with an island of agglomerated material (Figure 3.28(d)), while others are isolated (Figure 3.28(e)). The large structure in Figure 3.28(f) is a central island of apparently flat topography, surrounded by peripheral material. The average height of these flat islands is 2.01 ± 0.18 Å, while the average depth of the trenches is 1.97 ± 0.08 Å, in good agreement with the interplane separation for Cu(111) of 2.08 Å [50]. The peripheral material is approximately 0.7 Å in height. From this height analysis it is proposed that the central islands are Cu islands, while the peripheral material is decomposed porphyrin molecules. The XPS data presented in Figure 3.27 show

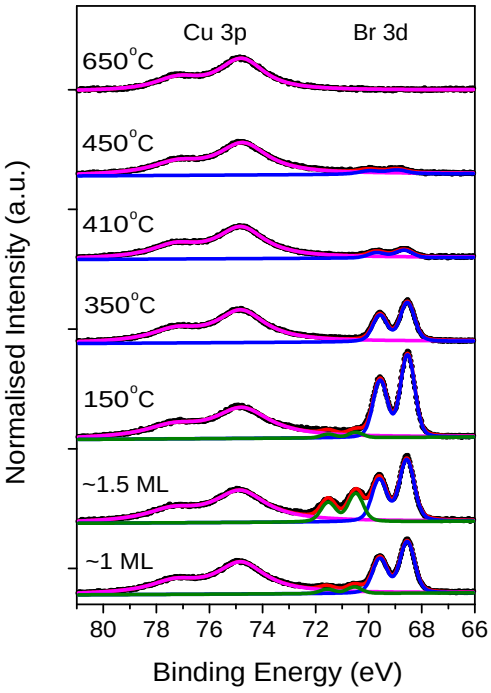

Figure 3.27: PES for H_2TBrPP deposited on room temperature Cu(111) and subsequently annealed up to 650 °C. Cu 3p and Br 3d region, hν = 150 eV. An additional 0.5 ML was deposited onto the initial coverage of 1 ML and the surface was annealed at the temperatures shown. Spectra normalised to the intensity of the Cu 3p doublet.

that a significant amount of dissociated Br is present on the surface up to 350 °C. A strong Br-Cu interaction has been reported to occur at approximately 100 °C for C_6H_5Br on Cu(111), resulting in the formation of CuBr and its subsequent desorption at 700 °C [51]. When the dissociated bromine desorbs from the surface at approximately 400 °C (Figure 3.27), it is possible that some Cu atoms are removed along with it. The vacancies created in the Cu terraces may then act as nucleation sites for trenches near step edges, such as those observed in Figure 3.28(c). These trenches may then act as a source of additional Cu adatoms, which then coalesce to form the islands observed in Figure 3.28 [52]. Pai *et al.* [53] have observed the formation of trenches in the Ag(110) surface following exposure to 300 L of O_2 at 10×10^{-5} mbar at room temperature.

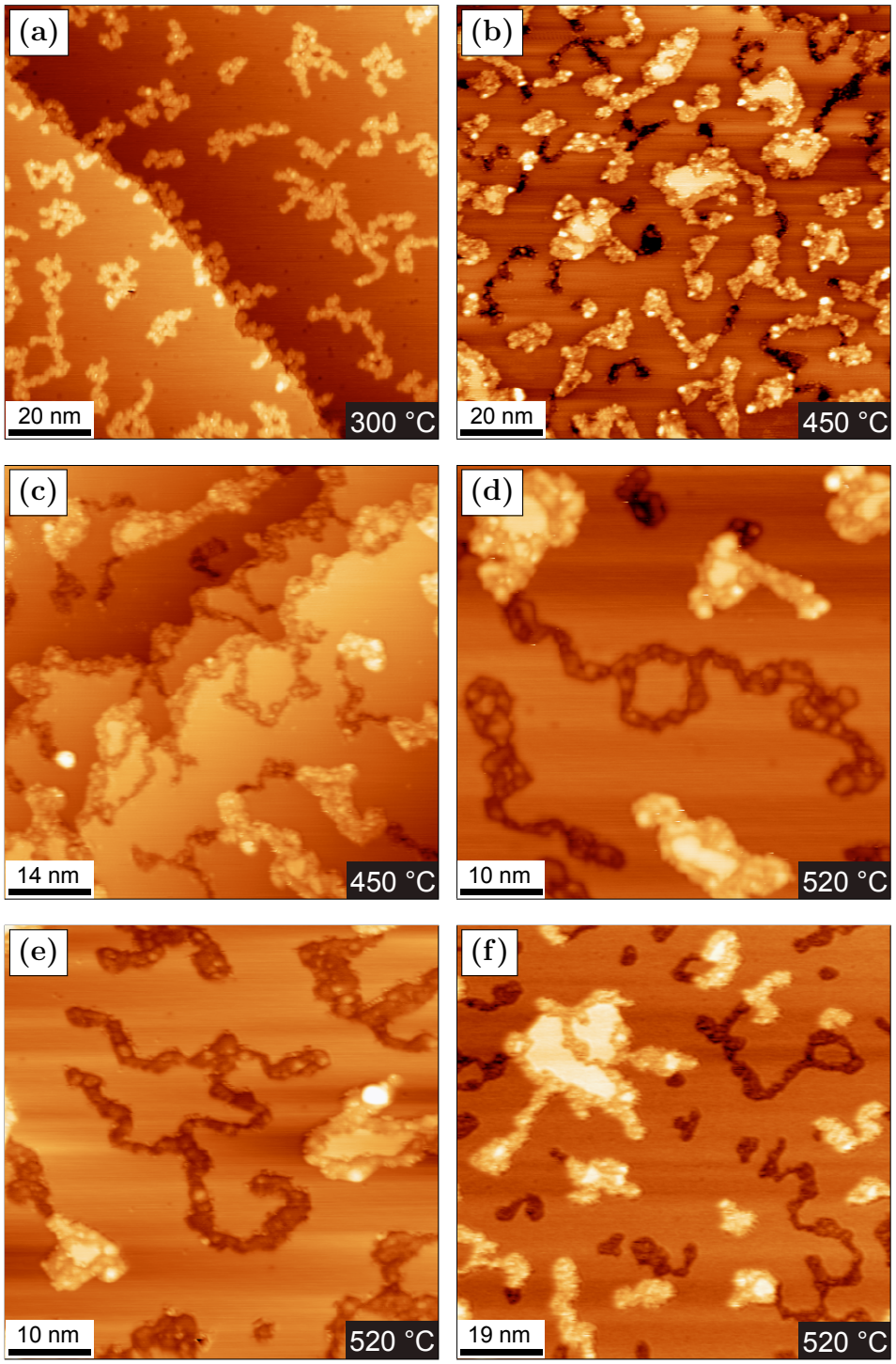

Figure 3.28: STM for H_2TBrPP deposited on room temperature Cu(111) and annealed at 300 °C, 450 °C and 520 °C. (a) (−1.45 V,1.98 nA), (b) (+1.00 V,1.00 nA), (c) (+0.84 V,0.86 nA), (d) (−1.82 V,0.25 nA), (e) (−1.24 V,1.22 nA), (f) (+0.91 V,0.93 nA). (a) shows the surface with 0.3 ML coverage (Figure 3.20(e)) annealed at 300 °C, (b) - (f) show the surface with 0.6 ML coverage (Figure 3.20(f)) annealed at the temperatures shown.

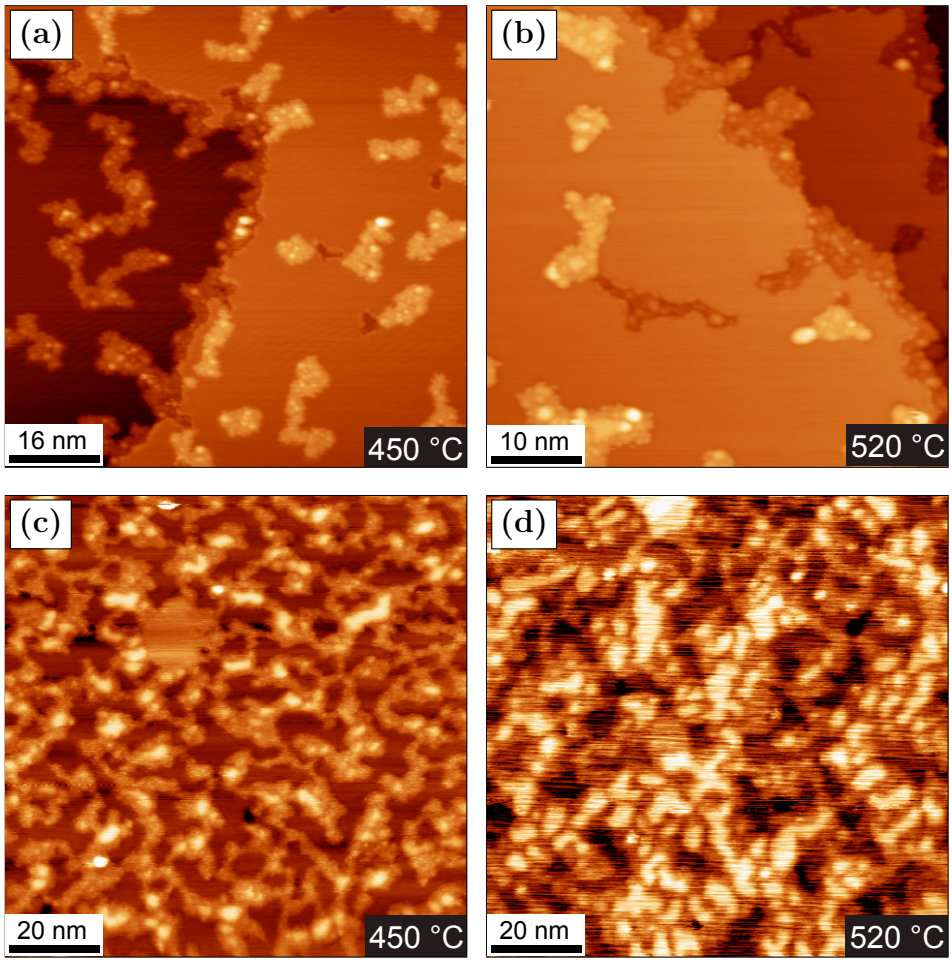

Figure 3.29: STM for NiTBrPP deposited on room temperature Cu(111) and subsequently annealed at 450 °C and 520 °C. (a) (−2.14 V,0.21 nA), (b) (−2.37 V,0.28 nA), (c) (−1.03 V,1.17 nA), (d) (−0.24 V,1.40 nA). (a) and (b) show the surface with 0.3 ML coverage (Figure 3.21) annealed at the temperatures shown, (c) and (d) show a differently prepared surface with 0.7 ML coverage annealed at the temperatures shown.

Figure 3.29 shows STM data measured after 0.3 ML (3.29(a) and 3.29(b)) and 0.7 ML (3.29(c) and 3.29(d)) of NiTBrPP was deposited on Cu(111) at room temperature and annealed at 450 °C and 520 °C. Structures very similar to those observed for H_2TBrPP on Cu(111) are present, consisting of islands and peripheral material approximately 2 Å and 0.7 Å in height respectively, and are again ascribed to Cu islands surrounded by decomposed porphyrin molecules. The islands observed for the NiTBrPP/Cu(111) system (Figure 3.29) are smaller in size than those for the H_2TBrPP/Cu(111) system (Figure 3.28). This difference may be attributed to the N-Cu interaction described above for H_2TBrPP on

Cu(111) (Figure 3.17); the removal of Cu atoms from the surface to metalate the free base porphyrin macrocycle may lead to an increased number of additional adatoms, promoting the formation of larger Cu islands.

Evidence for the decomposition of the porphyrin molecules at temperatures of 350 °C and higher is provided by x-ray absorption spectroscopy. Figure 3.30 shows C and N K-edge XA spectra for 5 ML and 1.5 ML of H_2TBrPP deposited on room temperature Cu(111). The 1.5 ML coverage was subsequently annealed up to 650 °C. The spectra for 5 ML, 1.5 ML and for 1.5 ML annealed at 150 °C have been previously shown (Figure 3.18, Figure 3.23, and Figure 3.24), and are included here as a comparison for the spectra recorded after annealing at higher temperatures.

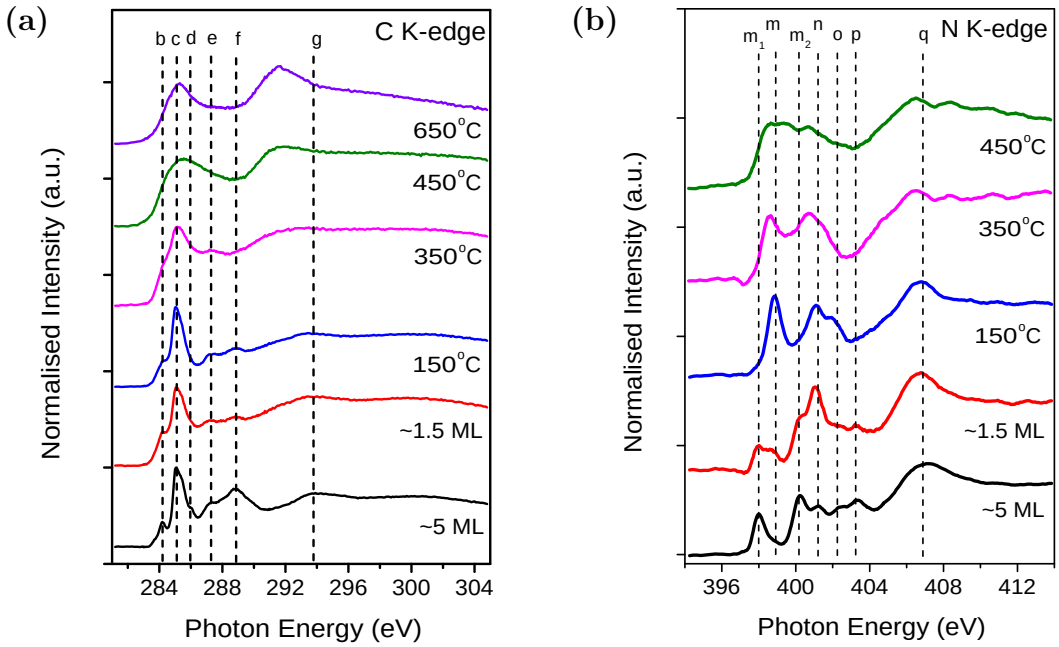

Figure 3.30: (a) C K-edge and (b) N K-edge XAS for H_2TBrPP deposited on room temperature Cu(111) and annealed at the temperatures shown. Spectra recorded at $\theta = 47°$. The 5 ML spectra were recorded from one surface, the 1.5 ML and annealed spectra were recorded from a second surface. 5 ML and 150 °C spectra previously shown in Figures 3.23 and 3.24. The dotted lines show the energies of the main absorption lines present for a 5 ML coverage of H_2TBrPP on Cu(111) (Figure 3.23).

The features in the C K-edge absorption spectra (Figure 3.30(a)) are no longer well-resolved after annealing at 350 °C. The resolution decreases further with increased anneal temperature, and after annealing at 650 °C the spectrum contains two very broad features with approximate energies of 285.3 eV and 291.6 eV. There is no longer any clear distinction between transitions to empty states centred on the macrocycle and those localised on the phenyl rings.

The H_2TBrPP are metalated with Cu after annealing at 150 °C, as evidenced by the absorption line m at 398.9 eV in the N K-edge spectrum (Figure 3.30(b)). There are no longer any discernible peaks in the absorption spectrum after annealing at 450 °C. The C and N absorption spectra together show that the porphyrin molecules are decomposed on the Cu(111) surface at temperatures of 450 °C and higher, and no longer comprise recognisable phenyl or pyrrole chemical environments.

Figure 3.31 shows C K-edge XA spectra for 1.5 ML of H_2TBrPP on Cu(111) annealed at 650 °C, measured at three different angles of incidence. Two broad

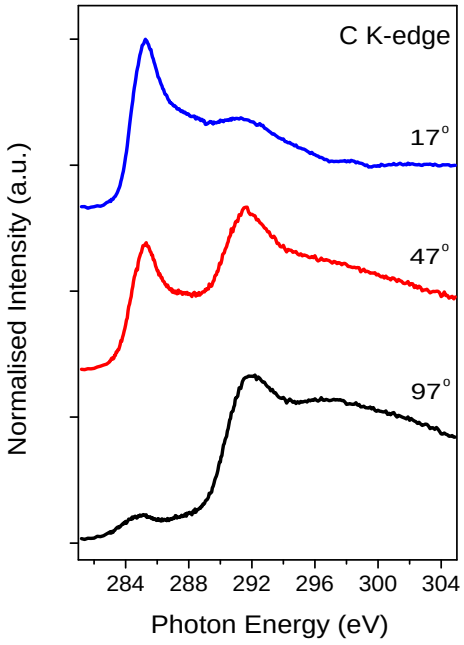

Figure 3.31: C K-edge XAS for 1.5 ML of H_2TBrPP deposited on room temperature Cu(111) and annealed at 650 °C. Spectra recorded at three different angles of incidence. 47° spectrum previously shown in Figure 3.30.

features are observed in the spectra; these peaks show an angular dependence. The feature at 285.3 eV decreases in intensity as θ goes from grazing to normal incidence, while the feature at 291.6 eV increases in intensity, indicating that one feature corresponds to transitions to empty states with π^* character, and the other to transitions to empty states with σ^* character. However, as no computational results are currently available for these structures, it is not possible to determine which chemical structures corresponds to π^* transitions, and which to σ^* transitions.

In summary, H_2TBrPP is metalated with Cu atoms from the substrate by annealing at 150 °C. An intermediate state whereby the iminic nitrogen atoms bond to a Cu atom while the pyrrolic nitrogen retain their hydrogen atoms is observed in photoemission and x-ray absorption spectroscopy. The formation of this intermediate state locally distorts the Cu surface in the vicinity of the adsorbed porphyrin molecules. Both H_2TBrPP and NiTBrPP form protopolymer networks on room temperature deposition, with NiTBrPP molecular structures mobile on the surface. Short covalently bonded chains of molecules are observed after annealing at both 150 °C and 200 °C. Annealing to 300 °C and higher results in the formation of large flat Cu islands and the formation of trenches in the Cu surface. The islands are surrounded by peripheral material of a lower height, proposed to be the decomposed porphyrin molecules that are known to be present on the surface from XA spectroscopy.

3.5 Summary

A 1 ML coverage of NiTBrPP self-assembles on Au(111) at room temperature and after annealing at 100 °C and 120 °C. Covalently bonded nano-networks are formed after annealing at 170 °C and higher. These networks are extensive, covering regions on the surface with areas on the order of 10 000 nm^2. However they are generally disordered, with square pores accounting for approximately 25 % of the total number of pores. Typical regions of ordered four-fold nano-mesh are comprised of ten to twenty NiTBrPP molecules. The networks are thermally stable up to 400 °C. Deposition of NiTBrPP onto Au(111) held at elevated temperatures results in nano-networks with a similar degree of ordering as those observed for room temperature deposition. Angle-dependent x-ray absorption spectroscopy indicates that the porphyrin macrocycles adopt a distorted geometry, with the phenyl rings rotated with respect to the macrocycle. The result of the delocalisation of electrons over the covalently

bonded nano-networks can be seen in the XA spectra measured after network formation, where the absorption lines are no longer well-resolved. Metalation of H_2TBrPP with Ni atoms has been achieved on Au(111), with the reaction proceeding via the formation of an intermediate state first proposed in 1960 by Fleischer and Wang [9] for porphyrin metalation in solution.

Dissociated bromine accounts for approximately 70 % of the total bromine signal for NiTBrPP deposited onto Ag(111) at room temperature. This leads to the formation of protopolymer networks coordinated by surface Ag atoms at room temperature and 100 °C. These protopolymer networks exhibit long-range order; some regions of ordered four-fold network are comprised of approximately 100 molecules. The networks become covalently bonded after annealing at 200 °C and higher, as evidenced by the shorter centre-to-centre distance between adjacent porphyrin molecules. These covalently bonded networks display a similar degree of order to networks formed on Au(111), and are also thermally stable to 400 °C.

H_2TBrPP has been metalated with surface copper atoms on Cu(111). These results represent the first direct observation of the intermediate state on a surface as proposed by Fleischer and Wang [9], as well as the first direct observation of *in situ* metalation of a free base porphyrin molecule using substrate atoms [19]. The bromine dissociates from the TBrPP molecules on deposition at room temperature, leading to the formation of protopolymer networks. In addition, the H_2TBrPP molecules are distorted by the formation of the intermediate state, which also causes local deformation in the Cu(111) surface. The porphyrin macrocycles exhibit a greater degree of distortion on Cu(111) compared to Au(111), as calculated from the angle-dependent XAS. Short covalently bonded porphyrin chains are observed after annealing at 150 °C and 200 °C, but no extensive networks are present on the surface. This is most likely due to the initial limitations on the porphyrin mobility caused by molecule-substrate interaction. Large flat islands approximately 2 Å in height surrounded by peripheral material approximately 0.7 Å in height, together with trenches in the Cu(111) substrate approximately 2 Å in depth, are observed after annealing both H_2TBrPP and NiTBrPP on Cu(111) at 300 °C and higher. XAS confirms that carbon and nitrogen are still present on the surface at these temperatures, however the spectra indicate that the molecules are decomposed. Hence the structures observed on the surface are attributed to Cu islands formed by the coalescence of adatoms, with the trenches and pits acting as sources of additional adatoms. The islands appear to be surrounded by decomposed molecular material.

3.6 Bibliography

[1] Hla, S.W., Bartels, L., Meyer, G., and Rieder, K.H., *Inducing all steps of a chemical reaction with the scanning tunneling microscope tip: Towards single molecule engineering*, Physical Review Letters, **85** (2000) pp. 2777–2780.

[2] Lipton-Duffin, J.A., Ivasenko, O., Perepichka, D.F., and Rosei, F., *Synthesis of Polyphenylene Molecular Wires by Surface-Confined Polymerization*, Small, **5** (2009) pp. 592–597.

[3] Gutzler, R., Walch, H., Eder, G., Kloft, S., Heckl, W.M., and Lackinger, M., *Surface mediated synthesis of 2D covalent organic frameworks: 1,3,5-tris(4-bromophenyl)benzene on graphite(001), Cu(111), and Ag(110)*, Chemical Communications, 29 (2009) pp. 4456–4458.

[4] Grill, L., Dyer, M., Lafferentz, L., Persson, M., Peters, M., and Hecht, S., *Nano-architectures by covalent assembly of molecular building blocks*, Nature Nanotechnology, **2** (2007) pp. 687–691.

[5] Krasnikov, S.A., Doyle, C.M., Sergeeva, N.N., Preobrajenski, A.B., Vinogradov, N.A., Sergeeva, Y.N., Zakharov, A.A., Senge, M.O., and Cafolla, A.A., *Formation of extended covalently bonded Ni porphyrin networks on the Au(111) surface*, Nano Research, **4** (2011) pp. 376–384.

[6] Lafferentz, L., Eberhardt, V., Dri, C., Africh, C., Comelli, G., Esch, F., Hecht, S., and Grill, L., *Controlling on-surface polymerization by hierarchical and substrate-directed growth*, Nature Chemistry, **4** (2012) pp. 215–220.

[7] Blunt, M.O., Russell, J.C., Champness, N.R., and Beton, P.H., *Templating molecular adsorption using a covalent organic framework*, Chemical Communications, **46** (2010) pp. 7157–7159.

[8] Walch, H., Gutzler, R., Sirtl, T., Eder, G., and Lackinger, M., *Material- and Orientation-Dependent Reactivity for Heterogeneously Catalyzed Carbon-Bromine Bond Homolysis*, Journal of Physical Chemistry C, **114** (2010) pp. 12604–12609.

[9] Fleischer, E.B. and Wang, J.H., *The Detection of a Type of Reaction Intermediate in the Combination of Metal Ions with Porphyrins*, Journal of the American Chemical Society, **82** (1960) pp. 3498–3502.

[10] Shubina, T.E., Marbach, H., Flechtner, K., Kretschmann, A., Jux, N., Buchner, F., Steinrueck, H.P., Clark, T., and Gottfried, J.M., *Principle and mechanism of direct porphyrin metalation: Joint experimental and theoretical investigation*, Journal of the American Chemical Society, **129** (2007) pp. 9476–9483.

[11] Kretschmann, A., Walz, M.M., Flechtner, K., Steinrueck, H.P., and Gottfried, J.M., *Tetraphenylporphyrin picks up zinc atoms from a silver surface*, Chemical Communications, 6 (2007) pp. 568–570.

[12] Flechtner, K., Kretschmann, A., Bradshaw, L.R., Walz, M.M., Steinrueck, H.P., and Gottfried, J.M., *Surface-confined two-step synthesis of the complex (ammine)(meso-tetraphenylporphyrinato)-zinc(II) on Ag(111)*, Journal of Physical Chemistry C, **111** (2007) pp. 5821–5824.

[13] Gottfried, J.M., Flechtner, K., Kretschmann, A., Lukasczyk, T., and Steinrueck, H.P., *Direct synthesis of a metalloporphyrin complex on a surface*, Journal of the American Chemical Society, **128** (2006) pp. 5644–5645.

[14] Buchner, F., Flechtner, K., Bai, Y., Zillner, E., Kellner, I., Steinrueck, H.P., Marbach, H., and Gottfried, J.M., *Coordination of iron atoms by tetraphenylporphyrin monolayers and multilayers on Ag(111) and formation of iron-tetraphenylporphyrin*, Journal of Physical Chemistry C, **112** (2008) pp. 15458–15465.

[15] Buchner, F., Schwald, V., Comanici, K., Steinrueck, H.P., and Marbach, H., *Microscopic evidence of the metalation of a free-base porphyrin monolayer with iron*, Chemphyschem, **8** (2007) pp. 241–243.

[16] Ecija, D., Trelka, M., Urban, C., de Mendoza, P., Mateo-Marti, E., Rogero, C., Martin-Gago, J.A., Echavarren, A.M., Otero, R., Gallego, J.M., and Mirandat, R., *Molecular conformation, organizational chirality, and iron metalation of meso-tetramesitylporphyrins on copper(100)*, Journal of Physical Chemistry C, **112** (2008) pp. 8988–8994.

[17] Di Santo, G., Castellarin-Cudia, C., Fanetti, M., Taleatu, B., Borghetti, P., Sangaletti, L., Floreano, L., Magnano, E., Bondino, F., and Goldoni, A., *Conformational Adaptation and Electronic Structure of*

2H-Tetraphenylporphyrin on Ag(111) during Fe Metalation, Journal of Physical Chemistry C, **115** (2011) pp. 4155–4162.

[18] Weber-Bargioni, A., Reichert, J., Seitsonen, A.P., Auwaerter, W., Schiffrin, A., and Barth, J.V., *Interaction of cerium atoms with surface-anchored porphyrin molecules*, Journal of Physical Chemistry C, **112** (2008) pp. 3453–3455.

[19] Doyle, C.M., Krasnikov, S.A., Sergeeva, N.N., Preobrajenski, A.B., Vinogradov, N.A., Sergeeva, Y.N., Senge, M.O., and Cafolla, A.A., *Evidence for the formation of an intermediate complex in the direct metalation of tetra(4-bromophenyl)-porphyrin on the Cu(111) surface*, Chemical Communications, **47** (2011) pp. 12134–12136.

[20] Diller, K., Klappenberger, F., Marschall, M., Hermann, K., Nefedov, A., Woell, C., and Barth, J.V., *Self-metalation of 2H-tetraphenylporphyrin on Cu(111): An x-ray spectroscopy study*, Journal of Chemical Physics, **136** (2012) pp. 014705–1–014705–13.

[21] Rojas, G., Simpson, S., Chen, X., Kunkel, D.A., Nitz, J., Xiao, J., Dowben, P.A., Zurek, E., and Enders, A., *Surface state engineering of molecule-molecule interactions*, Physical Chemistry Chemical Physics, **14** (2012) pp. 4971–4976.

[22] Goldoni, A., Pignedoli, C.A., Di Santo, G., Castellarin-Cudia, C., Magnano, E., Bondino, F., Verdini, A., and Passerone, D., *Room Temperature Metalation of 2H-TPP Monolayer on Iron and Nickel Surfaces by Picking up Substrate Metal Atoms*, ACS Nano, **6** (2012) pp. 10800–10807.

[23] Xiao, J., Ditze, S., Chen, M., Buchner, F., Stark, M., Drost, M., Steinrueck, H.P., Gottfried, J.M., and Marbach, H., *Temperature-Dependent Chemical and Structural Transformations from 2H-tetraphenylporphyrin to Copper(II)-Tetraphenylporphyrin on Cu(111)*, Journal of Physical Chemistry C, **116** (2012) pp. 12275–12282.

[24] Nowakowski, J., Waeckerlin, C., Girovsky, J., Siewert, D., Jung, T.A., and Ballav, N., *Porphyrin metalation providing an example of a redox reaction facilitated by a surface reconstruction*, Chemical Communications, **49** (2013) pp. 2347–2349.

[25] Diller, K., Klappenberger, F., Allegretti, F., Papageorgiou, A.C., Fischer, S., Wiengarten, A., Joshi, S., Seufert, K., Ecija, D., Auwaerter, W., and Barth, J.V., *Investigating the molecule-substrate interaction of prototypic tetrapyrrole compounds: Adsorption and self-metalation of porphine on Cu(111)*, Journal of Chemical Physics, **138** (2013) pp. 154710–1–154710–9.

[26] *ACD/ChemSketch*, URL `www.acdlabs.com/resources/freeware/chemsketch/`, accessed July 2013.

[27] Buchner, F., Kellner, I., Hieringer, W., Goerling, A., Steinrueck, H.P., and Marbach, H., *Ordering aspects and intramolecular conformation of tetraphenylporphyrins on Ag(111)*, Physical Chemistry Chemical Physics, **12** (2010) pp. 13082–13090.

[28] Lee, H.L., Strategies for the Formation of Covalently Bonded Nano-Networks on Metal Surfaces through Amine Reactions, Ph.D. thesis, Dublin City University, Dublin, 2012.

[29] Schmidt, N., Fink, R., and Hieringer, W., *Assignment of near-edge x-ray absorption fine structure spectra of metalloporphyrins by means of time-dependent density-functional calculations*, Journal of Chemical Physics, **133** (2010) pp. 054703–1–054703–13.

[30] Chen, M., Feng, X., Zhang, L., Ju, H., Xu, Q., Zhu, J., Gottfried, J.M., Ibrahim, K., Qian, H., and Wang, J., *Direct Synthesis of Nickel(II) Tetraphenylporphyrin and Its Interaction with a Au(111) Surface: A Comprehensive Study*, Journal of Physical Chemistry C, **114** (2010) pp. 9908–9916.

[31] Krasnikov, S.A., Sergeeva, N.N., Brzhezinskaya, M.M., Preobrajenski, A.B., Sergeeva, Y.N., Vinogradov, N.A., Cafolla, A.A., Senge, M.O., and Vinogradov, A.S., *An x-ray absorption and photoemission study of the electronic structure of Ni porphyrins and Ni N-confused porphyrin*, Journal of Physics: Condensed Matter, **20** (2008) pp. 235207–235212.

[32] Krasnikov, S.A., Preobrajenski, A.B., Sergeeva, N.N., Brzhezinskaya, M.M., Nesterov, M.A., Cafolla, A.A., Senge, M.O., and Vinogradov, A.S., *Electronic structure of Ni(II) porphyrins and phthalocyanine studied by soft X-ray absorption spectroscopy*, Chemical Physics, **332** (2007) pp. 318–324.

[33] Castellarin-Cudia, C., Vilmercati, P., Larciprete, R., Cepek, C., Zampieri, G., Sangaletti, L., Pagliara, S., Verdini, A., Cossaro, A., Floreano, L., Morgante, A., Petaccia, L., Lizzit, S., Battocchio, C., Polzonetti, G., and Goldoni, A., *Electronic structure and molecular orientation of a Zn-tetra-phenyl porphyrin multilayer on Si(111)*, Surface Science, **600** (2006) pp. 4013–4017.

[34] Stohr, J. and Outka, D.A., *Determination of Molecular Orientations on Surfaces from the Angular-Dependence of Near-Edge X-Ray-Absorption Fine-Structure Spectra*, Physical Review B, **36** (1987) pp. 7891–7905.

[35] Stohr, J., NEXAFS Spectroscopy, 2nd ed., Springer-Verlag, Heidelberg, 1996.

[36] Weber-Bargioni, A., Auwaerter, W., Klappenberger, F., Reichert, J., Lefrancois, S., Strunskus, T., Woell, C., Schiffrin, A., Pennec, Y., and Barth, J.V., *Visualizing the frontier orbitals of a conformationally adapted metalloporphyrin*, Chemphyschem, **9** (2008) pp. 89–94.

[37] Narioka, S., Ishii, H., Ouchi, Y., Yokoyama, T., Ohta, T., and Seki, K., *XANES Spectroscopic Studies of Evaporated Porphyrin Films - Molecular-Orientation and Electronic-Structure*, Journal of Physical Chemistry, **99** (1995) pp. 1332–1337.

[38] Ferri, A., Polzonetti, G., Iucci, G., Paolucci, G., Goldoni, A., Parent, P., Laffon, C., Contini, G., and Carravetta, V., *NEXAFS spectroscopy investigation on the electronic structure of newly synthesized Pt(II)/Zn-porphyrinato assemblies*, Surface and Interface Analysis, **30** (2000) pp. 407–409.

[39] Newbury, D.C., Ishii, I., and Hitchcock, A.P., *Inner shell electron energy loss spectroscopy of some heterocyclic molecules*, Canadian Journal of Chemistry, **64** (1986) pp. 1145–1155.

[40] Polzonetti, G., Battocchio, C., Goldoni, A., Larciprete, R., Carravetta, V., Paolesse, R., and Russo, M., *Interface formation between C_{60} and diethynyl-Zn-porphyrinato investigated by SR-induced photoelectron and near-edge X-ray absorption (NEXAFS) spectroscopies*, Chemical Physics, **297** (2004) pp. 307–314.

[41] Rojas, G., Chen, X., Bravo, C., Kim, J.H., Kim, J.S., Xiao, J., Dowben, P.A., Gao, Y., Zeng, X.C., Choe, W., and Enders, A., *Self-Assembly and Properties of Nonmetalated Tetraphenyl-Porphyrin on Metal Substrates*, Journal of Physical Chemistry C, **114** (2010) pp. 9408–9415.

[42] McCarty, G.S. and Weiss, P.S., *Formation and manipulation of protopolymer chains*, Journal of the American Chemical Society, **126** (2004) pp. 16772–16776.

[43] Wang, W., Shi, X., Wang, S., Van Hove, M.A., and Lin, N., *Single-Molecule Resolution of an Organometallic Intermediate in a Surface-Supported Ullmann Coupling Reaction*, Journal of the American Chemical Society, **133** (2011) pp. 13264–13267.

[44] Bjork, J., Hanke, F., and Stafstrom, S., *Mechanisms of Halogen-Based Covalent Self-Assembly on Metal Surfaces*, Journal of the American Chemical Society, **135** (2013) pp. 5768–5775.

[45] Brede, J., Linares, M., Lensen, R., Rowan, A.E., Funk, M., Broering, M., Hoffmann, G., and Wiesendanger, R., *Adsorption and conformation of porphyrins on metallic surfaces*, Journal of Vacuum Science & Technology B, **27** (2009) pp. 799–804.

[46] Brede, J., Linares, M., Kuck, S., Schwoebel, J., Scarfato, A., Chang, S.H., Hoffmann, G., Wiesendanger, R., Lensen, R., Kouwer, P.H.J., Hoogboom, J., Rowan, A.E., Broering, M., Funk, M., Stafstrom, S., Zerbetto, F., and Lazzaroni, R., *Dynamics of molecular self-ordering in tetraphenyl porphyrin monolayers on metallic substrates*, Nanotechnology, **20** (2009) pp. 275602–1–275602–10.

[47] Dyer, M.S., Robin, A., Haq, S., Raval, R., Persson, M., and Klimes, J., *Understanding the Interaction of the Porphyrin Macrocycle to Reactive Metal Substrates: Structure, Bonding, and Adatom Capture*, ACS Nano, **5** (2011) pp. 1831–1838.

[48] Lackinger, M. and Heckl, W.M., *A STM perspective on covalent intermolecular coupling reactions on surfaces*, Journal of Physics D - Applied Physics, **44** (2011) pp. 464011–1–464011–14.

[49] Buchner, F., Zillner, E., Roeckert, M., Glaessel, S., Steinrueck, H.P., and Marbach, H., *Substrate-Mediated Phase Separation of Two Porphyrin Derivatives on Cu(111)*, Chemistry - A European Journal, **17** (2011) pp. 10226–10229.

[50] Straumanis, M.E. and Yu, L.S., *Lattice Parameters, Densities, Expansion Coefficients and Perfection of Structure of Cu and of Cu-In α Phase*, Acta Crystallographica Section A, **25** (1969) pp. 676–682.

[51] Blake, M.M., Nanayakkara, S.U., Claridge, S.A., Fernandez-Torres, L.C., Sykes, E.C.H., and Weiss, P.S., *Identifying Reactive Intermediates in the Ullmann Coupling Reaction by Scanning Tunneling Microscopy and Spectroscopy*, Journal of Physical Chemistry A, **113** (2009) pp. 13167–13172.

[52] Lin, N., Payer, D., Dmitriev, A., Strunskus, T., Woell, C., Barth, J.V., and Kern, K., *Two-dimensional adatom gas bestowing dynamic heterogeneity on surfaces*, Angewandte Chemie International Edition, **44** (2005) pp. 1488–1491.

[53] Pai, W.W., Bartelt, N.C., Peng, M.R., and Reuttrobey, J.E., *Steps as Adatom Sources for Surface-Chemistry - Oxygen Overlayer Formation on Ag(110)*, Surface Science, **330** (1995) pp. L679–L685.

Chapter 4
Network Formation with Three-fold Symmetrical Brominated Molecules on Metal Surfaces

4.1 Introduction

The three-fold symmetrical 1,3,5-tris(4-bromophenyl) benzene (TBB) (Figure 4.1) molecule is suitable for forming hexagonal covalently bonded networks using the debromination reaction scheme already discussed. TBB has been deposited on a number of different surfaces, in both UHV and ambient conditions. Gutzler *et al.*. have deposited TBB on graphite(001), Cu(111), Ag(110), and Ag(111) in UHV [1, 2]. A self-assembled non-covalently bonded structure was observed on graphite(001), which exhibited poor thermal stability and desorbed from the surface after annealing at 320 °C [1]. The Ag and Cu substrates were sufficiently reactive to catalytically cleave the C-Br bond, in agreement with previous reports [3]. The debrominated molecules were then coordinated by surface atoms to form protopolymer networks, which were subsequently converted to covalently bonded structures on annealing [1, 2, 4].

Blunt *et al.* studied TBB on the Au(111) substrate in UHV conditions, where a close-packed arrangement of the molecules was observed on room temperature deposition [5]. Annealing the sample led to the formation of TBB dimers, but no extended hexagonal networks were observed. Deposition onto a hot substrate resulted in the growth of a nano-network containing pentagonal, hexagonal and heptagonal pores [5]. C_{60} molecules were deposited onto the network, with the fullerenes adsorbing in the pores. The droplet deposition of TBB onto Au(111) on mica using ethanol or butanol was also investigated [6]. Three distinct phases of molecular packing were observed at room temperature, while the formation of dimers was reported for deposition onto a hot substrate [6].

TBB was also deposited onto SiB(111), where it formed a regular, hexagonal network that was thermally stable to 130 °C. The network was used as a host structure for C_{60} molecules [7].

This chapter investigates the self-assembly, molecular ordering and covalent bonding of TBB on the Au(111), Au(110) and Cu(111) substrates. In addition, experimental C 1s core level photoemission spectroscopy and C K-edge absorption spectroscopy are compared with DFT calculations. STM data for the deposition of C_{60} onto a self-assembled monolayer of TBB on Au(110) at room temperature is also presented and discussed.

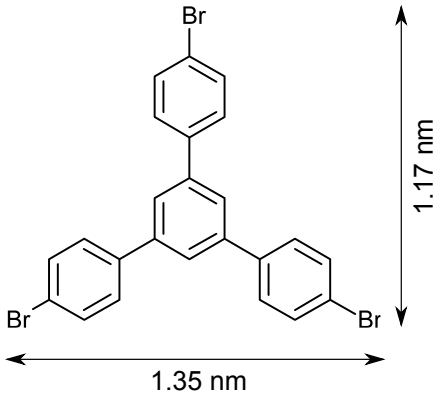

Figure 4.1: Structure of TBB ($C_{24}H_{15}Br_3$) with nominal dimensions determined from ChemSketch [8]. Hydrogen atoms not explicitly shown.

4.2 STM and Photoemission Study of TBB on the Au(111) Surface

4.2.1 Analysis for Deposition at Room Temperature

Molecular packing of monolayer coverages of TBB on Au(111) at room temperature has been reported in the literature [5]. In the present work submonolayer coverages of TBB molecules were deposited on the Au(111) $22\times\sqrt{3}$ substrate at room temperature, but were found to be mobile on the surface and could not be imaged with the STM. Following annealing at 190 °C, the TBB molecules were debrominated, leading to the formation of covalently bonded nano-

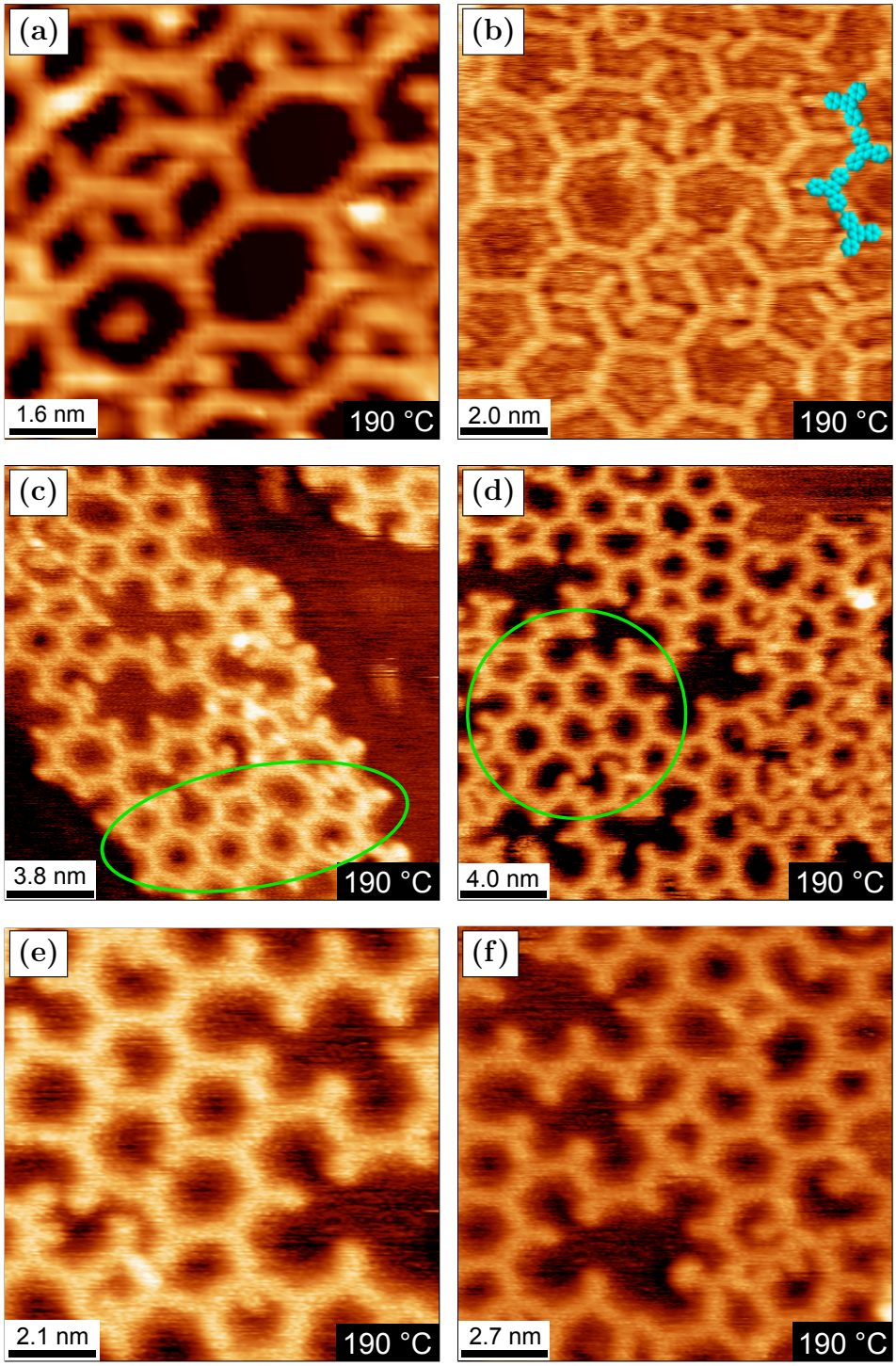

Figure 4.2: STM for TBB deposited on room temperature Au(111) and subsequently annealed at 190 °C. (a) (−1.93 V,0.14 nA), (b) (−0.11 V,2.15 nA), (c) (−1.40 V,0.20 nA), (d) - (f) (+1.71 V,0.15 nA). (a) shows a surface with 1 ML coverage, (b) shows a differently prepared surface with 0.9 ML coverage, and (c) - (f) show a differently prepared surface with 0.5 ML coverage.

networks. STM images of these structures are shown in Figure 4.2. The nano-networks include pentagonal, hexagonal, heptagonal, octagonal and irregular-shaped pores. Statistical analysis of nine STM images featuring a total of 460 pores shows that pentagonal and hexagonal pores each account for approximately 25 % of the total number of pores. Hence the TBB networks exhibit approximately the same defect density as the TBrPP networks (Section 3.2). The region of the surface shown in Figure 4.2(b) features four closed pores in addition to a large connected network of TBB molecules, similar to that observed by Blunt *et al.* [5]. Areas of hexagonal mesh are highlighted with green circles in Figure 4.2(c) and 4.2(d). The hexagonal pores in Figure 4.2 have a centre-to-centre distance of 2.20 ± 0.22 nm, calculated by analysing the mean value across several pores. The centre-to-centre distance between adjacent TBB molecules is 1.34 ± 0.17 nm, as measured from the STM images. The formation of TBB networks following room temperature deposition and subsequent annealing disagrees with previous reports in the literature, where network formation was only observed after deposition onto the Au(111) substrate held at 140 °C [5].

Figure 4.3 shows STM images recorded after annealing the networks at 300 °C. The $22 \times \sqrt{3}$ reconstruction of the underlying Au(111) surface can be seen in Figure 4.3(b). The green circle in Figure 4.3(b) highlights a typical region of TBB nano-network, where local hexagonal order is disrupted by a defect in the

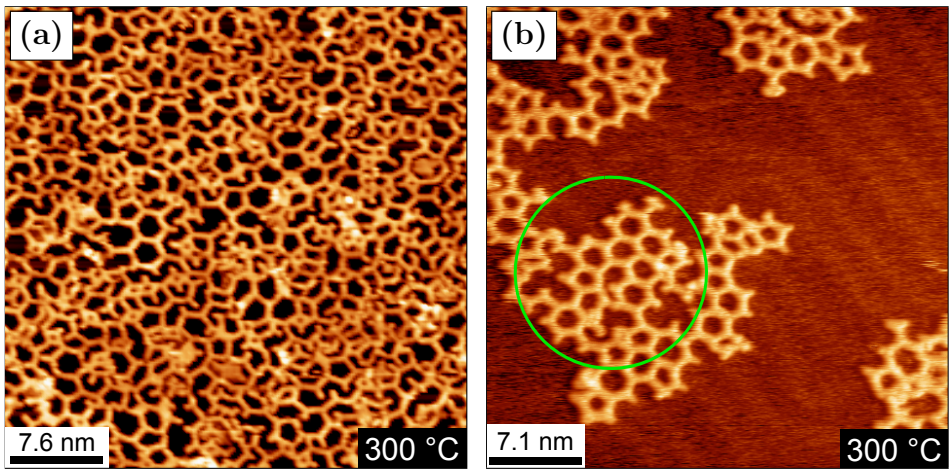

Figure 4.3: STM for TBB deposited on room temperature Au(111) and subsequently annealed at 300 °C. (a) (+1.82 V,1.00 nA), (b) (−2.09 V,0.21 nA). (a) shows the surface with 1 ML coverage (Figure 4.2(a)) annealed at 300 °C, (b) shows the surface with 0.5 ML coverage (Figure 4.2(c) - (f)) annealed at 300 °C.

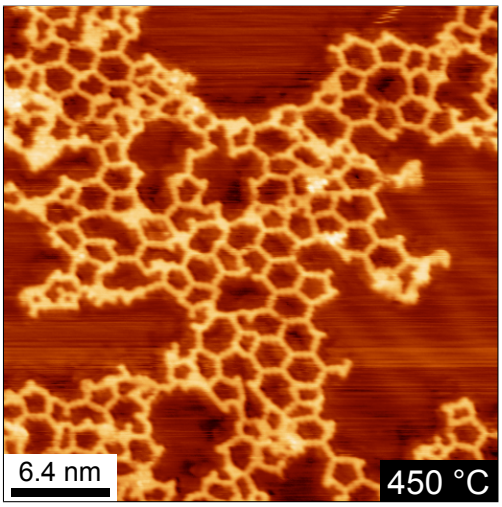

Figure 4.4: STM for TBB deposited on room temperature Au(111) and subsequently annealed at 450 °C. (+1.21 V,0.24 nA). Figure shows the surface with 0.5 ML coverage (Figures 4.2(c) - (f) and 4.3(b)) annealed at 450 °C.

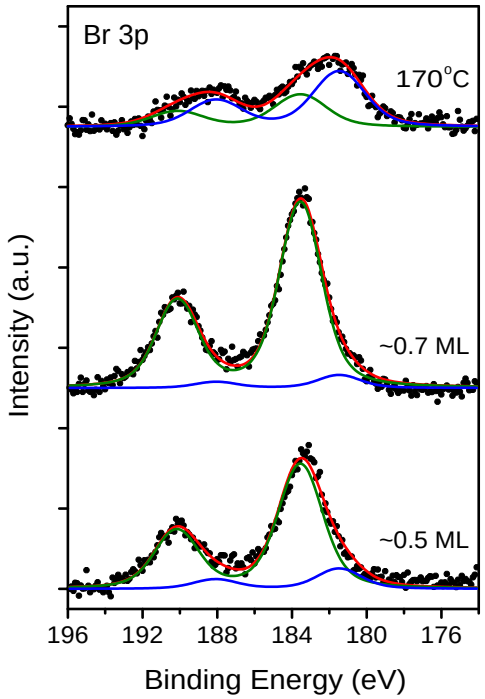

Figure 4.5: XPS for TBB on room temperature Au(111), initial deposition of 0.5 ML, followed by deposition of an additional 0.2 ML and subsequent annealing at 170 °C. Br 3p region, hν = 1486.7 eV.

molecular bonding. Figure 4.4 shows a nano-network after annealing at 450 °C for one hour and indicates that the TBB networks are thermally stable, up to at least that temperature. Hexagonal and pentagonal pores are present in the network, which has a similar appearance to networks in Figure 4.2 and Figure 4.3.

Figure 4.5 shows Br 3p XPS spectra recorded after deposition of 0.5 ML and an additional 0.2 ML of TBB on Au(111) at room temperature, followed by annealing at 170 °C. The spectra were fitted with two Voigt doublets with $3p_{3/2}$ binding energies of 181.5 eV and 183.6 eV respectively, and a spin-orbit splitting of 6.6 eV, which are assigned, as previously, to dissociated bromine (lower binding energy) and Br which remains bonded to the phenyl rings (high binding energy). The dissociated Br at 181.5 eV binding energy accounts for 14 % and 7 % of the total bromine signal for the 0.5 ML and 0.7 ML coverages respectively. This decrease may be due to Br dissociation preferentially occurring at certain adsorption sites, such as step edges. The total Br signal after annealing at 170 °C is 60 % of that recorded for 0.7 ML. This decrease is partially attributed to loss of TBB molecules from the surface during the annealing process, indicated by the corresponding C 1s XPS data.

Figure 4.6 shows fitted Br 3d core level PES spectra recorded after deposition of 6 ML of TBB. The spectra were fitted with two Voigt doublets with $3d_{5/2}$ binding energies of 69.7 eV and 70.2 eV respectively, and a spin-orbit splitting of 1.0 eV. The lower binding energy component is assigned to bromine in the first monolayer which has not dissociated from the TBB molecules but does demonstrate a minor interaction with the Au(111) substrate. The component at 70.2 eV is assigned to bromine in the second and subsequent layers which does not interact with the substrate. After annealing at 170 °C for 45 minutes the component at 70.2 eV is no longer present. Analysis of the corresponding C 1s spectrum indicates a monolayer coverage, showing that TBB molecules have desorbed from the substrate. In addition to the component at 69.7 eV, two further components with binding energies of 68.0 eV and 67.6 eV are present. These additional components are assigned to bromine which has dissociated from the TBB molecule and is present on the Au(111) substrate in two different chemical environments. These components may correspond to Br adsorbed in two distinct bonding sites on the surface, such as along step edges and on terraces. An alternative explanation is that some dissociated Br atoms have diffused underneath the molecular layer, while the remaining Br is adsorbed on the bare Au. The component with binding energy of 69.7 eV decreases in intensity

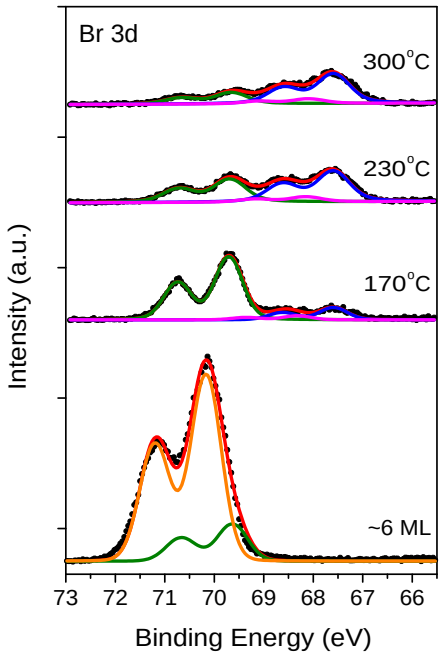

Figure 4.6: PES for 6 ML of TBB deposited on room temperature Au(111), followed by annealing at 170 °C, 230 °C and 300 °C. Br 3d region, hν = 170.0 eV.

with further annealing, and after annealing the sample at 300 °C the dissociated bromine accounts for approximately 75 % of the total Br signal. The resolution of the XPS system is not sufficient to distinguish between chemical environments that differ by 0.4 eV in energy, hence only one component relating to dissociated bromine is observed in Figure 4.5.

Figure 4.7 shows carbon K-edge x-ray absorption spectra for a TBB coverage of 6 ML recorded at three different angles of incidence of the synchrotron radiation. The absorption lines are assigned in Table 4.1; in making these assignments, previous XAS data for benzene (C_6H_6) and bromobenzene (C_6H_5Br) in the literature were used [9, 10].

Figure 4.8 shows the experimental spectra recorded at grazing and normal incidence (Figure 4.7) compared with the results of StoBe calculations for *p*- and *s*-polarised light, performed by Dr. Cormac McGuinness and Anna Lawless. The calculations were carried out for a single free molecule of TBB, according to previously published procedures [11]. A simulated C K-edge XA spectrum was

Table 4.1: Absorption line energies and assignments for C K-edge XA spectra for 6 ML of TBB deposited on Au(111) at room temperature shown in Figure 4.7. Also included is a comparison with the features observed in the C K-edge spectra of C_6H_5Br [9] and C_6H_6 [10].

Absorption Line	TBB (Fig. 4.7) (eV)	C_6H_5Br [a] (eV)	C_6H_6 [b] (eV)	Assignment [a,b]
a	285.1	285	285.0	π^*
b	286.0	286.3	—	$\sigma^*_{\text{C-Br}}$
c	287.0	287	287.2	$\sigma^*_{\text{C-H}}$
d	288.9	288.7	288.8	π^*
e	293.4	293.5	290.0	$\sigma^*_{\text{C-C}}$

a = [9], b = [10]

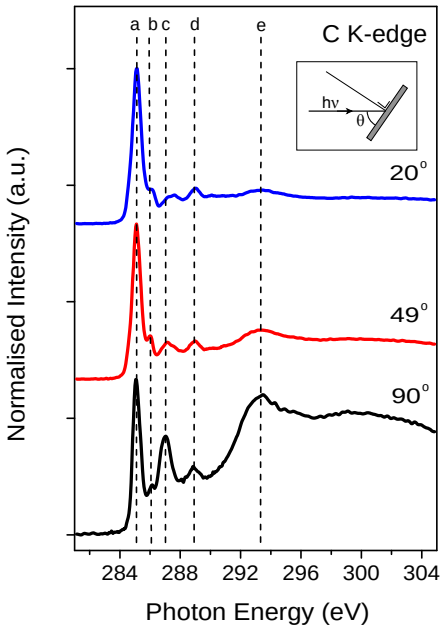

Figure 4.7: C K-edge XAS for 6 ML of TBB deposited on room temperature Au(111) (Figure 4.6), recorded at three different angles of incidence of the synchrotron radiation. Inset shows angle θ between incoming photons and sample normal. Refer to Table 4.1 for assignments.

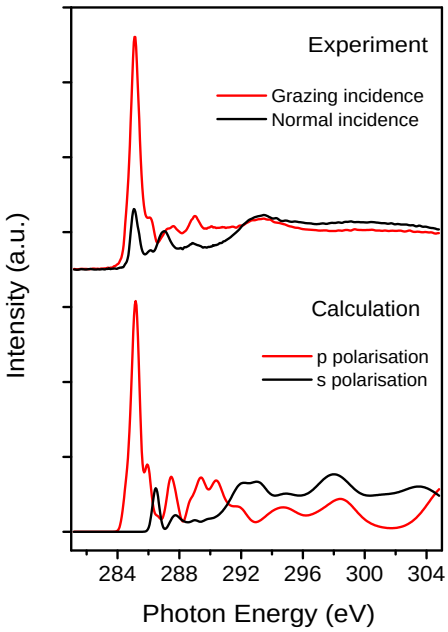

Figure 4.8: Experimental and calculated C K-edge XAS for TBB on Au(111). Experimental spectra measured from 6 ML deposited at room temperature, and recorded at $\theta = 20°$ and $\theta = 90°$ (Figure 4.7), theoretical spectra calculated for p- and s-polarised electric field vector.

generated from the calculated transitions between the 1s energy level and the unoccupied 2p levels for each of two orientations of the electric field vector; perpendicular to the plane of the central macrocycle (p-polarised), and in the plane of the central macrocycle (s-polarised) [12]. The respective correspondence between the grazing incidence experimental spectrum and the calculated p-polarised spectrum, and the normal incidence experimental spectrum and the calculated s-polarised spectrum, confirms that the π^* and σ^* orbitals are oriented perpendicularly and parallel to the molecular plane respectively. The calculated spectra indicate that the absorption line at 285.1 eV is purely π^* in character. As there is a feature at 285.1 eV in the experimental normal incidence spectrum, this shows that the molecules are not aligned parallel to the substrate, but are tilted at some angle with respect to the surface. This angle can be calculated using the method outlined in Section 2.7 [13, 14]. The ratio of the intensity of the absorption lines recorded at grazing and normal incidence is used in conjunction with equations 2.30, 2.31 and 2.32 to calculate an angle of $36 \pm 5°$

with respect to the substrate. This is in good agreement with literature, where XAS data gives values of (42 to 46)±5° for the orientation of both chlorobenzene and iodobenzene with respect to the surface plane [10], while XAS data for the aromatic compounds aniline and phenol give angles of $39 \pm 5°$ and $40 \pm 5°$ respectively [15].

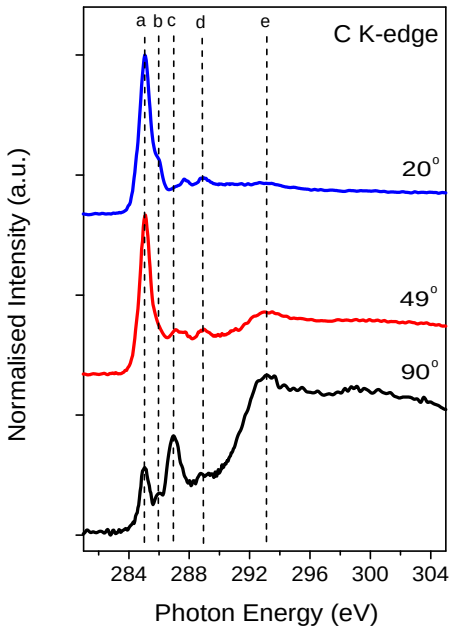

Figure 4.9: C K-edge XAS for 6 ML of TBB deposited on room temperature Au(111) and subsequently annealed at 140 °C. Refer to Table 4.1 for assignments. Spectra measured after the surface with 6 ML coverage (Figure 4.7) was annealed at 140 °C.

Figure 4.9 shows XA spectra recorded after the 6 ML TBB coverage was annealed at 140 °C. Carbon photoemission spectra (discussed below, Figure 4.12) indicate a monolayer coverage. The absorption line energies are in good agreement with the XA spectra recorded for a 6 ML coverage (Figure 4.7 and Table 4.1). Analysis of the angular dependence of the intensity of the absorption lines shows that the TBB molecules are now oriented at an angle of $20 \pm 3°$ with respect to the substrate, in contrast to the angle of $36 \pm 5°$ calculated for the 6 ML coverage.

Figure 4.10 shows carbon K-edge XA data recorded at grazing incidence for the 6 ML coverage of TBB deposited on Au(111) at room temperature and

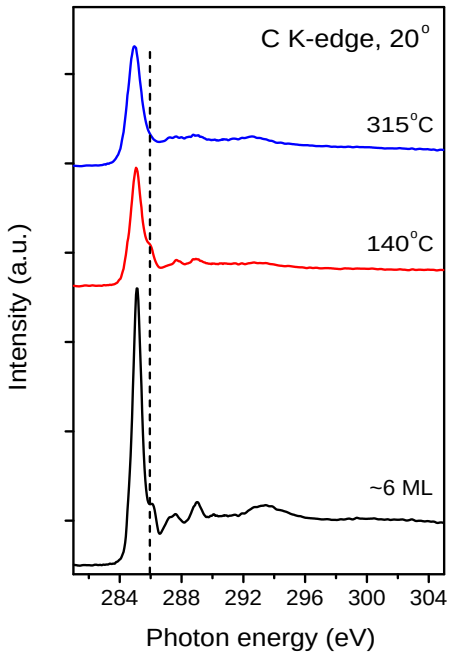

Figure 4.10: Grazing incidence C K-edge XAS for 6 ML of TBB deposited on room temperature Au(111) and subsequently annealed at 140 °C and 315 °C. 6 ML spectrum shown in Figure 4.7, 140 °C spectrum shown in Figure 4.9.

subsequently annealed at 140 °C and 315 °C. The absorption line at 286.0 eV, assigned to transitions from the C 1s core level to a $\sigma^*_{\text{C-Br}}$ molecular orbital (Table 4.1), decreases in intensity as the sample is annealed and is no longer present after annealing at 315 °C. This corresponds to the dissociation of bromine from the TBB molecule, and supports the assignment of the absorption line as a transition to a $\sigma^*_{\text{C-Br}}$ orbital.

Figure 4.11(a) shows the experimental and calculated C 1s core level PES spectrum for TBB. The experimental spectrum was measured from 6 ML of TBB deposited on Au(111) at room temperature. The calculations were performed using the StoBe DFT code [16]. The C 1s core level binding energies resulting from the XAS calculation discussed above were used to simulate the C 1s photoemission spectrum. The calculation was performed for an isolated TBB molecule, assuming a relaxed electronic structure after the removal of a core electron and taking into account the six carbon environments present in TBB (Figure 4.11(b)) [12].

The experimental data were fitted with six components using the calculated

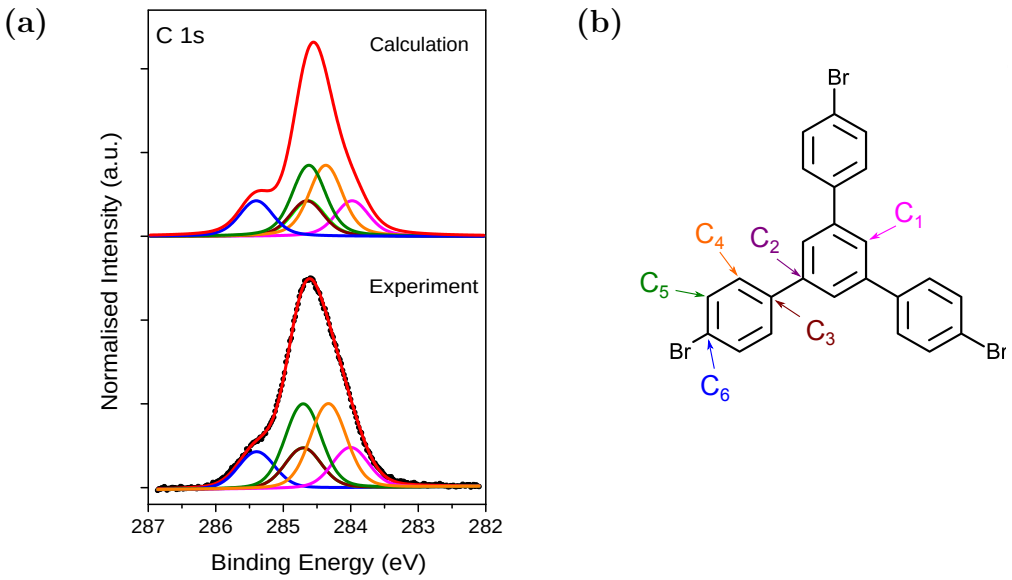

Figure 4.11: (a) Calculated and experimental C 1s PES for TBB. Calculation performed for an isolated molecule; experimental data recorded for a 6 ML coverage on room temperature Au(111). (b) Six carbon chemical environments present in TBB molecule, colour-coded with fitted components in (a).

binding energies and relative intensities as a guide (see Table 4.2). The component at 285.4 eV binding energy is assigned to the carbon atoms bonded to bromine in TBB. This is in good agreement with previous studies of bromobenzene, which reported a binding energy of 285.3 eV for the C-Br component [9]. The normalised intensity of this component is smaller in the fitted experimental data than the calculated spectrum. This decrease is attributed to the partial debromination of the molecule observed on the surface (Figure 4.5). The separation between the components assigned to C-Br (C_6)and C-H (C_4) of 0.9 eV agrees with the calculated energy difference for the analogous carbon atoms in bromobenzene [17].

Figure 4.12 shows the C 1s core level photoemission spectra from 6 ML of TBB deposited at room temperature and after subsequent annealing at 140 °C and 315 °C. The spectrum recorded after deposition is fitted with the components discussed above (Table 4.2). For the spectrum recorded after annealing at 140 °C, the component at 284.2 eV binding energy is assigned to the C_2, C_3, C_4 and C_5 chemical environments (Figure 4.11(b)), as there are no calculations available for comparison with the annealed spectra and the difference in binding energy of

Table 4.2: Binding energy and normalised intensity of components for calculated and experimental C 1s XPS data, Figure 4.11(a).

Label	Binding Energy (eV) (Calculation)	Binding Energy (eV) (Experiment)	Normalised Intensity (Calculation)	Normalised Intensity (Experiment)
C_1	284.0	284.0	0.125	0.123
C_2	284.6	284.7	0.125	0.123
C_3	284.6	284.7	0.125	0.123
C_4	284.4	284.3	0.250	0.258
C_5	284.6	284.7	0.250	0.258
C_6	285.4	285.4	0.125	0.113

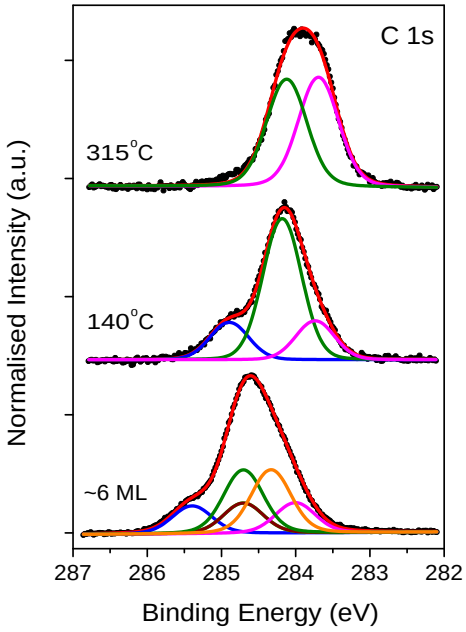

Figure 4.12: PES for 6 ML of TBB deposited on room temperature Au(111) and subsequently annealed at 140 °C and 315 °C. C 1s region, hν = 400.0 eV. 6 ML spectrum shown in Figure 4.11(a), and measured from the same surface as spectra shown in Figure 4.7. 140 °C spectrum measured from the same surface as data shown in Figure 4.9.

these chemical environments is too small to be resolved. As the spectrum recorded after annealing at 315 °C corresponds to a covalently bonded TBB network, only two carbon chemical environments are present; a C-C component at 284.1 eV assigned to the C_2, C_3 and C_6 environments, and a C-H component at 283.7 eV assigned to the C_1, C_4 and C_5 environments.

The higher binding energy component, C_6, assigned to the carbon atoms bonded to bromine, is still present after annealing at 140 °C but is absent after annealing at 315 °C (Figure 4.12). These results are in agreement with the XA spectra in which the absorption line assigned to the $\sigma^*_{\text{C-Br}}$ orbital decreases in intensity with annealing and is no longer present after annealing at 315 °C (Figure 4.10). It has been shown previously that bromine is still present on the surface after annealing at 315 °C, shifted to lower binding energy (Figure 4.6). As the carbon x-ray photoemission and absorption spectra indicate that there is no interaction between C and Br at this temperature, this confirms the assignment of the bromine chemical environments at 68.0 eV and 67.6 eV binding energy in Figure 4.6 to bromine dissociated from the TBB molecule.

The spectra shown in Figure 4.12 have been normalised to unit intensity for ease of comparison. There is a monolayer coverage of TBB present after annealing at 140 °C, compared to 6 ML on deposition. The C 1s core level spectrum shifts to lower binding energy with annealing. This energy shift is due to the change in thickness of the molecular layer. There are several reports in the literature of thicker molecular layers having greater binding energy than thinner layers [18–20], with one explanation being that as electrons are ejected from the surface by the photoelectron effect, the thicker molecular layer acts as an insulator and limits the flow of electrons from the bulk of the sample, causing the remaining electrons in the molecular layer to be more tightly bound.

4.2.2 STM and Photoemission Study of TBB/Au(111) Deposited at Elevated Temperatures

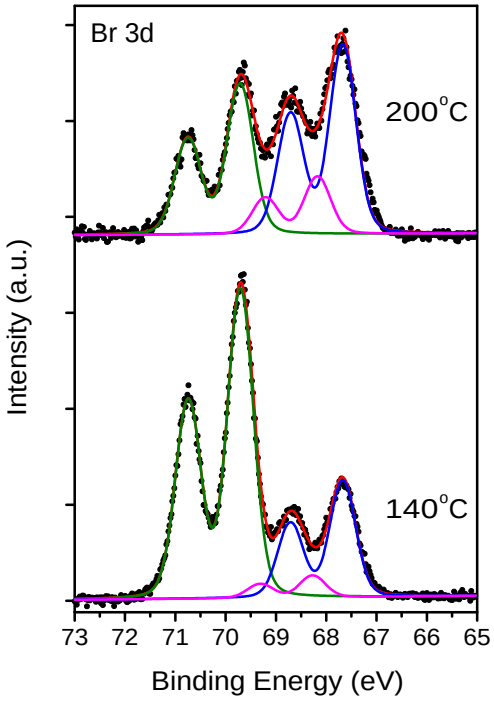

Figure 4.13: PES for 0.6 ML of TBB deposited on Au(111) held at 140 °C and subsequently annealed at 200 °C. Br 3d region, hν = 170.0 eV.

Figure 4.13 shows Br 3d core level photoemission spectra recorded from 0.6 ML of TBB deposited on Au(111) held at 140 °C, and subsequently annealed at 200 °C. The components with respective $3d_{5/2}$ binding energies of 67.7 eV and 68.2 eV are assigned to dissociated bromine as discussed above (Figure 4.6), while the component with a $3d_{5/2}$ binding energy of 69.7 eV is assigned to bromine atoms which are still bonded to the TBB. There is a difference in the relative intensities of the components for deposition onto a hot substrate compared to room temperature deposition and subsequent annealing (Figure 4.6). Dissociated bromine accounts for approximately 40 % of the total Br signal after depositing onto the hot surface at 140 °C (Figure 4.13), compared to 20 % for room temperature deposition and subsequent annealing at 170 °C (Figure 4.6). This indicates that the C-Br bond scission occurs more readily for deposition onto a hot substrate than for annealing following room temperature deposition. There is no

longer a discernible difference between the deposition methods after annealing at higher temperatures, as dissociated bromine accounts for approximately 65 % of the total Br signal after annealing at 200 °C (Figure 4.13) and 230 °C (Figure 4.6).

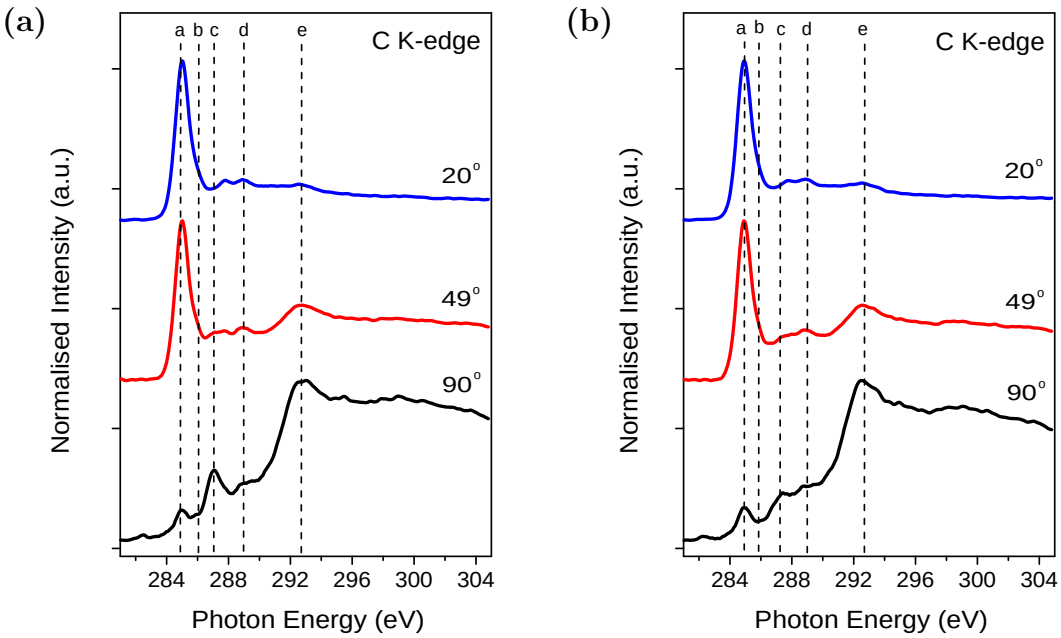

Figure 4.14: C K-edge for 0.6 ML of TBB deposited on Au(111) held at 140 °C (a) and subsequently annealed at 200 °C (b). Spectra recorded at three different values of θ. Refer to Table 4.1 for assignments. Spectra in (a) and (b) measured from the same surfaces as 140 °C and 200 °C spectra in Figure 4.13 respectively.

Figure 4.14 shows the corresponding XA spectra, for deposition onto the hot Au(111) substrate at 140 °C (Figure 4.14(a)) and subsequent annealing at 200 °C (Figure 4.14(b)). The absorption lines labelled *a* to *e* are in good agreement with the XA spectra recorded after room temperature deposition (Figure 4.7). Analysis of the intensity ratios for grazing and normal incidence [13] show that the angle of the molecules with respect to the surface plane is $17 \pm 3°$ for both deposition at 140 °C and annealing at 200 °C. This is in good agreement with the angle of $20 \pm 3°$ calculated for a monolayer coverage of TBB (Figure 4.9). As the angle for a 6 ML coverage was $36 \pm 5°$ (Figure 4.7), this suggests a coverage dependence of the molecular orientation.

In summary, TBB forms covalently bonded nano-networks on Au(111) after annealing at 190 °C and higher (Figure 4.2 and Figure 4.3). These networks are thermally stable up to 450 °C (Figure 4.4). The bromine that dissociates from the TBB molecule but remains on the surface is present in two different chemical environments on the surface (Figure 4.6). Analysis of XA spectra recorded at grazing and normal incidence shows that for a 6 ML coverage the TBB molecules are oriented at an angle of $36 \pm 5^{\circ}$ with respect to the surface plane (Figure 4.7), while the molecules are oriented at $20 \pm 3^{\circ}$ (Figure 4.9) and $17 \pm 3^{\circ}$ (Figure 4.14) with respect to the substrate for coverages of 1 ML and 0.6 ML respectively. The absorption lines in the XA spectra can be assigned to transitions to specific orbitals using literature assignments (Table 4.1). Hence the evolution of the intensity of the absorption line assigned to a transition from the C 1s core level to a $\sigma^*_{\text{C-Br}}$ orbital can be monitored as a function of temperature (Figure 4.10). Good agreement with the experimental data is obtained by fitting the C 1s core level photoemission spectrum with the components determined using DFT calculations (Figure 4.11).

4.3 STM and Photoemission Study of TBB on the Au(110 Surface)

4.3.1 Analysis for Deposition at Room Temperature

Figure 4.15 shows STM images of three different molecular packing configurations for TBB on room temperature Au(110), recorded after deposition onto a 2×1 reconstructed Au(110) surface (Figure 2.22 and 2.23). The unit cells are shown for each of the three distinct packing configurations, and the parameters are listed in Table 4.3. Unit cell dimensions were determined by analysing approximately one hundred unit cells for each packing configuration. Type 1 is the predominant packing configuration, with only small domains of Types 2 and 3 packing observed.

The row of molecules highlighted in Figure 4.15(c) is poorly resolved compared to the surrounding rows. One possible explanation is that the TBB molecules in that row are oscillating between two different orientations, causing several of the molecules to appear to have a fourth brominated phenyl ring, as shown in the inset in the figure. This oscillation may then lead to the disruption of the molecular packing in the region, highlighted by the overlaid TBB molecules. An

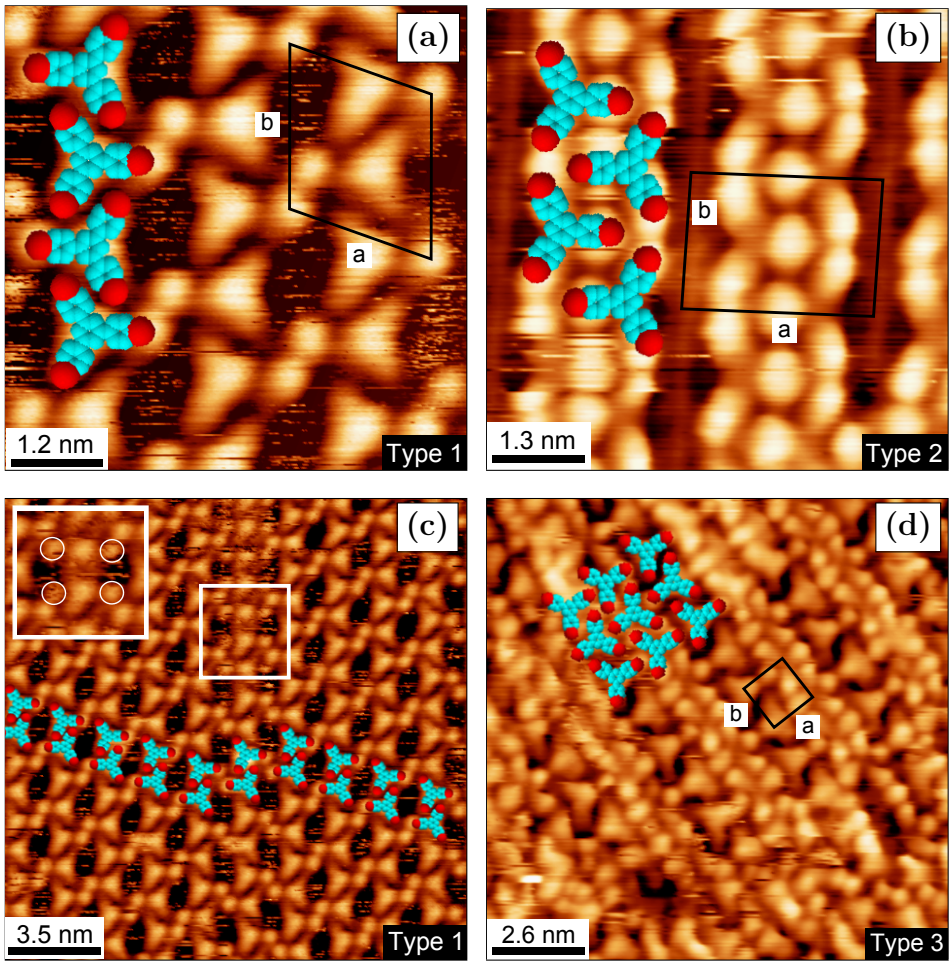

Figure 4.15: STM for TBB deposited on room temperature 2×1 Au(110). (a) (−0.97 V,0.54 nA), (b) (−1.26 V,0.53 nA), (c) (−0.97 V,0.84 nA), (d) (+1.42 V,0.14 nA). (a) and (c) show a surface with a 0.7 ML coverage, (b) shows a differently prepared surface with a 0.8 ML coverage, and (d) shows a differently prepared surface with a 0.7 ML coverage.

alternative explanation is that the row of molecules are poorly resolved due to a domain boundary effect.

Figure 4.16 shows STM images of TBB on room temperature Au(110), recorded after deposition onto a 3×1 reconstructed Au(110) surface (Figure 2.22 and 2.23). The 3×1 reconstruction has a periodicity of 1.26 ± 0.01 nm and is labelled in Figure 4.16(b). A fourth molecular packing is observed, labelled Type 4 in Figure 4.16(a). The parameters of the Type 4 unit cell are shown in Table 4.3. Type 4 packing is only observed for deposition onto a 3×1 reconstructed Au surface, while Type 1 packing is observed for both 3×1 and 2×1 reconstructions

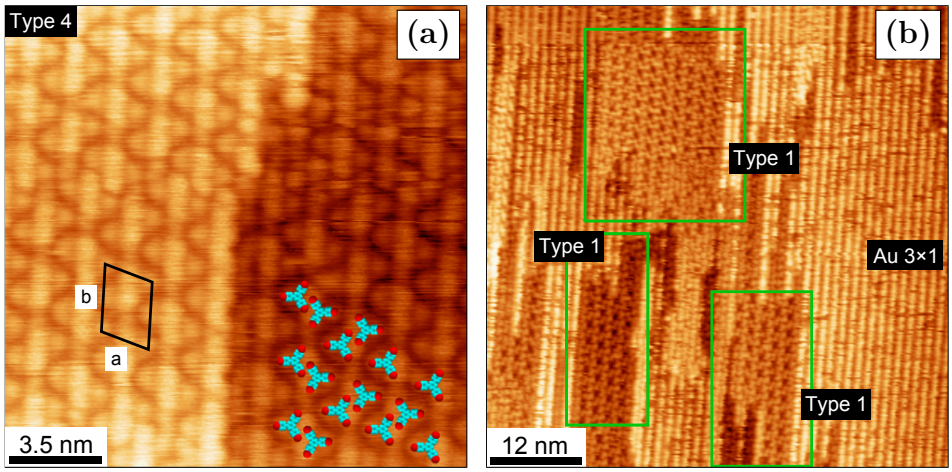

Figure 4.16: STM for TBB deposited on room temperature 3×1 Au(110). (a) (−1.37 V,0.37 nA), (b) (−1.24 V,0.23 nA). (a) and (b) show a surface with a 0.6 ML coverage.

Table 4.3: Length of unit cell vectors and angle between vectors for different molecular packing configurations of TBB on room temperature Au(110) shown in Figures 4.15 and 4.16.

Packing	a (nm)	b (nm)	θ (°)
Type 1	1.84 ± 0.04	2.22 ± 0.02	108.8 ± 1.1
Type 2	2.56 ± 0.03	1.82 ± 0.01	88.1 ± 1.6
Type 3	1.33 ± 0.01	1.19 ± 0.02	89.0 ± 1.2
Type 4	1.79 ± 0.08	2.42 ± 0.05	107.1 ± 2.8

(Figure 4.16(b) and 4.15(c)).

Figure 4.17 shows STM data recorded after annealing the self-assembled TBB molecular layer. After annealing a 0.7 ML coverage at 130 °C, hexagons, dimers and chains are all observed (Figure 4.17(a)). The average TBB-TBB centre-to-centre distance is measured as 1.40 ± 0.12 nm. Figures 4.17(b) to (d) were recorded from 0.6 ML of TBB on the 3×1 reconstructed Au surface annealed at temperatures of 200 °C and 220 °C. The 3×1 reconstruction is lifted after annealing, with the Au rows in Figure 4.17(b) exhibiting the 0.8 nm periodicity characteristic of the 2×1 reconstruction. The movement of the substrate atoms at this temperature precludes the formation of extensive nano-networks, with

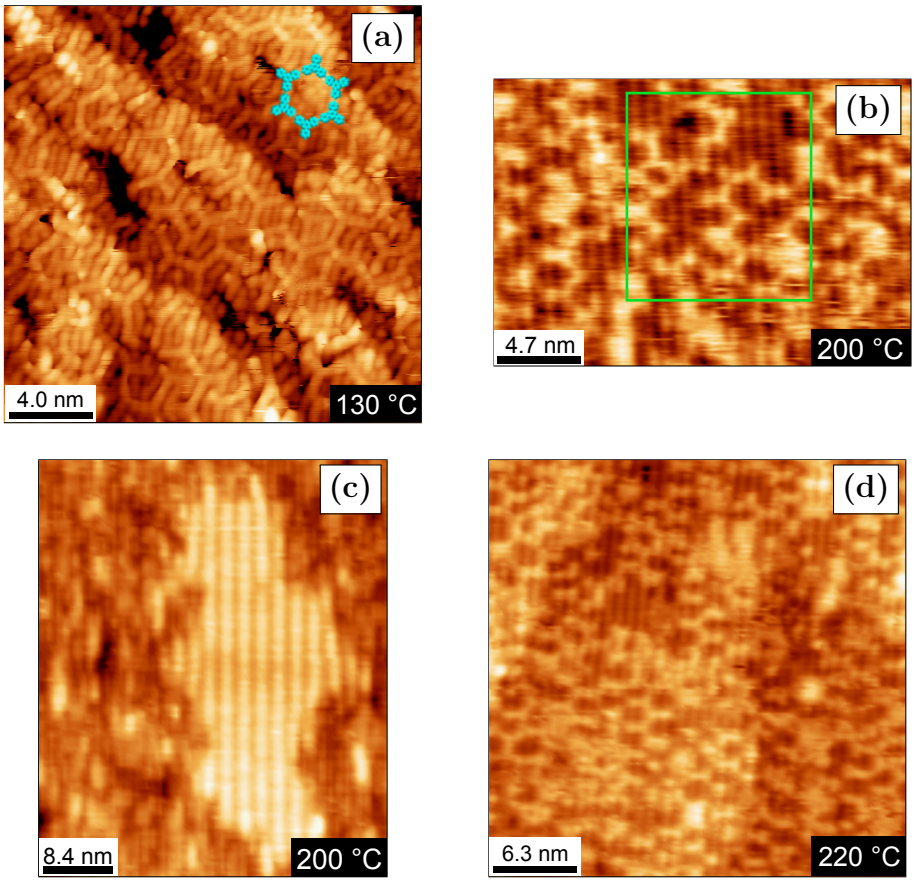

Figure 4.17: STM for TBB deposited on room temperature Au(110) and subsequently annealed at 130 °C, 200 °C and 220 °C. (a) (+0.45 V,0.34 nA), (b) (+1.48 V,0.10 nA), 23.5 nm × 16.0 nm, (c) (+1.42 V,0.04 nA), 42.0 nm × 50.0 nm, (d) (+1.58 V,0.17 nA). (a) shows the surface with a 0.7 ML coverage (Figure 4.15(d)) annealed at 130 °C, (b) - (d) show the surface with a 0.6 ML coverage (Figure 4.16) annealed at the temperatures shown. The 3×1 reconstruction is lifted after annealing, with the underlying Au surface exhibiting a 2×1 reconstruction in all cases.

only chains and incomplete pores present in Figure 4.17(b) and 4.17(d). In addition, there is evidence for a possible 5×1 Au reconstruction with a periodicity of 2.07 ± 0.06 nm (Figure 4.17(c)).

Figure 4.18 shows Br 3d PES and Br 3p XPS data for 0.6 ML and 2.7 ML respectively of TBB deposited on Au(110) at room temperature and subsequently annealed. Figure 4.18(a) shows Br 3d core level photoemission spectra for a coverage of approximately 0.6 ML. There is only one doublet present on deposition, with a $3d_{5/2}$ binding energy of 69.7 eV, and a spin-orbit splitting of 1.0 eV. After annealing at 120 °C, a component with a $3d_{5/2}$ binding energy

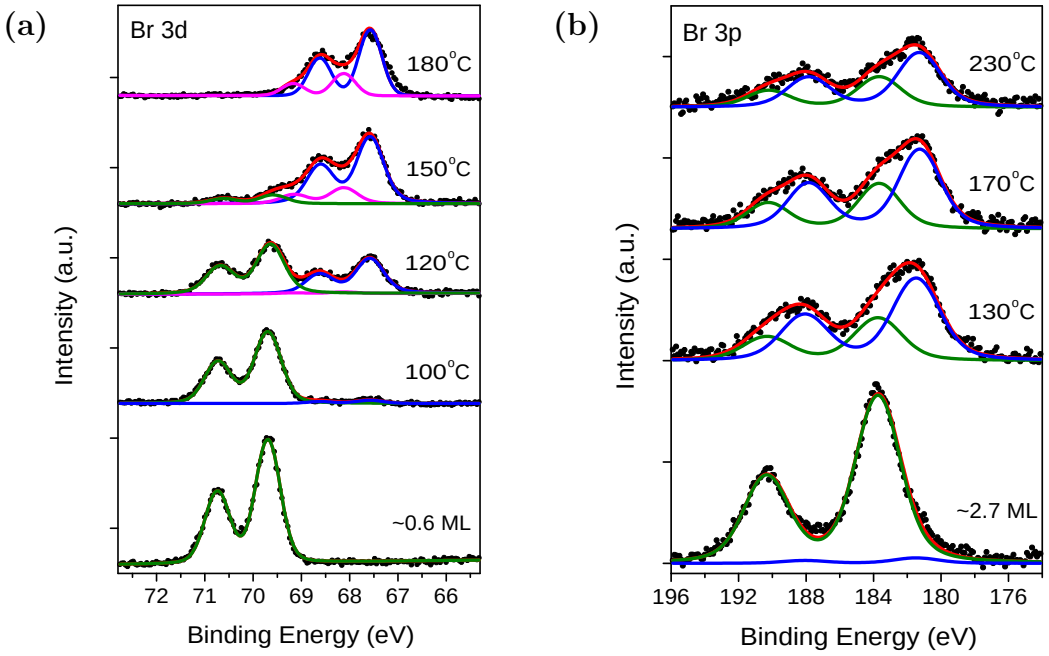

Figure 4.18: PES and XPS for TBB deposited on room temperature Au(110) and subsequently annealed at temperatures shown. (a) PES for Br 3d region, hν = 170.0 eV, (b) XPS for Br 3p region, hν = 1486.7 eV. (a) corresponds to a surface with a 0.6 ML coverage, (b) corresponds to a differently prepared surface with a 2.7 ML coverage.

of 67.6 eV, and a spin-orbit splitting of 1.0 eV accounts for approximately 40 % of the total Br signal and is assigned, as before, to bromine dissociated from the TBB molecule. As the sample is annealed to higher temperatures, the doublet at 69.7 eV binding energy decreases in intensity and is no longer present after annealing at 180 °C. In addition to the doublet at 67.6 eV binding energy there is a doublet with a $3d_{5/2}$ binding energy of 68.1 eV, and a spin-orbit splitting of 1.0 eV, indicating that the dissociated bromine is present on the surface in two chemical environments, as seen previously on Au(111) (Figure 4.6) and discussed above. Figure 4.18(b) shows Br 3p core level x-ray photoelectron spectra recorded after deposition of 2.7 ML of TBB. On deposition, approximately 97 % of the total Br signal is accounted for by a Voigt doublet with a $3p_{3/2}$ binding energy of 183.8 eV, and a spin-orbit splitting of 6.6 eV, assigned to bromine in the first and subsequent deposited layers which has not dissociated from the molecule.

The resolution is not sufficient to distinguish between bromine in the first layer which is interacting with the substrate, and bromine in subsequent layers which is not affected by the substrate. Following annealing of the sample, an additional doublet with a $3p_{3/2}$ binding energy of 181.5 eV, and a spin-orbit splitting of 6.6 eV is observed, which is assigned to bromine which has dissociated from the TBB. The two separate chemical environments for dissociated bromine seen in Figure 4.18(a) cannot be resolved in the XPS data. After annealing at 230 °C the doublet at 183.8 eV binding energy accounts for 35 % of the total Br signal, in contrast to Figure 4.18(a) where all remaining bromine has dissociated from the TBB molecules at 180 °C. This difference may be due to the higher initial coverage in Figure 4.18(b).

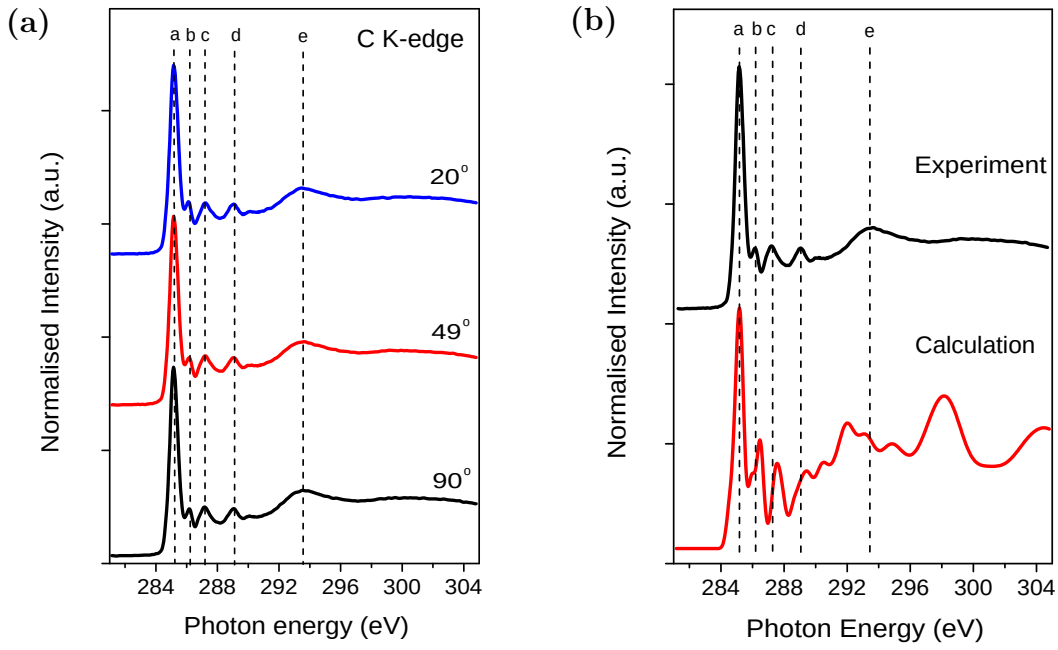

Figure 4.19: (a) C K-edge XAS for 15 ML of TBB deposited on room temperature Au(110). Spectra recorded at three different angles of incidence of the synchrotron radiation. (b) The experimental data recorded at 49° plotted with the calculated spectrum for a disordered layer. Refer to Table 4.1 for assignments.

Figure 4.19(a) shows XA spectra for 15 ML of TBB deposited on Au(110) at room temperature, recorded at three different angles of incidence. The absorption lines appear at the same photon energies recorded for TBB on the Au(111) surface (Figure 4.7), and are assigned as in Table 4.1. The relative intensity of the absorption lines do not vary with the angle of incidence, indicating that the molecules are completely disordered at this coverage. Figure 4.19(b) shows the experimental spectrum recorded at $\theta = 49°$ plotted with a calculated spectrum corresponding to an isotropic distribution of molecular orientations. This spectrum is the weighted sum of the calculated *s*- and *p*-polarised spectra shown in Figure 4.8, where the *s* and *p* contributions are combined in the ratio 2:1. The correspondence between the experimental and calculated spectra confirm that the molecular layer is completely disordered.

Figure 4.20 shows C K-edge XAS measured after annealing the 15 ML coverage at 115 °C; approximately 10 ML of TBB remain on the surface, as indicated by the corresponding C 1s core level PES data. There is now a difference in the

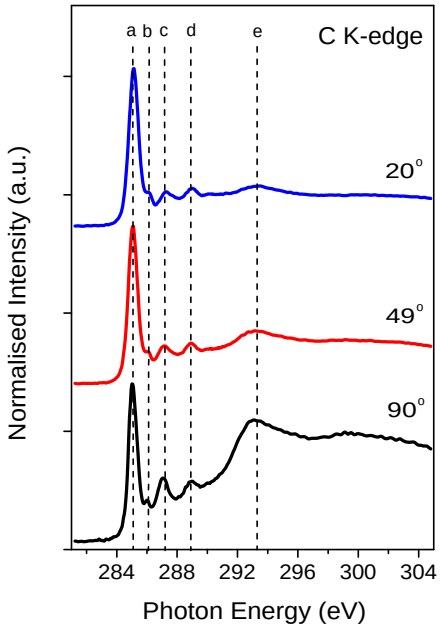

Figure 4.20: C K-edge XAS for 15 ML of TBB deposited on room temperature Au(110) (Figure 4.19(a)) and subsequently annealed at 115 °C. Spectra recorded at different values of θ. Refer to Table 4.1 for assignments.

intensities of the absorption lines for the three angles of incidence, indicating that the molecular layer has been ordered by the annealing process. The relative intensity of the absorption line at 285.0 eV, assigned to transitions to π^* states (Table 4.1), is greater at grazing incidence than normal incidence, indicating that the TBB molecules are oriented at a certain angle with respect to the substrate. The angle cannot be calculated using the analysis method of Stöhr and Outka [13]; for surfaces with two-fold symmetry, the azimuthal orientation of the molecules must be known for this type of analysis to be carried out.

4.3.2 C_{60} Deposition on a Self-Assembled TBB Monolayer on Room Temperature Au(110)

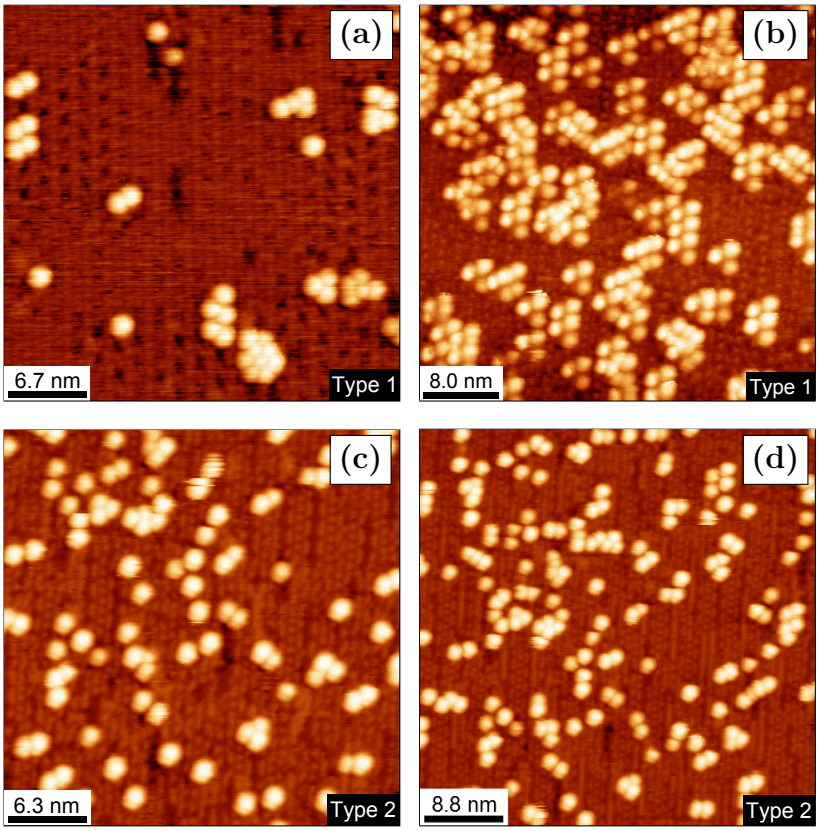

Figure 4.21: STM for C_{60} deposited on a monolayer TBB coverage on Au(110) at room temperature. Underlying TBB layer shows Type 1 ((a) and (b)) and Type 2 ((c) and (d)) packing. (a) (−0.66 V,0.54 nA), (b) (+1.05 V,0.53 nA), (c) (−0.84 V,0.61 nA), (d) (+0.84 V,0.60 nA). (a) - (d) show the same monolayer coverage of TBB molecules, with respective C_{60} coverages of 0.1 ML, 0.5 ML, 0.3 ML and 0.3 ML.

Figure 4.21(a) to (d) show STM images recorded after deposition of C_{60} molecules onto a self-assembled monolayer of TBB at room temperature, for respective C_{60} coverages of 0.1 ML, 0.5 ML, 0.3 ML and 0.3 ML. The underlying TBB layer displays Type 1 packing in Figure 4.21(a) and 4.21(b), and Type 2 packing in Figure 4.21(c) and 4.21(d). The ordering of the C_{60} layer is influenced by the packing of the TBB molecules, with the fullerenes deposited on Type 1 regions showing greater order than those deposited on Type 2 regions. This may be attributed to the regular pores of the Type 1 packing providing adsorption sites for the C_{60} molecules.

4.3.3 STM and Photoemission Study of TBB/Au(110) Deposited at Elevated Temperatures

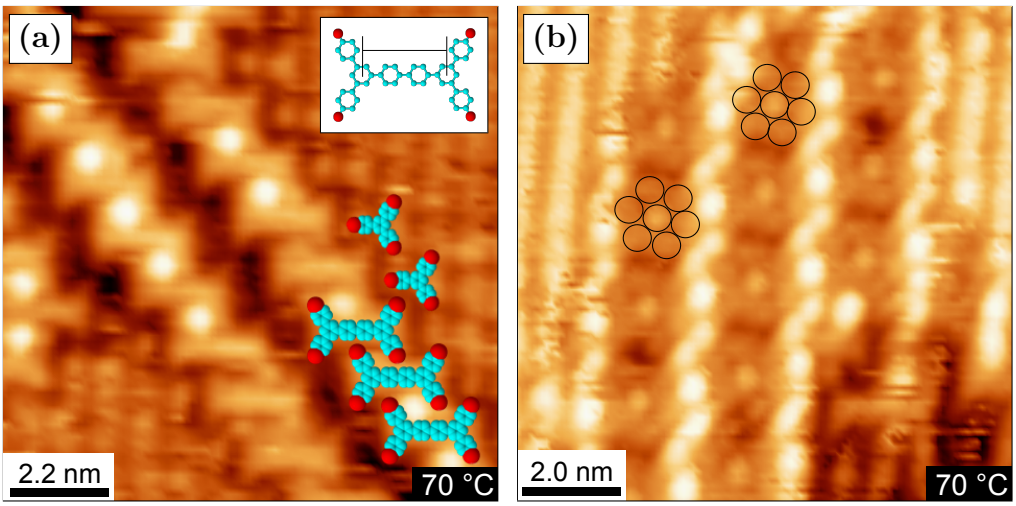

Figure 4.22: STM for TBB deposited on Au(110) with the substrate held at 70 °C. (a) (+1.29 V,0.34 nA), (b) (+1.71 V,1.55 nA). (a) and (b) show a surface with a 0.5 ML coverage.

Figure 4.22 shows STM images recorded after deposition of TBB molecules onto a Au(110) substrate held at 70 °C. Figure 4.22(a) shows rows of TBB dimers with single TBB molecules along the edge of the dimer rows. The length of the dimers, as shown in the inset, is measured as 1.33 ± 0.07 nm, in good agreement with the length of 1.39 nm predicted by Chemsketch [8]. Blunt *et al.* observed TBB dimers on Au(111) with experimental and calculated lengths of 1.29 ± 0.06 nm and 1.31 nm respectively [5].

Bright circular features are present between adjacent TBB dimers in both

Figure 4.22(a) and 4.22(b). The circular features in Figure 4.22(a) have a diameter of 0.66 ± 0.07 nm, while the circular features in Figure 4.22(b) have a diameter of 0.48 ± 0.04 nm and are arranged in groups of seven as indicated. The diameter of the features is sensitive to both the bias conditions at which the images were recorded, and the equalisation performed on the images afterwards. One explanation for these circular features is that they are bromine atoms dissociated from the TBB molecules but still present on the surface (Figure 4.18). The van der Waals diameter of bromine is 0.40 nm [21], in good agreement with the measured diameters of the circular features in Figure 4.22(b).

Figure 4.23(a) shows Br 3p core level XPS data recorded after deposition of TBB onto the Au(110) substrate held at various elevated temperatures. Each spectrum is decomposed into two Voigt line-shapes with $3p_{3/2}$ binding energies of

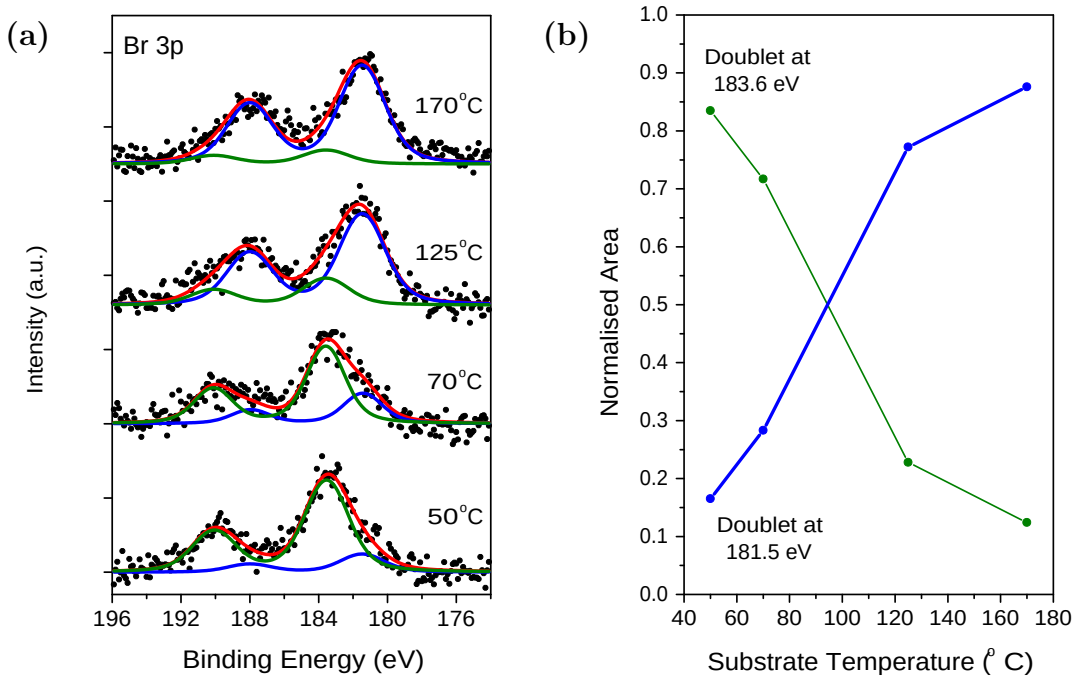

Figure 4.23: (a) XPS for TBB deposited on Au(110) held at 50 °C, 70 °C, 125 °C, and 170 °C. Br 3p region, hν = 1486.7 eV, (b) Normalised areas of doublets in (a) as a function of substrate temperature. The 50 °C, 70 °C, 125 °C, and 170 °C spectra in (a) correspond to four differently prepared surfaces, with coverages of 0.8 ML, 0.5 ML, 1 ML and 0.9 ML respectively. The 70 °C spectrum corresponds to the surface shown in Figure 4.22.

181.5 eV and 183.6 eV respectively, and a spin-orbit splitting of 6.5 eV. As above, these components are assigned to dissociated Br and bromine bonded to the TBB molecules respectively. The relative intensity of the doublets changes as a function of substrate temperature during deposition, as shown in Figure 4.23(b). For deposition onto the substrate held at 70 °C, approximately 30 % of the total Br signal is accounted for by dissociated bromine, which may be present on the surface as the bright circular features observed in the STM images shown in Figure 4.22.

In summary, TBB deposited on both 2×1 and 3×1 reconstructed Au(110) exhibits four separate types of molecular packing (Figures 4.15 and 4.16). Covalently bonded TBB chains and partial hexagonal pores are formed after annealing at 130 °C and higher, with the movement of the Au atoms at these temperatures inhibiting the formation of larger networks (Figure 4.17). For a 15 ML coverage, the TBB molecules are completely disordered on the Au(110) surface (Figure 4.19). 5 ML of TBB are desorbed after annealing at 115 °C, with the remaining molecules forming an ordered layer as seen from the angle dependent XA spectra (Figure 4.20). The order of a deposited layer of C_{60} is influenced by the packing of the underlying TBB monolayer, with Type 1 packing inducing greater order in the C_{60} overlayer than Type 2 packing.

4.4 STM and Photoemission Study of TBB on the Cu(111) Surface

4.4.1 Analysis for Deposition at Room Temperature

TBB has been deposited on Cu(111) by Gutzler *et al.* [1, 2]. It was found that C-Br bond scission occurred at room temperature, due to the reactive Cu surface. The TBB molecules were coordinated by surface Cu atoms to form the protopolymer networks discussed previously [1–4]. Further thermal annealing led to the covalent bonding of the TBB molecules [1, 2].

Figure 4.24 shows STM images recorded after deposition of 0.3 ML of TBB onto the Cu(111) substrate at room temperature (4.24(a) and 4.24(b)) and subsequent annealing at 300 °C (4.24(c) and 4.24(d)). The average centre-to-centre distances of the hexagonal pores and adjacent TBB molecules are listed in Table 4.4, together with the corresponding values for Au(111) and Au(110), and values in the literature [1, 2]. Figure 4.24(a) and 4.24(b) show that

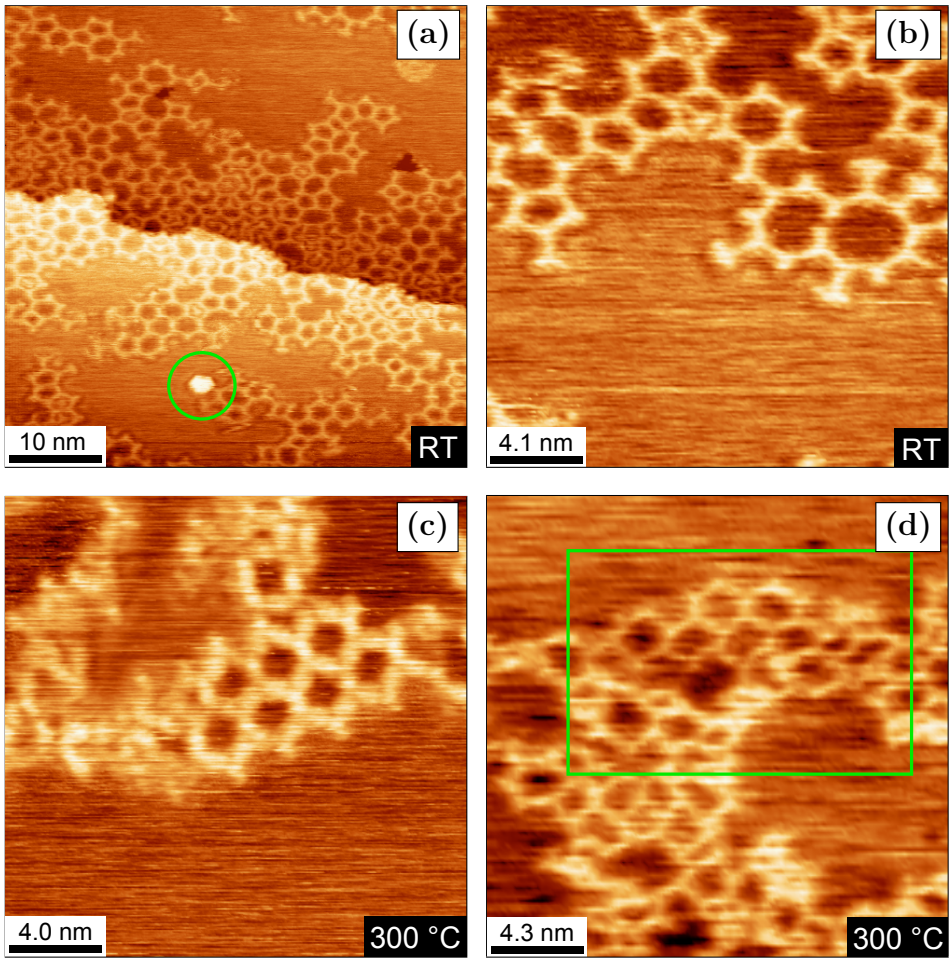

Figure 4.24: STM for TBB on Cu(111), room temperature deposition ((a) and (b)) followed by annealing at 300 °C ((c) and (d)). (a) (−1.45 V,0.37 nA), (b) (−1.45 V,0.37 nA), (c) (−1.01 V,0.34 nA), (d) (−1.00 V,1.00 nA). (a) - (d) show a surface with a 0.3 ML coverage.

TBB forms networks following deposition onto Cu(111) at room temperature; this is in contrast to the observed behaviour of TBB on the Au(111) and Au(110) surfaces described above. The measured centre-to-centre distance for adjacent TBB molecules on Cu(111) at room temperature is longer than that observed for covalently bonded networks on Au(111) and Au(110). Based on a comparison of the distances listed in Table 4.4, the molecules in the networks formed on Cu(111) are not covalently bonded but instead are coordinated by surface Cu atoms, forming the protopolymer networks discussed previously (Chapter 3) [1–4, 22]. Gutzler *et al.* have resolved the coordinating Cu atoms between TBB molecules in STM images of protopolymer networks [1]. While no linking Cu atoms are

Table 4.4: Centre-to-centre distances for hexagonal pores and adjacent TBB molecules on different substrates. Comparison with literature values for TBB molecules [1].

Substrate	Hexagonal Pore Centre-to-Centre Distance (nm)	TBB-TBB Centre-to-Centre Distance (nm)
Au(111) annealed (Figure 4.2 and 4.3)	2.20 ± 0.22	1.34 ± 0.17
Au(110) annealed (Figure 4.17)	—	1.40 ± 0.12
Cu(111) RT (Figure 4.24(a) and 4.24(b))	2.46 ± 0.28	1.57 ± 0.14
Cu(111) annealed (Figure 4.24(c) and 4.24(d))	2.30 ± 0.20	1.29 ± 0.26
Cu(111) RT [a]	—	1.49 ± 0.10
Cu(111) annealed [a]	2.2	1.24 ± 0.06

a = [1]

resolved in Figure 4.24(a) and 4.24(b), the centre-to-centre distance for adjacent TBB molecules of 1.57 ± 0.14 nm is in agreement with the average centre-to-centre distance for protopolymers of 1.49 ± 0.10 nm reported by Gutzler *et al.* [1].

Figure 4.24(c) and 4.24(d) show areas of hexagonal network formed after annealing the sample at 300 °C. The centre-to-centre distances for the hexagonal pores and adjacent TBB molecules, 2.30 ± 0.20 nm and 1.29 ± 0.26 nm respectively, are now in good agreement with the values for covalently bonded networks measured on Au(111) and Au(110) and reported by Gutzler [1] (Table 4.4). In addition, the centre-to-centre distance of 1.29 ± 0.26 nm for adjacent TBB molecules is in good agreement with the DFT calculation performed by Gutzler *et al.* which found a value of 1.28 nm for a covalently bonded network [1].

Figure 4.25 shows STM images recorded after the TBB nano-networks were annealed at 450 °C and 550 °C. In contrast to the Au(111), where intact networks

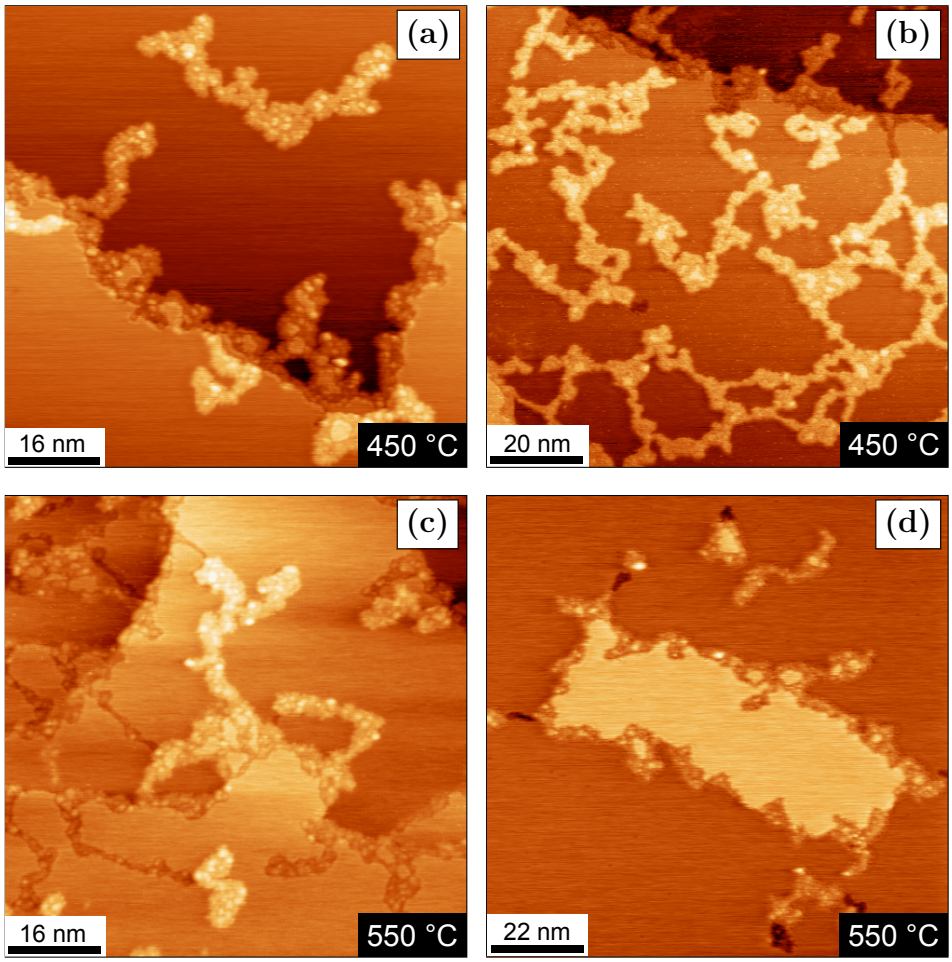

Figure 4.25: STM for TBB deposited on room temperature Cu(111) and annealed at 450 °C and 550 °C. (a) (−1.42 V,0.19 nA), (b) (−1.00 V,0.37 nA), (c) (+0.95 V,0.34 nA), (d) (+1.00 V,0.34 nA). (a) and (d) show a surface with a 0.2 ML coverage annealed at the temperatures shown, (b) and (c) show the surface with a 0.3 ML coverage (Figure 4.24) annealed at the temperatures shown.

were observed after annealing at 450 °C (Figure 4.4), the material on Cu(111) has agglomerated into large structures similar to those seen for H_2TBrPP on Cu(111) annealed at temperatures up to 520 °C (Section 3.4). The formation of islands is observed on the surface, as well as trenches originating from step edges (Figure 4.25). As before, these structures are respectively assigned to Cu adatom islands and trenches in the surface acting as sources of adatoms [23]. There is evidence for the formation of Cu adatom islands at room temperature, as the highlighted feature in Figure 4.24(a) has an appearance similar to Cu adatom islands observed on Ag(111) at room temperature [24]. The peripheral material

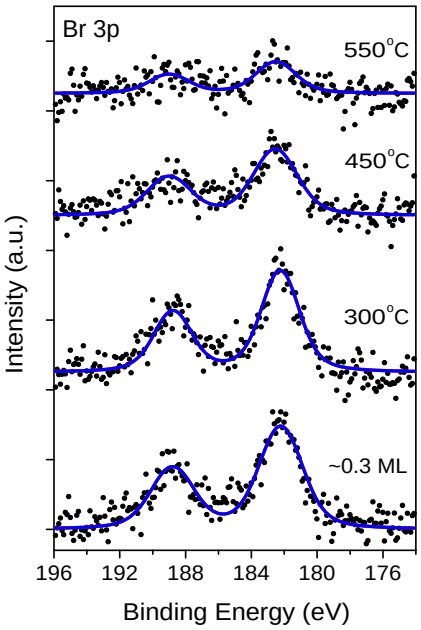

Figure 4.26: XPS for TBB deposited on room temperature Cu(111) and subsequently annealed at 300 °C, 450 °C and 550 °C. Br 3p region, hν = 1486.7 eV. Spectra correspond to the surface with a 0.3 ML coverage (Figures 4.24 and 4.25(b) and (c)).

around the adatom islands in Figure 4.25 is again assigned to decomposed molecules.

Figure 4.26 shows XPS data recorded after deposition of 0.3 ML of TBB onto Cu(111) at room temperature and subsequent annealing at 300 °C, 450 °C and 550 °C. The spectrum of the deposited layer is fitted with a single Voigt doublet at a $3p_{3/2}$ binding energy of 182.3 eV, and with a spin-orbit splitting of 6.6 eV, indicating that the bromine has dissociated from the TBB molecules on deposition, resulting in the formation of the protopolymers. The dissociated Br present after annealing the sample at 450 °C is approximately 65 % of the total Br signal present after deposition. There is a shift in binding energy of the $3p_{3/2}$ component to 182.6 eV after annealing at 450 °C, possibly relating to the formation of the larger structures seen in Figure 4.25. Approximately 30 % of the initial coverage of bromine remains after annealing at 550 °C.

In summary, TBB forms protopolymers coordinated by surface Cu atoms on room temperature Cu(111). These protopolymers are converted to covalently

bonded nano-networks after annealing at 300 °C (Figure 4.24). Annealing at 450 °C and 550 °C results in etching of the step edges and the growth of chain-like structures and islands on the surface (Figure 4.25), similar to those seen for H_2TBrPP on Cu(111) annealed at these temperatures. XPS data indicate that the bromine dissociates from the TBB molecules on deposition, and approximately 30 % of the initial bromine coverage is still present on the surface after annealing at 550 °C (Figure 4.26).

4.5 Summary

TBB is mobile on Au(111) at room temperature, precluding the recording of any STM images. After annealing at 190 °C and 300 °C, covalently bonded networks are formed which contain areas of hexagonal network. Approximately 25 % of the pores are hexagonal in shape. The networks are stable up to 450 °C, remaining intact on the surface. The dissociated bromine is present on the surface in two chemical environments. Analysis of XA spectra recorded at grazing and normal incidence indicate that the TBB molecules are oriented at $36 \pm 5^{\circ}$ with respect to the surface plane. The dissociation of bromine from the TBB molecules can also be observed in C K-edge XA spectra and C 1s core level photoemission spectra recorded as a function of temperature. For deposition onto the Au(111) substrate held at 140 °C, approximately 40 % of the bromine dissociates from the TBB molecules on deposition.

Four different types of molecular packing are observed for TBB on Au(110) at room temperature. TBB chains and incomplete hexagonal pores are formed after annealing at 130 °C, 200 °C and 220 °C. Analysis of grazing and normal incidence C K-edge XA spectra show that for a coverage of approximately 15 ML, the TBB molecules are completely disordered; following annealing at 115 °C, the angular dependence of the intensities of the absorption lines indicates that the molecules are now ordered. The ordering of C_{60} fullerenes deposited on a self-assembled TBB monolayer at room temperature is influenced by the molecular packing of the TBB, with fullerenes deposited on regions of Type 1 packing displaying a greater degree of order than those deposited on regions of Type 2 packing. TBB dimers are formed after deposition on the Au(110) substrate held at 70 °C, with bright circular features also in evidence which may be dissociated bromine atoms.

TBB forms Cu-coordinated protopolymers on room temperature Cu(111), as evidenced by the centre-to-centre distance for adjacent TBB molecules of 1.57 ± 0.14 nm which is longer than the analogous distance for covalently bonded

nano-networks on Au(111) and Au(110), and which agrees with literature values for TBB molecules exhibiting a C-Cu-C bond [1]. Covalently bonded networks are formed after annealing at 300 °C, indicated by the decreased centre-to-centre distance for both adjacent TBB molecules and hexagonal pores which agree with the values for nano-networks on the Au substrates. Annealing at 450 °C and 550 °C results in the formation of adatom islands and trenches in the surface, similar to those seen for H_2TBrPP on Cu(111) annealed at temperatures up to 520 °C.

4.6 Bibliography

[1] Gutzler, R., Walch, H., Eder, G., Kloft, S., Heckl, W.M., and Lackinger, M., *Surface mediated synthesis of 2D covalent organic frameworks: 1,3,5-tris(4-bromophenyl)benzene on graphite(001), Cu(111), and Ag(110)*, Chemical Communications, 29 (2009) pp. 4456–4458.

[2] Walch, H., Gutzler, R., Sirtl, T., Eder, G., and Lackinger, M., *Material- and Orientation-Dependent Reactivity for Heterogeneously Catalyzed Carbon-Bromine Bond Homolysis*, Journal of Physical Chemistry C, **114** (2010) pp. 12604–12609.

[3] Lipton-Duffin, J.A., Ivasenko, O., Perepichka, D.F., and Rosei, F., *Synthesis of Polyphenylene Molecular Wires by Surface-Confined Polymerization*, Small, **5** (2009) pp. 592–597.

[4] McCarty, G.S. and Weiss, P.S., *Formation and manipulation of protopolymer chains*, Journal of the American Chemical Society, **126** (2004) pp. 16772–16776.

[5] Blunt, M.O., Russell, J.C., Champness, N.R., and Beton, P.H., *Templating molecular adsorption using a covalent organic framework*, Chemical Communications, **46** (2010) pp. 7157–7159.

[6] Russell, J.C., Blunt, M.O., Garfitt, J.M., Scurr, D.J., Alexander, M., Champness, N.R., and Beton, P.H., *Dimerization of Tri(4-bromophenyl)benzene by Aryl-Aryl Coupling from Solution on a Gold Surface*, Journal of the American Chemical Society, **133** (2011) pp. 4220–4223.

[7] Baris, B., Luzet, V., Duverger, E., Sonnet, P., Palmino, F., and Cherioux, F., *Robust and Open Tailored Supramolecular Networks Controlled by the Template Effect of a Silicon Surface*, Angewandte Chemie International Edition, **50** (2011) pp. 4094–4098.

[8] *ACD/ChemSketch*, URL `www.acdlabs.com/resources/freeware/chemsketch/`, accessed July 2013.

[9] Lee, A.F., Chang, Z., Hackett, S.F.J., Newman, A.D., and Wilson, K., *Hydrodebromination of bromobenzene over Pt(111)*, Journal of Physical Chemistry C, **111** (2007) pp. 10455–10460.

[10] Yang, M.X., Xi, M., Yuan, H.J., Bent, B.E., Stevens, P., and White, J.M., *NEXAFS Studies of Halobenzenes and Phenyl Groups on Cu(111)*, Surface Science, **341** (1995) pp. 9–18.

[11] Holland, B.N., Peltekis, N., Farrelly, T., Wilks, R.G., Gavrila, G., Zahn, D.R.T., McGuinness, C., and McGovern, I.T., *NEXAFS studies of copper phthalocyanine on Ge(001)-2 x 1 and Ge(111)-c(2 x 8) surfaces*, Physica Status Solidi B - Basic Solid State Physics, **246** (2009) pp. 1546–1551.

[12] McGuinness, C., private communication, 2013.

[13] Stohr, J. and Outka, D.A., *Determination of Molecular Orientations on Surfaces from the Angular-Dependence of Near-Edge X-Ray-Absorption Fine-Structure Spectra*, Physical Review B, **36** (1987) pp. 7891–7905.

[14] Stohr, J., NEXAFS Spectroscopy, 2nd ed., Springer-Verlag, Heidelberg, 1996.

[15] Solomon, J.L., Madix, R.J., and Stohr, J., *Orientation and Absolute Coverage of Benzene, Aniline, and Phenol on Ag(110) Determined by NEXAFS and XPS*, Surface Science, **255** (1991) pp. 12–30.

[16] Hermann, K., et al., StoBe-deMon version 3.0. 2008.

[17] Bjork, J., Hanke, F., and Stafstrom, S., *Mechanisms of Halogen-Based Covalent Self-Assembly on Metal Surfaces*, Journal of the American Chemical Society, **135** (2013) pp. 5768–5775.

[18] Resta, A., Felici, R., Kumar, M., and Pedio, M., *Ni and Cu octaethyl porphyrins ordered monolayer on Au(111) surfaces*, Journal of Non-Crystalline Solids, **356** (2010) pp. 1951–1954.

[19] Sohn, Y., Wei, W., and White, J.M., *1-phenyl-1-propyne on Cu(111): TOFMS TPD, XPS, UPS, and 2PPE studies*, Langmuir, **23** (2007) pp. 12185–12191.

[20] Maxwell, A.J., Bruehwiler, P.A., Nilsson, A., Martensson, N., and Rudolf, P., *Photoemission, Autoionization, and X-Ray-Absorption Spectroscopy of Ultrathin-Film C_{60} on Au(110)*, Physical Review B, **49** (1994) pp. 10717–10725.

[21] Jones, R.G. and Kadodwala, M., *Bromine adsorption on Cu(111)*, Surface Science, **370** (1997) pp. L219–L225.

[22] Wang, W., Shi, X., Wang, S., Van Hove, M.A., and Lin, N., *Single-Molecule Resolution of an Organometallic Intermediate in a Surface-Supported Ullmann Coupling Reaction*, Journal of the American Chemical Society, **133** (2011) pp. 13264–13267.

[23] Pai, W.W., Bartelt, N.C., Peng, M.R., and Reuttrobey, J.E., *Steps as Adatom Sources for Surface-Chemistry - Oxygen Overlayer Formation on Ag(110)*, Surface Science, **330** (1995) pp. L679–L685.

[24] Lin, N., Payer, D., Dmitriev, A., Strunskus, T., Woell, C., Barth, J.V., and Kern, K., *Two-dimensional adatom gas bestowing dynamic heterogeneity on surfaces*, Angewandte Chemie International Edition, **44** (2005) pp. 1488–1491.

Chapter 5
Structural and Electronic Properties of Brominated Two-fold Symmetrical Porphyrin Molecules on Metal Surfaces

5.1 Introduction

The previous chapters have described the formation of covalently bonded networks for molecules of four-fold and three-fold symmetry. The same bonding strategy (Figure 1.2) can be applied to two-fold brominated molecules, to form nano-lines on the surface.

The formation of nano-lines via radical addition following dehalogenation of organic molecules has been studied on surfaces. Lipton-Duffin *et al.* [1] have grown polyphenylene lines on the Cu(110) surface, using the reactivity of the Cu surface to catalytically cleave the C-I bonds, leading to the formation of protopolymer structures coordinated by surface Cu atoms. These protopolymers can be subsequently converted to covalently bonded structures [2–4]. Grill *et al.* have studied the formation of porphyrin nano-lines as a precursor to network formation, using porphyrin molecules functionalised with bromine and iodine [5]. The porphyrin molecules can be dehalogenated in a step-wise fashion by thermal annealing, leading to the formation of covalently bonded nano-lines [5].

This chapter investigates the self-assembly, ordering and chemical interactions of Ni(II) 5,15-dibromo-10,20-diphenyl porphyrin (NiDBrDPP) on the Au(111), Au(110), Ag(111) and Cu(111) metal surfaces, using STM and XPS. In addition, a LEED study of ordered nano-lines on the Au(110) surface is carried out, and includes a comparison of a simulated LEED pattern with experimental data.

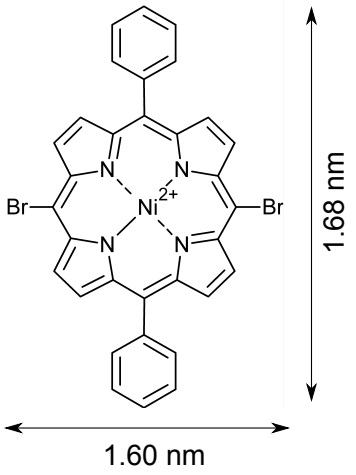

Figure 5.1: Structure of NiDBrDPP ($C_{32}H_{18}N_4NiBr_2$), nominal dimensions determined from ChemSketch [6]. Hydrogen atoms not explicitly shown.

5.2 STM and Photoemission Study of NiDBrDPP on the Au(111) Surface

5.2.1 Analysis for Deposition at Room Temperature

A 1 ML coverage of NiDBrDPP was deposited on the Au(111) $22 \times \sqrt{3}$ surface at room temperature. Six different molecular packing configurations were observed; Figure 5.2 shows STM images of these packing configurations, along with the unit cells and overlaid molecular models to illustrate the orientation of the NiDBrDPP molecules. The unit cell parameters are given in Table 5.1, and were determined by analysing approximately one hundred unit cells for each packing configuration. The $22 \times \sqrt{3}$ reconstruction of the underlying Au(111) substrate [7, 8] has not been lifted by the NiDBrDPP molecules (Figure 5.2(a)).

Figures 5.3 and 5.4 show additional STM images recorded for the 1 ML coverage of NiDBrDPP on room temperature Au(111). Three domains of Type 3 packing are shown in Figure 5.3(a), oriented at 120° to each other. This orientation suggests that the adsorption of the NiDBrDPP molecules is influenced by the [110] directions of the Au(111) substrate. Figure 5.3(b) shows an enlarged view of the area highlighted with a green square in Figure 5.3(a), where further examples of the 2×1 reconstruction discussed previously (Section 3.2) are observed. The reconstruction has a periodicity of 0.49 ± 0.01 nm in the 2×

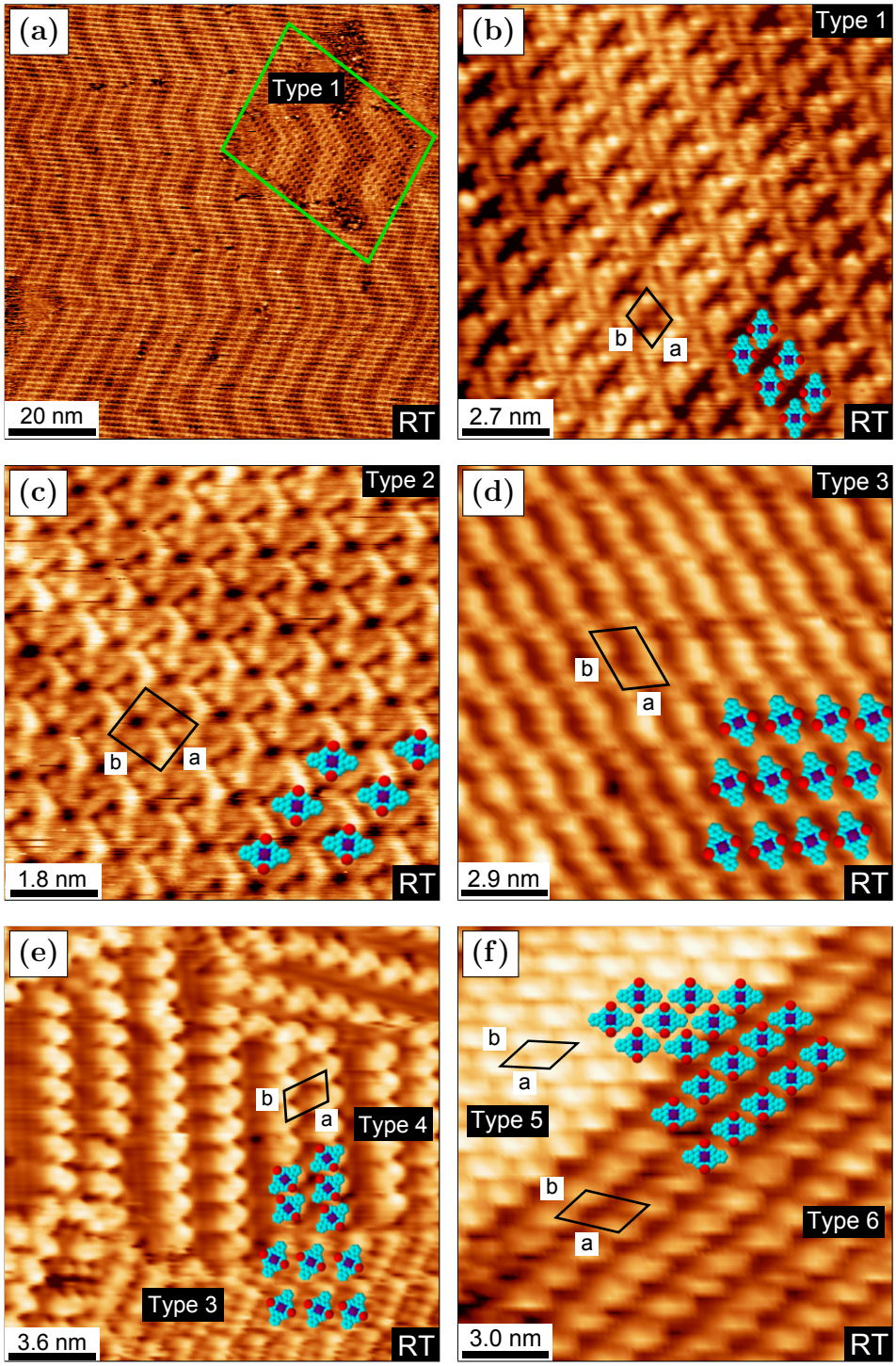

Figure 5.2: STM for 1 ML of NiDBrDPP deposited on room temperature Au(111). (a) (+1.54 V,0.41 nA), (b) (+1.54 V,0.35 nA), (c) (+1.54 V,0.24 nA), (d) (+0.95 V,0.25 nA), (e) (+1.21 V,0.26 nA), (f) (+0.95 V,0.25 nA). (a) - (f) show the same surface.

Table 5.1: Length of unit cell vectors and angle between vectors for different molecular packing configurations of NiDBrDPP on room temperature Au(111) shown in Figure 5.2.

Packing	a (nm)	b (nm)	θ (°)
Type 1	1.02 ± 0.06	1.28 ± 0.01	80.3 ± 4.8
Type 2	1.14 ± 0.04	1.30 ± 0.01	93.2 ± 3.3
Type 3	1.50 ± 0.02	2.41 ± 0.03	116.1 ± 3.9
Type 4	1.98 ± 0.08	1.21 ± 0.02	65.9 ± 2.3
Type 5	1.77 ± 0.05	1.19 ± 0.04	41.5 ± 2.7
Type 6	2.13 ± 0.16	1.28 ± 0.03	51.6 ± 4.1

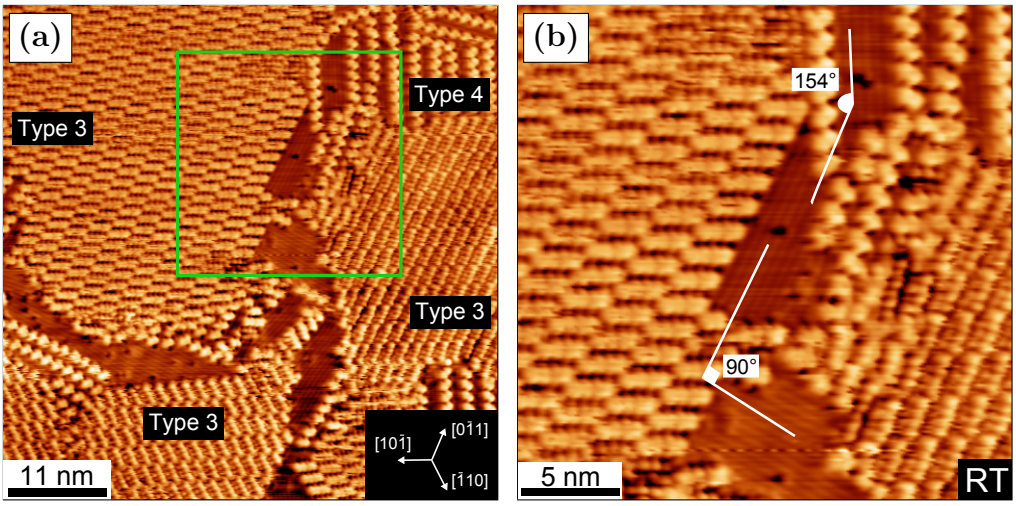

Figure 5.3: STM for 1 ML of NiDBrDPP deposited on room temperature Au(111). (+1.21 V,0.26 nA), (b) shows the area in (a) highlighted with a green square. The surface is the same as that shown in Figure 5.2.

direction. Three domains of the 2×1 reconstruction are observed, at orientations of $90 \pm 2°$ and $154 \pm 2°$ to each other. The fact that these 2×1 domains are not oriented at 120° to each other implies that they are not influenced by the underlying substrate.

STM images indicate that the NiDBrDPP molecules can change their local packing arrangement, either spontaneously or under the influence of the scanning tip. Figure 5.4(a) and 5.4(b) show the same region of the surface, imaged over

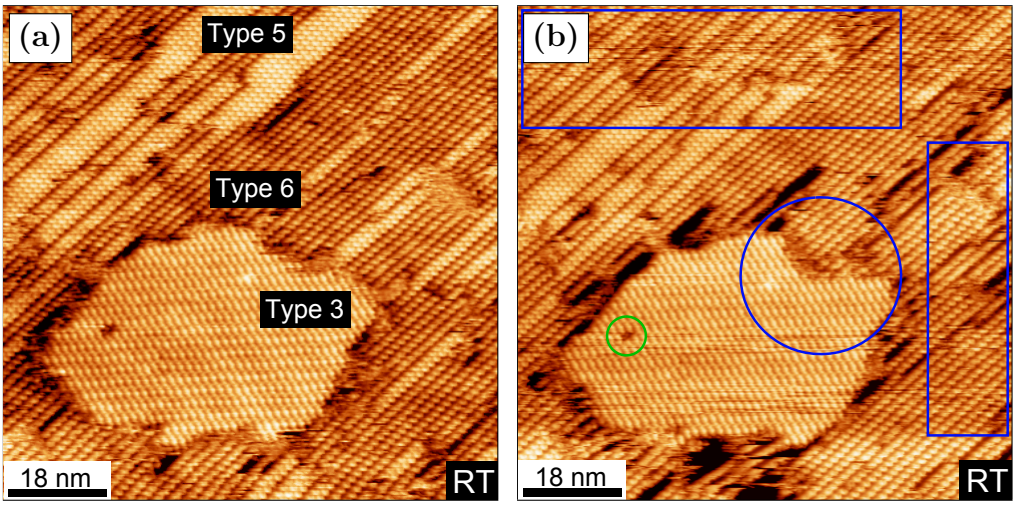

Figure 5.4: STM for 1 ML of NiDBrDPP deposited on room temperature Au(111). (+0.95 V,0.25 nA), (a) and (b) show the same region imaged three minutes apart. The green circle in (b) highlights a defect also visible in (a), while the blue circle and rectangles in (b) indicate areas where the molecular packing has changed. The surface is the same as that shown in Figure 5.2 and Figure 5.3.

a period of three minutes. A NiDBrDPP island of Type 3 packing, adjacent to domains exhibiting Type 5 and Type 6 packing, is observed in Figure 5.4(a). Changes in the molecular packing in Figure 5.4(b) are highlighted with blue rectangles. The defect in the island of Type 3 packing, present in both images and highlighted in Figure 5.4(b) with a green circle, confirms that each STM image shows the same region of the surface.

Figure 5.5 show STM images recorded after annealing at 170 °C, resulting in the formation of covalently bonded NiDBrDPP nano-lines. The centre-to-centre distance along the nano-lines is 1.13 ± 0.06 nm, calculated by analysing the mean value along the length of each nano-line and averaging over several nano-lines. The molecules in adjacent nano-lines are offset from each other by 0.45 ± 0.07 nm in the direction of the nano-line, which corresponds to 40 % of the centre-to-centre distance. The majority of the nano-lines lie approximately parallel to each other in straight lines; however curvature of the nano-lines is observed in some regions, as seen in the right hand side of Figure 5.5(a). The fact that the nano-lines can curve while remaining connected confirms that they are covalently bonded.

Figure 5.6 shows a further example of the 2×1 reconstruction discussed earlier (Section 3.2). The periodicity in the 2× direction is 0.48 ± 0.01 nm. As before, the

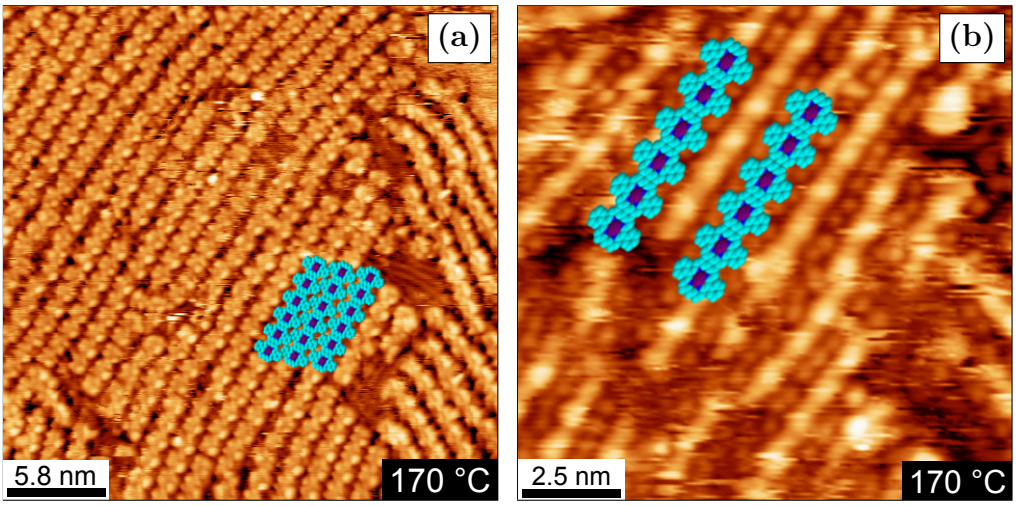

Figure 5.5: STM for 0.7 ML of NiDBrDPP deposited on room temperature Au(111) and subsequently annealed at 170 °C. (a) (+1.24 V,0.31 nA), (b) (+1.24 V,0.64 nA). (a) and (b) show the same surface.

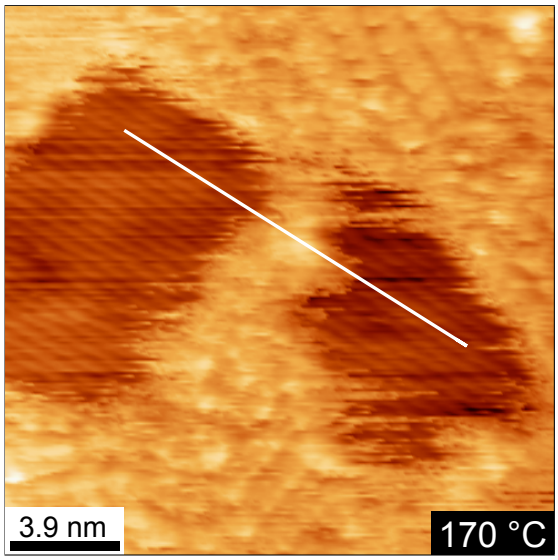

Figure 5.6: STM for NiDBrDPP deposited on room temperature Au(111) and subsequently annealed at 170 °C. Region of surface with 2×1 structure. (+0.95 V,0.54 nA). White line demonstrates continuity of 2×1 reconstruction. The surface is the same as that shown in Figure 5.5.

2×1 reconstruction is observed for a region of the surface enclosed by molecules. However in this case, the 2×1 reconstruction is shown to be continuous on either side of a NiDBrDPP molecular structure, confirming that the reconstruction is a real surface feature, rather than a tip effect.

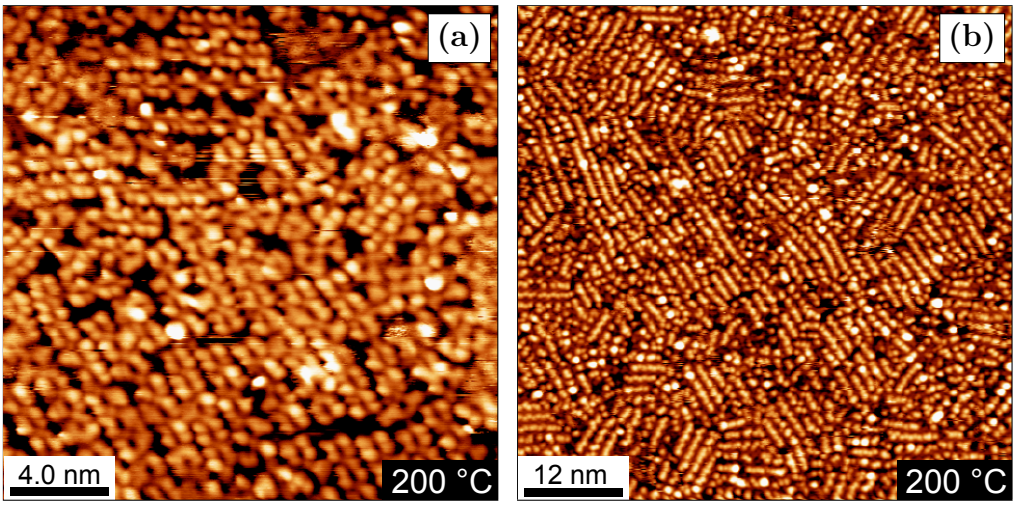

Figure 5.7: STM for 1 ML of NiDBrDPP deposited on room temperature Au(111) and subsequently annealed at 200 °C. (a) (+1.37 V,0.20 nA), (b) (−1.21 V,0.28 nA). (a) and (b) show the same surface.

Figure 5.7 shows STM images recorded after annealing a NiDBrDPP/Au(111) surface at 200 °C. Nano-lines are present on the surface, together with areas of disordered NiDBrDPP molecules. The nano-lines are shorter and more fragmented than those imaged after annealing at 170 °C (Figure 5.5). A region of the surface featuring nano-lines oriented in different directions is shown in Figure 5.7(b).

Figure 5.8 shows Br 3p core level XPS data recorded after deposition of NiDBrDPP on the Au(111) $22\times\sqrt{3}$ surface at room temperature. Figure 5.8(a) shows XPS data recorded after an initial deposition of 2 ML, and a subsequent deposition of an additional 3 ML. The 5 ML coverage of NiDBrDPP was then annealed at 150 °C. The spectra were fitted with two Voigt doublets at $3p_{3/2}$ binding energies of 181.5 eV and 183.6 eV respectively, with a spin-orbit splitting of 6.5 eV. These components are assigned to dissociated Br and bromine that remains bonded to the NiDBrDPP macrocycle respectively. Dissociated Br accounts for 16 % and 12 % of the Br signal for the coverages of 2 ML and 5 ML respectively. After annealing the 5 ML coverage at 150 °C, the intensity of the component at 183.6 eV binding energy decreases by a factor of two, while the corresponding C 1s core level XPS spectra show that the carbon signal decreases by a factor of 1.4. Hence some NiDBrDPP molecules are desorbed during the anneal, with additional Br dissociated from the molecules. As the total Br signal

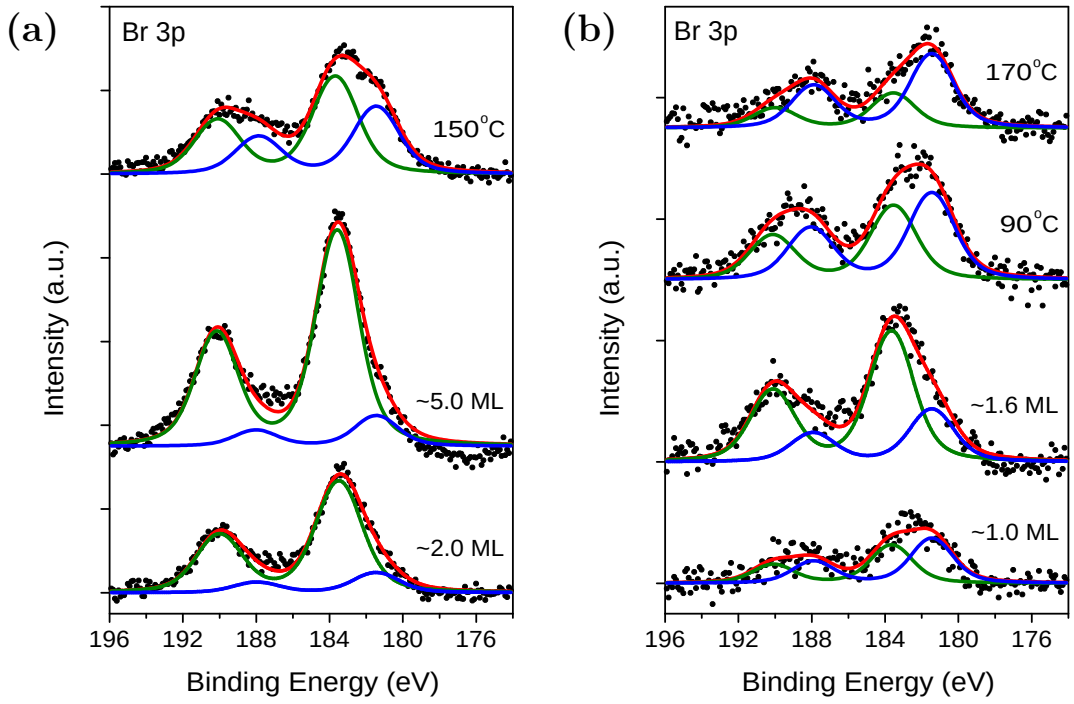

Figure 5.8: XPS for NiDBrDPP deposited on room temperature Au(111) and subsequently annealed at the temperatures indicated in the figure. Br 3p region, hν = 1486.7 eV. Spectra in (a) measured following an initial deposition of 2 ML, an additional deposition of 3 ML and subsequent annealing at 150 °C. Spectra in (b) measured after an initial deposition of 1 ML, an additional deposition of 0.6 ML and subsequent annealing at 90 °C and 170 °C.

decreases by a factor of 1.3, this indicates that not all of the Br dissociated during the anneal is desorbed from the surface.

Figure 5.8(b) shows Br 3p core level XPS spectra recorded after an initial deposition of 1 ML of NiDBrDPP, and a subsequent deposition of an additional 0.6 ML. The 1.6 ML coverage was then annealed at 90 °C and 170 °C. The spectra were again fitted with two Voigt doublets at $3p_{3/2}$ binding energies of 181.5 eV and 183.6 eV respectively, with a spin-orbit splitting of 6.5 eV, which are assigned as discussed above. The dissociated Br component at 181.5 eV binding energy accounts for 54 % and 28 % of the total Br signal for the 1 ML and 1.6 ML coverages respectively. After annealing at 90 °C and then 170 °C, the component at high binding energy preferentially desorbs, with the dissociated Br accounting for 70 % of the Br signal.

5.2.2 STM and Photoemission Study of NiDBrDPP/Au(111) Deposited at Elevated Temperatures

NiDBrDPP nano-line formation was studied for deposition onto the hot Au(111) $22 \times \sqrt{3}$ surface. Figure 5.9 shows Br 3p and C 1s core level XPS data recorded after three successive depositions onto the Au(111) surface held at 200 °C. Figure 5.9(a) shows that none of the depositions resulted in any significant amounts of bromine being deposited on the surface, indicating that the bromine-carbon bond thermally dissociates once the molecule makes contact with the hot surface. The corresponding C 1s XPS data shown in Figure 5.9(b) have been fitted with a single Voigt line-shape with a binding energy of 284.3 eV. As expected, the carbon signal increases with each deposition, confirming that material is being deposited onto the Au(111) surface.

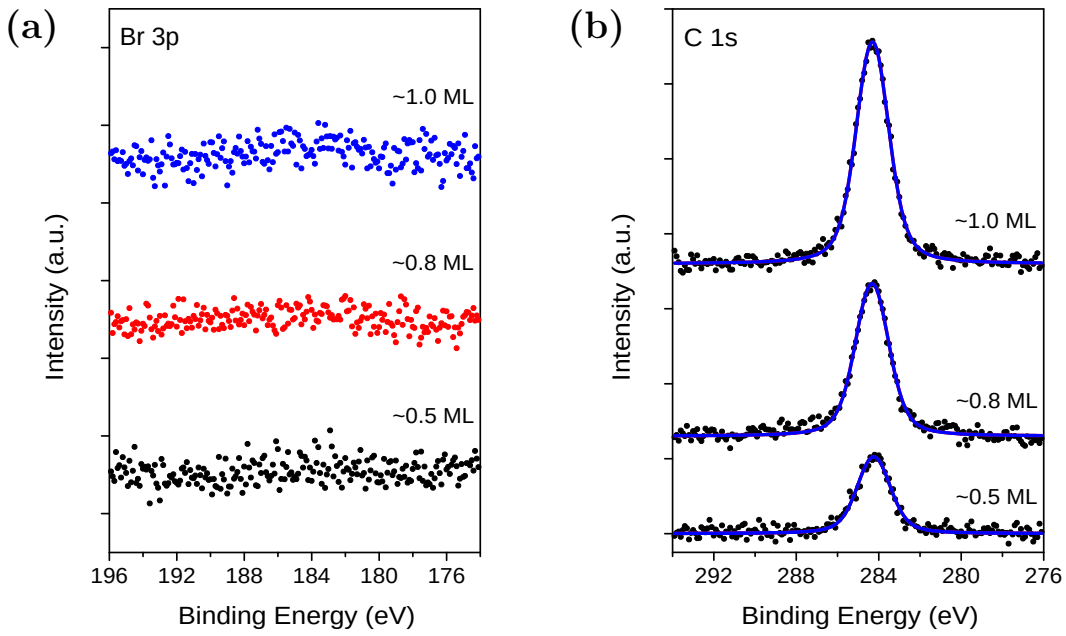

Figure 5.9: XPS for three successive depositions of NiDBrDPP on Au(111) held at 200 °C. hν = 1486.7 eV. (a) Br 3p region, (b) C 1s region. Spectra in (a) and (b) measured after an initial deposition of 0.5 ML followed by two additional depositions of 0.3 ML and 0.2 ML respectively.

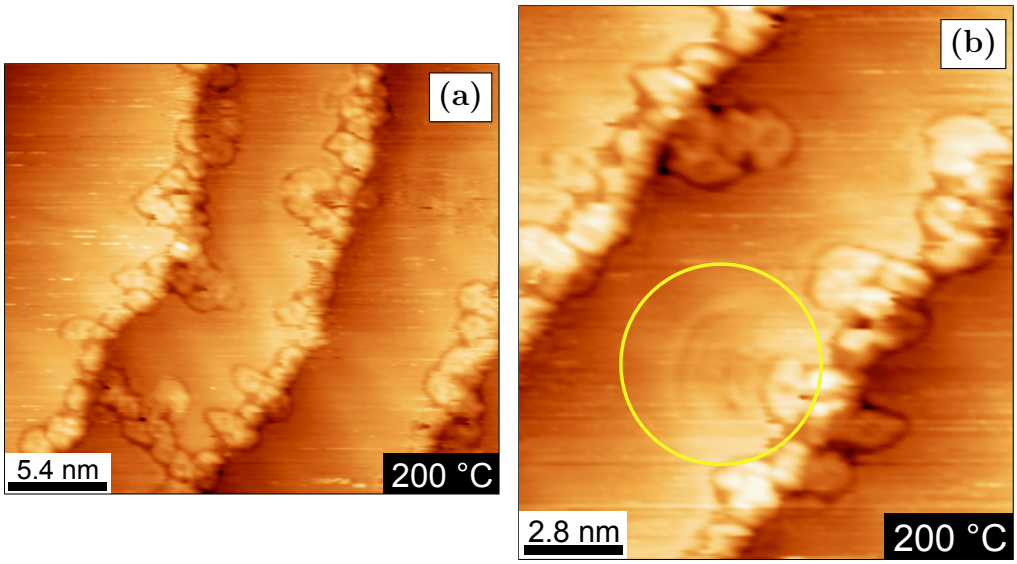

Figure 5.10: STM for 0.5 ML of NiDBrDPP deposited on Au(111) held at 200 °C. (−1.03 V,1.17 nA), (a) 27.1 nm × 23.6 nm, (b) 13.9 nm × 15.5 nm. (a) and (b) measured from the same surface as the 0.5 ML spectra in Figure 5.9.

Figure 5.10(a) and 5.10(b) show STM images recorded after the deposition of 0.5 ML of NiDBrDPP onto the Au(111) substrate held at 200 °C. At this coverage the molecules decorate the step edges, with very little coverage on the steps themselves.

The NiDBrDPP molecules have formed short covalently bonded chains (Figure 5.10(a)), with one chain extending across a terrace to link molecules on two adjacent steps. Figure 5.10(b) shows a molecule oscillating on the step (highlighted by a yellow circle). The path of the oscillation visible in the image suggests that the NiDBrDPP molecule is anchored to the molecules on the step edge at a former bromine site, and is oscillating around this fixed point.

Figure 5.11 shows STM images recorded after the second successive deposition of NiDBrDPP onto the Au(111) substrate held at 200 °C, resulting in a coverage of 0.8 ML. The porphyrin molecules have formed covalently bonded nano-lines along step edges and on the terraces. Figure 5.11(b) shows an enlarged view of the nano-lines on the terrace. The nano-lines are straight and parallel, and do not display any of the curvature noted in the nano-lines formed after room temperature deposition and subsequent annealing to 170 °C (Figure 5.5). They are aligned so that the phenyl rings of one nano-line can fit between the phenyl rings of adjacent nano-lines, as shown by the overlaid molecular

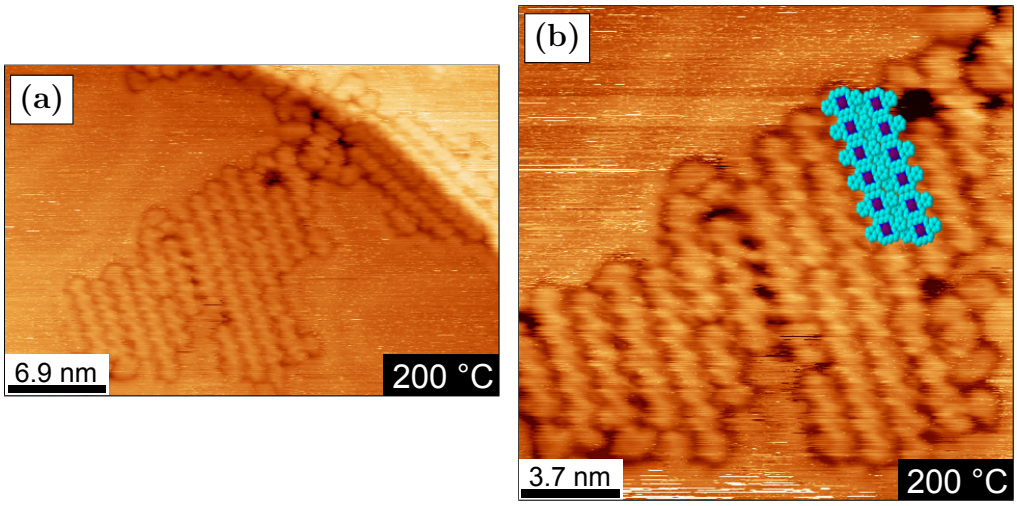

Figure 5.11: STM for 0.8 ML of NiDBrDPP deposited on Au(111) held at 200 °C. (a) (−1.07 V,0.29 nA), 34.6 nm × 23.1 nm, (b) (−1.07 V,0.20 nA). (a) and (b) measured from the same surface as the 0.8 ML spectra in Figure 5.9.

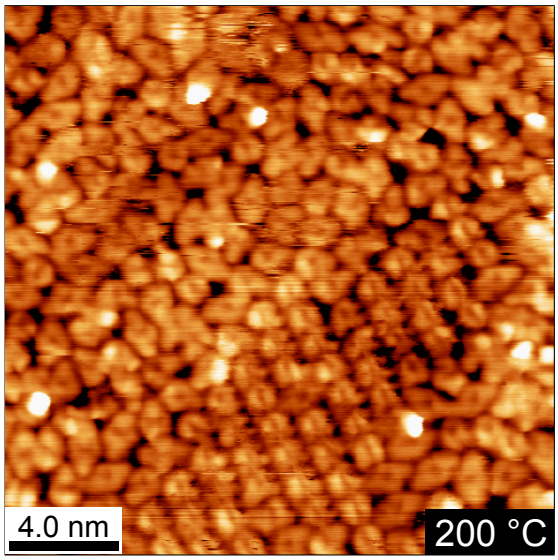

Figure 5.12: STM for 1 ML of NiDBrDPP deposited on Au(111) held at 200 °C. (−1.29 V,0.20 nA). Data measured from the same surface as the 1 ML spectra in Figure 5.9.

structure in Figure 5.11(b). The centre-to-centre distance along the nano-lines is 1.09 ± 0.03 nm, calculated as discussed above, and is in good agreement with the value of 1.13 ± 0.06 nm measured for the nano-lines shown in Figure 5.5.

Figure 5.12 shows a typical STM image recorded after the third deposition of NiDBrDPP onto the hot Au(111) surface at 200 °C, resulting in a 1.0 ML coverage.

Nano-lines similar to those observed after the second deposition (Figure 5.11) are present, in addition to disordered NiDBrDPP molecules. The centre-to-centre distance along the nano-lines is 1.12 ± 0.02 nm, in good agreement with previously measured centre-to-centre distances (Figures 5.5 and 5.11).

In conclusion, the formation of covalently bonded NiDBrDPP nano-lines is observed on Au(111), for both deposition at room temperature followed by annealing at 170 °C, and deposition onto the hot Au(111) substrate at 200 °C. Br 3p and C 1s core level XPS data indicate that the bromine atoms dissociate from the porphyrin molecules and desorb from the surface for depositions onto the hot substrate.

5.3 STM, Photoemission and LEED Study of NiDBrDPP on the Au(110) Surface

5.3.1 Analysis for Deposition at Room Temperature

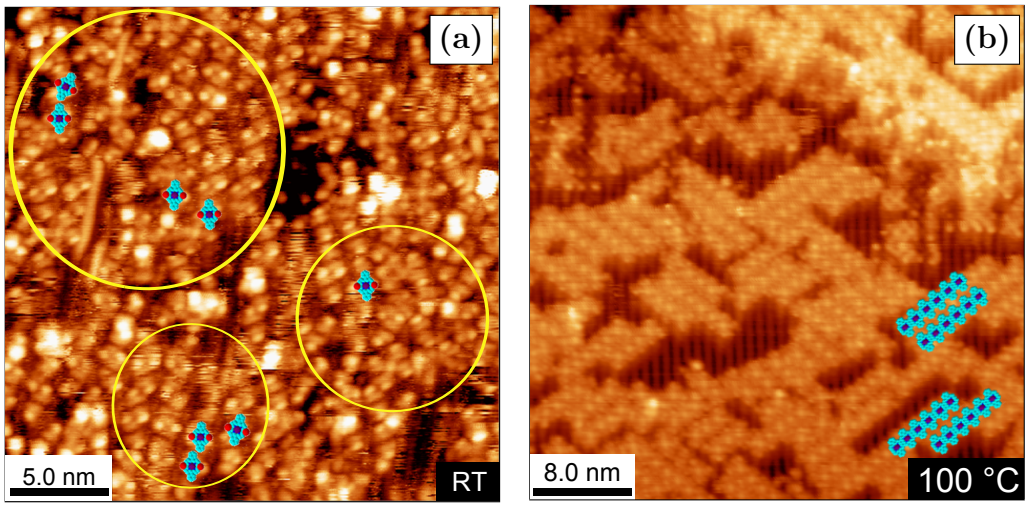

Figure 5.13: STM for 0.6 ML of NiDBrDPP on Au(110). (a) recorded after room temperature deposition, (b) recorded after that surface was annealed at 100 °C. (a) (+0.76 V,0.41 nA), (b) (+0.95 V,0.06 nA). Yellow circles in (a) indicate areas where molecules are visible.

The formation of NiDBrDPP nano-lines was investigated on the Au(110) 2×1 surface. Figure 5.13(a) shows an STM image recorded after the deposition of 0.6 ML of NiDBrDPP onto the Au(110) subtrate at room temperature. The molecules are predominantly oriented along the row direction of the Au(110) 2×1

reconstruction. Areas of the surface where molecules exhibit an overall random orientation are highlighted with yellow circles. There is no evidence for large scale ordered molecular domains such as those observed for room temperature deposition on the Au(111) substrate (Subsection 5.2.1).

Figure 5.13(b) shows an STM image recorded after the NiDBrDPP/Au(110) surface was annealed at 100 °C. A significant change in the molecular orientation is observed. The NiDBrDPP molecules have formed nano-lines along two directions, oriented at angles of $127.3 \pm 2.2°$ and $230.0 \pm 2.1°$ with respect to the Au(110) rows. The centre-to-centre distance along the nano-lines is 1.11 ± 0.06 nm, calculated as above, which is in good agreement with the covalently bonded nano-lines formed on Au(111) after annealing at 170 °C (Figure 5.5). The 2×1 reconstruction of the underlying Au(110) substrate can be seen in Figure 5.13(b).

Figure 5.14 shows Br 3p core level XPS data recorded after deposition of 0.6 ML of NiDBrDPP at room temperature, and subsequent annealing at 100 °C. The spectrum recorded after deposition at room temperature was fitted with two Voigt doublets at $3p_{3/2}$ binding energies of 181.5 eV and 183.6 eV respectively,

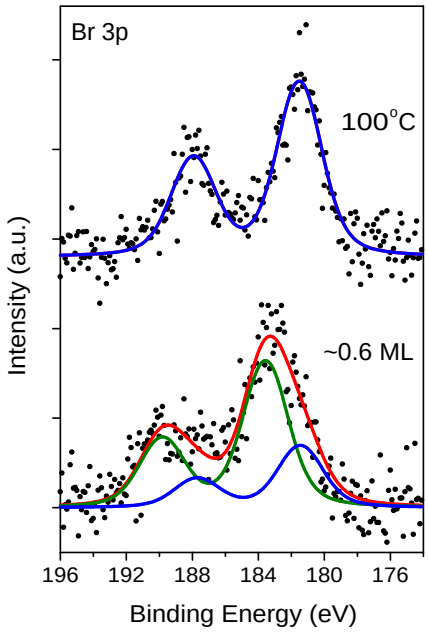

Figure 5.14: XPS for 0.6 ML of NiDBrDPP deposited on room temperature Au(110) and subsequently annealed at 100 °C. Br 3p region, $h\nu = 1486.7$ eV. Spectra measured from the surfaces shown in Figure 5.13.

and with a spin-orbit splitting of 6.3 eV. The components are assigned to dissociated bromine, and bromine bonded to the NiDBrDPP molecules, respectively. After annealing, the component at 183.6 eV binding energy is no longer present, while the intensity of the component at 181.5 eV has increased. Hence all Br has dissociated from the porphyrin molecules at this temperature.

5.3.2 LEED, STM and Photoemission Study of NiDBrDPP/Au(110) Deposited at Elevated Temperatures

Figure 5.15 shows STM images recorded after deposition of submonolayer coverages of NiDBrDPP on the Au(110) 2×1 surface held at 100 °C and 130 °C. The formation of covalently bonded nano-lines oriented along two different directions with respect to the Au rows is observed. The nano-lines make angles of $126.8 \pm 3.4°$ and $230.3 \pm 1.6°$ with the missing rows of the Au(110) 2×1 reconstruction, as indicated in Figure 5.15(a). The centre-to-centre distance along the nano-lines is 1.11 ± 0.03 nm, calculated as above, in agreement with nano-lines previously seen on Au(111) (Figures 5.5(a) and 5.11(b)) and on Au(110) (Figure 5.13(b)). The inter-row centre-to-centre distance, calculated by analysing the mean value across several nano-lines and averaging along the direction of the nano-lines, is 1.76 ± 0.05 nm, with an angle between the unit cell vectors of $90 \pm 10°$. The overlayer unit cell is shown in Figure 5.15(d). Previous XPS data (for example Figure 5.14) indicate that bromine remains on the surface after dissociating from the molecule, but there is little evidence for where this bromine may be located on the surface in STM images. Small circular features are observed in Figure 5.15(c), highlighted with yellow ellipses, which appear to lie in the missing rows of the Au(110) 2×1 reconstruction. These features lie parallel to the direction of the nano-lines, in some cases lying adjacent to the outermost nano-line while in other cases being more isolated. One explanation for these circular features is that they are bromine atoms which have dissociated from the molecule but remain present on the surface.

Figure 5.16 shows LEED images recorded after deposition of NiDBrDPP on the Au(110) substrate held at 100 °C. The kinetic energy of the incident electrons was 16.2 eV and 27.4 eV respectively. A square pattern of diffraction spots is visible due to the molecular overlayer. Using the method outlined in Section 2.4 [9, 10], a calibration curve was constructed in order to extract the

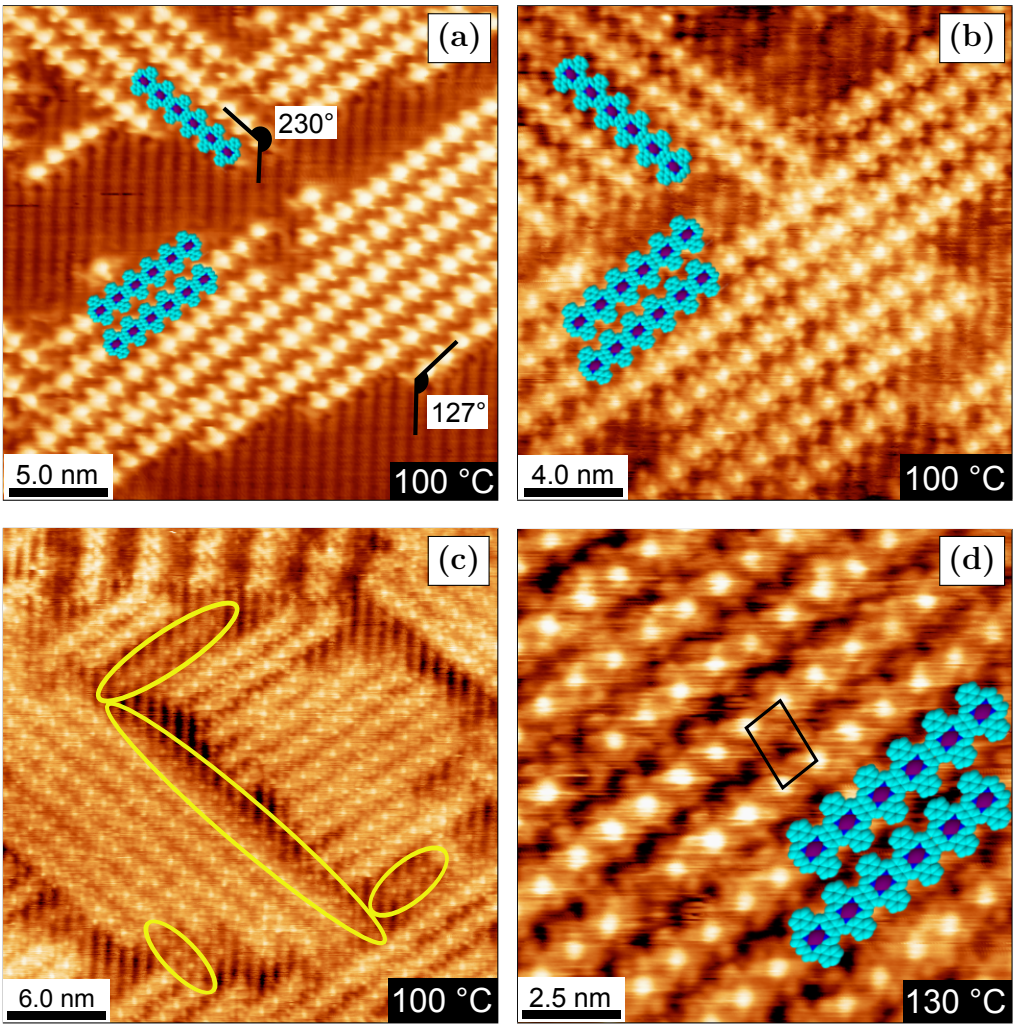

Figure 5.15: STM for NiDBrDPP deposited on Au(110) held at (a) - (c) 100 °C and (d) 130 °C. (a) (+1.0 V,0.1 nA), (b) (−0.16 V,0.55 nA), (c) (+0.05 V,0.69 nA), (d) (+0.71 V,0.43 nA). Overlayer unit cell is shown in (d). Yellow ellipses in (c) highlight circular features in missing rows. (a) - (c) show a surface with a 0.7 ML coverage, (d) shows a differently prepared surface with a 0.6 ML coverage.

lattice parameter of the molecular overlayer (Figure 5.17). Taking an arbitrary distance in pixels, in this case 80 pixels, the corresponding values for inverse square root of the kinetic energy were used in conjunction with Equation 2.28 to calculate the lattice parameter of the overlayer relative to the substrate lattice parameters. As the unit cell of the Au(110) 2×1 reconstruction has lattice parameters of 0.816 nm and 0.289 nm [11, 12], the lattice parameter for the NiDBrDPP overlayer was calculated as 1.75 ± 0.16 nm. This value is in good

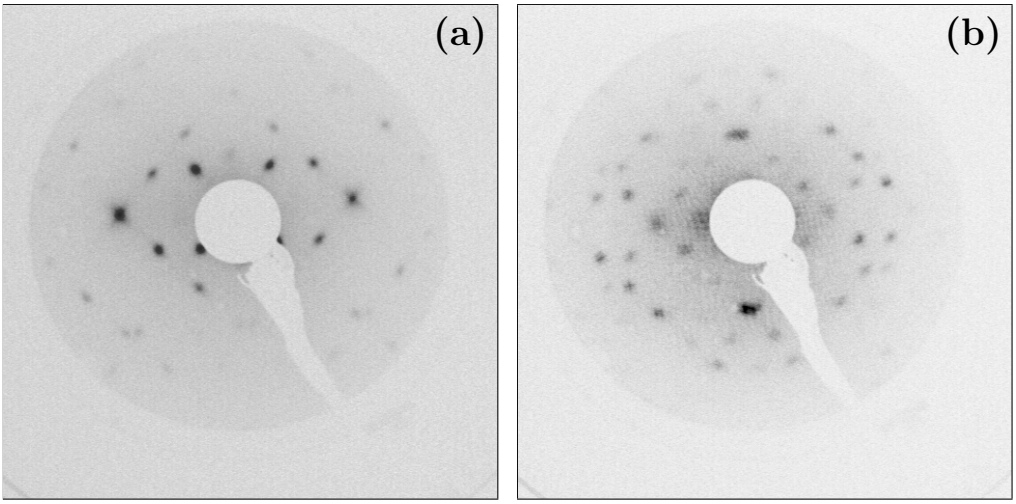

Figure 5.16: LEED for NiDBrDPP deposited on Au(110) held at 100 °C. (a) recorded at 16.2 eV, (b) recorded at 27.4 eV. (a) and (b) measured from the surface shown in Figure 5.15(a) - (c).

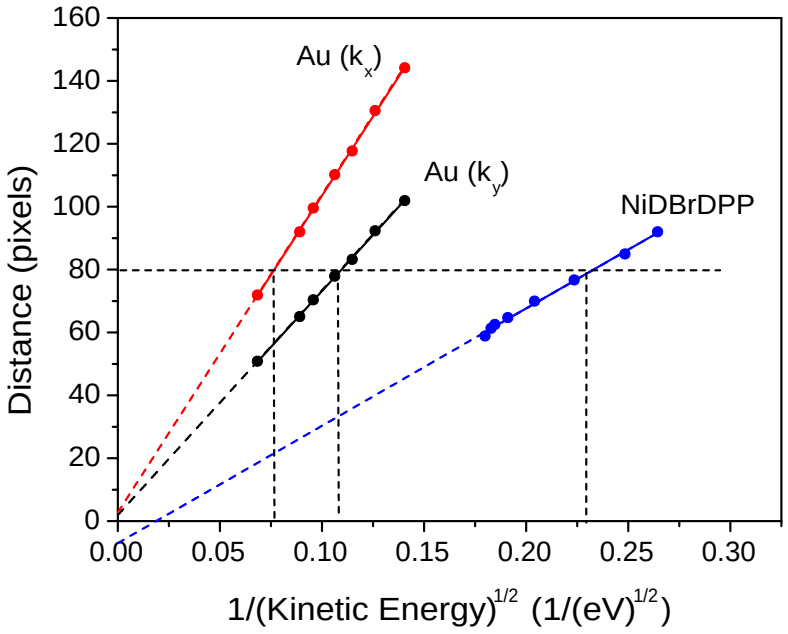

Figure 5.17: Calibration graph to calculate the overlayer lattice parameter. Reciprocal space distance in pixels for Au(110) substrate and NiDBrDPP overlayer calculated from LEED images as a function of the inverse of the square root of the kinetic energy of the LEED electrons.

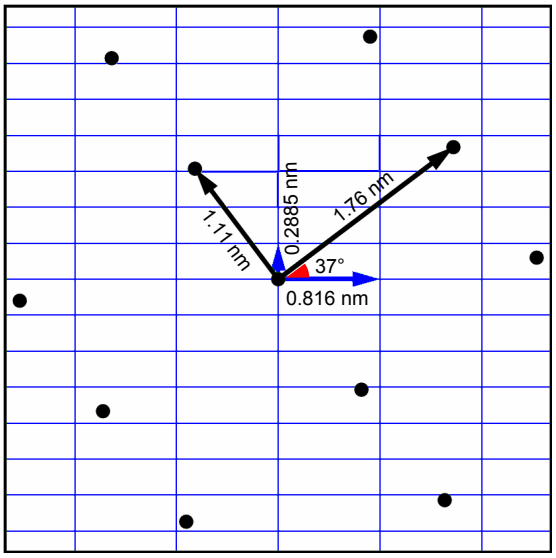

Figure 5.18: Au(110) and NiDBrDPP overlayer real space unit vectors. Blue lines are Au(110) vectors, black are molecular overlayer vectors measured from STM images (Figure 5.15). Generated using LEEDpat [13].

agreement with the centre-to-centre inter-row distance of $1.76 \pm 0.05\,\text{nm}$ as measured from the STM data (Figure 5.15).

The NiDBrDPP overlayer is incommensurate with the Au(110) substrate, as is shown by the relative orientation of the basis vectors of the molecular overlayer and Au substrate (Figure 5.18). A simulated LEED pattern was generated with the LEEDpat software [13] using these basis vectors, and is described by the following matrix:

$$\begin{pmatrix} 1.7225 & 3.6714 \\ -0.8186 & 3.0727 \end{pmatrix}$$

Figure 5.19 shows experimental LEED data recorded after deposition of NiDBrDPP on the Au(110) 2×1 surface held at 100 °C, together with the simulated LEED pattern. The dashed lines in Figure 5.19(b) are added as a guide to emphasise the agreement between the LEED data and the model. The red and blue spots in Figure 5.19(b) are due to the presence of two domains corresponding to the two orientations of NiDBrDPP nano-lines observed on the surface (Figure 5.15). The Miller indices of the highlighted diffraction spots are given in Table 5.2 for each domain.

The spots marked ‘x’ in Figure 5.19(a) are brighter than the adjacent spots, due to the fact that the spots from the two domains coincide at those points, as seen in Figure 5.19(b). The spots marked ‘y’ are resolved as two separate spots,

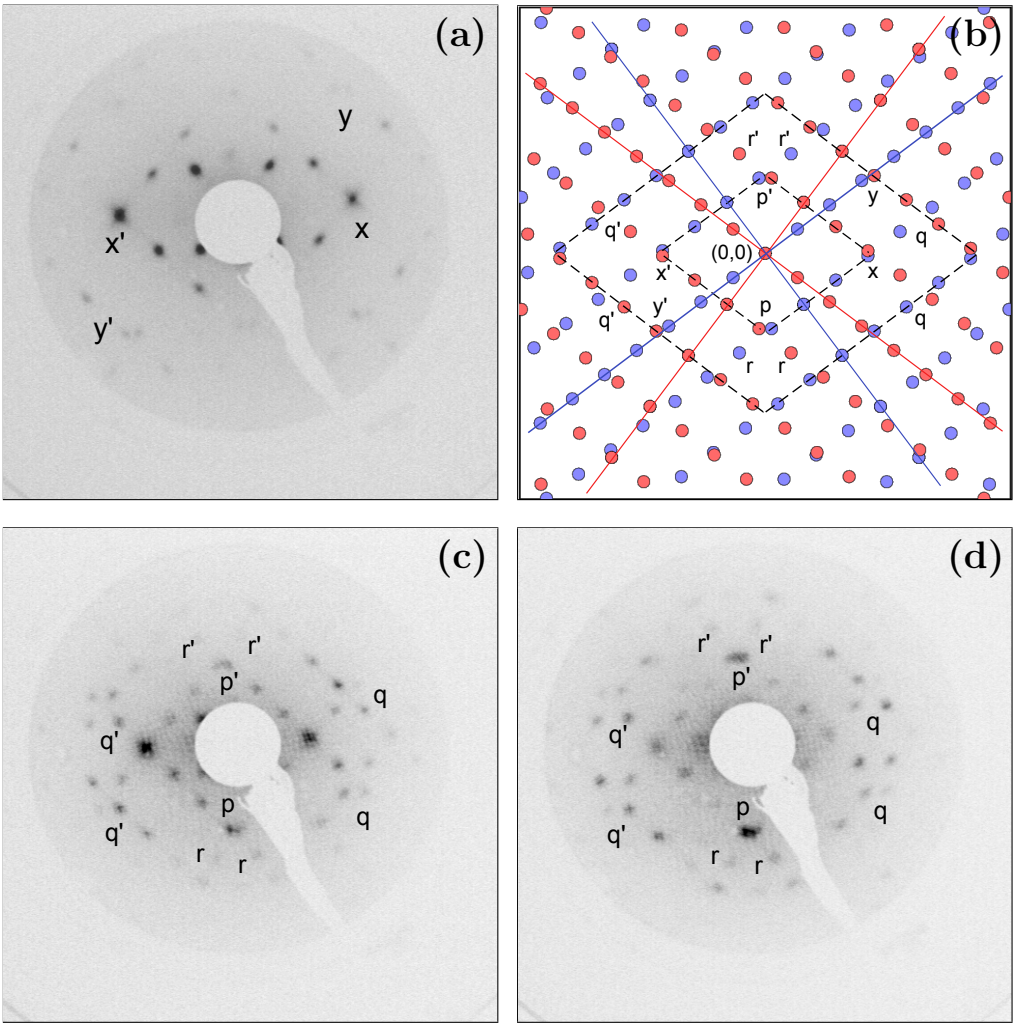

Figure 5.19: Experimental LEED data and reciprocal space model for NiDBrDPP on Au(110), 100 °C deposition. (a), (c) and (d) recorded at 16.2 eV, 29.9 eV and 27.4 eV respectively. (b) generated using the LEEDpat software [13]. (a), (c) and (d) measured from the surface shown in Figure 5.15(a) - (c). Figure 5.19(a) and (d) already shown in Figure 5.16.

in agreement with the simulated pattern, Figure 5.19(b), which shows diffraction spots from each of the two domains as very close but not coincident. There is also very good agreement between the experimental and theoretical LEED data for higher kinetic energies. The spots marked 'p' in Figure 5.19(b) are resolved as two separate spots in Figure 5.19(c) and (d). The four diffraction spots marked 'q' in the simulated pattern are present in both Figure 5.19(c) and (d). The spots marked 'r' are present in Figure 5.19(c) and (d). The excellent agreement between the measured LEED data and the model confirms the relative orientation of the

Table 5.2: Coordinates for diffraction spots observed in LEED data for NiDBrDPP deposited on Au(110) held at 100 °C (Figure 5.19). Coordinates of spots labelled as prime are not listed.

Spot Label	Coordinates Domain 1 (red spots)	Coordinates Domain 2 (blue spots)
x	$(2,1)$	$(1,2)$
y	$(1,2)$	$(0,3)$
p	$(1,-1)$	$(1,-1)$
q	$(2,2)$, $(3,2)$, $(3,1)$, $(4,1)$	$(1,3)$, $(1,4)$, $(2,2)$,$(2,3)$
r	$(2,-1)$	$(1,-2)$

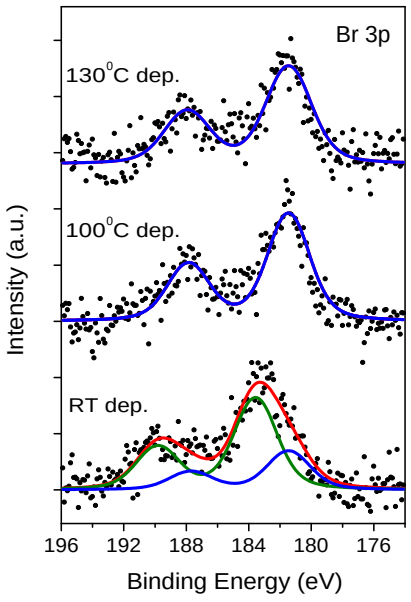

Figure 5.20: XPS for NiDBrDPP on Au(110), three different depositions with the substrate held at room temperature, 100 °C and 130 °C. Br 3p region, hν = 1486.7 eV. The RT spectrum has been shown in Figure 5.14, and was measured from the surface with 0.6 ML coverage shown in Figure 5.13. The 100 °C and 130 °C spectra were measured from differently prepared surfaces with coverages of 0.7 ML and 0.6 ML respectively, shown in Figure 5.15.

substrate and overlayer vectors (Figure 5.18).

Figure 5.20 shows Br 3p core level XPS data recorded after deposition of NiDBrDPP on the Au(110) substrate held at room temperature, 100 °C and 130 °C. The spectrum recorded at room temperature was discussed previously (Figure 5.14) and is included here for comparison. The spectra recorded after deposition onto the hot Au surface were fitted with a single Voigt doublet at a $3p_{3/2}$ binding energy of 181.5 eV, with a spin-orbit splitting of 6.5 eV, assigned to dissociated bromine. Hence the bromine dissociates from the NiDBrDPP on deposition onto the hot substrate, enabling the NiDBrDPP molecules to form covalently bonded nano-lines. This bromine may be present on the surface as the small, circular features observed in Figure 5.15(c).

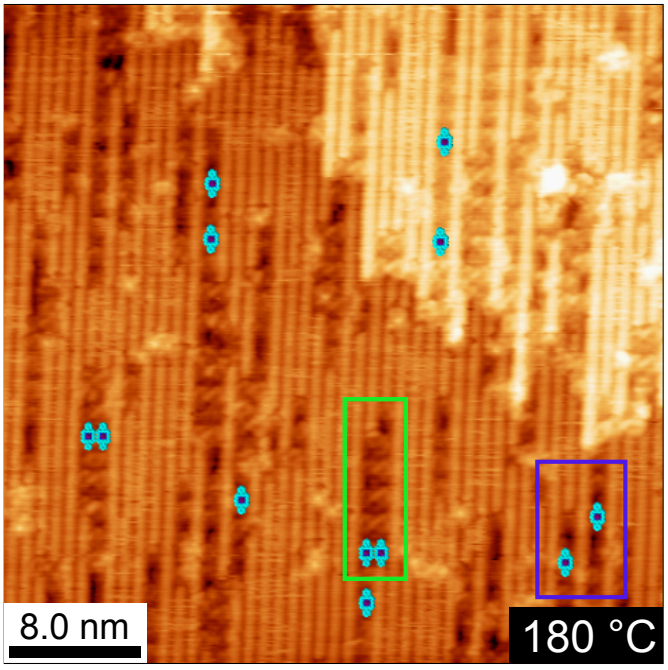

Figure 5.21: STM for 0.5 ML of NiDBrDPP deposited on Au(110) held at 180 °C. (+0.45 V,0.68 nA). Blue and green rectangles highlight areas of local 4×1 and 6×1 Au(110) reconstruction respectively.

Figure 5.21 shows an STM image recorded after deposition of 0.5 ML of NiDBrDPP onto the Au(110) surface held at 180 °C. The cell temperature and deposition time were the same as for the previous depositions on Au(110) held at room temperature, 100 °C and 130 °C (Figures 5.13 and 5.15), but the resulting coverage is approximately half that of the previous depositions, due to the reduced sticking coefficient of the molecules at this temperature. No nano-line

formation is observed, however the NiDBrDPP molecules that remain on the surface have disrupted the 2×1 reconstruction. Single NiDBrDPP molecules cause the formation of a local 4×1 reconstruction, as highlighted by the blue rectangle in Figure 5.21, while the presence of NiDBrDPP dimers leads to a local 6×1 reconstruction, highlighted by the green rectangle in Figure 5.21. The NiDBrDPP molecules appear to be lying between the Au rows. Material on top of the 2×1 reconstruction is observed in Figure 5.21; this may be the displaced Au atoms. The reduced sticking coefficient of the NiDBrDPP on the Au(110) surface at 180 °C and the tendency for the molecules to displace Au atoms and lie between the Au rows is unfavourable for nano-line formation. This agrees with previous results which showed that extensive nano-networks were not formed on the Au(110) substrate at temperatures higher than 130 °C (Figure 4.17).

In conclusion, the formation of covalently bonded NiDBrDPP nano-lines is observed after room temperature deposition followed by annealing at 100 °C, and after deposition onto the Au(110) substrate held at 100 °C and 130 °C. Two orientations of nano-lines are present on the surface, at angles of $126.8 \pm 3.4^{\circ}$ and $230.3 \pm 1.6^{\circ}$ with respect to the rows of the Au(110) 2×1 reconstruction. A simulated LEED image generated using the Au(110) lattice parameters and molecular overlayer parameters measured from STM images shows very good agreement with experimental LEED data. Br 3p core level XPS data show that the bromine dissociates from the NiDBrDPP molecules on deposition onto the hot Au surface. STM images show local disruption of the Au(110) 2×1 reconstruction following deposition onto the surface held at 180 °C.

5.4 Photoemission Study of NiDBrDPP on the Ag(111) Surface

5.4.1 Analysis for Deposition at Room Temperature

Figure 5.22 shows Br 3p core level XPS data recorded after the deposition of 2 ML of NiDBrDPP onto a Ag(111) 1×1 surface at room temperature, and subsequent annealing at 230 °C. The spectra were fitted with two Voigt doublets at $3p_{3/2}$ binding energies of 181.8 eV and 184.1 eV respectively, with a spin-orbit splitting of 6.5 eV. The binding energies of the components are in agreement with the fitted Br 3p XPS spectra for NiTBrPP deposited on Ag(111) (Figure 3.12). The component at lower binding energy is assigned to dissociated bromine, while the

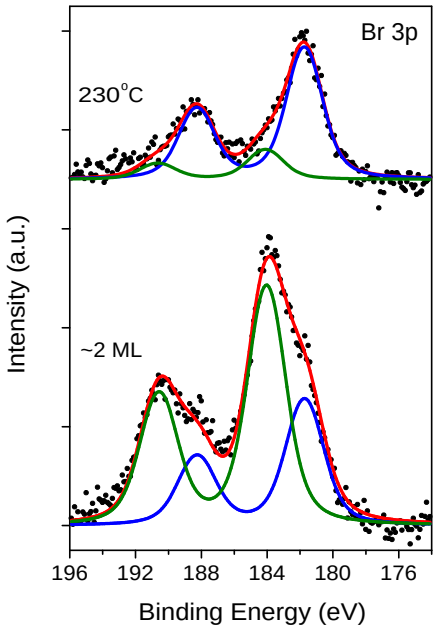

Figure 5.22: XPS for 2 ML of NiDBrDPP deposited on room temperature Ag(111) and subsequently annealed at 230 °C. Br 3p region, hν = 1486.7 eV.

doublet at higher binding energy is assigned to Br bonded to the NiDBrDPP molecule. Dissociated bromine accounts for 35 % of the Br signal after deposition at room temperature, and 80 % of the Br signal after annealing at 230 °C.

In conclusion, Br 3p core level XPS data show that some debromination of the NiDBrDPP occurs on Ag(111) at room temperature, with further bromine dissociation observed after thermal annealing. Due to time constraints, an STM study of NiDBrDPP/Ag(111) has not been carried out.

5.5 STM and Photoemission Study of NiDBrDPP on the Cu(111) Surface

5.5.1 Analysis for Deposition at Room Temperature

Figure 5.23 shows STM images recorded after the deposition of 0.25 ML of NiDBrDPP on a Cu(111) 1×1 surface. Figure 5.23(a) - 5.23(f) were recorded at regular intervals on the same region of the surface over a 15 minute interval. This particular region of the surface is clearly identifiable by the defect in the centre of the porphyrin rows, where two porphyrins are either missing from the molecular structure or are imaging as much darker than the surrounding NiDBrDPP molecules. The centre-to-centre distance along the nano-lines is 1.06 ± 0.09 nm, calculated as above, and is again in good agreement with previous centre-to-centre distances for nano-lines (Figures 5.5(a), 5.11(b), 5.13(b), 5.15). However, previous results for NiTBrPP, H_2TBrPP and TBB molecules deposited on Cu(111) at room temperature (Sections 3.4 and 4.4) suggest that the NiDBrDPP structures observed in Figure 5.23 are protopolymer nano-lines, coordinated with surface Cu atoms [1–4].

As the region was repeatedly scanned, individual NiDBrDPP molecules were observed moving parallel to the molecular structure (Figure 5.23(c), 5.23(d) and 5.23(e)). There was no evidence of NiDBrDPP molecules moving perpendicular to the direction of the nano-lines; all observed diffusion was along the sides of the initial structure. Figure 5.23(f) shows the formation of two additional nano-lines on either side of the initial molecular structure. A similar phenomenon has been reported for benzene adsorbed on Cu(111) [14, 15]. So-called 'phantom rows' of benzene were observed parallel to adsorbed rows of benzene along Cu step edges [14]. These phantom rows were attributed to benzene diffusing along the adsorbed rows of molecules, under the influence of the tip [14, 15]. This behaviour was attributed to the adsorbed molecules creating perturbations in the local density of states of the surface, which then acted as binding sites for additional benzene molecules [14, 15]. A similar explanation is proposed for the mobile NiDBrDPP molecules observed in Figure 5.23, with the initial structure of five coordinated protopolymers creating binding sites for additional porphyrin molecules, which then diffuse along the nano-lines as the region is scanned with the STM tip. This mobility of the porphyrin molecules on the Cu(111) surface at room temperature

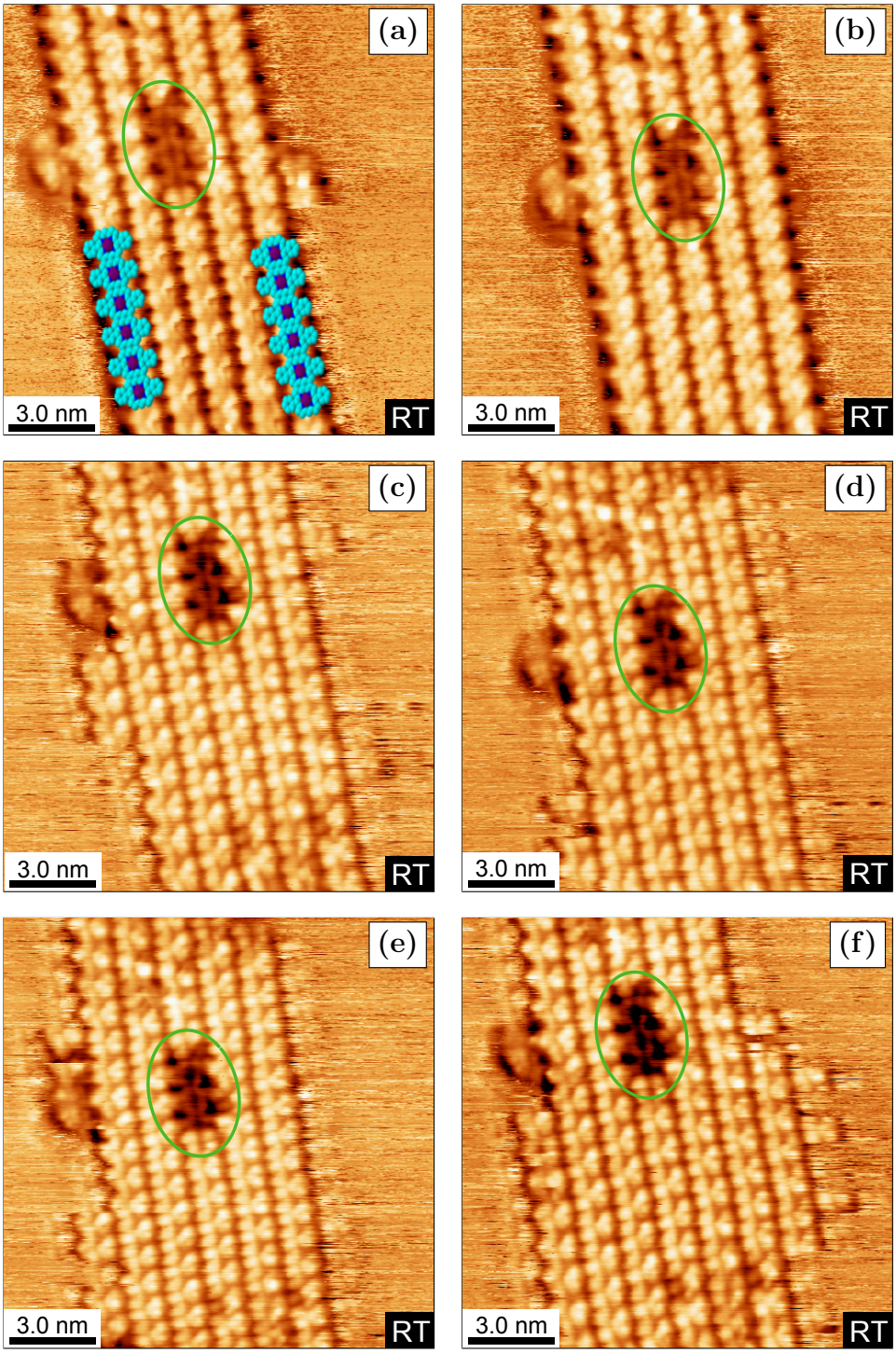

Figure 5.23: STM for 0.25 ML of NiDBrDPP deposited on room temperature Cu(111). Six sequential images of the same region recorded over 15 minutes. Tip was repositioned after recording (a) and (c) in order to recentre on highlighted defect. (a) and (b) (−0.81 V,0.13 nA), (c) to (f) (+0.81 V,0.13 nA).

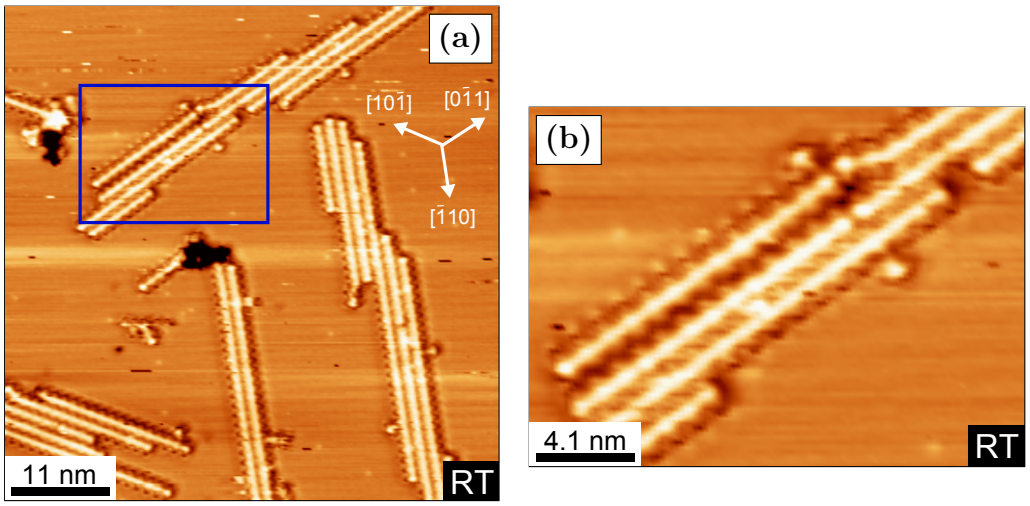

Figure 5.24: STM for 0.25 ML of NiDBrDPP deposited on room temperature Cu(111). (−0.45 V,0.31 nA), (b) 20.5 nm × 14.8 nm. Blue rectangle in (a) highlights region which is enlarged in (b). Surface is the same as that shown in Figure 5.23.

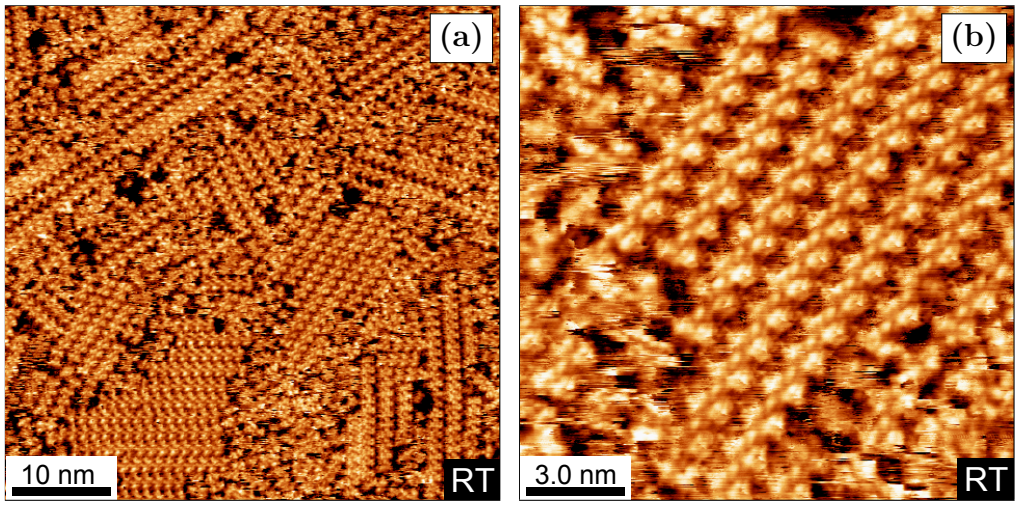

Figure 5.25: STM for a 1 ML coverage of NiDBrDPP deposited on room temperature Cu(111). (a) (−0.13 V,0.06 nA), (b) (+0.13 V,0.06 nA). (a) and (b) show the same surface.

is in agreement with observations of NiTBrPP on Cu(111) (Figure 3.21), and implies that these molecular structures are not covalently bonded.

Figure 5.24 shows additional STM images recorded after deposition of 0.25 ML of NiDBrDPP onto the Cu(111) surface at room temperature. Figure 5.24(b) shows the region in Figure 5.24(a) highlighted with a blue rectangle. The

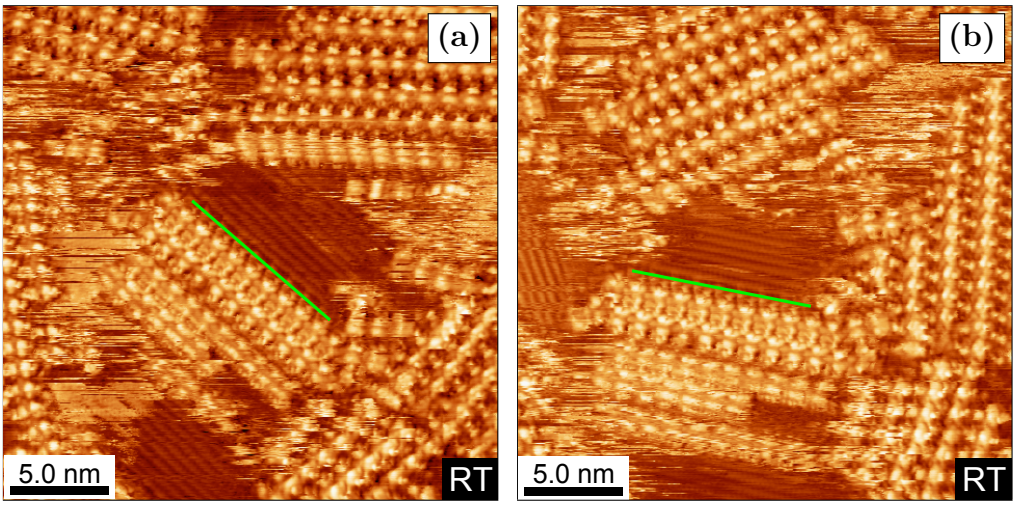

Figure 5.26: STM for 0.8 ML of NiDBrDPP deposited on room temperature Cu(111), regions of 2×1 structure. (+0.03 V,0.50 nA). (a) and (b) show same region of the surface. Scan angle for (b) was rotated 30° with respect to scan angle for (a). Green line added as a guide.

porphyrin macrocycles are imaged as a continuous line running through the nano-line in Figure 5.24(a). The nano-lines are oriented at 120° to each other, suggesting that their orientation is influenced by the principal crystallographic directions of the Cu(111) surface. The nano-lines also tend to grow from defect sites, with two separate nano-line structures originating from the same defect site in Figure 5.24(a).

Figure 5.25 shows STM images recorded after the deposition of a 1 ML coverage of NiDBrDPP onto the Cu(111) surface at room temperature. Different domains of ordered NiDBrDPP nano-lines are observed, together with regions of disordered molecules (Figure 5.25(a)). A series of bright spots are present between adjacent NiDBrDPP molecules along the nano-lines (Figure 5.25(b)). These features may be the coordinating Cu atoms, which have been previously seen in STM images of TBB protopolymer networks on Cu(111) [2].

Figure 5.26 shows STM images for 0.8 ML of NiDBrDPP deposited on Cu(111) at room temperature where the 2×1 reconstruction previously discussed (Section 3.2) is present. The reconstruction has a periodicity of 0.50 ± 0.02 nm in the 2× direction. Two 2×1 domains are present, oriented at 120° to each other. Figure 5.26(b) was recorded at a scan angle rotated 30° with respect to the scan angle at which Figure 5.26(a) was recorded. As the orientation of the 2×1 region rotates with the scan angle, this is further confirmation that the 2×1

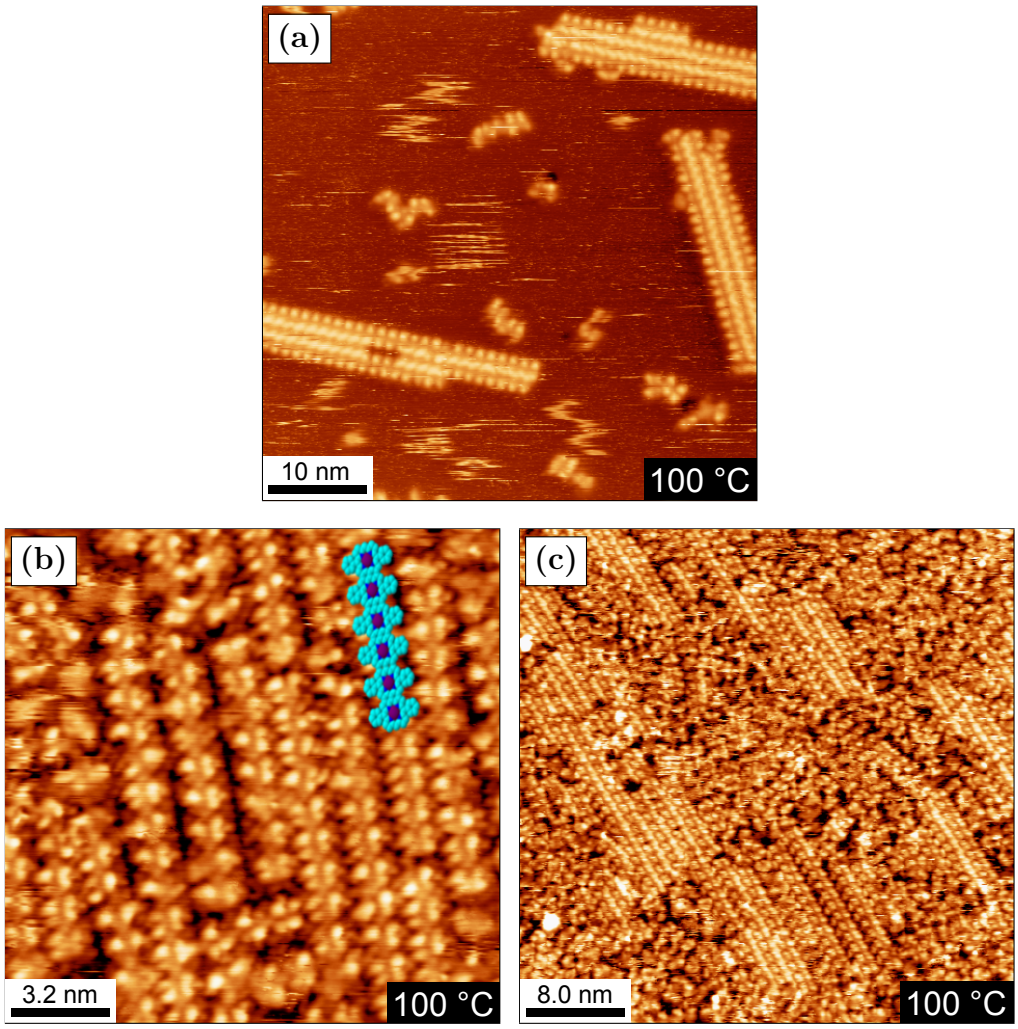

Figure 5.27: STM for NiDBrDPP deposited on room temperature Cu(111) and subsequently annealed at 100 °C. (a) (−1.82 V,0.16 nA), (b) (−0.48 V,0.20 nA), (c) (−0.20 V,0.37 nA). (a) shows the surface with a coverage of 0.25 ML (Figures 5.23 and 5.24) annealed at 100 °C, (b) and (c) show a differently prepared surface with a 1 ML coverage annealed at 100 °C.

reconstruction is a real feature of the surface, and not an artifact.

Figure 5.27 shows STM images recorded after the NiDBrDPP protopolymers were annealed at 100 °C. At lower coverages, the nano-lines appear similar to those shown in Figure 5.24, with the addition of mobile NiDBrDPP molecules and chains (Figure 5.27(a)). At higher coverages, the surface appears similar to the structures shown in Figure 5.25(a) and (b), with ordered nano-lines present, together with regions of disordered porphyrin molecules (Figure 5.27(b) and (c)). The centre-to-centre distance along the nano-lines is 1.01 ± 0.03 nm, calculated as

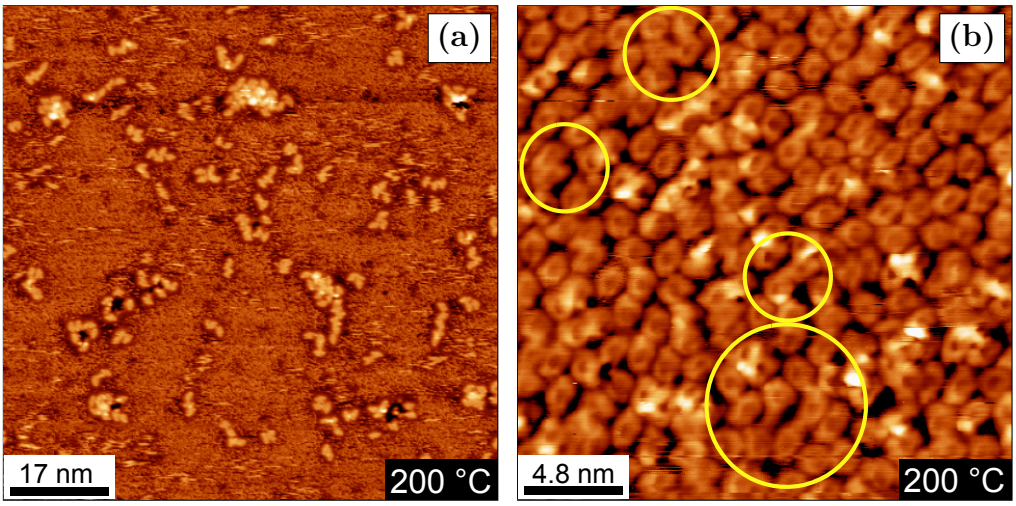

Figure 5.28: STM for NiDBrDPP deposited on room temperature Cu(111) and subsequently annealed at 200 °C. (a) (−0.82 V,0.50 nA), (b) (+1.40 V,0.37 nA). Yellow circles in (b) indicate NiDBrDPP molecules which appear to be bonded. (a) shows the surface with a 0.25 ML coverage (Figures 5.23, 5.24 and 5.27(a)) annealed at 200 °C, (b) shows the surface with a coverage of 1 ML (Figure 5.25) annealed at 200 °C.

above, in agreement with the distance of 1.09 ± 0.01 nm measured for nano-lines at room temperature (Figure 5.25). The similarity between the NiDBrDPP molecular structures at room temperature and after annealing at 100 °C implies that the structures remain coordinated by surface Cu atoms and have not been converted to covalently bonded structures. This agrees with published reports of the release of coordinating Cu atoms and the subsequent conversion of protopolymers to covalently bonded structures occurring after thermal annealing at 300 °C [2].

Figure 5.28 shows STM images recorded after the NiDBrDPP/Cu(111) surface was annealed at 200 °C. Significant changes are observed; there are no longer nano-lines present on the surface. For lower coverages, any molecular material still present on the surface has agglomerated together to form islands of various sizes (Figure 5.28(a)), similar to the behaviour observed for NiTBrPP, H_2TBrPP and TBB structures on Cu(111) at temperatures of 300 °C and higher (Sections 3.4 and 4.4). For a monolayer coverage, the molecules are disordered on the surface (Figure 5.28(b)). The bonding of adjacent molecules is observed, with some examples highlighted with yellow circles in Figure 5.28(b), suggesting that some covalent bonding has occurred; however the majority of the porphyrin molecules

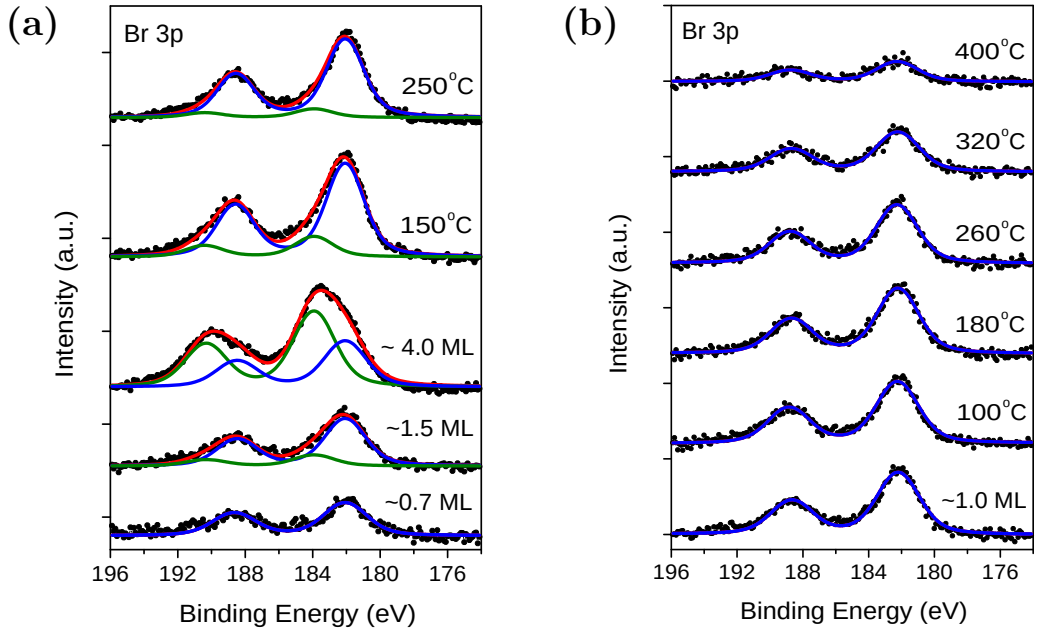

Figure 5.29: XPS for NiDBrDPP deposited on room temperature Cu(111) and subsequently annealed at temperatures shown. Br 3p region, hν = 1486.7 eV. Spectra in (a) correspond to an initial deposition of 0.7 ML, two additional depositions of 0.8 ML and 2.5 ML respectively, and subsequent annealing at 150 °C and 250 °C. Spectra in (b) correspond to a 1 ML coverage annealed at the temperatures shown. The 100 °C spectrum was measured from the surface shown in Figure 5.27(b) and (c).

appear to be unbonded. A possible explanation is that the coordinating Cu atoms were released during the anneal, but the molecular coverage was too high to allow diffusion and covalent bonding of the porphyrins.

Figure 5.29(a) shows Br 3p core level XPS spectra recorded after three depositions of NiDBrDPP onto the Cu(111) surface at room temperature, resulting in a coverage of 4 ML, and subsequent annealing at 150 °C and 250 °C. The spectrum recorded after deposition of 0.7 ML was fitted with a single Voigt doublet at a $3p_{3/2}$ binding energy of 182.2 eV, with a spin-orbit splitting of 6.5 eV. An additional component with a $3p_{3/2}$ binding energy of 183.9 eV was necessary for fitting of the spectra corresponding to coverages greater than 1 ML. The components at 182.2 eV and 183.9 eV are assigned to dissociated bromine atoms, and Br that remains bonded to the NiDBrDPP molecule. The spectra indicate

that for submonolayer coverages, the porphyrin molecules are fully debrominated on deposition onto the Cu surface at room temperature, while the 4 ML coverage of NiDBrDPP is almost completely debrominated after annealing at 250 °C. The intensity of the component at 182.2 eV after annealing at 250 °C is equal to 62 % of the Br signal observed for the 4 ML coverage at room temperature, indicating that many dissociated bromine atoms do not desorb from the surface at that temperature. The Br dissociation at room temperature again confirms that the Cu substrate catalyses the C-Br bond scission at room temperature [1, 2]. This agrees with the STM images showing the formation of NiDBrDPP protopolymer structures at room temperature (Figures 5.23, 5.24, and 5.25).

Figure 5.29(b) shows Br 3p core level XPS data recorded after deposition of 1 ML of NiDBrDPP onto the Cu(111) surface at room temperature, and subsequent annealing up to 400 °C. All spectra were fitted with a single Voigt doublet at a $3p_{3/2}$ binding energy of 182.2 eV, with a spin-orbit splitting of 6.5 eV, assigned to dissociated bromine. There is still bromine present on the surface at 400 °C, demonstrating that the dissociated bromine is strongly bonded to the Cu(111) surface. These results agree with XPS spectra recorded for the TBB/Cu(111) surface, (Figure 4.26).

5.5.2 STM and Photoemission Study of NiDBrDPP/Cu(111) Deposited at Elevated Temperatures

Figure 5.30 shows STM images recorded after the deposition of 0.5 ML of NiDBrDPP on the Cu(111) surface held at 100 °C. The surface appears similar to that observed after annealing at 100 °C following a room temperature deposition (Figure 5.27). Ordered nano-lines are present, together with some shorter chains. Figure 5.30(b) shows an enlarged view of the protopolymers, where the four pyrrole rings of the macrocycle are visible.

Figure 5.31 shows STM images recorded after a 0.5 ML coverage was deposited on the Cu(111) surface at 200 °C. Short molecular chains and nano-line fragments are observed on the surface, similar to those seen after a 0.25 ML coverage of NiDBrDPP was deposited at room temperature and annealed at 200 °C (Figure 5.28).

Figure 5.32 shows Br 3p core level XPS data recorded after the deposition of NiDBrDPP on the Cu(111) surface at room temperature, 100 °C, and 200 °C.

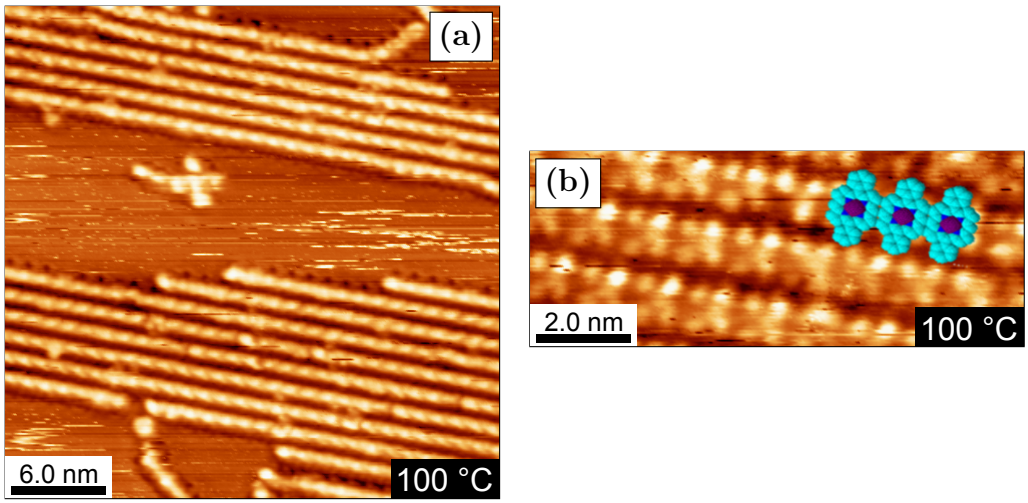

Figure 5.30: STM for 0.5 ML of NiDBrDPP deposited on Cu(111) held at 100 °C. (a) (−1.67 V,0.08 nA), (b) (+1.16 V,0.09 nA), 10.0 nm × 3.9 nm. (a) and (b) show the same surface.

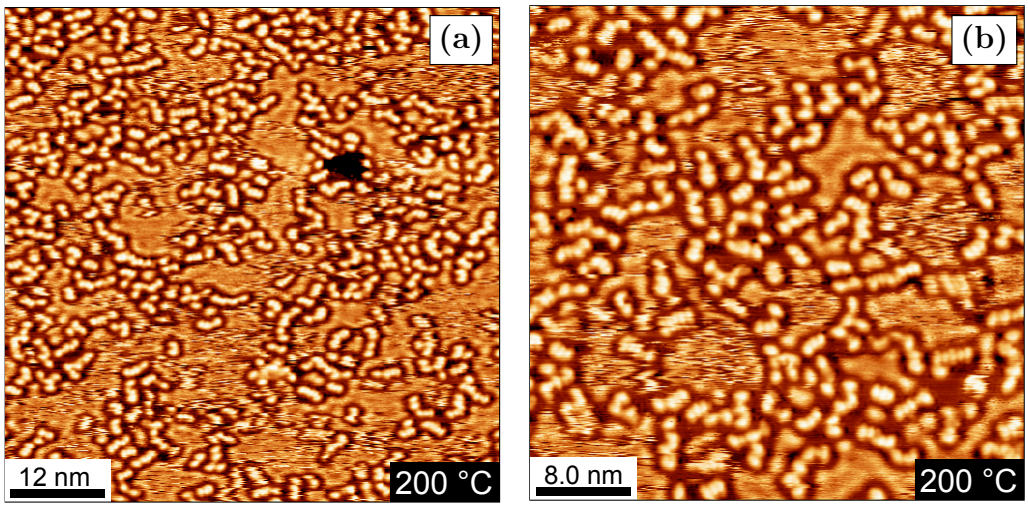

Figure 5.31: STM for 0.5 ML of NiDBrDPP deposited on Cu(111) held at 200 °C. (−1.37 V,0.05 nA). (a) and (b) show the same surface.

The two room temperature spectra were discussed previously (Figure 5.29) and are shown here for comparison. All spectra were normalised to the lower binding energy component in the room temperature spectrum corresponding to multi-layer deposition. The spectra recorded after deposition at 100 °C and 200 °C were fitted with a single Voigt doublet at a $3p_{3/2}$ binding energy of 182.2 eV, assigned to dissociated Br, confirming that the NiDBrDPP molecules are debrominated on deposition. This is in contrast to the depositions on Au(111)

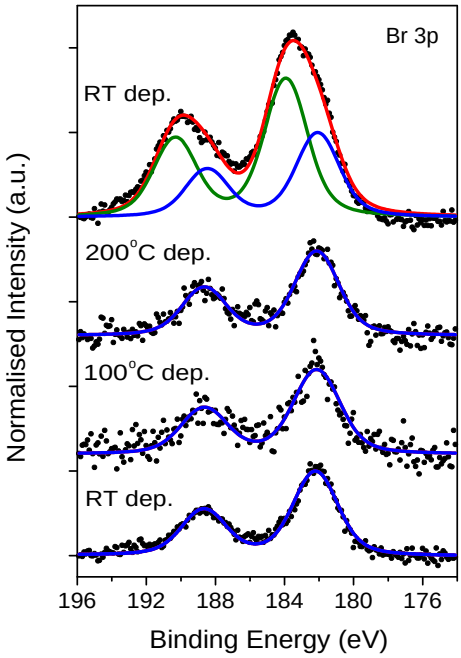

Figure 5.32: XPS for NiDBrDPP on Cu(111), two depositions with the substrate held at room temperature, and depositions with the substrate held at 100 °C and 200 °C. Br 3p region, hν = 1486.7 eV. The room temperature spectra were shown previously in Figure 5.29, and the 100 °C and 200 °C spectra were measured from the surfaces shown in Figures 5.30 and 5.31 respectively.

at 200 °C, where no bromine was present on the surface after three successive depositions (Figure 5.9(a)), again confirming the higher reactivity of the Cu substrate [16].

In conclusion, the formation of NiDBrDPP protopolymers is observed for deposition on the Cu(111) surface at room temperature. The porphyrins are observed to be mobile under the influence of the tip, diffusing along the protopolymer structures and forming phantom rows. Br 3p core level XPS spectra show the debromination of the NiDBrDPP molecules at room temperature. Dissociated Br is present on the surface after annealing at 400 °C.

5.6 Summary

Six different packing configurations of NiDBrDPP are observed on the Au(111) surface at room temperature. STM data show that the NiDBrDPP molecules can change how they self-assemble on the surface, under the influence of the tip. Covalently bonded nano-lines are formed by annealing at 170 °C, with a centre-to-centre distance of 1.13 ± 0.06 nm. Two Br 3p core level components with $3p_{3/2}$ binding energies of 181.5 eV and 183.6 eV respectively and a spin-orbit splitting of 6.5 eV are present in the XPS data. The components at 181.5 eV and 183.6 eV binding energy are assigned to dissociated bromine atoms on the surface, and bromine bonded to the *meso* carbon atoms in the NiDBrDPP macrocycle respectively. Nano-lines are formed after deposition onto the Au(111) substrate at 200 °C; bromine dissociates from the porphyrin molecules and desorbs from the surface on deposition.

There is no evidence of any ordered molecular domains after deposition of NiDBrDPP onto the Au(110) surface at room temperature. Nano-line formation is observed after annealing at 100 °C, with the nano-lines oriented at approximately 127° and 230° to the Au(110) rows. Nano-lines are formed on deposition of NiDBrDPP on the hot Au(110) surface held at 100 °C and 130 °C, and exhibit an intra-row centre-to-centre distance of 1.11 ± 0.03 nm and an inter-row centre-to-centre distance of 1.76 ± 0.05 nm. Small circular features visible in the missing rows of the underlying Au(110) substrate may be dissociated bromine atoms, which the XPS data indicate are still on the surface. A simulated LEED pattern calculated with the known Au(110) lattice parameters and the measured unit cell vectors of the NiDBrDPP overlayer is in very good agreement with experimental LEED data recorded after deposition onto Au(110) held at 100 °C. Deposition onto the surface at 180 °C results in local 4×1 and 6×1 reconstruction of the Au(110) surface.

The formation of NiDBrDPP protopolymer nano-lines is observed on the Cu(111) substrate for room temperature deposition. These nano-lines have a centre-to-centre distance of 1.06 ± 0.09 nm. The NiDBrDPP molecules are mobile on the surface under the influence of the STM tip, diffusing along the protopolymer structures and forming phantom rows of molecules. The NiDBrDPP molecules debrominate on deposition at room temperature for coverages up to a monolayer, as indicated by XPS data. Dissociated Br is present on the surface after annealing at 400 °C.

5.7 Bibliography

[1] Lipton-Duffin, J.A., Ivasenko, O., Perepichka, D.F., and Rosei, F., *Synthesis of Polyphenylene Molecular Wires by Surface-Confined Polymerization*, Small, **5** (2009) pp. 592–597.

[2] Gutzler, R., Walch, H., Eder, G., Kloft, S., Heckl, W.M., and Lackinger, M., *Surface mediated synthesis of 2D covalent organic frameworks: 1,3,5-tris(4-bromophenyl)benzene on graphite(001), Cu(111), and Ag(110)*, Chemical Communications, 29 (2009) pp. 4456–4458.

[3] Walch, H., Gutzler, R., Sirtl, T., Eder, G., and Lackinger, M., *Material- and Orientation-Dependent Reactivity for Heterogeneously Catalyzed Carbon-Bromine Bond Homolysis*, Journal of Physical Chemistry C, **114** (2010) pp. 12604–12609.

[4] McCarty, G.S. and Weiss, P.S., *Formation and manipulation of protopolymer chains*, Journal of the American Chemical Society, **126** (2004) pp. 16772–16776.

[5] Lafferentz, L., Eberhardt, V., Dri, C., Africh, C., Comelli, G., Esch, F., Hecht, S., and Grill, L., *Controlling on-surface polymerization by hierarchical and substrate-directed growth*, Nature Chemistry, **4** (2012) pp. 215–220.

[6] *ACD/ChemSketch*, URL `www.acdlabs.com/resources/freeware/chemsketch/`, accessed July 2013.

[7] Van Hove, M.A., Koestner, R.J., Stair, P.C., Biberian, J.P., Kesmodel, L.L., Bartos, I., and Somorjai, G.A., *The Surface Reconstructions of the (100) Crystal Faces of Iridium, Platinum and Gold: 1. Experimental-Observations and Possible Structural Models*, Surface Science, **103** (1981) pp. 189–217.

[8] Kilian, L., Umbach, E., and Sokolowski, M., *A refined structural analysis of the PTCDA monolayer on the reconstructed Au(111) surface - "Rigid or distorted carpet?"*, Surface Science, **600** (2006) pp. 2633–2643.

[9] Lackinger, M., Griessl, S., Heckl, W.M., and Hietschold, M., *Coronene on Ag(111) investigated by LEED and STM in UHV*, Journal of Physical Chemistry B, **106** (2002) pp. 4482–4485.

[10] Lee, H.L., Strategies for the Formation of Covalently Bonded Nano-Networks on Metal Surfaces through Amine Reactions, Ph.D. thesis, Dublin City University, Dublin, 2012.

[11] Kuehnle, A., Linderoth, T.R., Hammer, B., and Besenbacher, F., *Chiral recognition in dimerization of adsorbed cysteine observed by scanning tunnelling microscopy*, Nature, **415** (2002) pp. 891–893.

[12] dos Reis, D.D., Negreiros, F.R., de Carvalho, V.E., and Soares, E.A., *Geometry of the Au(110)-(1 x 2) missing-row clean surface: A New LEED and DFT study*, Surface Science, **604** (2010) pp. 568–573.

[13] Hermann, K. and Van Hove, M.A., *LEEDpat*, URL `http://www.fhi-berlin.mpg.de/KHsoftware/LEEDpat/`, accessed July 2013.

[14] Sykes, E.C.H., Han, P., Kandel, S.A., Kelly, K.F., McCarty, G.S., and Weiss, P.S., *Substrate-mediated interactions and intermolecular forces between molecules adsorbed on surfaces*, Accounts of Chemical Research, **36** (2003) pp. 945–953.

[15] Stranick, S.J., Kamna, M.M., and Weiss, P.S., *Interactions and Dynamics of Benzene on Cu(111) at Low-Temperature*, Surface Science, **338** (1995) pp. 41–59.

[16] Bjork, J., Hanke, F., and Stafstrom, S., *Mechanisms of Halogen-Based Covalent Self-Assembly on Metal Surfaces*, Journal of the American Chemical Society, **135** (2013) pp. 5768–5775.

Chapter 6
Photoemission Study of the Exchange of Ni and Cu Ions for Porphyrin Molecules on the Cu(111) Surface

6.1 Introduction

In situ modification of the porphyrin macrocycle has been studied extensively in the last decade, as it offers many functionalisation possibilities. There have been several reports of *in situ* metalation of free base porphyrin molecules on surfaces using co-deposited metal atoms including zinc [1–3], cobalt [1, 4], iron [5–7], and cerium [8]. A similar experiment is described in Chapter 3 of this thesis, whereby H_2TBrPP molecules are metalated on Au(111) using Ni atoms.

Chapter 3 also describes the first reported *in situ* metalation of a free base porphyrin molecule using surface atoms, for H_2TBrPP on the Cu(111) surface [9]. There have been several subsequent studies of metalation using surface atoms [10–14].

This chapter investigates the *in situ* modification of a metalated porphyrin macrocycle. A Ni-Cu ion exchange is studied for two molecular systems: NiDBrDPP/Cu(111) and NiTBrPP/Cu(111). The ion exchange is characterised using photoemission and x-ray absorption spectroscopy, and the energetics of the exchange reaction are also analysed. The results presented in this chapter show that metalated porphyrins may be modified by surface atoms, such that the central metal ion is replaced by an atom from the substrate. To our knowledge, such a reaction has not yet been reported in the literature.

6.2 Photoemission Study of the Ni-Cu Ion Exchange for NiDBrDPP on the Cu(111) Surface

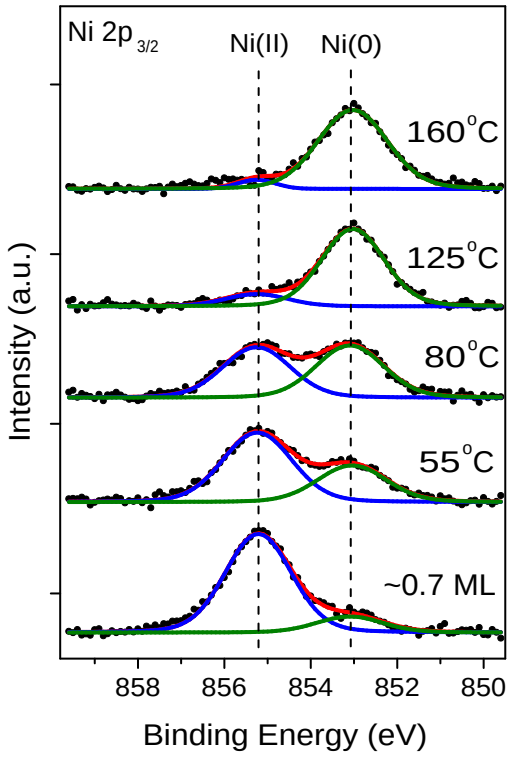

Figure 6.1: XPS for 0.7 ML of NiDBrDPP deposited on room temperature Cu(111) and annealed at the temperatures shown. Ni $2p_{3/2}$ region, $h\nu = 1253.6$ eV.

Figure 6.1 shows Ni $2p_{3/2}$ core level XPS data for 0.7 ML of NiDBrDPP deposited on Cu(111) at room temperature and annealed to sequentially higher temperatures for 45 minutes. The spectra were fitted with two Voigt peaks, at $2p_{3/2}$ binding energies of 855.2 eV and 853.0 eV respectively. The ratio of the areas of the two components is approximately 7:1 for room temperature deposition. The component at 855.2 eV binding energy is assigned to nickel in the macrocycle of the porphyrin, i.e. nickel in the 2+ state (Ni(II)) [15]. The component at 853.0 eV is assigned to nickel that is not in the macrocycle core, i.e. nickel with an

oxidation number of zero (Ni(0)) [16]. On increasing the annealing temperature the Ni(II) component decreases in intensity with a corresponding increase in the Ni(0) component. After annealing the sample at 160 °C for 45 minutes, nearly all the nickel present on the surface is in the Ni(0) state. Figure 6.2 shows the ratio of the intensity of the Ni(II) component to that of the Ni(0) component as a function of annealing temperature. The error bars are calculated from the standard deviation of multiple fits to room temperature data.

It is proposed that the Ni(II) ions in the macrocycle react with the Cu(111) surface and are replaced by copper atoms from the surface. Hence, the Ni(0) component at lower binding energy derives from nickel atoms on the copper surface which have exchanged with copper atoms. The presence of a Ni(0) component on deposition indicates that this exchange already occurs at room temperature, and is related to the reactivity of this particular substrate. As the sample is annealed the exchange proceeds until eventually there is only a very small percentage of nickel still present in the expected Ni(II) environment. The observed Ni-Cu exchange is similar to the previously reported metalation of H_2TBrPP by substrate atoms from the Cu(111) surface (Section 3.4) [9].

Figure 6.3 shows N 1s core level photoemission spectra for 1 ML of NiDBrDPP deposited on Cu(111) at room temperature and subsequently annealed at 100 °C

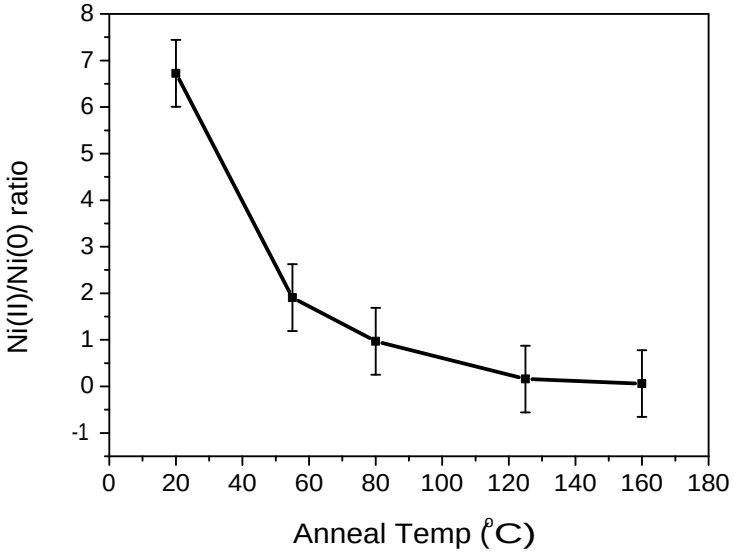

Figure 6.2: Ratio of intensities of Ni(II) and Ni(0) components as a function of annealing temperature for NiDBrDPP spectra shown in Figure 6.1.

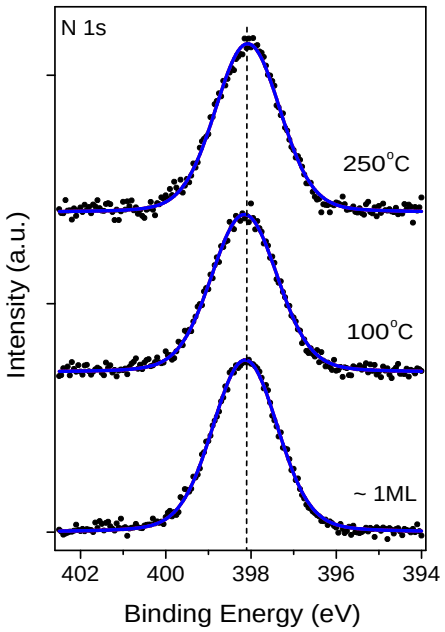

Figure 6.3: PES for 1 ML of NiDBrDPP deposited on room temperature Cu(111) and annealed at 100 °C and 250 °C. N 1s region, hν = 490 eV.

and 250 °C for 20 minutes. The spectra were each fitted with a single Voigt component, at a binding energy of 398.10 ± 0.08 eV, with a FWHM of 1.79 ± 0.06 eV. The presence of a single peak at each stage of the experiment indicates that the porphyrin molecules remain metalated throughout the experiment; there is no evidence for the presence of two N 1s components, which are characteristic of free base porphyrins. Hence, when the majority of nickel atoms are present on the surface in the Ni(0) state (see Figure 6.1), the NiDBrDPP molecules still have a metal atom in the centre of the macrocycle. A difference in the binding energy of the N 1s core level in Cu and Ni porphyrins could not be resolved.

Further evidence for the exchange of Ni and Cu ions is provided by x-ray absorption for the Ni *L*-edge for NiDBrDPP on Cu(111) measured on beamline D1011 in MAX-lab, Lund, Sweden in my absence (Figure 6.4). The molecules were deposited at room temperature, the sample was then cooled to 0 °C and later annealed to 240 °C for 140 minutes. The spectrum corresponding to the deposited and cooled molecular layer has a shoulder at 856.2 eV which is a

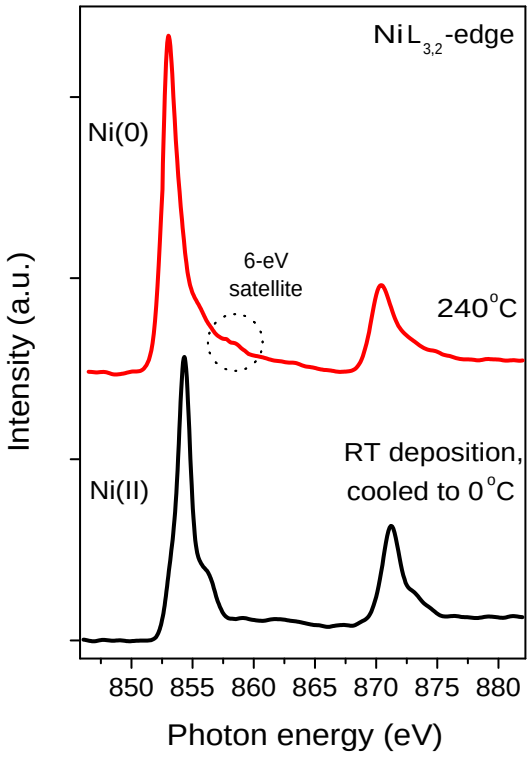

Figure 6.4: Ni $L_{3,2}$-edge XAS for NiDBrDPP deposited on room temperature Cu(111), cooled to 0 °C and annealed at 240 °C. Spectra were recorded at $\theta = 45°$.

characteristic feature of the Ni(II) $L_{3/2}$-edge for a nickel atom in the porphyrin macrocycle. Krasnikov *et al.* assign this feature to transitions of Ni $2p_{3/2}$ electrons to hybridized Ni 3d-N 2p empty states [17]. The spectrum recorded after annealing the sample to 240 °C has the sharp onset and asymmetric profile characteristic of a metallic peak. The spectrum has a main absorption line at 853.1 eV and a smaller feature approximately 6 eV higher in energy. Both of these features are associated with metallic nickel [17–21]. The smaller '6-eV' satellite (indicated with a dashed circle in Figure 6.4) has been well-documented in literature [18–21]. Ufuktepe *et al.* [20] have shown that the intensity of the 6-eV satellite is coverage dependent, and that for a Ni film 12 Å in thickness the satellite is weak. The coverage of Ni in the present experiment is much lower than 12 Å - the NiDBrDPP coverage is on the order of 1 ML, and there is only

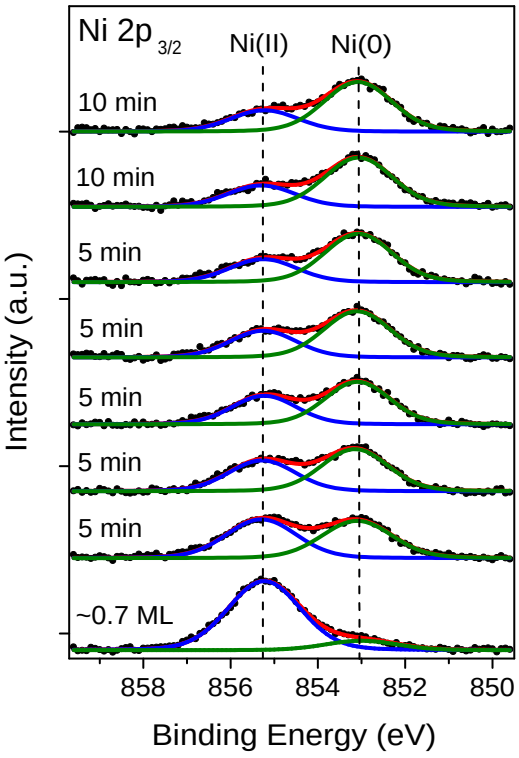

Figure 6.5: XPS for 0.7 ML of NiDBrDPP deposited on room temperature Cu(111) and repeatedly annealed at 100 °C. Ni $2p_{3/2}$ region, hν = 1253.6 eV.

one nickel atom per porphyrin. Hence the 6-eV feature in the present data is weak. It has been shown previously that Ni coverages of 0.07 ML still exhibit the spectral features characteristic of metallic Ni [21], therefore it is not unexpected that a 0.04 ML coverage of Ni on a copper substrate would still display metallic character.

The Ni(0) spectrum was fitted with a Doniac-Sunjic line-shape to account for the asymmetrical shape of the metallic peak. The Ni(0) peak position of 853.1 eV is in agreement with the accepted literature value for the metallic Ni absorption edge [18]. The Ni(II) absorption edge was fitted with a Voigt line-shape to represent the Ni(II) character and a Doniac-Sunjic line-shape to represent the slight shoulder at the L_3 edge due to a small Ni(0) component present in the room temperature spectrum. The presence of a component due to metallic nickel in the deposited molecular layer agrees with the XPS data previously shown

(Figure 6.1) where a small Ni(0) peak is observed on deposition - the ratio of the intensities of the Ni(II) and Ni(0) components is 5.4 for the XA spectra and 6.2 for the XPS data. The energy separation between the Ni(II) and Ni(0) absorption edges is 1.2 eV, in good agreement with values quoted in the literature [17]. The metallic character of the Ni present on the Cu(111) substrate after annealing the sample to 240 °C is further support for the proposed Ni-Cu exchange.

To further investigate the Ni-Cu exchange, 0.7 ML of NiDBrDPP was deposited on Cu(111) at room temperature and then repeatedly annealed to 100 °C in order to follow the evolution of the Ni signal. The first five anneals were of five minutes duration, the sixth and seventh were for ten minutes. After each anneal the Ni $2p_{3/2}$ region was scanned (Figure 6.5). The areas of the different components in the room temperature spectrum indicate that approximately 88 % of the nickel atoms are in the Ni(II) environment. The remainder have already exchanged with copper atoms from the substrate and are now present on the surface in the Ni(0) oxidation state.

Figure 6.6 shows the areas of the Ni(II) and Ni(0) components of the spectra in Figure 6.5 as a function of annealing time, where the areas of the component peaks were normalised to the total Ni signal for each spectrum. It can be seen from Figure 6.6 that the time dependence of the normalised areas of the Ni(II)

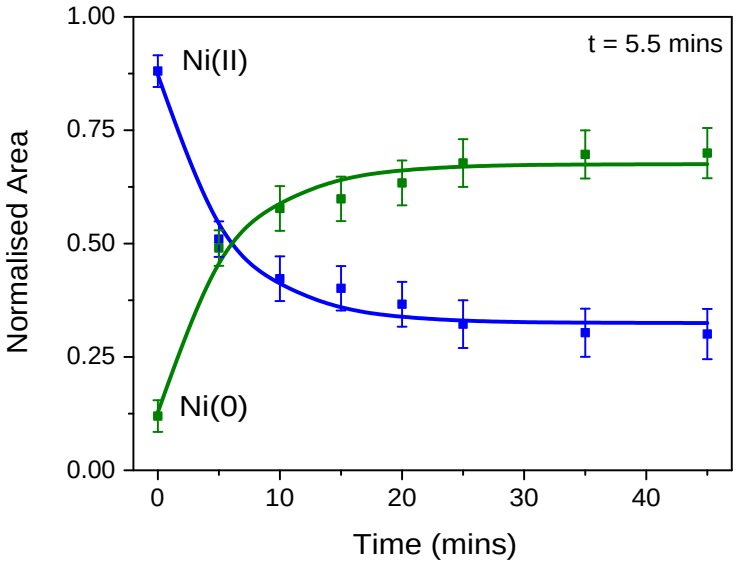

Figure 6.6: Normalised areas of Ni(II) and Ni(0) peaks for NiDBrDPP on Cu(111) from spectra in Figure 6.5 as a function of time.

peaks follows an exponential decay, with a time constant of 5.5 minutes. After approximately 25 minutes the data has reached a plateau, with the areas of the two component peaks showing very little change - 30 % and 70 % of the Ni atoms are in the Ni(II) and Ni(0) states respectively.

In conclusion, evidence for an exchange of Ni-Cu ions for NiDBrDPP on Cu(111) with a time constant of 5.5 minutes has been observed in both x-ray photoemission and x-ray absorption spectra.

6.3 Photoemission Study of the Ni-Cu Ion Exchange for NiTBrPP on the Cu(111) Surface

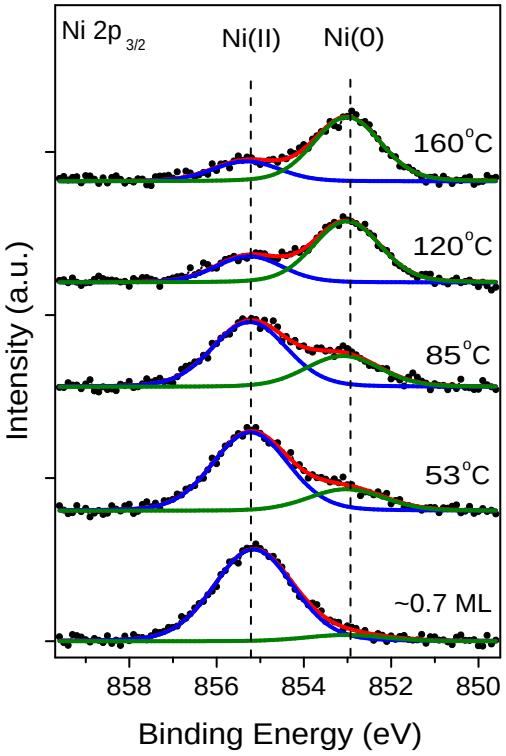

Figure 6.7: XPS for 0.7 ML of NiTBrPP deposited on room temperature Cu(111) and subsequently annealed at the temperatures shown. Ni $2p_{3/2}$ region, $h\nu = 1253.6$ eV.

The Ni-Cu exchange which takes place for NiDBrDPP on Cu(111) is also observed for NiTBrPP on Cu(111). Figure 6.7 shows Ni $2p_{3/2}$ XPS data recorded after a 0.7 ML coverage of NiTBrPP was deposited on Cu(111) at room temperature and annealed at the temperatures shown for 45 minutes. Similar behaviour to the NiDBrDPP experiment described above (Figure 6.1) is observed. The spectra were fitted with two Voigt components at $2p_{3/2}$ binding energies of 855.2 eV and 852.9 eV respectively. These components are assigned to Ni(II) and Ni(0) respectively. Figure 6.8 shows the ratio of the intensity of the Ni(II) component to that of the Ni(0) component as a function of annealing temperature. The ratio of the Ni components for NiDBrDPP previously shown in Figure 6.2 is also shown in red for comparison. The error bars are calculated from the standard deviation of multiple fits to room temperature data. At room temperature the Ni(II)/Ni(0) ratio is approximately 7:1 for NiTBrPP, similar to NiDBrDPP. Figure 6.8 shows that the Ni-Cu exchange proceeds at a slower rate for the NiTBrPP than for NiDBrDPP.

0.7 ML of NiTBrPP was deposited on Cu(111) at room temperature and then annealed to 100 °C eight times. The first six anneals were for five minutes each, the seventh anneal was for ten minutes, and the eighth anneal was for twenty

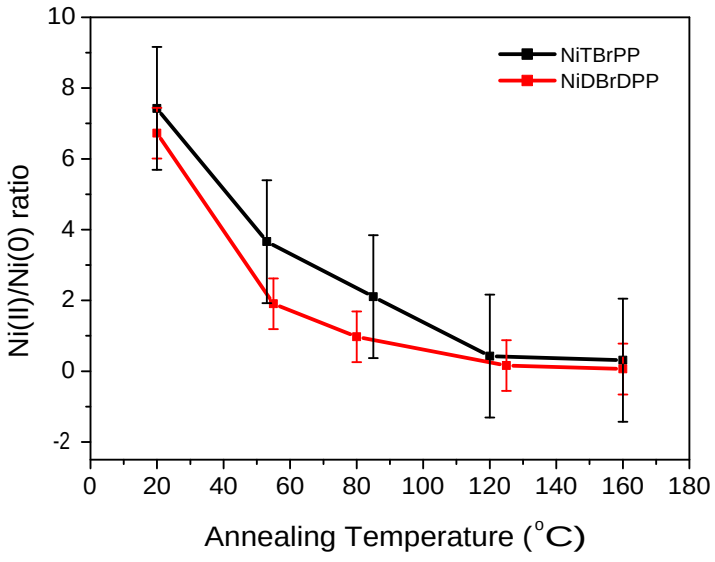

Figure 6.8: Ratio of intensities of Ni(II) and Ni(0) components as a function of annealing temperature for NiTBrPP spectra shown in Figure 6.7. Ratio of Ni component intensities for NiDBrDPP (Figure 6.2) plotted in red for comparison.

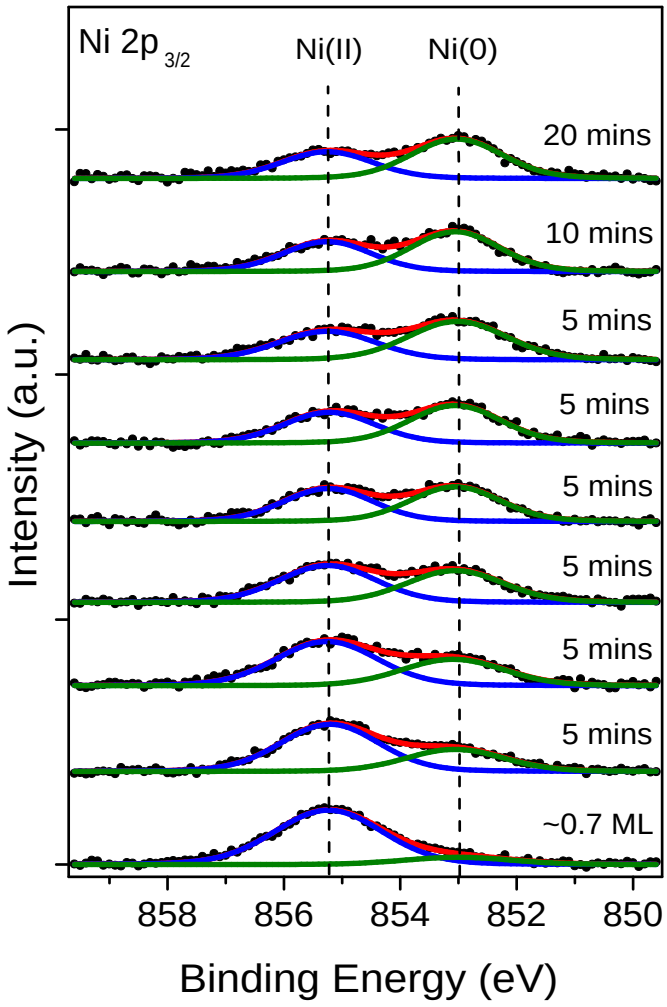

Figure 6.9: XPS for 0.7 ML of NiTBrPP deposited on room temperature Cu(111) and repeatedly annealed at 100 °C. Ni $2p_{3/2}$ region, hν = 1253.6 eV.

minutes. Figure 6.9 shows the resultant Ni $2p_{3/2}$ core level XPS spectra. The areas of the Ni peaks on deposition indicate that 88 % of the nickel atoms are in the Ni(II) environment. After the first anneal to 100 °C, 68 % of the nickel atoms are in the Ni(II) state. This again differs significantly from the NiDBrDPP data (Figure 6.5), where the Ni(II) and Ni(0) peak intensities are approximately equal after the first five minute anneal at 100 °C. In contrast, Figure 6.9 indicates that the two components are approximately equal in area only after the third

anneal to 100 °C (15 minutes) in the case of NiTBrPP. After the eighth anneal to 100 °C approximately 60 % of the nickel atoms are in the Ni(0) state for NiTBrPP, compared to 70 % for the NiDBrDPP experiment (Figure 6.5). This again indicates that the exchange is proceeding at a slower rate for NiTBrPP. The NiTBrPP molecular layer was annealed at 100 °C for a total of 60 minutes, however a smaller percentage of Ni atoms exchanged with copper than did for the NiDBrDPP molecular layer which was annealed for a total of 45 minutes at 100 °C.

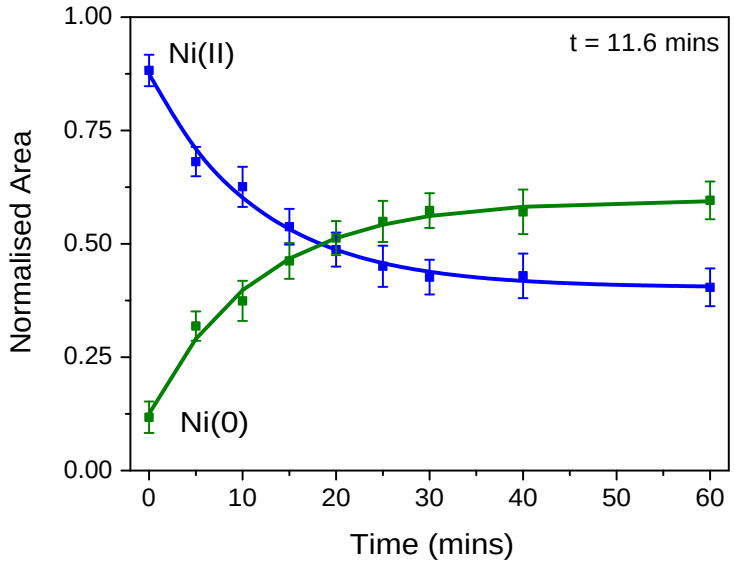

Figure 6.10: Normalised areas of Ni(II) and Ni(0) peaks for NiTBrPP on Cu(111) from spectra in Figure 6.9 as a function of time.

Figure 6.10 shows the normalised areas of the spectra in Figure 6.9 as a function of time, where the areas of the Ni(II) and Ni(0) peaks were normalised to the total Ni signal for each spectrum. Similar to the NiDBrDPP case (Figure 6.6) the time dependence of the Ni(II) areas can be fitted with an exponential decay curve. The NiTBrPP data has a time constant of 11.6 minutes, compared to 5.5 minutes for the NiDBrDPP data. Figure 6.10 also shows that the two curves corresponding to the Ni(II) and Ni(0) normalised areas intersect at 18 minutes, compared to 6 minutes for the NiDBrDPP molecules (Figure 6.6). For the NiTBrPP molecules a plateau is reached after approximately 40 minutes with 40 % and 60 % of nickel atoms in the Ni(II) and Ni(0) environments respectively compared to 30 % and 70 % for NiDBrDPP. It is clear that the Ni-Cu exchange

proceeds at a slower rate for the NiTBrPP relative to the NiDBrDPP molecules. This may be due to the increased height of the NiTBrPP macrocycle from the substrate caused by the twisting of the phenyl rings [22, 23].

6.4 Analysis of the Energetics of the Ni-Cu Ion Exchange

It has been shown that for annealing at 100 °C the Ni(II)/Ni(0) ratio stops changing after 25 minutes for NiDBrDPP (Figure 6.6) and after 40 minutes for NiTBrPP (Figure 6.10). Therefore each spectrum shown in Figure 6.1 and Figure 6.7 corresponds to an equilibrium at that anneal temperature, as the anneals were of 45 minutes duration.

The Ni-Cu exchange can be written as follows:

$$\text{Ni(II)P} + \text{Cu(0)} \Leftrightarrow \text{Cu(II)P} + \text{Ni(0)} \tag{6.1}$$

As the equilibrium constant K is defined as [24]

$$K = \frac{\text{concentration of products}}{\text{concentration of reactants}} \tag{6.2}$$

the equilibrium constant for the Ni-Cu exchange at each anneal temperature is given by

$$K = \frac{[\text{CuP}][\text{Ni}]}{[\text{NiP}][\text{Cu}]} \tag{6.3}$$

Noting that the concentration of surface Cu atoms is in large excess relative to the Ni porphyrin molecules and hence can be considered constant throughout the exchange [25], and normalising to the initial concentration of Ni porphyrin, Equation 6.3 can then be rewritten as

$$K = \frac{[\text{1-NiP}][\text{Ni}]}{[\text{NiP}]} \tag{6.4}$$

The areas of the components in Figure 6.1 and Figure 6.7 can be used to calculate the equilibrium constant K at each anneal temperature.

The behaviour of K as a function of temperature is given by the van't Hoff equation [25],

$$\frac{\mathrm{d}\,\ln K}{\mathrm{d}\,T} = \frac{\Delta_r H}{R T^2} \tag{6.5}$$

where $\Delta_r H$ is the reaction enthalpy at a given temperature T, and R is the molar gas constant, $8.314\,\mathrm{J\,mol^{-1}\,K^{-1}}$ [25]. The reaction isotherm equation [25],

$$\Delta G = -R\,T\ln K \tag{6.6}$$

where ΔG is the reaction Gibbs energy, can be substituted into the Gibbs Free Energy equation [25],

$$\Delta G = \Delta_r H - T\Delta S \tag{6.7}$$

where ΔS represents a change in entropy to give [24]

$$-R\,T\ln K = \Delta_r H - T\Delta S \tag{6.8}$$

which can be rewritten as [24]

$$\ln K = -\frac{\Delta_r H}{R\,T} + \frac{\Delta S}{R} \tag{6.9}$$

Hence a plot of $\ln K$ versus $1/T$ will have a slope equal to $-\Delta_r H/R$ and an intercept equal to $\Delta S/R$. Figure 6.11 shows $\ln K$ as a function of $1/T$ for both NiDBrDPP (black dataset) and NiTBrPP (red dataset). The Ni-Cu exchange is an endothermic reaction, as indicated by the negative slope [25]. The NiDBrDPP data has a slope of -6009 ± 209 and an intercept of 17 ± 1, while the NiTBrPP data has a slope of -5917 ± 588 and an intercept of 15 ± 2. From Equation 6.9 the reaction enthalpy $\Delta_r H$ for NiDBrDPP and NiTBrPP is $50 \pm 2\,\mathrm{kJ\,mol^{-1}}$ and $49 \pm 5\,\mathrm{kJ\,mol^{-1}}$ respectively. The reaction enthalpy is a measure of the difference in energy between the initial and final states of the reaction [25]. As a Ni atom is being replaced in the macrocycle by a Cu atom for both NiDBrDPP and NiTBrPP it is not surprising that the reaction enthalpy for each system is the same within experimental error.

From Equation 6.9 the entropy for the NiDBrDPP/Cu(111) and NiTBrPP/Cu(111) systems is $141 \pm 8\,\mathrm{J\,mol^{-1}\,K^{-1}}$ and $125 \pm 17\,\mathrm{J\,mol^{-1}\,K^{-1}}$ respectively. The difference in entropy for the two molecular systems is $16 \pm 19\,\mathrm{J\,mol^{-1}\,K^{-1}}$, with the NiDBrDPP/Cu(111) system having the higher value. This is to be expected as the NiDBrDPP molecules have a two-fold symmetry while the NiTBrPP molecules have four-fold symmetry. The contribution to the difference in entropy due to the difference in symmetry of the molecules can be evaluated using the Boltzmann equation [25],

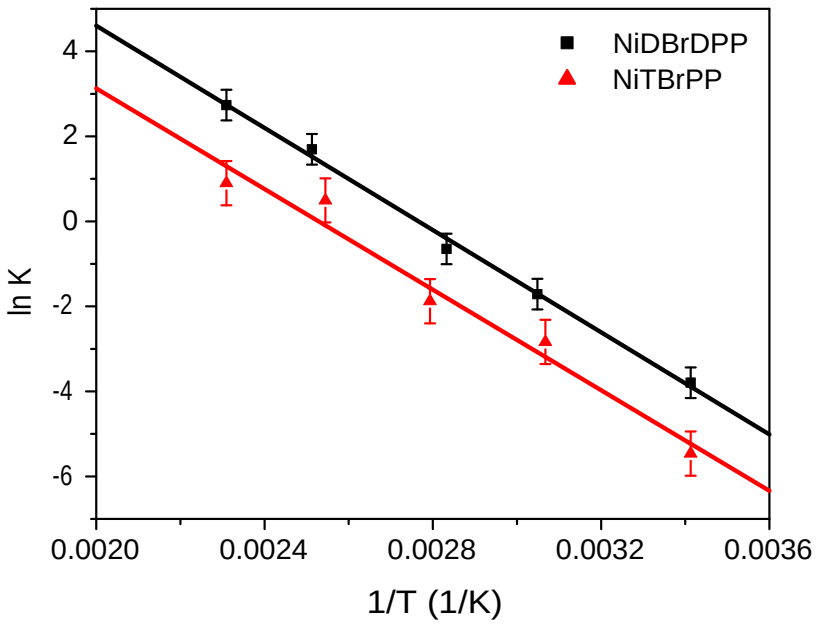

Figure 6.11: van't Hoff plot for NiDBrDPP (black) and NiTBrPP (red) on Cu(111) based on spectra in Figure 6.1 and Figure 6.7.

$$S = k_B \ln \Omega \tag{6.10}$$

where k_B is the Boltzmann constant ($1.38 \times 10^{-23}\,\mathrm{J\,K^{-1}}$) and Ω is the number of microstates available to the molecule. The two-fold symmetrical NiDBrDPP will have twice as many microstates as the four-fold symmetrical NiTBrPP, so it follows from Equation 6.10 that the difference in ΔS due to symmetry can be calculated as

$$\Delta_{sym} = k_B \ln 2 \tag{6.11}$$

For a mole of material this gives a Δ_{sym} of $6\,\mathrm{J\,mol^{-1}\,K^{-1}}$. This does not fully account for the $16 \pm 19\,\mathrm{J\,mol^{-1}\,K^{-1}}$ difference in entropy between the two systems. Distortions in the macrocycle and phenyl rings of the molecules may also contribute to the difference in entropy. It has been shown that for CuTPP on Cu(111) the phenyl rings exhibit a twist angle of 40°–50° [10]. Similar twisting of phenyl substituents has been observed for porphyrins on other metallic surfaces [22, 23]. In addition, saddling and ruffling of the pyrrole rings of porphyrins in general [26–28] and Ni porphyrins in particular [29] has been reported. Such

distortions will be factors in determining the entropy of the two systems.

In conclusion, the Ni-Cu exchange has the same reaction enthalpy for the NiDBrDPP/Cu(111) and NiTBrPP/Cu(111) systems. However there is a difference in entropy between the systems, with the NiDBrDPP/Cu(111) system having the higher value. Probable contributing factors to this difference in entropy include the different symmetries of the two molecules, and the distortions of the macrocycle and phenyl rings that are expected for porphyrin molecules deposited on a surface.

6.5 Summary

A Ni-Cu ion exchange has been observed for both NiDBrDPP and NiTBrPP on Cu(111). X-ray photoemission spectra for the Ni $2p_{3/2}$ core level show the Ni(II) peak decreasing with anneal temperature while the Ni(0) peak increases. The N 1s core level XPS spectra indicate that the porphyrins remain metalated throughout the experiment, therefore the Ni ion has been replaced by a Cu atom from the surface on annealing. X-ray absorption measurements for the Ni $L_{3,2}$-edge confirm the presence of metallic nickel on the surface after annealing. The time dependence of the Ni-Cu exchange was studied by repeated annealing of the NiDBrDPP/Cu(111) and NiTBrPP/Cu(111) surfaces to 100 °C. The decrease of the intensity of the Ni(II) peak as a function of time was fitted with an exponential decay using a time constant of 5.5 minutes for NiDBrDPP/Cu(111) and 11.6 minutes for NiTBrPP/Cu(111).

The equilibrium constant K at each anneal temperature was calculated for NiDBrDPP/Cu(111) and NiTBrPP/Cu(111). The reaction enthalpy and the entropy for each molecular system was calculated from a plot of ln K as a function of the inverse of anneal temperature. The reaction enthalpy for NiDBrDPP/Cu(111) and NiTBrPP/Cu(111) is $50 \pm 2\,\mathrm{kJ\,mol^{-1}}$ and $49 \pm 5\,\mathrm{kJ\,mol^{-1}}$ respectively. It is reasonable that the two systems have very similar values for reaction enthalpy as the same Ni-Cu exchange is happening in each case. There is a difference in entropy between the two systems of $16 \pm 19\,\mathrm{J\,mol^{-1}\,K^{-1}}$, with NiDBrDPP/Cu(111) having the higher value. This is to be expected as the different symmetry of NiDBrDPP and NiTBrPP leads to a greater number of available microstates for NiDBrDPP. Other factors such as distortions of the macrocycle and phenyl rings on the surface will also contribute to the difference in entropy between the two systems.

6.6 Bibliography

[1] Shubina, T.E., Marbach, H., Flechtner, K., Kretschmann, A., Jux, N., Buchner, F., Steinrueck, H.P., Clark, T., and Gottfried, J.M., *Principle and mechanism of direct porphyrin metalation: Joint experimental and theoretical investigation*, Journal of the American Chemical Society, **129** (2007) pp. 9476–9483.

[2] Kretschmann, A., Walz, M.M., Flechtner, K., Steinrueck, H.P., and Gottfried, J.M., *Tetraphenylporphyrin picks up zinc atoms from a silver surface*, Chemical Communications, 6 (2007) pp. 568–570.

[3] Flechtner, K., Kretschmann, A., Bradshaw, L.R., Walz, M.M., Steinrueck, H.P., and Gottfried, J.M., *Surface-confined two-step synthesis of the complex (ammine)(meso-tetraphenylporphyrinato)-zinc(II) on Ag(111)*, Journal of Physical Chemistry C, **111** (2007) pp. 5821–5824.

[4] Gottfried, J.M., Flechtner, K., Kretschmann, A., Lukasczyk, T., and Steinrueck, H.P., *Direct synthesis of a metalloporphyrin complex on a surface*, Journal of the American Chemical Society, **128** (2006) pp. 5644–5645.

[5] Buchner, F., Flechtner, K., Bai, Y., Zillner, E., Kellner, I., Steinrueck, H.P., Marbach, H., and Gottfried, J.M., *Coordination of iron atoms by tetraphenylporphyrin monolayers and multilayers on Ag(111) and formation of iron-tetraphenylporphyrin*, Journal of Physical Chemistry C, **112** (2008) pp. 15458–15465.

[6] Buchner, F., Schwald, V., Comanici, K., Steinrueck, H.P., and Marbach, H., *Microscopic evidence of the metalation of a free-base porphyrin monolayer with iron*, Chemphyschem, **8** (2007) pp. 241–243.

[7] Ecija, D., Trelka, M., Urban, C., de Mendoza, P., Mateo-Marti, E., Rogero, C., Martin-Gago, J.A., Echavarren, A.M., Otero, R., Gallego, J.M., and Mirandat, R., *Molecular conformation, organizational chirality, and iron metalation of meso-tetramesitylporphyrins on copper(100)*, Journal of Physical Chemistry C, **112** (2008) pp. 8988–8994.

[8] Weber-Bargioni, A., Reichert, J., Seitsonen, A.P., Auwaerter, W., Schiffrin, A., and Barth, J.V., *Interaction of cerium atoms with surface-anchored*

porphyrin molecules, Journal of Physical Chemistry C, **112** (2008) pp. 3453–3455.

[9] Doyle, C.M., Krasnikov, S.A., Sergeeva, N.N., Preobrajenski, A.B., Vinogradov, N.A., Sergeeva, Y.N., Senge, M.O., and Cafolla, A.A., *Evidence for the formation of an intermediate complex in the direct metalation of tetra(4-bromophenyl)-porphyrin on the Cu(111) surface*, Chemical Communications, **47** (2011) pp. 12134–12136.

[10] Diller, K., Klappenberger, F., Marschall, M., Hermann, K., Nefedov, A., Woell, C., and Barth, J.V., *Self-metalation of 2H-tetraphenylporphyrin on Cu(111): An x-ray spectroscopy study*, Journal of Chemical Physics, **136** (2012) pp. 014705–1–014705–13.

[11] Rojas, G., Simpson, S., Chen, X., Kunkel, D.A., Nitz, J., Xiao, J., Dowben, P.A., Zurek, E., and Enders, A., *Surface state engineering of molecule-molecule interactions*, Physical Chemistry Chemical Physics, **14** (2012) pp. 4971–4976.

[12] Goldoni, A., Pignedoli, C.A., Di Santo, G., Castellarin-Cudia, C., Magnano, E., Bondino, F., Verdini, A., and Passerone, D., *Room Temperature Metalation of 2H-TPP Monolayer on Iron and Nickel Surfaces by Picking up Substrate Metal Atoms*, ACS Nano, **6** (2012) pp. 10800–10807.

[13] Xiao, J., Ditze, S., Chen, M., Buchner, F., Stark, M., Drost, M., Steinrueck, H.P., Gottfried, J.M., and Marbach, H., *Temperature-Dependent Chemical and Structural Transformations from 2H-tetraphenylporphyrin to Copper(II)-Tetraphenylporphyrin on Cu(111)*, Journal of Physical Chemistry C, **116** (2012) pp. 12275–12282.

[14] Diller, K., Klappenberger, F., Allegretti, F., Papageorgiou, A.C., Fischer, S., Wiengarten, A., Joshi, S., Seufert, K., Ecija, D., Auwaerter, W., and Barth, J.V., *Investigating the molecule-substrate interaction of prototypic tetrapyrrole compounds: Adsorption and self-metalation of porphine on Cu(111)*, Journal of Chemical Physics, **138** (2013) pp. 154710–1–154710–9.

[15] Chen, M., Feng, X., Zhang, L., Ju, H., Xu, Q., Zhu, J., Gottfried, J.M., Ibrahim, K., Qian, H., and Wang, J., *Direct Synthesis of Nickel(II) Tetraphenylporphyrin and Its Interaction with a Au(111) Surface: A*

Comprehensive Study, Journal of Physical Chemistry C, **114** (2010) pp. 9908–9916.

[16] Marcus, P. and Hinnen, C., *XPS study of the early stages of deposition of Ni, Cu and Pt on HOPG*, Surface Science, **392** (1997) pp. 134–142.

[17] Krasnikov, S.A., Preobrajenski, A.B., Sergeeva, N.N., Brzhezinskaya, M.M., Nesterov, M.A., Cafolla, A.A., Senge, M.O., and Vinogradov, A.S., *Electronic structure of Ni(II) porphyrins and phthalocyanine studied by soft X-ray absorption spectroscopy*, Chemical Physics, **332** (2007) pp. 318–324.

[18] Chen, C.T., Sette, F., Ma, Y., and Modesti, S., *Soft-X-Ray Magnetic Circular-Dichroism at the $L_{2,3}$ Edges of Nickel*, Physical Review B, **42** (1990) pp. 7262–7265.

[19] Hsieh, H.H., Chang, Y.K., Pong, W.F., Pieh, J.Y., Tseng, P.K., Sham, T.K., Coulthard, I., Naftel, S.J., Lee, J.F., Chung, S.C., and Tsang, K.L., *Electronic structure of Ni-Cu alloys: The d-electron charge distribution*, Physical Review B, **57** (1998) pp. 15204–15210.

[20] Ufuktepe, Y., Akgul, G., Aksoy, F., and Nordlund, D., *Thickness and angular dependence of the L-edge X-ray absorption of nickel thin films*, X-Ray Spectrometry, **40** (2011) pp. 427–431.

[21] Nietubyc, R., Fohlisch, A., Glaser, L., Lau, J.T., Martins, M., Reif, M., and Wurth, W., *L-edge x-ray absorption fine structure study of growth and morphology of ultrathin nickel films deposited on copper*, Physical Review B, **70** (2004) pp. 235414–1–235414–8.

[22] Brede, J., Linares, M., Kuck, S., Schwoebel, J., Scarfato, A., Chang, S.H., Hoffmann, G., Wiesendanger, R., Lensen, R., Kouwer, P.H.J., Hoogboom, J., Rowan, A.E., Broering, M., Funk, M., Stafstrom, S., Zerbetto, F., and Lazzaroni, R., *Dynamics of molecular self-ordering in tetraphenyl porphyrin monolayers on metallic substrates*, Nanotechnology, **20** (2009) pp. 275602–1–275602–10.

[23] Buchner, F., Kellner, I., Hieringer, W., Goerling, A., Steinrueck, H.P., and Marbach, H., *Ordering aspects and intramolecular conformation of tetraphenylporphyrins on Ag(111)*, Physical Chemistry Chemical Physics, **12** (2010) pp. 13082–13090.

[24] Petrucci, R.H., Herring, F.G., and Harwood, W.S., General Chemistry: Principles and Modern Applications, 8th ed., Prentice Hall, New Jersey, 2002.

[25] Atkins, P.W., Atkins' Physical Chemistry, 8th ed., Oxford University Press, Oxford, 2006.

[26] Kim, H., Son, W.J., Jang, W.J., Yoon, J.K., Han, S., and Kahng, S.J., *Mapping the Electronic Structures of a Metalloporphyrin Molecule on Au(111) by Scanning Tunneling Microscopy and Spectroscopy*, Physical Review B, **80** (2009) pp. 245402–1–245402–6.

[27] Yang, Z.Y. and Durkan, C., *Edge and Terrace Structure of CoTPP on Au(111) Investigated by Ultra-High Vacuum Scanning Tunnelling Microscopy at Room Temperature*, Surface Science, **604** (2010) pp. 660–665.

[28] Klappenberger, F., Weber-Bargioni, A., Auwaerter, W., Marschall, M., Schiffrin, A., and Barth, J.V., *Temperature Dependence of Conformation, Chemical State, and Metal-Directed Assembly of Tetrapyridyl-porphyrin on Cu(111)*, Journal of Chemical Physics, **129** (2008) pp. 214702–1–214702–10.

[29] Senge, M.O., *Exercises in molecular gymnastics - bending, stretching and twisting porphyrins*, Chemical Communications, 3 (2006) pp. 243–256.

Chapter 7
Summary and Future Work

7.1 Summary of Results

The work presented in this thesis investigates the deposition, self-assembly, network formation, and molecule-substrate interaction of brominated molecules of different symmetry on metal surfaces, characterised using STM, XPS, LEED, and synchrotron radiation based PES and XAS. DFT calculations using the StoBe code were also carried out for comparison with some experimental results.

The four-fold porphyrin molecules, NiTBrPP and H_2TBrPP, and the three-fold TBB molecules form covalently bonded nano-networks on Au(111) extending over areas of the surface on the order of 10 000 nm^2. These networks are generally disordered, with approximately 25 % of pores exhibiting the ideal shape - square for the TBrPP networks, hexagonal for the TBB networks. The structures are thermally stable up to 500 °C, allowing for the recovery of the networks following exposure to ambient conditions [1]. The two-fold NiDBrDPP molecules form arrays of nano-lines on the Au(111) substrate, extending over regions of the surface on the order of 1000 nm^2. On the Au(110) substrate, NiDBrDPP nano-lines are oriented at angles of 127° and 230° with respect to the rows of the underlying Au 2×1 reconstruction.

Protopolymer networks are observed on Ag(111) and Cu(111) for depositions onto substrates held at elevated temperatures up to 100 °C. These structures are composed of debrominated molecules coordinated by metal atoms. Their formation at room temperature indicates that Ag and Cu are sufficiently reactive to catalytically cleave the C-Br bonds. These protopolymers are distinguished from covalently bonded networks by the larger centre-to-centre distance between adjacent molecules. Further thermal annealing results in the conversion of the protopolymer networks to covalently bonded structures.

It is found that the reactivity of the metal substrate has a significant effect

on the network formation. While there is minimal molecule-substrate interaction on Au(111), resulting in the formation of extensive nano-networks, the stronger molecule-substrate interaction on Cu(111) inhibits network formation and leads to significant disruption of the Cu surface after annealing at 350 °C and higher. Mass transport of Cu atoms and the related formation of islands, trenches and pits in the Cu surface are observed for high temperature annealing of NiTBrPP, H_2TBrPP, and TBB on Cu(111), demonstrating that the phenomenon is not specific to a particular molecule.

The *in situ* metalation of the free base H_2TBrPP molecule is investigated. The porphyrin is metalated on Au(111) with co-deposited Ni atoms, and is also metalated on Cu(111) using surface atoms. The latter is the first reported *in situ* metalation using atoms from the substrate [2]. The metalation reaction takes place via an intermediate state whereby the two iminic nitrogen atoms in the porphyrin macrocycle bond to the Cu atom while the two pyrrolic nitrogen atoms remain bonded to hydrogen atoms. Subsequent annealing leads to the release of the hydrogen and the full metalation of the porphyrin. The H_2TBrPP/Cu(111) metalation experiment carried out in the present work is the first reported direct observation of the intermediate state on a surface [2].

A Ni-Cu ion exchange is also observed for both NiTBrPP and NiDBrDPP on Cu(111), whereby the Ni(II) ion in the porphyrin macrocycle exchanges with a Cu atom from the substrate, resulting in Cu-metalated porphyrin molecules and metallic Ni atoms on the surface. The energetics of this exchange reaction are investigated, revealing that both the NiTBrPP/Cu(111) and NiDBrDPP/Cu(111) systems have the same enthalpy, but that the NiDBrDPP/Cu(111) has greater entropy, due in part to the difference in the symmetry of the molecules.

7.2 Future Work

In terms of future work, it would be interesting to investigate network formation with a four-fold doubly brominated, doubly iodinated porphyrin molecule. Building on the work of Grill *et al.* [3], this would allow for the stepwise dissociation of the halogens, resulting in the initial formation of nano-lines which can subsequently be cross-linked to form a nano-network. The Au(110) substrate may increase the ordering of the network, if the porphyrins show a preferential adsorption geometry in the 2×1 and 3×1 rows.

Cai *et al.* [4] have demonstrated the formation of graphene nano-ribbons using the same debromination bonding strategy as employed in this work and a subsequent cyclodehydrogenation reaction, using dibromo bianthryl molecules. It could be fruitful to modify this scheme by incorporating brominated porphyrin molecules into the nano-ribbons, for example by alternating the dibromo bianthryl molecule with the NiDBrDPP or a similar dibromo porphyrin. This would allow for the functionalisation of the graphene nano-ribbons by exploiting the many possible applications of porphyrins, for example their ability to axially coordinate ligands.

There are significant advantages to growing nano-networks on an insulating layer, as this allows the structures to be electronically decoupled from the metal substrates. Provided the insulating layer is sufficiently thin, the networks can still be imaged with STM. The growth of a phthalocyanine network on ultrathin NaCl islands deposited on the lattice matched Ag(100) surface has been previously reported [5]. Formation of porphyrin nano-networks on similar NaCl islands on Ag(100) could be attempted. If successful, the networks would be decoupled from the substrate in addition to being recoverable after exposure to ambient. Molecular deposition onto alkali halide islands on the Cu(111) surface could possibly lead to improved network formation compared to that observed in the present work, as the presence of the alkali halide layer would alter the molecule-substrate interaction.

The ion exchange observed for Ni-metalated porphyrin molecules on Cu(111) could be attempted with porphyrins synthesised with different metal centres, such as Co or Mn. This would allow the rate of ion exchange and the enthalpy and entropy of the different systems to be investigated. The ion exchange may also be affected by the presence or absence of an axial ligand. For example, Mn porphyrin is known to readily coordinate Cl. However, once deposited on a surface, the Cl

can be removed by pulsing with the STM tip, or annealing [6, 7]. If the Mn only exchanged with the Cu atoms following dissociation of the Cl, this would open up the possibility of a controllable *in situ* ion exchange.

The XPS and PES results in this thesis indicate that a significant number of Br atoms remain on the surface following dissociation from the molecules. However no conclusive evidence for the presence of the dissociated Br has been observed in the STM data, despite previous reports of Br on atomically clean surfaces [8–10]. Deposition of Br from a AgBr pellet source [11] would be a useful reference experiment, in order to elucidate the location of the Br on the surface after dissociation.

Further Density Functional Theory calculations would be a useful aid in interpreting the data. C and N K-edge XAS and C and N core level PES calculations for the nano-networks would be helpful in assigning absorption lines in experimental XA data and fitting component peaks to photoemission spectroscopy results. Calculated STM images would allow some of the more complicated STM data to be explained more readily.

7.3 Bibliography

[1] Krasnikov, S.A., Doyle, C.M., Sergeeva, N.N., Preobrajenski, A.B., Vinogradov, N.A., Sergeeva, Y.N., Zakharov, A.A., Senge, M.O., and Cafolla, A.A., *Formation of extended covalently bonded Ni porphyrin networks on the Au(111) surface*, Nano Research, **4** (2011) pp. 376–384.

[2] Doyle, C.M., Krasnikov, S.A., Sergeeva, N.N., Preobrajenski, A.B., Vinogradov, N.A., Sergeeva, Y.N., Senge, M.O., and Cafolla, A.A., *Evidence for the formation of an intermediate complex in the direct metalation of tetra(4-bromophenyl)-porphyrin on the Cu(111) surface*, Chemical Communications, **47** (2011) pp. 12134–12136.

[3] Lafferentz, L., Eberhardt, V., Dri, C., Africh, C., Comelli, G., Esch, F., Hecht, S., and Grill, L., *Controlling on-surface polymerization by hierarchical and substrate-directed growth*, Nature Chemistry, **4** (2012) pp. 215–220.

[4] Cai, J., Ruffieux, P., Jaafar, R., Bieri, M., Braun, T., Blankenburg, S., Muoth, M., Seitsonen, A.P., Saleh, M., Feng, X., Muellen, K., and Fasel, R., *Atomically precise bottom-up fabrication of graphene nanoribbons*, Nature, **466** (2010) pp. 470–473.

[5] Abel, M., Clair, S., Ourdjini, O., Mossoyan, M., and Porte, L., *Single Layer of Polymeric Fe-Phthalocyanine: An Organometallic Sheet on Metal and Thin Insulating Film*, Journal of the American Chemical Society, **133** (2011) pp. 1203–1205.

[6] Hulsken, B., van Hameren, R., Gerritsen, J.W., Khoury, T., Thordarson, P., Crossley, M.J., Rowan, A.E., Nolte, R.J.M., Elemans, J.A.A.W., and Speller, S., *Real-time single-molecule imaging of oxidation catalysis at a liquid-solid interface*, Nature Nanotechnology, **2** (2007) pp. 285–289.

[7] Beggan, J.P., Krasnikov, S.A., Sergeeva, N.N., Senge, M.O., and Cafolla, A.A., *Control of the axial coordination of a surface-confined manganese(III) porphyrin complex*, Nanotechnology, **23** (2012) pp. 235606–1–235606–10.

[8] Jones, R.G. and Kadodwala, M., *Bromine adsorption on Cu(111)*, Surface Science, **370** (1997) pp. L219–L225.

[9] Inukai, J., Osawa, Y., and Itaya, K., *Adlayer structures of chlorine, bromine, and iodine on Cu(111) electrode in solution: In-situ STM and ex-situ LEED studies*, Journal of Physical Chemistry B, **102** (1998) pp. 10034–10040.

[10] Nanayakkara, S.U., Sykes, E.C.H., Fernandez-Torres, L.C., Blake, M.M., and Weiss, P.S., *Long-range electronic interactions at a high temperature: Bromine adatom islands on Cu(111)*, Physical Review Letters, **98** (2007) pp. 206108–1–206108–4.

[11] Berner, N.C., Towards Stable Molecular Nanostructures on a Semiconductor Surface, Ph.D. thesis, Trinity College Dublin, Dublin, 2012.